IITK Directions

Krishanu Biswas
Sri Sivakumar
Nilesh Gurao *Editors*

Electron Microscopy in Science and Engineering

MOREMEDIA

Springer

IITK Directions

Volume 6

Editor-in-Chief

A. R. Harish, Indian Institute of Technology Kanpur, Kanpur, Uttar Pradesh, India

IITK Directions is an institutional series of the Indian Institute of Technology Kanpur. IITK Directions aims at presenting original contributions and reviews of important and cutting-edge topics by the faculty members and other stakeholders of IIT Kanpur in a consolidated manner. It is a platform that reflects upon the ongoing research and development activities, major achievements, and evolving trends. Each volume in the series focuses on a particular area of science and technology with chapters written by the faculty members, students and research staff. Each chapter is written in a journalistic tone for the peer group – readability and accessibility being important parameters. The volumes contain a survey of the subject as a whole and the extent of contributions recorded by the Institute faculty and students who participate so extensively in research.

The volumes in this series will be useful to researchers, practitioners, students, industry leaders, government officials and policy makers. Above all, the series serves as platform to publish the most cutting edge research summaries and evaluate the applications and impact of the research work undertaken at IIT Kanpur.

More information about this series at https://link.springer.com/bookseries/15345

Krishanu Biswas • Sri Sivakumar •
Nilesh Gurao
Editors

Electron Microscopy in Science and Engineering

Springer

Editors
Krishanu Biswas
Department of Materials Science and Engineering
Indian Institute of Technology Kanpur
Kanpur, India

Sri Sivakumar
Department of Chemical Engineering
Indian Institute of Technology Kanpur
Kanpur, India

Nilesh Gurao
Department of Materials Science and Engineering
Indian Institute of Technology Kanpur
Kanpur, India

ISSN 2509-6591 ISSN 2509-6605 (electronic)
IITK Directions
ISBN 978-981-16-5100-7 ISBN 978-981-16-5101-4 (eBook)
https://doi.org/10.1007/978-981-16-5101-4

This Springer imprint is published by the registered company Springer Nature Singapore Pte Ltd.
The registered company address is: 152 Beach Road, #21-01/04 Gateway East, Singapore 189721, Singapore

Series Editor's Preface

Several electron microscopes installed across various engineering and science departments at IIT Kanpur, India, have been used extensively to solve various problems catering to the need of both internal and external users. The current issue of Directions on Electron Microscopy (EM) is focused on the extensive use of scanning and transmission electron microscopy in multiple research frontiers including small-scale deformation studies, in situ testing, micro-composition analysis, advanced imaging, study of phase transformation behavior, morphological characterization of cells and viruses, electron-back-scatter diffraction, etc., that are currently being investigated at IIT Kanpur. The contents also provide a detailed and comprehensive view of the basic features and advanced capabilities of EM facilities to the scientific community.

I am thankful to the authors for their active participation in contributing the articles and to the editors for extensive review in raising the quality of the publication.

Based on the earlier experience, we expect this issue too to reach a wider community through the Springer platform.

A. R. Harish
Dean, Research and Development
Indian Institute of Technology Kanpur
Kanpur, India

Preface

Electron microscopy (EM) has become integral part of research and development of almost all the fields of science and engineering. 'Seeing is believing' is used as a common slogan for any experimental observation to justify the claims made, and hence, this is a common practice to make electron microscopes as 'part-and-parcel' of research activities. Electron microscopes vary a lot depending on the need and the observations we would like to make. The most common one is scanning electron microscope (SEM), whereas the sophisticated transmission electron microscope (TEM) and reflection electron microscope (REM) belong to a niche class of characterization tools. The first one uses a technique of raster scanning of high-energy electron beams to produce gamut of signals, utilized for imaging (standard and orientation imaging) and spectroscopy. On the other hand, TEM is an original type of microscope, allowing us to form images due to direct scattering of electron by means of passing through a high-voltage electron beam. Both imaging and spectroscopic analyses can routinely be performed in TEM with high resolution (sub nm level) and extremely high precision. The last type of EM, the REM, in general, uses the technique of detection of elastically scattered electron beam, reflected in any specimen. The commonly used methods involve reflection high-energy electron diffraction (RHEED) and reflection high-energy loss spectroscopy (RHELS), providing a host of information from the specimen under investigation.

In the last ten years, a substantial number of electron microscopy (EM) facilities have been set up in IIT Kanpur. A large number of scanning electron microscopes (SEMs) have been installed and utilized by researchers across various engineering (BSBE, CHE, CE, EE, ME, MSE) and science (CHM, ES, PHY) departments. Some of these microscopes are managed by individual departments, and some are housed in various central facilities (ACMS, AIC, Ion Beam Facility (IBF), Nanoscience and Soft Nanotechnology (Nano Center). The SEM facilities attached to the individual department are mainly utilized by the researchers from the respective departments. ACMS, IBF, Nano Center, being one of the major centers, housing large number of characterization facilities catering to the need of a large number of researchers from various departments, centers, and interdepartmental programs. In 2015, a new center, known as Advanced Imaging Center (AIC), has been established to house state-of-the-art facilities for high-resolution transmission electron microscopes. The TITAN® microscope has widely been utilized by institute communities for various research projects. This facility is capable of atomic resolution imaging, fast compositional analyses, and Lorenz microscopy for magnetic samples. In addition, there is a TEM (120 kV) for high-contrast cryomicroscopy with low beam dosage. Similarly, ACMS has augmented EM facilities recently with the addition of new SEMs and remote access to National Facility for Atom Probe Tomography (NFAPT) at IIT Madras. The ion beam facility has the dual-beam focused ion beam facility for wider use in the institute. IIT Kanpur is also going to establish a national facility of cryo-electron microscopy to cater to the need of burgeoning need of the researchers working at the interface of biological and other associated applied fields.

Therefore, these facilities have extensively been utilized by the large number of researchers, actively involving in the institute as well as other institutes from the region. It can be anticipated that the usage of EM facilities will see an exponential rise due to the increase of the research scholars and the need to perform high-quality research. Hence, it is pertinent to

provide a snapshot of these facilities with research performed utilizing these facilities, specifications, and capabilities of EM facilities available in various departments and central facilities. The special issue of direction will provide a detailed and comprehensive view of the basic features and advanced capabilities of the existing EM facilities to the scientific community within the institute as well as outside users. The present issue is intended to provide both 'breadth' and 'depth' of various EM facilities available in the institute.

We would like to thank all the contributing authors for their valuable contribution, patience, and meticulous corrections, the office of Dean (Research & Development), present (Prof. H. R. Harish), immediate past Dean (Prof. S. Ganesh) for providing all logistics and approval for the issue. It is also important to thank the Springer team, whose friendly reminders kept us engaged in the job of completion. We shall feel happy and elated if the community finds the content of the issue useful and worthy.

Kanpur, India

Krishanu Biswas
Sri Sivakumar
Nilesh Gurao

Contents

About the Editors

Dr. Krishanu Biswas Ranjit Singh Chair Professor at Department of Material Science and Engineering, Indian Institute of Technology (IIT) Kanpur has made significant contribution towards understanding of several important scientific and technological aspects of metallurgy and materials engineering. He obtained his Ph.D. from Indian Institute of Science (IISc) and B. Tech. from National Institute of Technology (NIT) Durgapur, India. His research interests ranges from complex concentrated alloys, high entropy materials, electron microscopy, novel processing of ceramic composites, development of alloy catalysis for energy and environment. He has received a number of awards, fellowships and professional reorganization. He has published over 190 papers in international repute peer reviewed journals, three patents, ten book chapters, two books and delivered 50 invited talks in different national and international conferences. He has completed several projects from Indian Space Research Organization (ISRO) and Indian National Science Academy (INSA) to bigger projects from Department of Science and Technology (DST), Department of Biotechnology (DBT), Board of Research on Nuclear Sciences (BRNS). He is a member of Indian National Young Academy of Sciences (INYAS) and Global Young Academy (GYA). He is also recipient of Young Faculty fellowship from IIT Kanpur.

Dr. Sri Sivakumar is currently working as professor in Department of Chemical Engineering, Indian Institute of Technology (IIT) Kanpur. He also serves as Associate Faculty in Materials Science Programme and Co-ordinator of Centre for Nanoscience and Advanced Imaging Centre. He obtained his B.Sc. (Tech) and M.Sc. (Tech) degree from University Institute of Chemical Technology (ICT), Mumbai in 1997 and 2001 respectively. He obtained his Ph.D. degree from University of Victoria in 2006. Dr. Sivakumar carried out his postdoctoral research at the University of Melbourne. Dr. Sivakumar's research focuses on development of functional nanomaterials for biological and environmental/catalytic applications. He has authored over 100 publications, four book chapters, 11 patents and edited one book. He has obtained thirteen grants worth of Rs. 13 crores from government agencies as well as from industry (Chevron, HPCL, Aarti Industries, and TCS). Furthermore, he has graduated 17 Ph.D. students and is currently supervising ten Ph.D. students. Professor Sivakumar works on synthesis of functional nanomaterials for catalysis and biomedical applications. His work on catalysis includes both chemical and electro catalysis.

Dr. Nilesh Gurao is currently an Associate Professor at the Department of Materials Science and Engineering at Indian Institute of Technology (IIT) Kanpur. He obtained his Ph.D. in Materials Engineering from Indian Institute of Science (IISc), Bengaluru, India in 2010 and Bachelors in Technology from Visvesvaraya National Institute of Technology, India in 2005 prior to attending the University of Saskatchewan, Saskatoon, Canada for a postdoctotoral position. He has established the Microstructure-Texture-Stress Laboratory at IIT Kanpur and has graduated five Ph.D. and 12 master's students till date. The research work from the group has resulted in multiple projects with different government and private funding agencies and high quality journal publications. Dr. Gurao is a recipient of the INSA Young Scientist award

from the Indian National Science Academy and the Young Metallurgist of the Year award from Ministry of Steel, Government of India. His current research interests include mechanical behavior of materials, crystallographic texture, crystal plasticity simulations and diffraction studies with special emphasis on in situ diffraction experiments across real and reciprocal space.

Small-Scale Deformation Experiments Inside an SEM

Sumit Basu

1 Introduction

The first prototype of the scanning electron microscope (SEM) was built in 1937 by Manfred von Ardenne in Germany. Commercialization of the SEM by the Cambridge Scientific Instrument Company began in 1965. Reports of in-situ deformation and fracture experiments on small-scale samples conducted inside the vacuum chamber of started appearing soon after, in mid-70s and 80s (Ujiiye et al. 1971; Dingley 1973; Stephens and Hoeppner 1988; Roberts and Lehtinen 1976; Nakagawa et al. 1980).

In-situ deformation experiments are now routinely performed, and all modern microscopes provide ports on the vacuum chamber that can be used to interface deformation stages with control instrumentation outside (see, Fig. 1). Deformation stages (which basically are miniature universal testing machines or UTMs), often with a facility to heat the sample during deformation, are also available. These miniature UTMs are customized to 'dovetail' snugly into the movable stage of microscopes of all major makes. A compression stage assembled from off-the-shelf components and instrumented at IIT Kanpur is shown in Fig. 2.

Small-scale deformation experiments offer a few very unique opportunities to the materials scientist. Micro-deformation mechanisms that operate during deformation and fracture of materials can often be clearly visualized on the surface of small samples. In-situ visualization of micro-mechanical events leading to plastic deformation and failure has been explored most widely for steel (Alaie et al. 2015; gang Liu et al. 2019; Prochazka et al. 2017; Li et al. 2019; Yang et al. 2015), titanium (Barkia et al. 2015; Jun et al. 2016; Jieping et al. 1989; Bao et al. 2010), and its alloys (Niwa and Ito 1987; Zhang et al. 2018; Li et al. 2014; Zhang et al. 2019), though other metals like aluminum alloys (Motsi et al. 2014), e.g., nickel (Perusin et al. 2004) and chromium (Fritz et al. 2017) have been studied as well. Often, imaging of the micro-deformation process is accompanied by simultaneous electron backscatter diffraction (EBSD)-based crystallographic characterization (Wu et al. 2016; Li et al. 2008; min Wang et al. 2005; Bruck et al. 1989).

For non-metals too, several innovative experiments have been reported. Investigation of brittle fracture in thermal barrier coatings (Wu et al. 2008; Arai et al. 2010), cell wall plasticity in open cell forms (Zhou et al. 2004), cell deformation in wood (Adusumalli et al. 2010), and breakage mechanisms in micron-sized silica, alumina, and titania particles (Romeis et al. 2015; Sarobol et al. 2016; Herre et al. 2017) are examples where insights into the micro-deformation processes leading to fracture could not have been obtained without resorting to small-scale in-situ experiments. A slideshow accompanying this article showcases some in-situ deformation experiments that have been conducted at IIT Kanpur.

Is it possible to perform more quantitative experiments in-situ? For instance, can we accurately determine the uniaxial stress–strain response or the fracture toughness of a micron-sized sample while observing the micro-mechanisms driving its deformation? Such experiments are especially useful when we need to quantify structure property relationships in hazaradous materials like irradiated steel (Bruck et al. 1989), which can be handled only in very small quantities.

Electronic Supplementary Material
The online version of this chapter (https://doi.org/10.1007/978-981-16-5101-4_1) contains supplementary material, which is available to authorized users.

S. Basu (✉)
Department of Mechanical Engineering, Indian Institute of Technology Kanpur, Kanpur, Uttar Pradesh 208016, India
e-mail: sbasu@iitk.ac.in

K. Biswas et al. (eds.), *Electron Microscopy in Science and Engineering*, IITK Directions 6,
https://doi.org/10.1007/978-981-16-5101-4_1

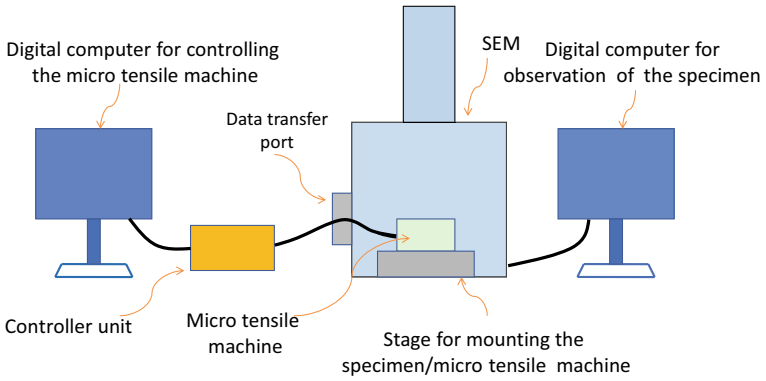

Fig. 1 Schematic of an in-situ micro-deformation set up. The deformation stage is placed inside the vacuum chamber of the SEM. It communicates with the control hardware placed outside through connectors on a port on the chamber

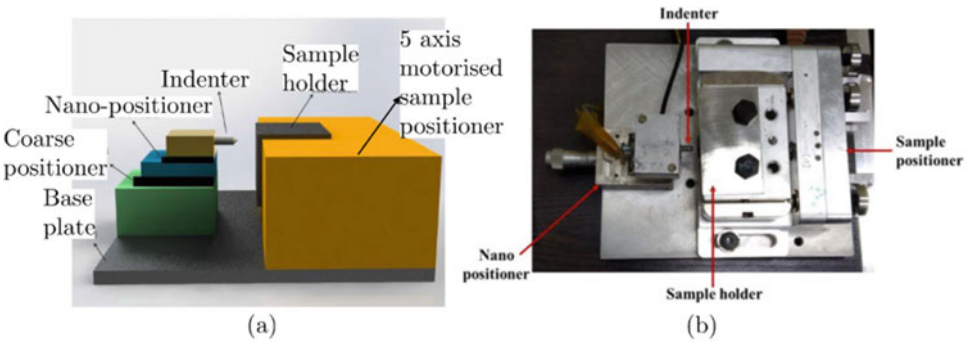

Fig. 2 Block diagram of a micro-compression device assembled at IIT Kanpur is shown in (**a**). Top view of the actual device is shown in (**b**). This device is designed to fit into the stage of a Zeiss Sigma VM FESEM

2 In-Situ Digital Image Correlation

2.1 A Brief Introduction to DIC

A miniature stage like the one shown in Fig. 2 is equipped with a load cell and a linear actuator, both of which communicate with softwares outside the vacuum chamber (see Fig. 1). The load applied to the specimen is directly obtained from the load cell. However, the position of the actuator gives the displacement imparted to the gripped end of the specimen. This can be converted into an average strain over the entire specimen. In case of non-homogeneous deformation, the average strain is not a reliable measure. If accurate and localized strain measurement is required (as would be the case when deformation is large and localized, e.g., at shear bands), more sophisticated techniques will be required. How can we measure the strain accurately over a surface while it is being simultaneously deformed and exposed to an electron beam inside the vacuum chamber? As far as conducting quantitative in-situ experiments is concerned, this is a difficult hurdle.

Fortunately, in recent years, an elegant solution has emerged in the form of two-dimensional digital image correlation (DIC), which is a full-field technique for measuring displacements and strains over a specified domain on the surface of the sample (Chu et al. 1985; Bruck et al. 1989; Sutton et al. 2007, 2009). A brief description of the method is given here. Several detailed reviews of the theoretical underpinnings and implementation of the method are available (Sutton et al. 2009; Pan et al. 2009; Hild and Roux 2006).

First, a random speckle pattern is generated all over a domain on the flat surface of the deforming body (lying, say, on the $x-y$ plane), over which displacements $u(x, y)$, $v(x, y)$ are to be determined. In two-dimensional DIC, it is assumed that out of plane displacements are absent. The speckle pattern can be generated by spraying black and white paint on the surface. Alternatively, the natural texture of the surface can be used. In any case, the domain over which displacements and its gradients are measured must have a random gray-scale intensity distribution. For ex-situ DIC, the surface of the specimen is imaged with a digital camera while it is deforming. An image of the deformed domain is compared with the initial reference domain to find the displacement and strain fields.

If a point (x, y) in the reference image maps to a point (x^*, y^*) in the deformed, it is assumed that the intensity $f(x, y)$ in the reference image is equal to $f^*(x^*, y^*)$ in the

deformed. Note that both f and f^* are functions that take only integer values between 0 and 255, corresponding to the gray-scale levels.

Consider the domain shown on the left of Fig. 3 which deforms as shown on the right. A sub-domain of $m \times n$ pixels shown by the red rectangle in the left figure deforms to the red quadrilateral in the right one. Provided the sub-domain is small, the displacement of an arbitrary point Q (to Q') inside it can be related to that of its center P (to P'). If the coordinates of P are (x_0, y_0) and that of Q are $(x_0 + \Delta x, y_0 + \Delta y)$, the deformed position of Q' can be written as

$$x_{Q'} = x_Q + u_0 + \partial u \partial x|_P \Delta x + \partial u \partial y|_P \Delta y,$$
$$y_{Q'} = y_Q + v_0 + \partial v \partial x|_P \Delta x + \partial v \partial y|_P \Delta y.$$

Here, (u_0, v_0) are displacements of the center of the sub-domain and $x_Q = x_0 + \Delta x, y_Q = y_0 + \Delta y$.

In the above, the quantities $u_0, v_0, \partial u \partial x, \partial u \partial y, \partial v \partial x, \partial v \partial y$ are unknown for a given sub-domain. They are obtained using the assumption that, for the best choice of these six quantities, the correlation between the intensities of the $m \times n$ pixels in the red rectangle and the red quadrilateral will be the highest among all possible red quadrilaterals that can be placed in the image of the deformed domain. In other words, a measure of the correlation

$$C = \sum_{m \times n} [f(x, y) - f^*(x^*, y^*)] \sum_{m \times n} f^2(x, y), \qquad (1)$$

attains a maximum when we hit upon the correct set of the six quantities. The search is carried out in a systematic manner using standard algorithms that are described in, e.g., Bruck et al. (1989).

2.2 Issues Associated with In-Situ DIC

The above procedure works well for macroscopic samples ex-situ. For experiments conducted inside the vacuum chamber of an SEM, several additional issues need to be addressed. Many of these are related to the manner in which an image is produced in the SEM. A labeled schematic showing the major components of a typical field emission scanning electron microscope (FESEM) is presented in Fig. 4a.

The electron beam emerging from the field emitter follows the central axis and passes sequentially through micron-sized apertures and is focused by the electro-magnetic fields of the lens system. Finally, the scan coils that are part of the objective lens displace the beam through computer control so that it is focused to a sequence of points on the area of interest (see, Fig. 4b). The gray-scale value of a pixel on each digital image is a measure of the interaction of the electron beam with a corresponding point on the sample as recorded by a electron detector (e.g., an Everhart–Thornley detector for secondary electrons emanated from the surface on interaction with the incoming beam). The image produced by the raster scanning action of the beam is different from the 'true image' produced in a light microscope.

In an SEM micrograph, all pixels are not imaged at the same time. This is unlike an 'true image' taken under normal light. Assume that the scanning of the area on the sample involves W locations along a line, repeated for H lines (see, Fig. 4b). It is mapped onto a gray-scale image, where $\boldsymbol{\zeta} : (\boldsymbol{m}, \boldsymbol{n})$ denotes a pixel position. In a stack of N images taken in succession, if the time at which scanning for image

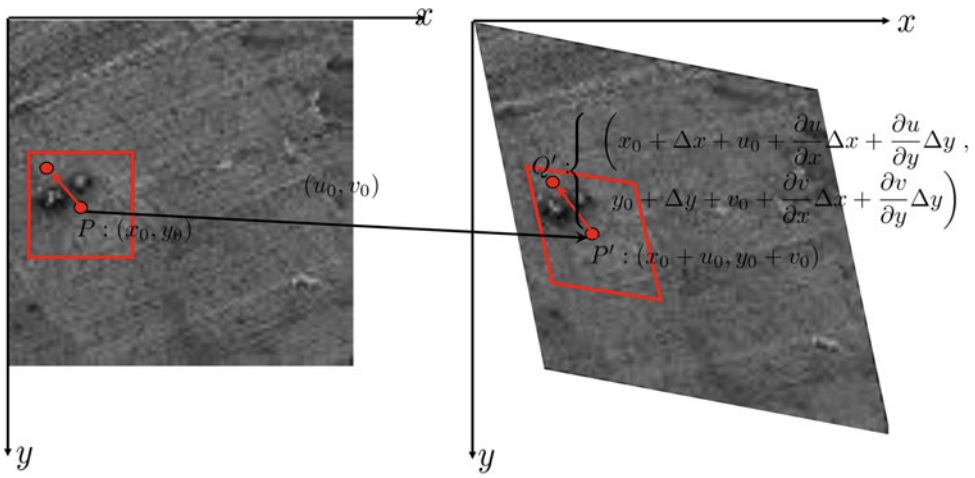

Fig. 3 The complete initial domain over which displacement field is computed by DIC is shown in the left. This domain deforms in the manner shown on the right. The point $P : (x_0, y_0)$ lies at the center of the red rectangular sub-domain, which deforms to the red quadrilateral. Deformed positions of neighboring points P and Q in the initial sub-domain are denoted by P' and Q'. The displacement components of point P are given by $u_0(x, y)$ and $v_0(x, y)$

i was started is t_i, the time at which the pixel at $\boldsymbol{\zeta}$ is scanned, will be given by:

$$t(\boldsymbol{\zeta}) = \boldsymbol{t_i} + (\boldsymbol{m} - \boldsymbol{1})\boldsymbol{t_l} + (\boldsymbol{n} - \boldsymbol{1})\boldsymbol{t_d}, \tag{2}$$

where t_d is the time spent by the beam on each location (marked by a solid circle in Fig. 4b) on the sample, t_d is the time required to reposition the beam from the end of a line to the beginning of the next. The time required to scan a line $t_l = Wt_d + t_p$.

The major artifacts in an SEM image and their underlying reasons are well established (Jin and Li 2015; Snella 2010; Kammers and Daly 2013; Maraghechi et al. 2018, 2019). These can be divided into time independent and dependent ones.

The most important time-independent artifact is spatial distortion. As explained in Maraghechi et al. (2018), spatial distortion is probably caused by the slight non-uniformity of the electromagnetic field created by the objective lens. Images with lower magnification exhibit higher spatial distortion because the beam in these cases, needs to deviate significantly from the central axis. In doing so, it is affected by the non-uniform fields that exist near the outer periphery of the objective lens (Kammers and Daly 2013).

Drift distortions on the other hand are time-dependent artifacts that are present at all magnifications. These distortions occur due to relative motion between the beam and the surface of the specimen. Among other reasons, they are caused by interaction of the beam with a sample surface that has acquired charges or is undergoing thermal deformation. The extent of drift distortion can change nonlinearly with time and its temporal variation is often dependent on the conditions in which the test is performed.

An example of drift distortion is shown in Fig. 5. Exactly the same region in a stationary sample is scanned at two different points of time. The results are shown in Fig. 5a, b. The rectangular box in Fig. 5a, b is centered at the same pixel location. A close look at the feature inside the box shows that it has shifted a bit in the later image. The extent of the shift can be quantified by performing a DIC using the first image as the reference and the second as the deformed (see, Fig. 6a, b). This reveals that the second image has shifted due to drift by $\sim 15 - 20$ pixels in both the x and y directions.

Some of the artifacts can be reduced by adjusting the SEM parameters. Faster scanning (to reduce the difference between t_i and $t(\boldsymbol{\zeta})$), higher beam voltage leading to smaller spot sizes, and software-based averaging techniques may help in alleviating some of the distortions. However, it should be noted that many of these adjustments add noise to the SEM image. In fact, filtering noise from the images obtained is an essential first step in applying DIC to them. Correlations tend to be erratic if this is not done properly.

Lastly, the issue of creating a proper speckle pattern on a sample has to be kept in mind while performing in-situ deformation experiments that rely on DIC. The natural texture was used in all cases reported here. But this may not be always possible. We have attempted to create nanospeckle patterns by 'sprinkling' nanoparticles on the surface of interest. Fluorescent nanoparticles have been used to map nanoscale displacement fields around silica micro-particles (embedded in an elastomer matrix deformed in tension) through DIC (Berfield et al. 2006).

3 Toward Effective Distortion Correction Techniques

Methods for correcting for both drift and spatial distortions have been proposed by Sutton et al. (2007, 2009). More recently, a unified framework for digital correlation incorporating corrections for distortions has been proposed (Maraghechi et al. 2018). We have implemented the methods due to Sutton et al. (2007, 2009) where images need to be post-processed before regular DIC techniques are applied. Post-processing includes initial de-noising and correcting for spatial and drift distortions.

The effects of all the artifacts are described through a set of virtual examples. In Fig. 7a, a 600×500 pixel-sized virtual sample with an equilateral triangular cut-out at the center is prepared using MATLAB. Random noise is added to the non-white pixels to incorporate an essential feature of a real SEM micrograph. Imagine that we are scanning a 319×287 pixel-sized sub-domain (i.e., $H = 287$ and $W = 319$) around the triangular cut-out in this sample. The total scanning time is $T = H(Wt_d + t_p)$

Imagine that the sample deforms in simple shear at a slow rate $\dot{\gamma}$, such that $1/\dot{\gamma} \gg T$. In this case, the equilateral triangle distorts marginally during the scan as shown in Fig. 7b. However, if $1/\dot{\gamma} \simeq T$, the distortion becomes significant as shown in Fig. 7c. This distortion is simply due to the fact that all pixels in the sub-domain are not scanned simultaneously. Spatial distortion, added to this, causes significantly blurring of the edges of the triangle (see, Fig. 7d). Finally, we have added a fictitious downward displacement due to drift distortion that is simply a linear function of time (and, unrealistically, not a function of position). This causes further distortion of the triangular feature. Performing correlation between Fig. 7e and the corresponding sub-domain of (a) will not reveal that the underlying mechanical deformation being imparted is just a simple shear.

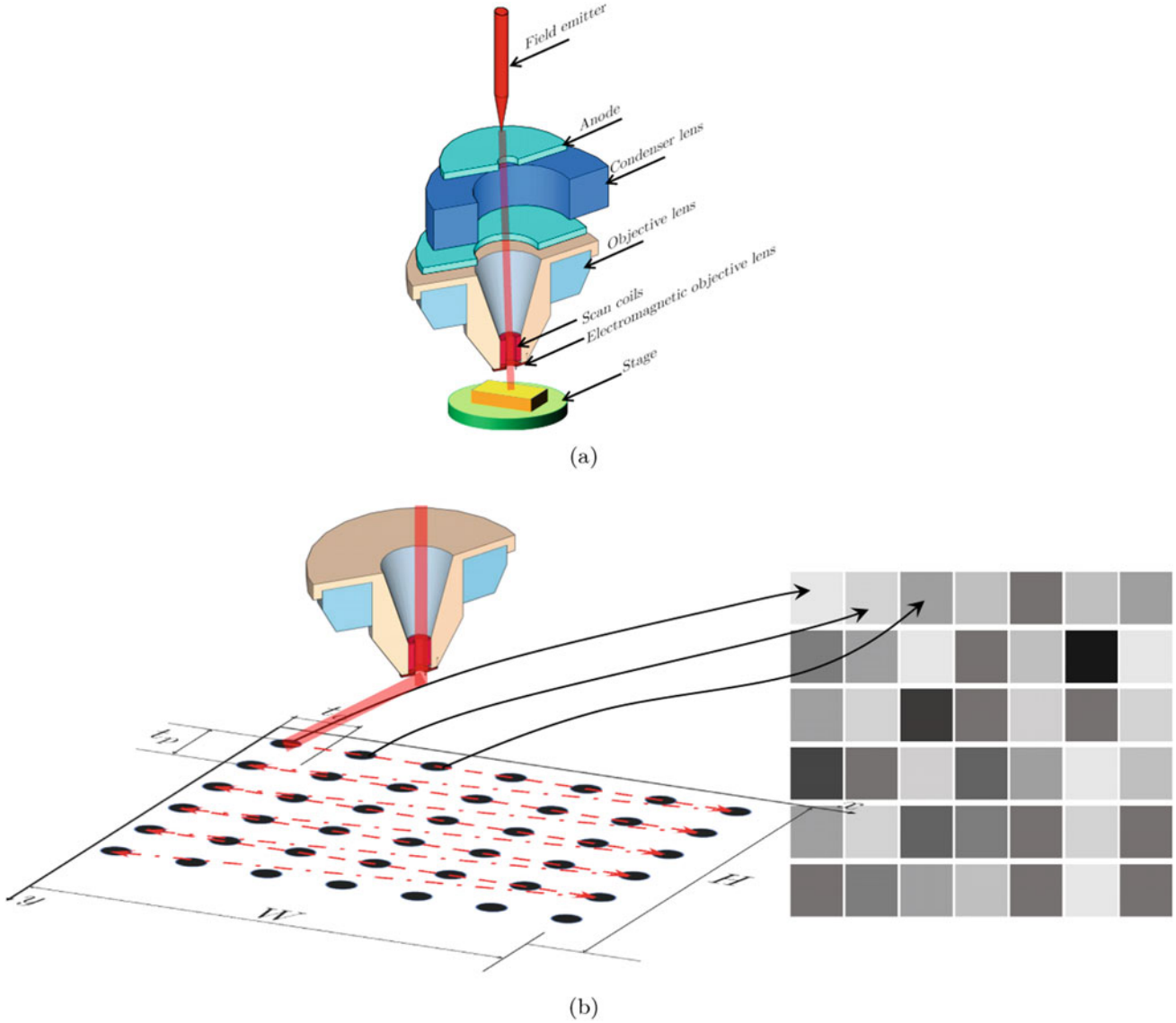

Fig. 4 Major components in the beam column of a FESEM are shown in (**a**). The process by which a digital image is produced from a raster scan of the sample surface with the electron beam is shown in (**b**)

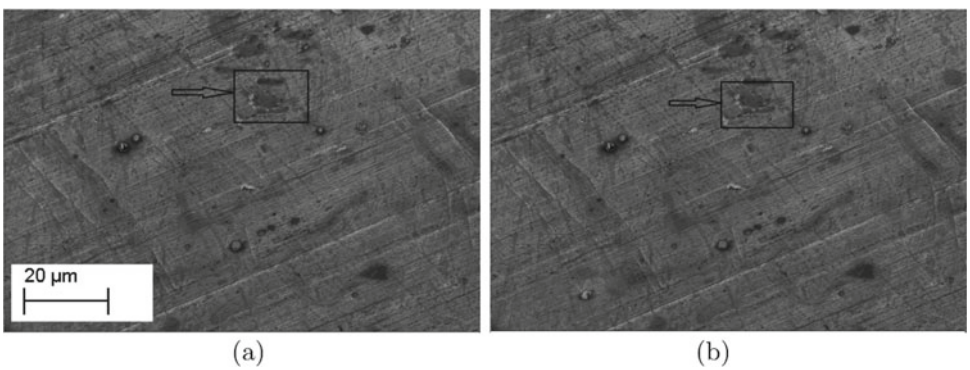

Fig. 5 FESEM images of exactly the same region in a sample taken a few seconds apart. The black rectangle is used to mark the same sub-region in both the images. Drift of the feature inside the rectangle has caused it to shift slightly. The natural texture in the images is used to compute the full-field displacements over the region. The u component is shown in (**c**) while V is in (**d**)

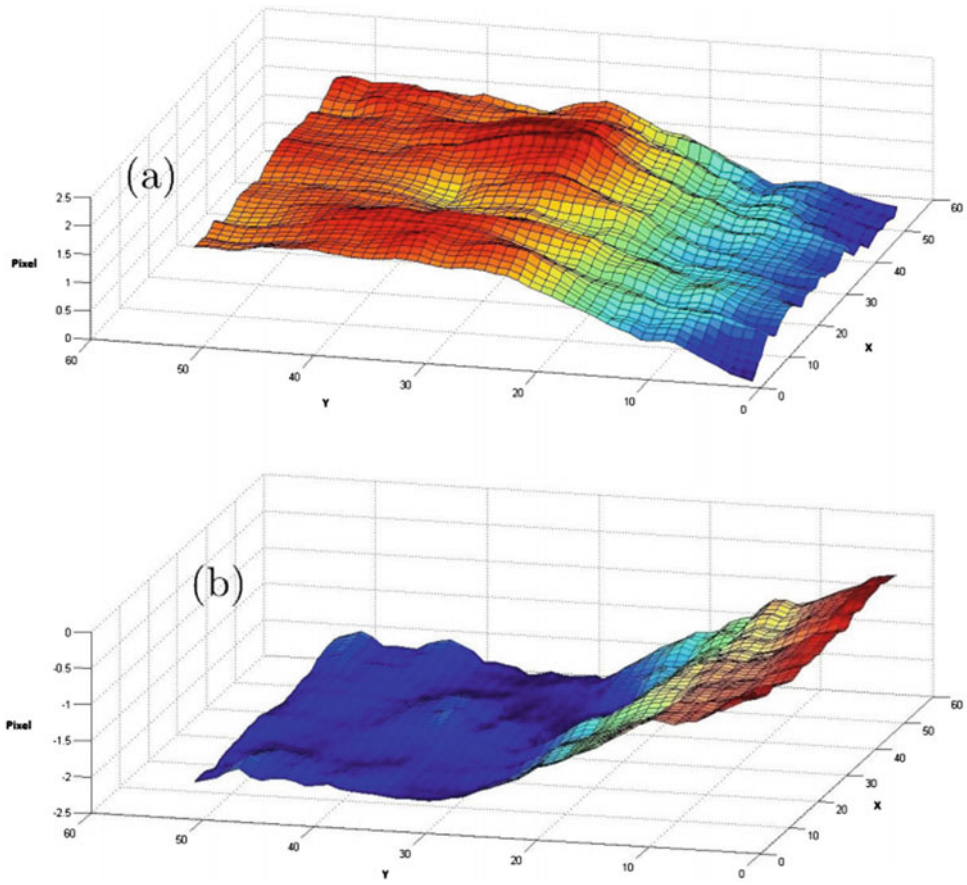

Fig. 6 Natural texture in the images in Fig. 5 are used to compute the displacements over the entire region. The u component over this region is shown in (**a**) and the v in (**d**). The x and y axes are divided into 50 equally spaced points each

3.1 Correcting for Drift Distortion

Consider Fig. 8, where the deformation event of Fig. 3 is shown again. A point P at $\boldsymbol{X}$ in the reference image suffers a deformation to map onto a point Q at $\boldsymbol{\zeta} = \boldsymbol{X} + \boldsymbol{u}$ in the deformed. However, apart from the mechanical deformation, it suffers a further drift displacement $\boldsymbol{d}$, which is a function of the time $t(\boldsymbol{\zeta})$ at which the location $\boldsymbol{\zeta}$ is scanned. The challenge is to recover the actual location $\boldsymbol{\zeta}$, reached by deformation, from $\boldsymbol{x} = \boldsymbol{X} + \boldsymbol{u} + \boldsymbol{d}(t(\boldsymbol{\zeta}))$. To achieve this, some information about the variation of $\boldsymbol{d}$ at the location $\boldsymbol{\zeta}$ with time is required.

To acquire information on $\boldsymbol{d}(t(\boldsymbol{\zeta}))$, a calibration procedure needs to be performed (Sutton et al. 2007) just before conducting the actual deformation experiments. The idea is illustrated in Fig. 9. A total of nine image pairs are taken. A pair i (where $i = 1, 3, 5 \ldots 9$) is captured in quick succession without moving the sample. In between pairs, a purely x or purely y translation is imparted. The total translation in either direction is approximately about 25 % of the total field of view.

Between the image pairs i and $i+1$ ($i = 1, 3, 5 \ldots 9$), only drift distortion exists. Suppose that a point $\boldsymbol{x_i}$ in image i maps to a point $\boldsymbol{x_{i+1}}$ in image $i+1$. If we perform a DIC between images i and $i+1$, we will obtain the displacement at $\boldsymbol{x}$ as

$$\boldsymbol{u}(\boldsymbol{x}) = \boldsymbol{x_{i+1}}(t(\boldsymbol{x_{i+1}})) - \boldsymbol{x_i}(t(\boldsymbol{x_i})), \tag{3}$$

where $t(\boldsymbol{x_{i+1}})$ and $t(\boldsymbol{x_i})$ are the times at which the points are scanned.

Now, for both images i and $i+1$, the position in the calibration stage is the same, $\boldsymbol{\zeta_i}$. Thus $\boldsymbol{x_i} = \boldsymbol{\zeta_i} + \boldsymbol{d}(\boldsymbol{x})(t(\boldsymbol{x_i}))$ and $\boldsymbol{x_{i+1}} = \boldsymbol{\zeta_i} + \boldsymbol{d}(\boldsymbol{x})(t(\boldsymbol{x_{i+1}}))$. Since the sample is stationary, and no spatial distortion is present $\boldsymbol{u}(\boldsymbol{x})$ computed through DIC equals the change in drift $\Delta\boldsymbol{d}(\boldsymbol{x_i}) = \boldsymbol{d}(\boldsymbol{x})(t(\boldsymbol{x_{i+1}})) - \boldsymbol{d}(\boldsymbol{x})(t(\boldsymbol{x_i}))$ at $\boldsymbol{x_i}$ between images i and $i+1$. The drift velocity at $\boldsymbol{x_i}$ can then be calculated as

$$\boldsymbol{v}(\boldsymbol{x_i}) \simeq \frac{\Delta\boldsymbol{d}(\boldsymbol{x_i})}{\boldsymbol{t}(\boldsymbol{x_{i+1}}) - \boldsymbol{t}(\boldsymbol{x_i})}. \tag{4}$$

This is taken to be the drift velocity at time $t(\boldsymbol{x_{i+1}}) + \boldsymbol{t}(\boldsymbol{x_i})/\boldsymbol{2}$.

From the definition of t,

$$t(\boldsymbol{x_i}) = \boldsymbol{t_i} + (\boldsymbol{\zeta_x} + \boldsymbol{d_x}(\boldsymbol{x_i}) - \boldsymbol{1})\boldsymbol{t_d} + (\boldsymbol{\zeta_y} + \boldsymbol{d_y}(\boldsymbol{x_i}) - \boldsymbol{1})\boldsymbol{t_p}, \tag{5}$$

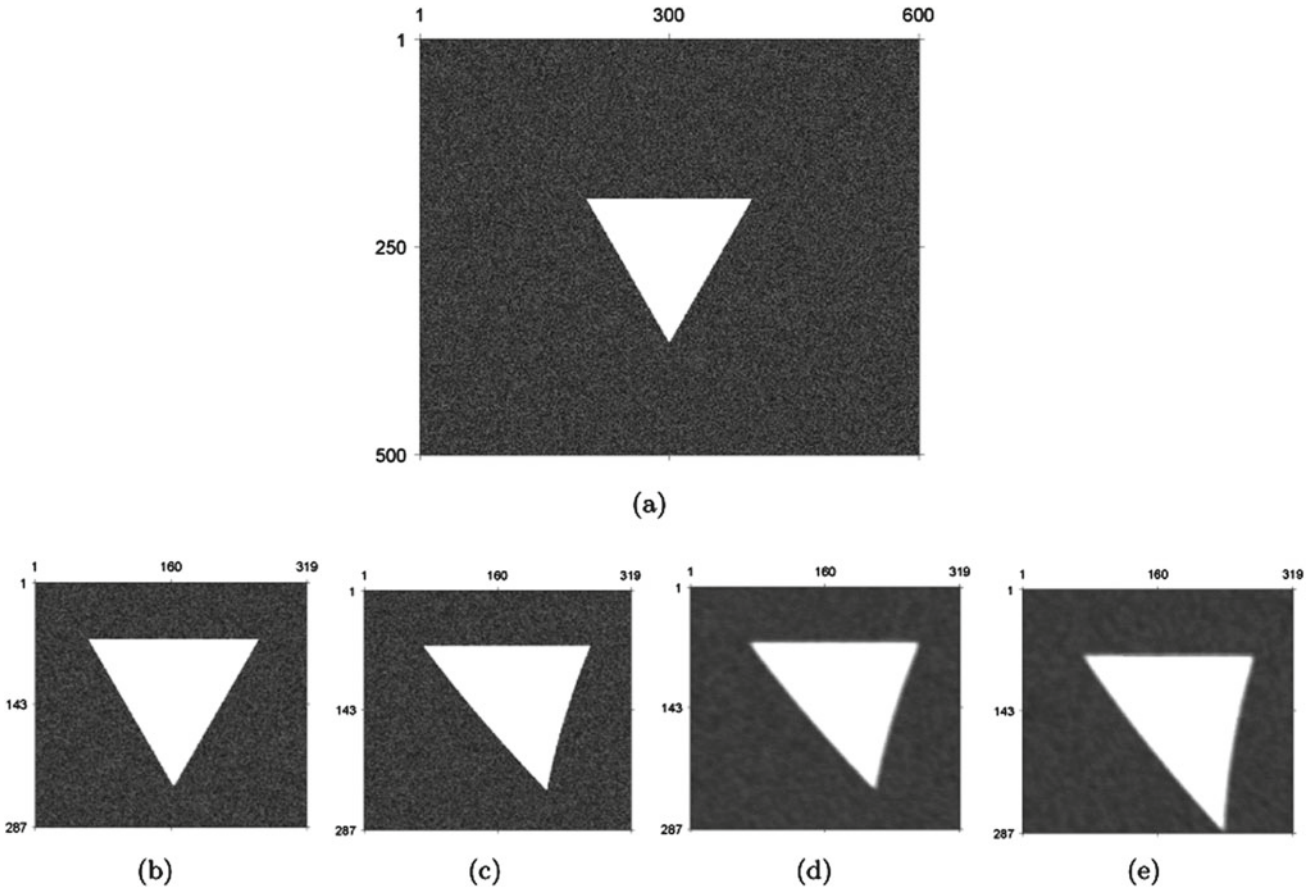

Fig. 7 **a** A 600 × 500 pixel-sized virtual domain with a cut-out in the form of an equilateral triangle is created in MATLAB. Random noise has been added to the intensities of the dark part. A 319 × 287 pixel-sized sub-domain around the triangle is scanned. The deformed configurations when the sub-domain is deformed under simple shear with very slow and very fast shear rates are shown in (**b**) and (**c**), respectively. For fast deformation, the effect of spatial distortion is shown in (**d**). Additionally, the effect of an unrealistic drift distortion linear in time and independent of position is shown in (**e**)

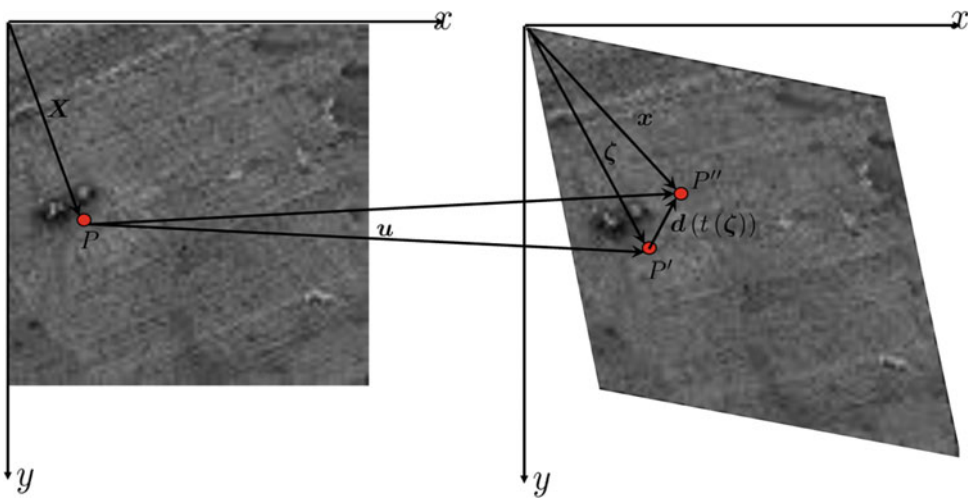

Fig. 8 The point P in the reference image is mapped to P' by mechanical deformation. But distortion causes a further drift $\boldsymbol{d}$ that makes the point appear at P''

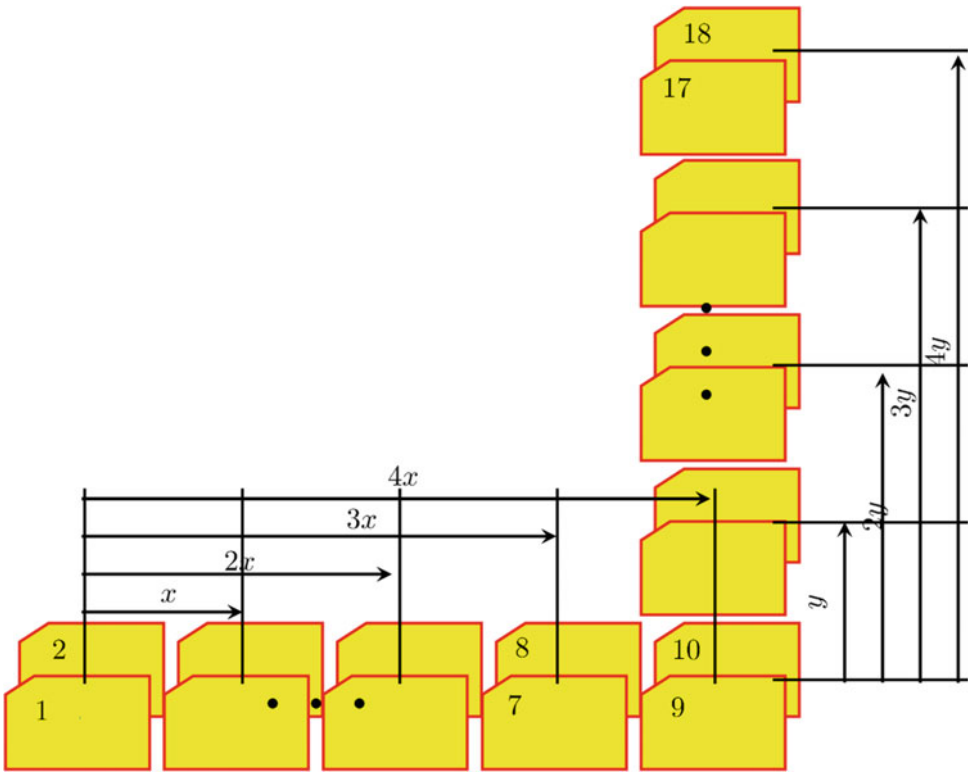

Fig. 9 In the calibration phase, nine pairs of images are taken. For each pair, the stage is translated by first by an amount x and then by y. For a pair, two images are captured in quick succession

and

$$t(\boldsymbol{x}_{i+1}) = \boldsymbol{t}_{i+1} + (\zeta_x + \boldsymbol{d}_x(\boldsymbol{x}_{i+1}) - \boldsymbol{1})\boldsymbol{t}_d + (\zeta_y + \boldsymbol{d}_y(\boldsymbol{x}_{i+1}) - \boldsymbol{1})\boldsymbol{t}_p, \tag{6}$$

so that,

$$t(\boldsymbol{x}_{i+1}) - \boldsymbol{t}(\boldsymbol{x}_i) = \boldsymbol{T} + \Delta\boldsymbol{t}_i + \Delta\boldsymbol{d}_x(\boldsymbol{x}_i)\boldsymbol{t}_d + \Delta\boldsymbol{d}_y(\boldsymbol{x}_i)\boldsymbol{t}_p, \tag{7}$$

where,

$$\Delta d_x(\boldsymbol{x}_i) = (\boldsymbol{d}_x(\boldsymbol{x}_{i+1}) - \boldsymbol{d}_x(\boldsymbol{x}_i)), \Delta\boldsymbol{d}_y(\boldsymbol{x}_i) = \big(\boldsymbol{d}_y(\boldsymbol{x}_{i+1}) - \boldsymbol{d}_y(\boldsymbol{x}_i)\big). \tag{8}$$

Finally, the difference between the start times for images i and $i+1$ is $t_{i+1} - t_i = T + \Delta t_i$, where Δt_i is the interval between the end of scanning of i and beginning of $i+1$.

A set of nine pairs of images used for calibration are shown in Fig. 9. Pairs 1–5 are obtained by translating the stage in the x direction while 5–9 are in the y direction. The x and y components of the drift velocity $\boldsymbol{v}$, u_{dr} and v_{dr} are plotted against time in Fig. 10 for a generic point on the odd-numbered images. Cubic splines are fitted to the data for u_{dr} and v_{dr}. This exercise has to be repeated for every pixel in the odd-numbered images. For any pixel location $\boldsymbol{x}$ in an image i $(i = 1, 3, 5\ldots 9)$, the drift corrected position is obtained as

$$\zeta = \boldsymbol{x}(\boldsymbol{t}(\boldsymbol{x})) - \int_0^{t(x)} \boldsymbol{v}\boldsymbol{d}\boldsymbol{t}. \tag{9}$$

3.2 Correcting for Spatial Distortion

After the odd-numbered images are corrected for drift, they can be used to correct for spatial distortion. The rigid body displacement of an image i from the first image is known to be $\boldsymbol{\zeta}_i$. Now, a DIC between the first image and drift corrected image i will yield a displacement $\boldsymbol{u}_i(\boldsymbol{x}_i)$. The spatial distortion is extracted as $\boldsymbol{s}(\boldsymbol{x}_i) = \boldsymbol{u}_i(\boldsymbol{x}_i) - \boldsymbol{\zeta}_i$ for all $\boldsymbol{x}_i$ and i. The spatial distortion is independent of time and remains nominally constant over the duration of an experiment.

The load displacement response of a rather slow miniature dog-bone specimen under uniaxial tension in the x direction is shown in Fig. 11. The u displacements obtained from 12 images taken at monotonically increasing loads are corrected for both drift and spatial distortions.

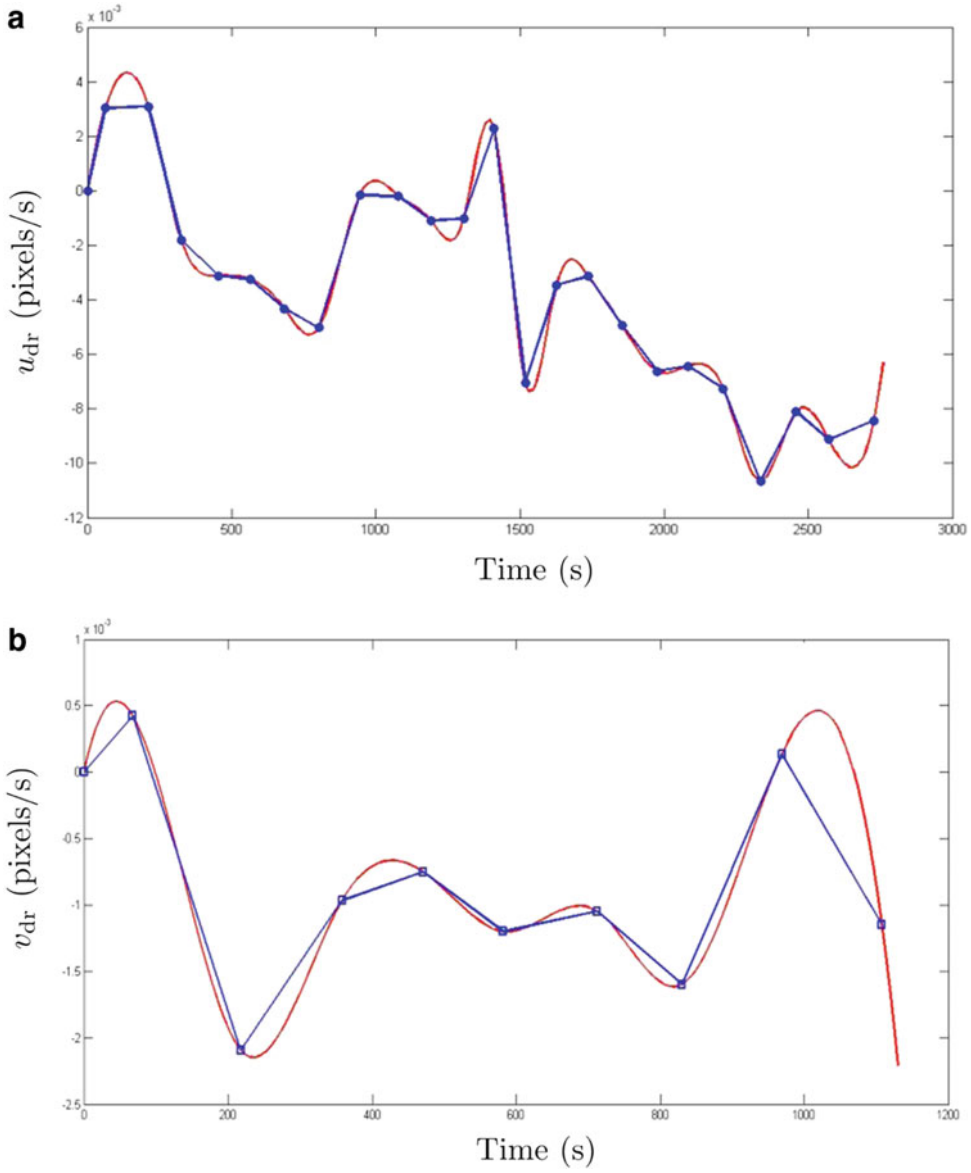

Fig. 10 Drift velocity components, **a** u_{dr} in the x direction and **b** v_{dr} in the y direction are obtained from the calibration phase of the in-situ experiment as functions of time. Cubic splines are fitted to the data in order to have a smooth functional form that can be readily used for drift correction in the actual testing phase

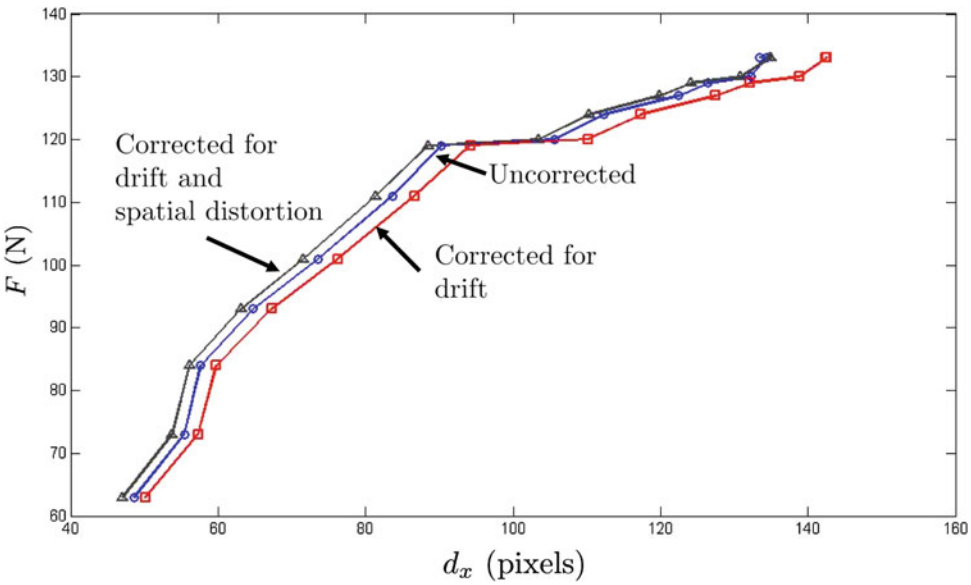

Fig. 11 Load displacement responses of a miniature dog-bone specimen deformed in uniaxial tension in-situ. The uncorrected response and those after correction for only drift and both drift and spatial distortions are shown

4 Conclusions

Conducting quantitative in-situ deformation experiments inside the vacuum chamber of a scanning electron microscope is useful under many circumstances. However, owing to the nature of image generation in an SEM, quantitative measurements of full-field displacements and strains pose unique challenges. We have shown that the raster scanning process by which the electron beam generates a digital image leads to artifacts that can potentially derail attempts to apply digital image correlation-based techniques to compute displacements. In this article, we have discussed recently proposed methods for correcting drift and spatial distortions in SEM images. These two imaging artifacts seem to have the largest effects on the displacements on the surface of a specimen. We are in the process of conducting many small-scale experiments where algorithms for correction discussed in this article are applied to several different materials under a range of two-dimensional deformation protocols. Development of a software package that seamlessly integrates deformation measurement through DIC following corrections for drift and spatial distortions is also underway.

Acknowledgements The algorithms for DIC and correction of imaging artifacts have been implemented in MATLAB at IIT Kanpur by Suhas Vilas Powar in the period 2014–2015. Micro-compression stages for conducting in-situ tests were assembled and instrumented by Rachit Nayak also in 2015. A miniature tensile stage was procured as part of a project funded by the Department of Science and Technology, Govt. of India, titled 'Modeling Of Interface Deformation And Failure Through A Combination Of Finite Element Analysis And Digital Image Correlation,' in 2009, in collaboration with Prof. P. Venkitanarayanan. Various test results mentioned as part of this article are taken from the works of Dr T Guruprasad, Dr Chatanya K Desai, S Arun Kumar, Moonish Mustafa, and Ankur Patel.

References

Adusumalli R-B, Raghavan R, Ghisleni R, Zimmermann T, Michler J (2010) Deformation and failure mechanism of secondary cell wall in spruce late wood. Appl Phys A: Mater Sci Process 100(2):447–52

Alaie A, Kadkhodapour J, Ziaei Rad S, Asadi Asadabad M, Schmauder S (2015) Formation and coalescence of strain localized regions in ferrite phase of dp600 steels under uniaxial tensile deformation. Mater Sci Eng : A (Structural Materials: Properties, Microstructure and Processing) 623: 133 – 44

Arai M, Wu X, Fujimoto K (2010) Inelastic deformation of freestanding plasma-sprayed thermal barrier coatings. J Solid Mech Mater Engi 4(2):2212–234

Bao Lei, Lecomte J-S, Schuman C, Philippe M-J, Zhao X, Esling C (2010) Study of plastic deformation in hexagonal metals by interrupted in-situ ebsd measurement. Adv Eng Mater 12(10):1053–1059

Barkia B, Doquet V, Heripre E, Guillot I (2015) Characterization and analysis of deformation heterogeneities in commercial purity titanium. Mater Characterization 108:94–101

fritz2017 fritz2017 Fritz R, Wimler D, Leitner A, Maier-Kiener V, Kiener D (2017) Dominating deformation mechanisms in ultrafine-grained chromium across length scales and temperatures. Acta Mater 140:176–187

Gussev MN, Leonard KJ (2019) In situ sem-ebsd analysis of plastic deformation mechanisms in neutron-irradiated austenitic steel. J Nuclear Mater 517:45–56

Bruck HA, McNeill SR, Sutton M, Peters WHIII (1989) Digital image correlation using newton-raphson method of partial differential correction. Experimental Mech 29:261–267

Chu TP, Ranson WF, Sutton M (1985) Applications of digital-image-correlation techniques to experimental mechanics. Experimental Mech 25:232–244

Dingley DJ (1973) In situ studies of deformations of metals in an s.e.m, pp 112–117

Liu X, Wang C, Gui J, Xiao Q, Guo B (2019) Effect of mns inclusions on deformation behavior of matrix based on in-situ experiment. Mater Sci Engi: A (Structural Materials: Properties, Microstructure and Processing) 746: 239–247

Herre P, Romeis S, Makovi M, Przybilla T, Paul J, Schwenger J, Torun B, Grundmeier G, Spiecker E, Peukert W (2017) Deformation behavior of nanocrystalline titania particles accessed by complementary in situ electron microscopy techniques. J Am Ceramic Soc 100(12):5709–22

Hild F, Roux S (2006) Digital image correlation: from displacement measurement to identification of elastic properties: a review. Strain 42:69–80

Zhang J, Gu H, Zhou H, Zhang S, Laird C (1989) Tensile deformation and fracture in high purity titanium: in situ observation by scanning electron microscopy. Mater Scie Eng A (Structural Materials: Properties, Microstructure and Processing) A114: 89–96

Jin P, Li X (2015) Correction of image and drift distortion in a scanning electron microscopy. J Microscopy 260:268–280

Jun T-S, Sernicola G, Dunne FPE, Britton TB (2016) Local deformation mechanisms of two-phase ti alloy. Mater Sci Eng: A (Structural Materials: Properties, Microstructure and Processing) 649: 39–47

Kammers AD, Daly S (2013) Digital image correlation under scanning electron. Experimental Mech 53:1743–1761

Li H, Boehlert CJ, Bieler TR, Crimp MA (2014) Analysis of the deformation behavior in tension and tension-creep of ti-3al-2.5v (wt pct) at 296 k and 728 k (23 c and 455 c) using insitu sem experiments. Metall Mater Trans A 45(13): 6053–6066

Li J, Mishara RK, Kubic R (2008) In-situ ebsd analysis on the microstructures during deformation. J Chinese Electron Microscopy Soc 27(6):439–442

Li S, Wang Y, Wang X (2019) In situ observation of the deformation and fracture behaviors of long-term thermally aged cast duplex stainless steels. Metals 9(2): 258 (9 pp)

Maraghechi S, Hoefnagels JPM, Peerlings RHJ, Geers MGD (2018) Correction of scan line shift artifacts in scanning electron microscopy: an extended digital image correlation framework. Ultramicroscopy 187:144–163

Maraghechi S, Hoefnagels JPM, Peerlings RHJ, Rokos O, Geers MGD (2019) Correction of scanning electron microscope imaging artifacts in a novel digital image correlation framework. Experimental Mech 59:489–516

Wang M, Lu W, Zhang D, Qin J, Fan T, Ji B, Zhu F, Ji S (2005) An ebsd and tem study on the microstructural evolution of in situ synthesized (tib + tic)/ti matrix composites during superplastic deformation. Mater Trans 46(8):1833–1838

Motsi GT, Olubambi PA, Sono TJ, Shoke L (2014) In situ electron microscopy studies on the tensile deformation mechanisms in aluminium 5083 alloy. Adv Mater Res 1019:103–11

Nakagawa K, Maeda K, Takeuchi S (1980) Plastic deformation of cdte single crystals. i. microscopic observations. J Phys Soc Jpn 49(5): 1909–1915

Niwa N, Ito K (1987) In-situ sem observation of deformation process in uniaxial tension of ti-13-11 alloy. Annual Report of the Engineering Research Institute, Faculty of Engineering, University of Tokyo 46:207–12

Pan B, Qian K, Xie H, Asundi A (2009) Two dimensional digital image correlation for in-plane displacement and strain measurement: a review. Measurement Sci Technol 20:062001

Perusin S, Viguier B, Salabura JC, Oquab D, Andrieu E (2004) Behaviour of the oxide scale during sem in situ plastic deformation of pure nickel foil. Mater Sci Eng A. Properties, Microstructure and Processing, Structural Materials

Prochazka J, Kuerova L, Bystriansky M (2017) Evaluation of in-situ deformation experiments of trip steel, vol 179, pages 012059 (7 pp)

Roberts W, Lehtinen B (1976) An in situ sem study of void development around inclusions in steel during plastic deformation. Acta Metallurgica 24(8):745–58

Romeis S, Paul J, Herre P, Hanisch M, Klupp Taylor RN, Schmidt J, Peukert W (2015) In situ deformation and breakage of silica particles inside a sem. Proc Eng 102:201–210

Sarobol P, Chandross M, Carroll JD, Mook WM, Bufford DC, Boyce BL, Hattar K, Kotula PG, Hall AC (2016) Room temperature deformation mechanisms of alumina particles observed from in situ micro-compression and atomistic simulations. J Thermal Spray Technol 25(1–2):82–93

Snella MT (2010) Drift correction for scanning electron microscopy. Master's thesis, Massachusetts Institute of Technology

Stephens RR, Hoeppner DW (1988) New apparatus for studying fatigue deformation at high magnifications. Rev Sci Instruments 59(8):1412–19

Sutton M, Li N, Garcia D, Cornille N, Orteu JJ, McNeill SR, Schreier HW, Li X, Reynolds AP (2007) Scanning electron microscopy for quantitative small and large deformation measurements part ii: experimental validation for magnifications from 200 to 10,000. Experimental Mech 47:789–804

Sutton M, Li N, Joy DC, Reynolds AP, Li X (2007) Scanning electron microscopy for quantitative small and large deformation measurements part i: Sem imaging at magnifications from 200 to 10,000. Experimental Mech 47:775–787

Sutton MA, Orteu JJ, Hubert S (2009) Image correlation for shape. Motion and deformation measurements, Springer, US

Ujiiye N, Kimoto S, Kawasaki Y (1971) Observation of deformation and fracture in metals-a dynamic application of sem, pp 97–104

Wu XH, Arai M, Fujimoto K, Sun Q (2008) Inelastic deformation of free-standing plasma-sprayed thermal barrier coatings, vol 7375, p 73755M (6 pp)

Wu Z, Sandlobes S, Wu L, Hu W, Gottstein G, Korte-Kerzel S (2016) Mechanical behaviour of zn-al-cu-mg alloys: Deformation mechanisms of as-cast microstructures. Mater Sci Eng: A (Structural Materials: Properties, Microstructure and Processing) 651: 675–687

Fuqiang Yang, Renbo Song, Yaping Li, Ting Sun, Kaikun Wang (2015) Tensile deformation of low density duplex fe-mn-al-c steel. Mater Desi 76:32–9

Song Zhang, Yilong Liang, Qifan Xia, Meigui Ou (2019) Study on tensile deformation behavior of tc21 titanium alloy. J Mater Eng Performance 28(3):1581–90

Xuehua Zhang, Shuangyin Zhang, Qinyang Zhao, Yongqing Zhao, Rong Li, Weidong Zeng (2018) In-situ observations of the tensile deformation and fracture behavior of a fine-grained titanium alloy sheet. J Alloys Compounds 740:660–8

In-Situ Micromechanical Testing in Scanning Electron Microscopy

R. Sarvesha and Sudhanshu S. Singh

1 Introduction

In-situ electron microscopy is a fast-growing and leading field in the materials research. It is an indispensable tool in understanding the material behavior in real-time. Additionally, the rapid miniaturization of the components for technological devices, that approaches micron and nanoscale dimensions, requires accurate size-specific properties (Gianolaet 2011) as it has been shown that the properties at a small length scale can be significantly different from the bulk counterpart (Dimiduk et al. 2005; Uchic et al. 2004; Volkert et al. 2008). Besides, in the multi-phase materials, the properties measured at a small length scale can be used as input to carry out microstructure-based modeling, which further assists in understanding the bulk deformation behavior (Guo et al. 2014).

To understand the material behavior in real-time, and at small length scales, a number of improvements in the microscopy techniques have been made over the years. Several two-dimensional (2D) microscopy techniques [e.g., optical, Raman, scanning electron microscopy (SEM), electron backscattered diffraction (EBSD), electron channeling contrast imaging (ECCI)] and three-dimensional (3D) techniques [e.g., transmission electron microscopy (TEM), X-ray tomography, neutron imagining, atom probe tomography (APT), focused ion beam (FIB) tomography] cover a range of length scales (Singh et al. 2014a,2015,2017; Gianolaet 2011; Volkert et al. 2008; Guo et al. 2014; Legros et al. 2010). Among these, the electron microscopy technique is well suited to elucidate the microstructural changes, with time, for micron- and submicron-sized specimens.

In-situ electron microscopy can be used to understand different phenomena depending upon the attachments equipped in SEM. For instance, a customized or commercial mechanical testing jig assists in unraveling the complex deformation mechanisms (Singh et al. 2014a). Further, EBSD and digital image correlation (DIC) techniques can assist in understanding the strain partitioning between different phases or grains in the materials. Novel microscopy techniques, such as electron channeling contrast imaging (ECCI) (Slama et al. 2019), can further assist in the quantification of the deformation systems generated under the application of load. FIB machining and deposition enable the sample preparation, which aids in evaluating the site-specific properties at small length scales using specialized attachments, such as nanoindentation system in a SEM (Sarvesha et al. 2020; Guo et al. 2014; Singh et al. 2014b). In recent years, irradiation properties of the nuclear materials have been studied by irradiating different ions, such as Fe+ , W+, He+, on the microscale test structures in assistance with FIB (Armstrong et al. 2015). Furthermore, a couple of *in-situ* SEM studies have also been carried out to evaluate the corrosion properties in environmental SEM (Proff et al. 2010), where a special *in-situ* jig was used to simulate the corrosion environment (Kim et al. 2020).

A powerful way of capturing real-time deformation microstructure is acoustic emission (AE) along with the conventional *in-situ* measurements. The AE method is based on sound emitted due to the activation of deformation mechanisms or fracture during deformation and thus provides highly time-resolved information (Wisner et al. 2015).

Figure 1 summarizes the various *in-situ* tests performed in SEM. *In-situ* tests in combination with SE/BSE imaging and EBSD in SEM are the most attractive methods used to understand the deformation behavior. This article discusses a few case studies showing the use of *in-situ* electron microscopy in evaluating the deformation behavior of metallic systems (Sn whisker, 7075 aluminum alloys, and AZ80 magnesium alloy).

R. Sarvesha · S. S. Singh (✉)
Department of Materials Science and Engineering, IIT Kanpur, Kanpur, India
e-mail: sudhanss@iitk.ac.in

K. Biswas et al. (eds.), *Electron Microscopy in Science and Engineering*, IITK Directions 6,
https://doi.org/10.1007/978-981-16-5101-4_2

2 Case Studies

2.1 Case Study I: *In-Situ* Tensile Behavior of Sn Whiskers

Environment-friendly Pb-free solders are predominantly based on Sn-rich alloys, where whiskers are known to grow on the Sn plates (Mathew et al. 2009). An understanding of the mechanical response of Sn whisker is vital for the soldering community. Whiskers are single crystals and contain minimal defects, which assists in the free flow of electron, thus making them an excellent conductor. The phenomenon of Sn whisker formation has been studied for decades (Galyon 2005); however, only a few studies have been performed to evaluate the mechanical properties of Sn whiskers (Dunn 1987; Powell and Skove 2004). This is due to adversity involved in handling whiskers. This case study deals with the *in-situ* evaluation of tensile properties of Sn whisker using a micro–electro–mechanical system (MEMS) tensile stage in assistance with a focused ion beam (FIB) (Singh et al. 2014a).

Sn whiskers on a Sn plate, having a very high aspect ratio, are shown in Fig. 2a. The steps of *in-situ* sample preparation using FIB are shown in Fig. 2. Manipulator needle was brought close to the base of the Sn whisker (Fig. 2b) and carefully welded using Pt (Fig. 2c). Sn whisker was then cut using Ga ions, as shown in Fig. 2d. The whisker was then brought to the MEMS device and welded in the trenches using Pt, as shown in Fig. 2e–g. In the end, the needle was released by cutting the whisker using Ga ions (Fig. 2h).

The MEMS device is shown in Fig. 3a (details of construction of the MEMS stage are reported elsewhere (Han and Saif 2006; Han et al. 2007)), and welded whisker on it is shown in Fig. 3b. A quasistatic loading was applied during the tensile test until fracture. The fractured Sn whisker is shown in Fig. 3c. The magnified image of the whisker shows that its surface is irregular. Therefore, to evaluate the stress, the surface area was calculated using image processing software (ImageJ), as shown in Fig. 3d. Two successful tests were performed, and in both the case linear stress–strain behavior was observed for the Sn whisker (Fig. 3e). The values of Young's modulus of both the whiskers were measured to be 42 and 45 GPa, which are close to the theoretical value of the modulus for pure Sn. The fracture strength and strain to failure for the two tests were 720 MPa, 880 MPa, and 2%, 3%, respectively. The observed high fracture strength and limited ductility may be attributed to a lack of defects in the single crystal Sn whiskers.

Limited *ex-situ* experiments have been performed to evaluate the mechanical properties of Sn whiskers (Dunn 1987; Powell and Skove 2004). Powell and Skove (2004) observed the linear load–displacement behavior. However, the properties of the whiskers were not reported. Dunn (1987) obtained Young's modulus using the cantilever method. However, a large variability (8–85 GPa) was observed. One of the crucial shortcomings in Dunn's study was the measurement of the cross-sectional area in which the whisker was assumed to have a circular cross section. However, it should be noted that in the bending theory, Young's modulus varies with the fourth power of the radius, and thus, a small change in the radius would result in a significant deviation in the measurement of modulus. In comparison with the *ex-situ* testing, which had inherent limitations in handling the whiskers, the *in-situ* tensile testing in SEM assisted in evaluating the reliable mechanical properties of the Sn whisker.

2.2 Case Study II: Evaluation of Mechanical Properties of the Constituent Particles in Al 7075 by Micro-pillar Compression

Aluminum alloys are predominantly used as structural materials due to their high strength-to-weight ratio (Bucci et al. 2000; Starke and Staley 2011). These alloys contain second-phase particles (Fe-containing: Al_7Cu_2Fe and Si-containing: Mg_2Si), also called as constituent particles, which form during casting and do not dissolve in the

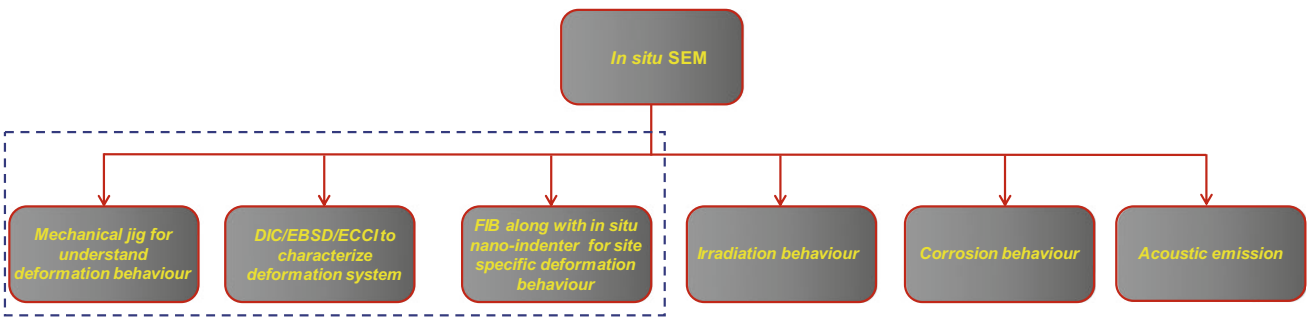

Fig. 1 Summary of the *in-situ* test performed in a scanning electron microscope

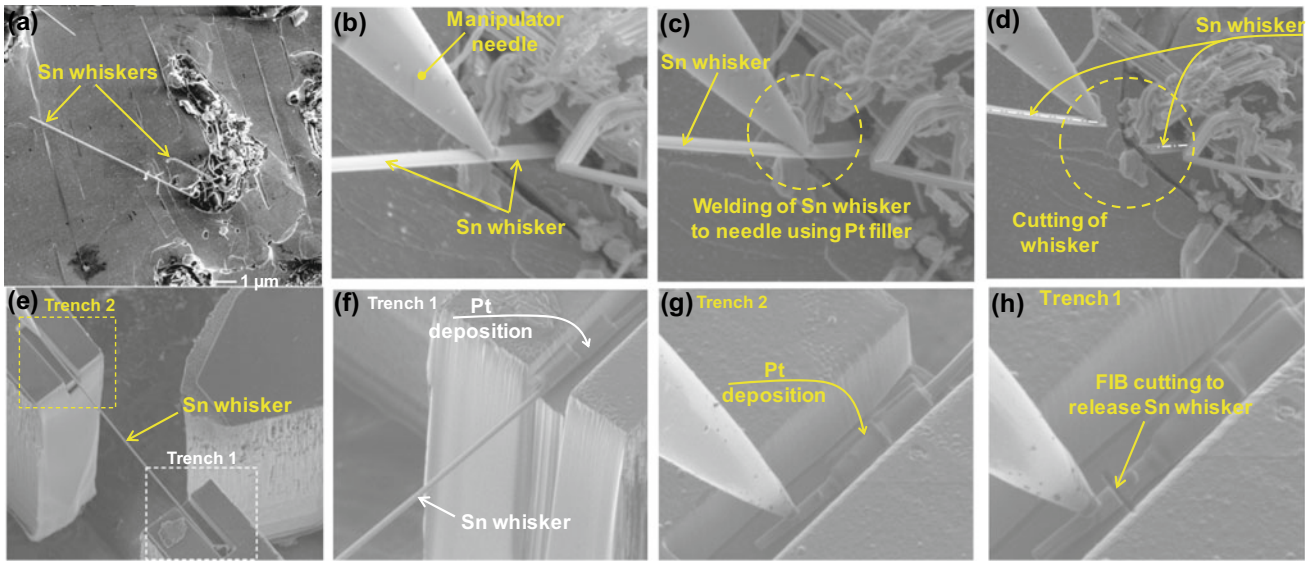

Fig. 2 **a** SEM image of Sn whiskers. Steps of whisker lift off and placement in MEMS inside FIB/SEM, **b** manipulator needle in contact with whisker, **c** welding of whisker using Pt filler, **d** FIB cutting of the whisker, **e–g** placement and welding of whisker in the trenches, and **h** FIB cutting to release the needle (Singh et al. 2014a)

subsequent thermomechanical treatment of the alloy (Payne et al. 2010; Xue et al. 2007). These particles have been observed to affect the overall deformation behavior of the alloy as they are the source for crack nucleation and propagation during static or dynamic loading (Pearson 1975; Weiland et al. 2009; Maire et al. 2011; Lugo et al. 2011). Hence, the overall mechanical response of the Al7075 alloy depends on the characteristic of constituent particles. This present case study deals with the evaluations of the stress–strain behavior of the constituent particles under uniaxial compression of micro-pillars (Singh et al. 2015).

The SEM micrograph (Fig. 4a) shows two types of constituent particles (one black and another white). The corresponding EDS analysis (Fig. 4b) indicates that the bright particle is Fe-bearing inclusions and the dark particle is Si-bearing inclusion. The approximate atomic ratio of Al, Cu, and Fe in Fe-bearing inclusion is 7:2:1, indicating them to be Al_7Cu_2Fe. Similarly, for Si-bearing inclusion, the atomic ratio of Mg and Si is 2:1, indicating them to be Mg_2Si. The micro-pillar fabrication sequence for Mg_2Si using dual-beam focused ion beam (FIB) is shown in Fig. 4c–f. The same procedure was followed for Al_7Cu_2Fe and Al7075 matrix. Initially, a circular trench of ~25 μm diameter was milled out (shown in Fig. 4c), which provides clearance for the flat punch during compression. A course pillar with ~7 μm was made at the inclusion center (refer to Fig. 4d). Further, the pillar diameter was reduced to ~3.5 μm (Fig. 4e), and milling was continued until an aspect ratio of 2.7–3.4 was maintained. During the final process, a low current was utilized, so the taper is less than 3° (shown in Fig. 4f).

The SEM micrographs before loading and after fracture of the pillars are shown in Fig. 5a1, b1, c1 and a2, b2, c2, respectively. The stress–strain behavior of the constituent particles and the matrix of the repeat test is shown in Fig. 5d. Linear stress–strain behavior is observed till fracture for the Al_7Cu_2Fe particles. The fracture stress is ~2.5 ± 0.2 GPa, and strain is approximately 2%. SEM micrograph of the fractured pillar (Fig. 5a2) indicates catastrophic failure. In the case of the Mg_2Si particle, the stress value increased linearly with strain in the initial region, followed by strain bursts. The significant strain hardening is due to the dislocation activity, which is also visible in the SEM micrograph (steps indicated by the arrow in Fig. 5b2). The compressive yield strength of Mg_2Si was calculated to be ~1.8 ± 0.1 GPa. The Al7075 matrix has similar stress–strain behavior as Mg_2Si with a lower yield strength of ~0.5 ± 0.1 GPa. The strength values are in-line with the hardness value obtained by nanoindentation (Kim et al. 2020), i.e., the highest hardness for Al_7Cu_2Fe particle followed by Mg_2Si particle and Al7075 matrix.

Previously, studies have been conducted on the evaluation of mechanical properties of Al_7Cu_2Fe and Mg_2Si by fabricating bulk samples through the powder metallurgy route. While both Al_7Cu_2Fe and Mg_2Si were found to be brittle (Laplanche et al. 2014; Wang et al. 2007; Muñoz-Palos et al. 1996; Takeuchi et al. 1996), limited plasticity for Mg_2Si was observed in this study. This difference in behavior could be attributed to the difference in microstructure like grain size, defect concentration, and type (such as residual porosity), etc. It has been recently shown in several micro-pillar compression studies that a brittle

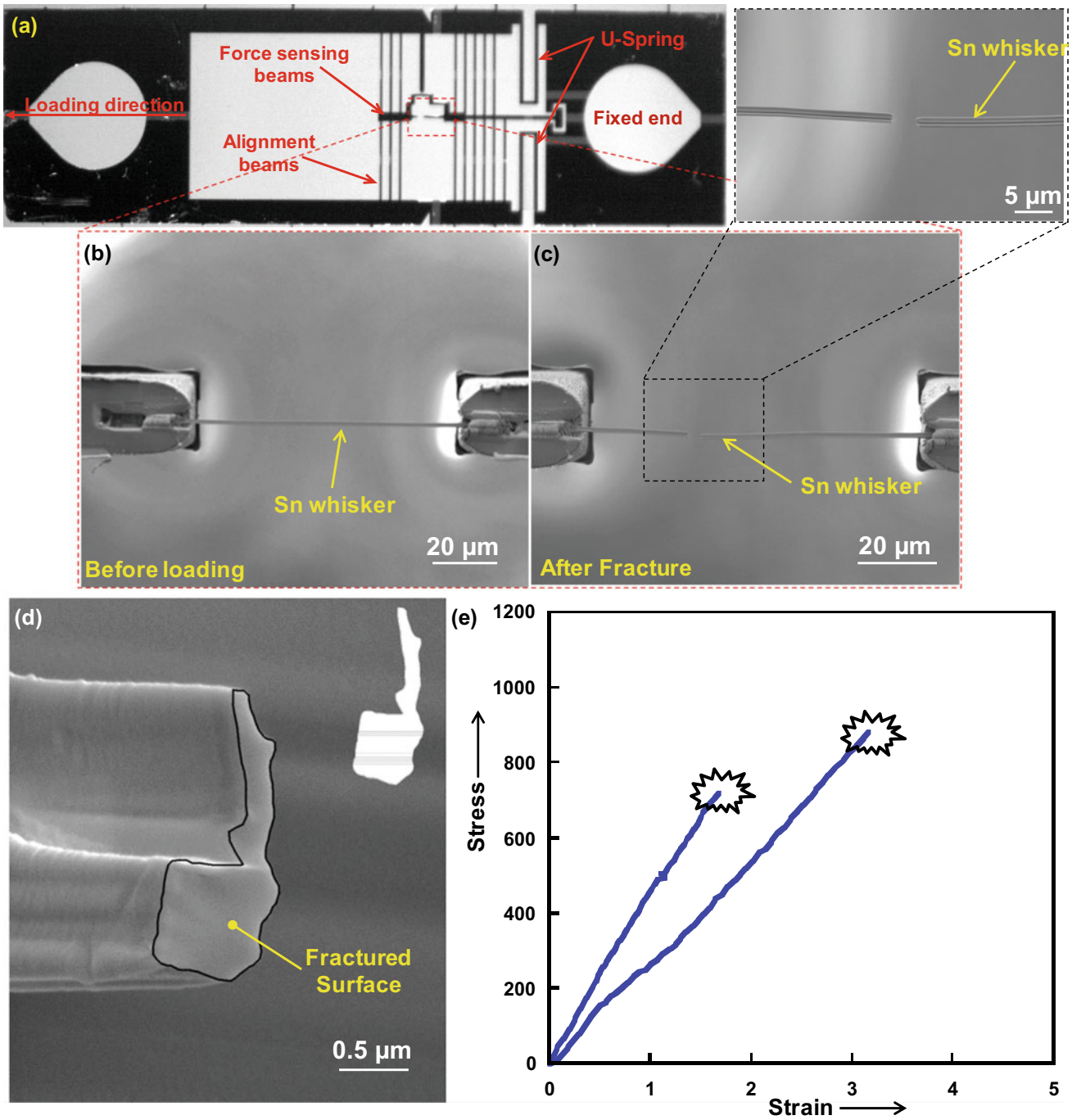

Fig. 3 **a** Optical micrograph of MEMS stage for tensile testing of whisker, **b** zoomed image of Sn whisker before loading, **c** fracture Sn whisker, **d** SE micrograph of fractured surface and inset is a binary image of the fractured surface, **e** nominal stress–strain in the behavior of Sn whisker (Singh et al. 2014a)

material (in bulk) can show plastic deformation at a small length scale (Östlundet 2009; Michler et al. 2007; Korte and Clegg 2011; Östlund 2011). Hence, reducing the size of the sample suppresses cracking, resulting in plastic deformation when the test sample is made significantly small (Östlundet 2009). Oswald (2003) evaluated the hardness and Young's modulus using nanoindentation and predicated stress–strain behavior. Even though the highest strength and modulus was reported for Al_7Cu_2Fe, a similar yield strength was predicated for Al-matrix and Mg_2Si due to their similar hardness

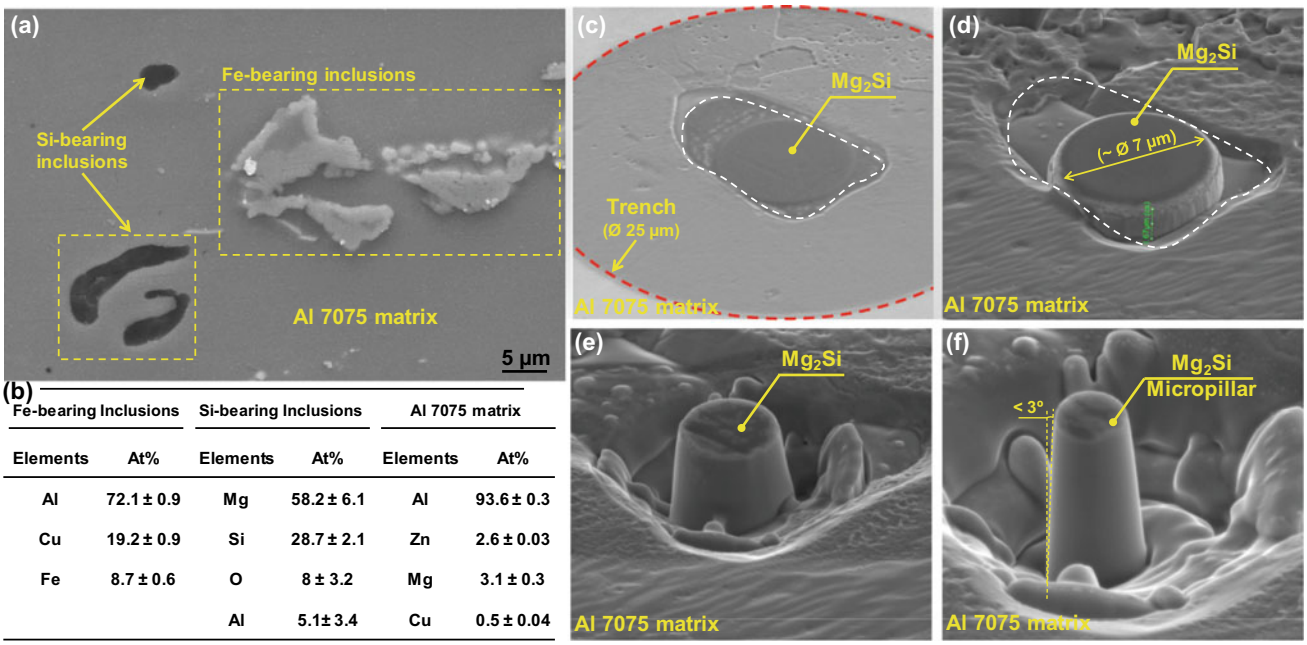

(b)

Fe-bearing Inclusions		Si-bearing Inclusions		Al 7075 matrix	
Elements	At%	Elements	At%	Elements	At%
Al	72.1 ± 0.9	Mg	58.2 ± 6.1	Al	93.6 ± 0.3
Cu	19.2 ± 0.9	Si	28.7 ± 2.1	Zn	2.6 ± 0.03
Fe	8.7 ± 0.6	O	8 ± 3.2	Mg	3.1 ± 0.3
		Al	5.1 ± 3.4	Cu	0.5 ± 0.04

Fig. 4 **a** SEM image showing Fe- and Si-bearing inclusions in Al7075, **b** EDS analysis of the second-phase particles, and **c**–**f** micro-pillar fabrication using dual-beam FIB

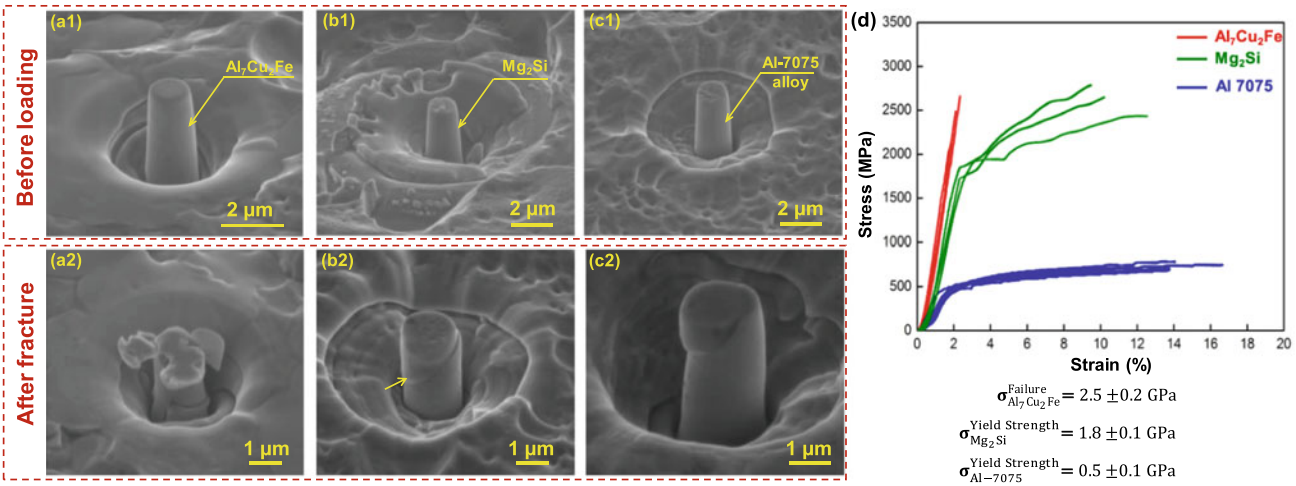

Fig. 5 **a1**, **b1**, **c1** and **a2**, **b2**, **c2** show Al_7Cu_2Fe, Mg_2Si, Al7075 micro-pillars before loading and after fracture, respectively, and (d) stress–strain behavior of the second-phase particles and the matrix (Singh et al. 2015)

values. However, the present study shows that Mg_2Si exhibits higher yield strength as compared to the matrix, which corroborates with the hardness values reported in other studies (Singh et al. 2014c).

In summary, the mechanical properties of the constituent particles were evaluated by micro-pillar compression testing, the knowledge of which will allow a better understanding of the bulk deformation behavior of Al7075 alloys.

2.3 Case Study III: Role of Second-Phase Particles on the Deformation Behavior of AZ80 Magnesium Alloys

The role of second-phase particles on the deformation behavior of AZ80 alloy has been divided into two separate studies. One study (Sarvesha et al. 2021) deals with understanding the role of these particles on the fracture process of

the alloy using *in-situ* tensile testing, and another study (Sarvesha et al. 2020) is on the measurement of mechanical properties of the particles using micro-pillar compression.

2.3.1 Effect of Second-Phase Particle on Crack Propagation in Magnesium alloy via *in-situ* Tensile Testing

Magnesium and its alloys exhibit the highest strength-to-weight ratio, which assists in a weight reduction, thus have potential in the automobile, aerospace, and electronics industries (Kulekci 2008; Blawert et al. 2004). Mg-Al-Zn alloys, designated as AZ series alloys, which are a prominent class of magnesium alloys, contain Mg-Al precipitate and Al-Mn inclusions, (Zindal et al. 2018,2017). These second-phase particles have been found to affect the mechanical properties of magnesium alloys significantly (Lugo et al. 2011; Yakubtsov et al. 2008).

A typical as-cast optical micrograph (OM) of Mg-9.3Al-0.45Zn-0.15Mn is shown in Fig. 6a, which shows two types of micron-sized second-phase particles. The corresponding backscattered electron (BSE) image (Fig. 6b) shows gray and white particles due to difference in composition. The energy dispersive spectroscopy (EDS) map (Fig. 6c) shows that the gray particle is enriched with Mg and Al with Zn segregation. In contrast, the white particle is enriched with Mn and Al with the segregation of Fe and Si. Furthermore, the optical microscopic image (dark field mode) shows that Mg-Al precipitate has porosities, which is called a discontinuous eutectic precipitate. In addition, additional dark regions (indicated by arrows in Fig. 6a) correspond to continuous precipitates, which are formed adjacent to eutectic precipitate (refer SE micrograph in Fig. 6b). Electron backscatter diffraction (EBSD) maps suggest that the micron-sized Mg-Al precipitate corresponds to $Mg_{17}Al_{12}$ (space group $I\bar{4}3m$), which are polycrystalline and forms along the grain boundaries of the α-Mg matrix, whereas the Al-Mn inclusion corresponds to Al_8Mn_5 particle (space group R3m) and has a rhombohedral crystal structure.

Gatan *in-situ* tensile testing stage, along with the sample dimension, are shown in Fig. 7a, b, respectively. The sequence of secondary electrons (SE) micrographs at different strain (ε) levels (refer Fig. 7c) shows that crack propagation occurred predominantly through $Mg_{17}Al_{12}$ precipitates. The visible crack appeared at strain (ε) 0.0376. To further ascertain the strain at which the crack initiates in $Mg_{17}Al_{12}$, in-situ testing was performed with a focus on a single $Mg_{17}Al_{12}$ particle, as shown in Fig. 8a. It can be observed that at $\varepsilon = 0.017$, the crack initiates in the second-phase particle, which is in the linear portion of the stress–strain curve (shown in inset). With an increase in strain, more cracks appear perpendicular to the loading direction, as indicated by arrows in Fig. 8a.

Further, to understand the strain partitioning between the matrix and the precipitate, *in-situ* tensile testing, assisted with EBSD, was performed. A 70° pre-tilt in-situ stage (shown in Fig. 7a) was employed for EBSD scanning. The secondary electron (SE) micrographs (at 70° tilt) along with the EBSD maps, before loading and after fracture, are shown in Fig. 8b, c, respectively. Kernel average misorientation (KAM) maps in Fig. 8b, c are generated from EBSD scanning. KAM calculates the average misorientation between each pixel and its nearest neighbors and indicates strain in different phases during external loading. KAM map in Fig. 8b shows no strain in the matrix as well as in the particle before loading. However, after fracture, the strain is predominately distributed in the matrix, as the matrix shows higher KAM values (Fig. 8c). The KAM value of the precipitate is approximately zero, indicating the $Mg_{17}Al_{12}$ fractured in a brittle manner.

Previously, Yakubtsov et al. (2008) observed an increase in the ductility of AZ80 (Mg-8.2Al-0.51Zn) alloy with a decrease in the volume fraction of $Mg_{17}Al_{12}$precipitate. Lü et al. (2000) observed the crack formation near $Mg_{17}Al_{12}$ precipitate during tensile deformation, and it was postulated that the crack initiated at the interface between Mg/$Mg_{17}Al_{12}$. In the present study, it is evident from *in-situ* tensile testing, fracture initiates at $Mg_{17}Al_{12}$ at low strain and propagates through the $Mg_{17}Al_{12}$ phase.

2.3.2 Mechanical Property Evaluation of Second-Phase Particle in Magnesium Alloy by Micro-pillar Compression

It is clear from the previous study (Sect. 2.3.1) that the second-phase particles significantly affect the deformation characteristics of magnesium alloys. Therefore, it is essential to understand the mechanical properties of the individual particle. However, due to the small size of these particles, their mechanical properties cannot be evaluated by conventional techniques. Thus, this study deals with the evaluation of mechanical properties (stress–strain behavior) of these second-phase particles using *in-situ* micro-pillar compression (Sarvesha et al. 2020).

The micro-pillar fabrication process has already been discussed in Case II. The undeformed and deformed pillars of the matrix and second-phase particles are shown in Fig. 9, and the stress–strain behavior is shown in Fig. 10a. During compression, slip bands form on the α-Mg matrix surface (shown in Fig. 8a1 inset), which manifests as strain bursts in stress–strain curves (Fig. 10a)—a general characteristic of ductile metals/alloy (Schneider et al. 2013). In contrast, the stress–strain behavior of $Mg_{17}Al_{12}$ showed linear behavior until a massive strain burst (Fig. 10a). The corresponding SE micrograph shows a noticeable change in the shape of the $Mg_{17}Al_{12}$ pillar (Fig. 9b2), which could be due to strong

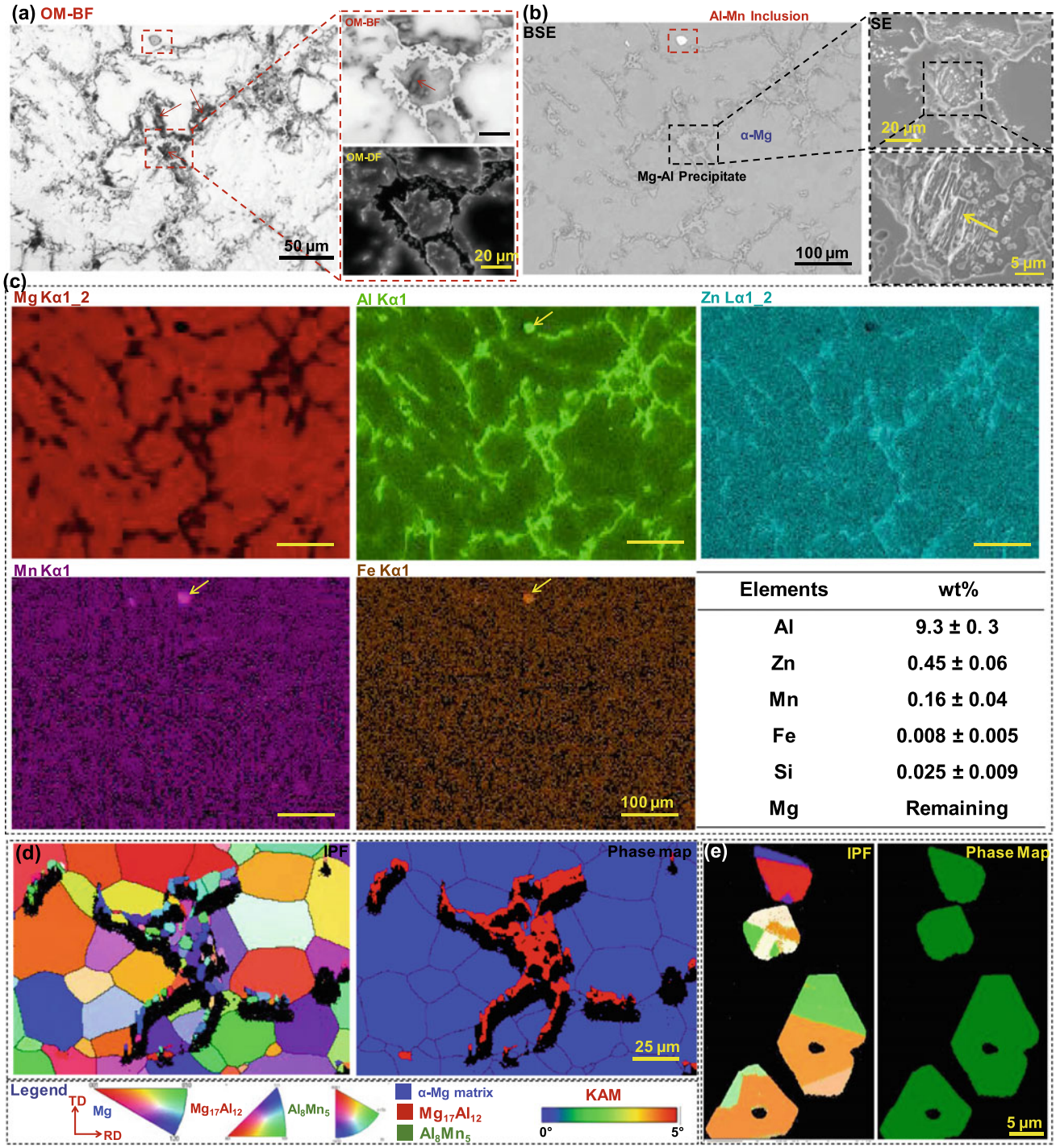

Fig. 6 **a** Optical micrograph (OM)-bright filed (BF) image, **b** SE micrograph, **c** EDS map of Mg, Al, Zn, Mn and Fe. **d**, **e** EBSD maps of $Mg_{17}Al_{12}$/α-Mg matrix and Al_8Mn_5 particle, respectively

strain localization without dislocation movement (Song et al. 2018). Further, it is evident from the stress–strain behavior of Al_8Mn_5 (Fig. 10a) particle that it exhibits the highest strength and ductility. SEM micrograph of the deformed Al_8Mn_5 pillar (Fig. 9c2) shows slip lines, which manifest as load drops in stress–strain curves (Fig. 10a). Al_8Mn_5 particle exhibits the highest yield strength of ~3084 ± 630 MPa, followed by $Mg_{17}Al_{12}$ with ~814 ± 141 MPa, and α-Mg matrix with ~134 ± 22 MPa.

The site-specific transmission electron microscopy (TEM) of Al_8Mn_5 deformed micro-pillar shows the dislocation structure (shown by the arrow in Fig. 10b). It can be

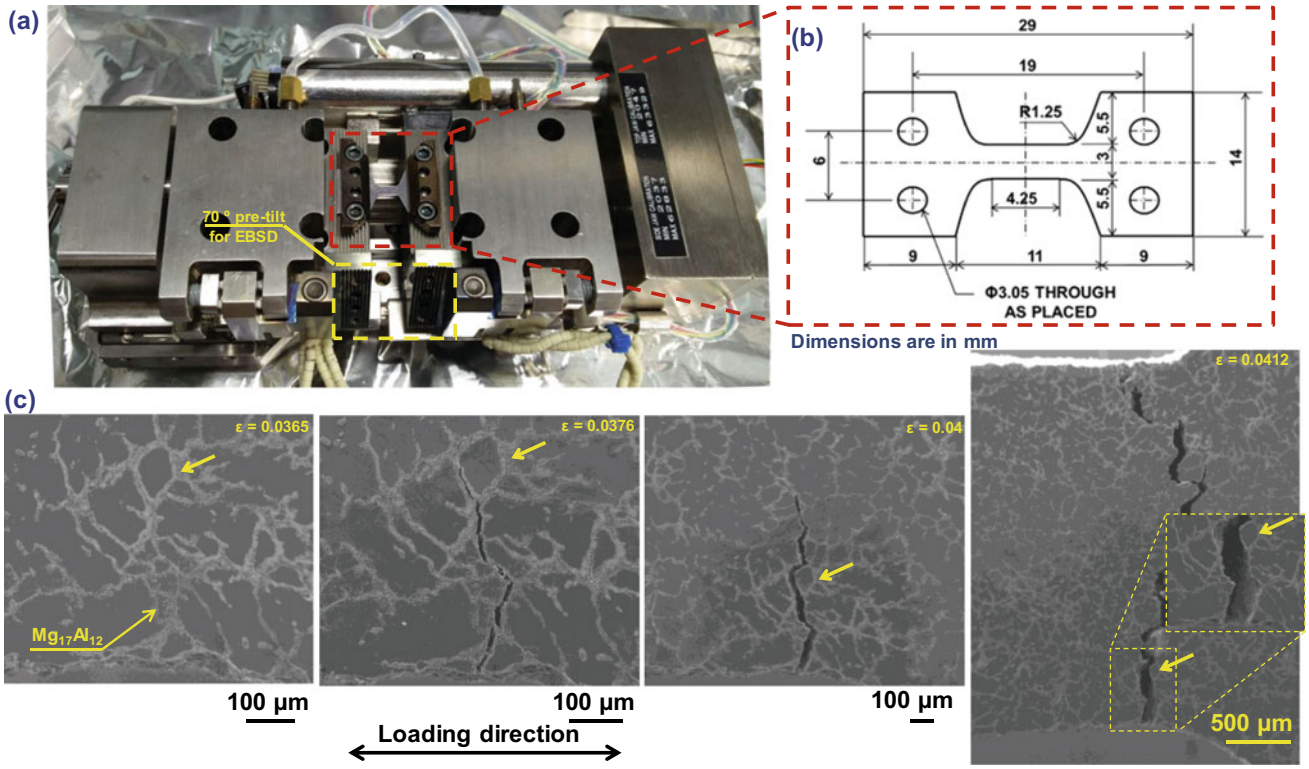

Fig. 7 **a** In-situ tensile testing stage, **b** sample dimension, **c** SEM images showing crack propagation through $Mg_{17}Al_{12}$ precipitates (arrow indicate reference region) in an as-cast sample

noticed that one type of dislocation structure is queued on the slip plane. The selective area diffraction pattern (SADP) along the $[100]$ zone axis is shown in Fig. 10c. The angle between $(01\bar{1})$ and (021) is around 88.7°, which corresponds to the rhombohedral crystal structure (Zeng et al. 2018).

Additionally, to verify the deformation behavior of each phase, qualitative analysis was also performed using nanoindentation. The indentation was performed at 60 mN load for the Al_8Mn_5 particle and 35 mN load for the $Mg_{17}Al_{12}$ particle and the matrix. SEM micrographs, atomic force microscopy (AFM) images, and corresponding line profiles of the indents made on the Al_8Mn_5 particle, the $Mg_{17}Al_{12}$ particle, and the matrix are shown in Fig. 10d–f, respectively. The line profiles along the corner (*C*) to edge (*E*) were used to observe the pile-up and sink-in phenomenon. Line profiles for the Al_8Mn_5 particle clearly show pile-up along all the edges, whereas the $Mg_{17}Al_{12}$ particle does not show pile-up or sink-in along the edges. The α-Mg matrix shows both pile-up and sink-in (indicated in AFM in Fig. 10f). In addition, both pile-up and sink-in were visible along the same edge of the indent (shown in SE micrograph in Fig. 10f). It is already known that the plastically deformable materials show pile-up characteristics (Fischer-Cripps 2004). The observed pile-up's in the case of Al_8Mn_5 particle corroborate with the observation made previously, i.e., the Al_8Mn_5 particles exhibit ductility. In contrast, the absence of pile-up and sink-in in the case of $Mg_{17}Al_{12}$ particles indicates the absence of plastic deformation, which is also evident from micro-pillar compression (Fig. 9).

A couple of studies are available for the bulk deformation of $Mg_{17}Al_{12}$ (Ragani et al. 2011; Fukuchi and Watanabe 1980). However, no study has been carried out to evaluate the stress–strain behavior of Al_8Mn_5 particles. Ragani et al. (2011) fabricated bulk $Mg_{17}Al_{12}$ through levitation casting and measured the room temperature compressive fracture strength and strain to be ~325 MPa and ~2%, respectively. Fukuchi and Watanabe (1980) evaluated the bulk properties of $Mg_{17}Al_{12}$ at elevated temperature (between 360 and 435 °C), where particles were found to exhibit ductility. However, it should be noted that both the studies were carried out in the bulk form, which can show different properties than that at a small length scale. In fact, it has been shown that the mechanical response at large and small length scales might be different (Singh et al. 2015; Michler et al. 2007; Korte and Clegg 2011). In the present case, interestingly, the $Mg_{17}Al_{12}$ particle exhibits distinct behavior at room temperature, i.e., sudden failure after a significant strain burst, unlike the brittle nature reported in the bulk samples (Ragani et al. 2011).

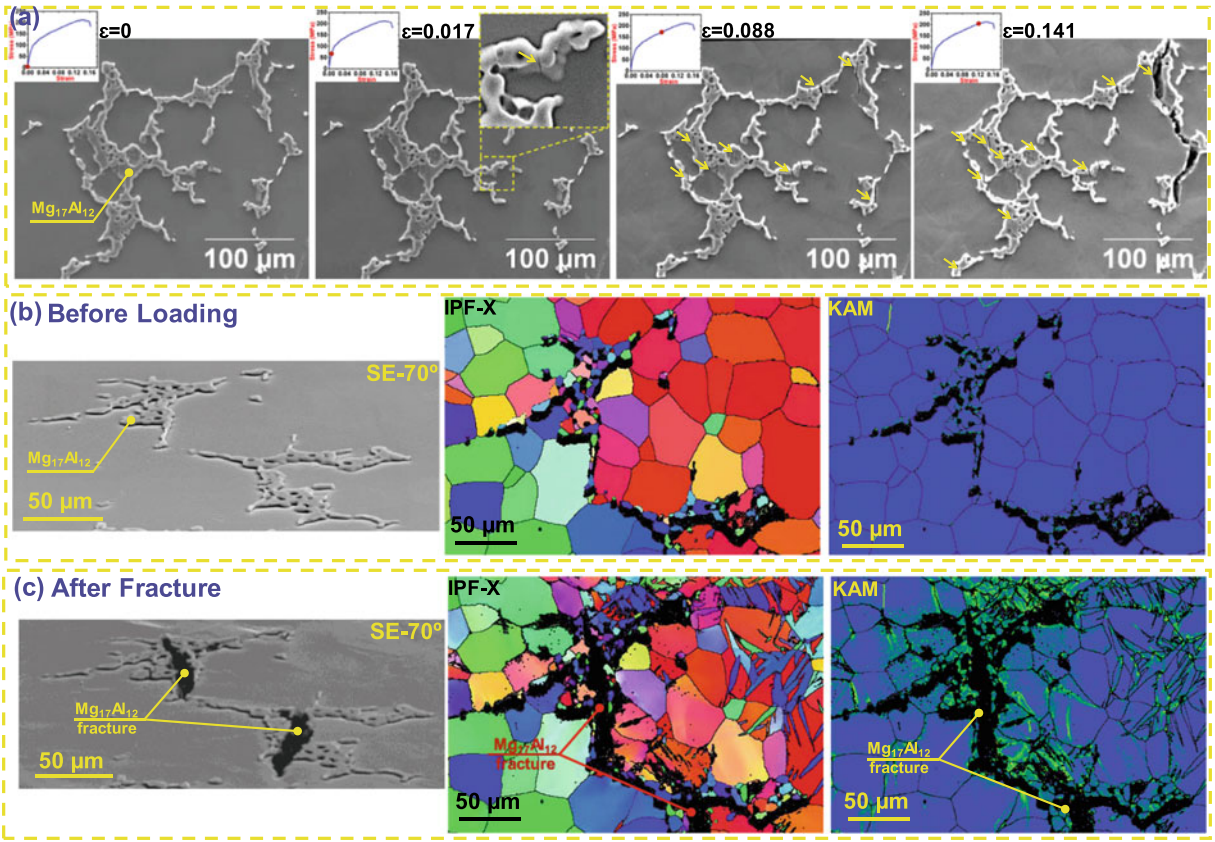

Fig. 8 **a** SEM micrographs of in-situ tensile testing of $Mg_{17}Al_{12}$ at different strain levels along with the stress–strain diagram. SE micrograph and corresponding area IPF-X and KAM map **b** before loading and **c** after fracture. (Loading is along *X* direction). (For legends, refer Fig. 6)

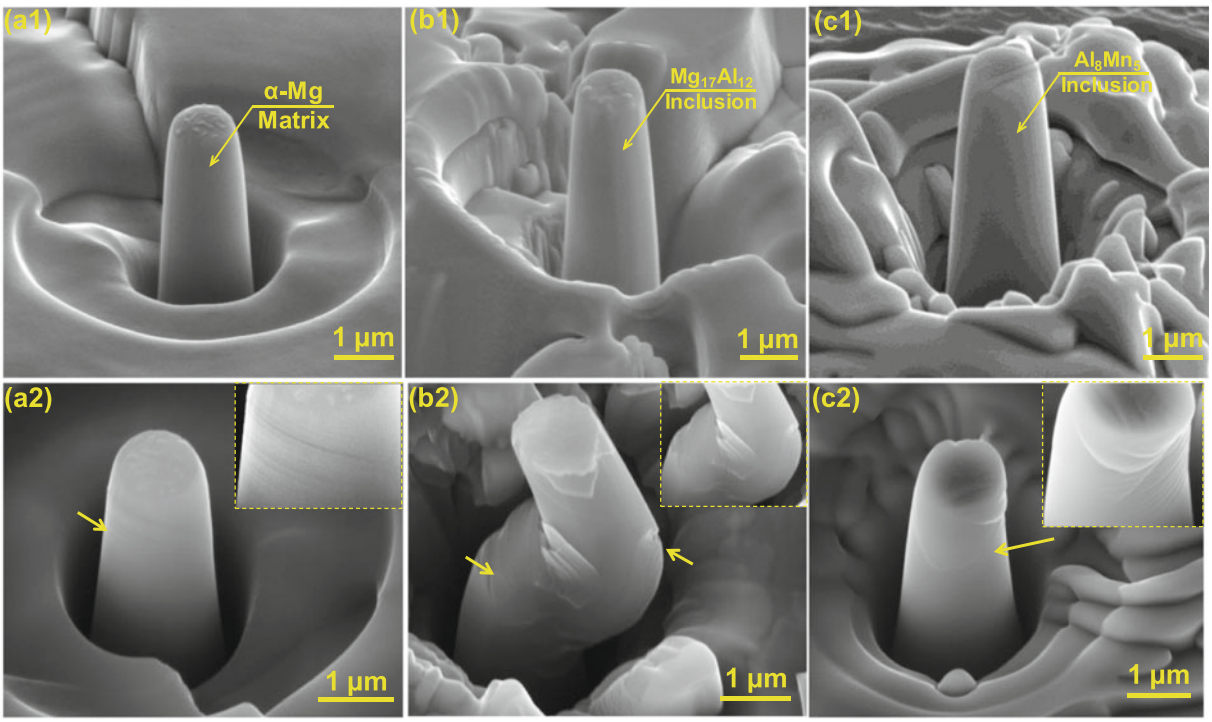

Fig. 9 **a1**, **b1**, **c1** and **a2**, **b2**, **c2** before and after deformation of α-Mg matrix, $Mg_{17}Al_{12}$, and Al_8Mn_5 micro-pillar, respectively (Sarvesha et al. 2020)

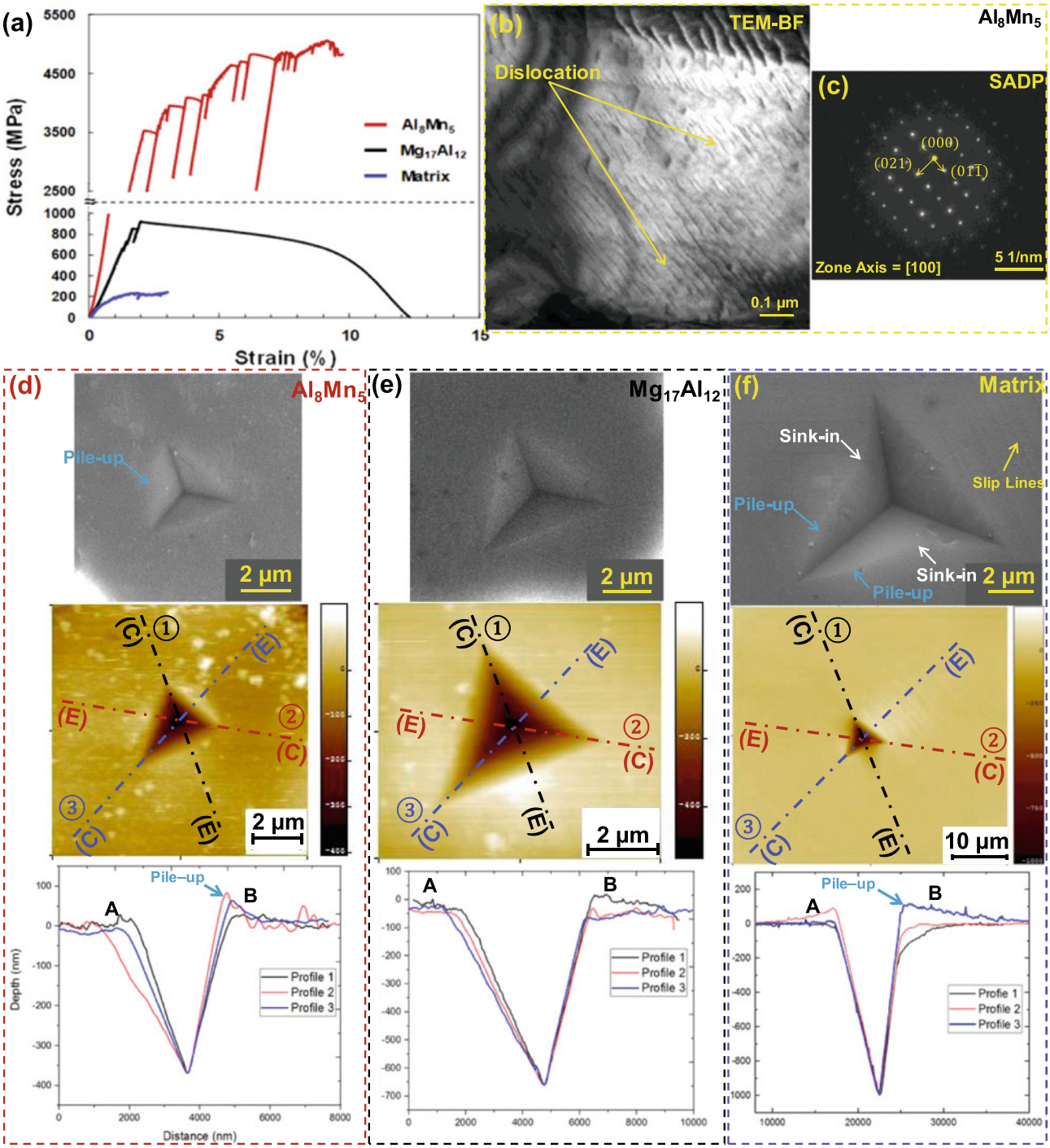

Fig. 10 **a** Stress–strain behavior of the matrix and particles, **b** TEM-BF, and **c** SADP of deformed Al_8Mn_5 pillar. **d–f** are the SE micrographs, AFM images, and line profile of the indents made using nanoindentation on Al_8Mn_5, $Mg_{17}Al_{12}$, and α-Mg matrix, respectively (Sarvesha et al. 2020)

3 Summary

The mechanical properties of materials change significantly with a reduction in size. Due to the inherent problems associated the conventional mechanical testing in understanding the deformation behavior of materials at a small length scale, i*n-situ* electron microscopy has gained interest in recent years. The advancement in instrumentation in the electron microscopes, such as FIB and nanoindentation in SEM, has made it possible to understand the deformation behavior in real time. Also, techniques such as EBSD/ECCI/DIC assist in the quantification of the deformation characteristics of the materials. The present article shows the importance of electron microscopy in understanding the deformation behavior of metallic systems by using three case studies.

Acknowledgements SSS would like to thank Prof. Nikhilesh Chawla at Arizona State University for his valuable suggestions on case studies I and II. Authors also acknowledge the support of ACMS facility, IIT Kanpur, and Prof. Jayant Jain, IIT Delhi, for case study III.

References

Fischer-Cripps AC (2004) Nanoindentation, 2nd ed. Springer, New York

Armstrong DEJ, Hardie CD, Gibson JSKL, Bushby AJ, Edmondson PD, Roberts SG (2015) Small-scale characterisation of irradiated nuclear materials: part II nanoindentation and micro-cantilever testing of ion irradiated nuclear materials. J Nucl Mater 462:374–381

Blawert C, Hort N, Kainer KU (2004) Automotive applications of magnesium and its alloys. Trans Indian Inst Metals 57(4):12

Bucci RJ, Warren CJ, Starke EA Jr (2000) Need for new materials in aging aircraft structures. J Aircr 37(1):122–129

Dimiduk DM, Uchic MD, Parthasarathy TA (2005) Size-affected single-slip behavior of pure nickel microcrystals. Acta Mater 53 (15):4065–4077

Dunn BD (1987) Eur Space Agency (ESA) J 11:1

Fukuchi M, Watanabe K (1980) Tensile behavior of γ-phase in Al-Mg system at elevated temperatures. J Japan Inst Light Metals 30 (5):253–257

Galyon GT (2005) Annotated tin whisker bibliography and anthology. IEEE Trans Electron Pack Manuf 28(1):94–122

Gianolaet DS (2011) In situ nanomechanical testing in focused ion beam and scanning electron microscopes. Rev Sci Instrum 82 (6):063901

Guo E-Y, Singh SS, Xie H, Williams JJ, Jing T, Chawla N (2014) Microstructure-based modeling of deformation in steels based on constitutive relationships from micropillar compression. Steel Res Int 85(6):946–953

Han JH, Saif MTA (2006) In-situ microtensile stage for electromechanical characterization of nanoscale freestanding films. Rev Sci Instrum 77(4):045102

Han JH, Rajagopalan J, Saif MTA (2007) MEMS-based testing stage to study electrical and mechanical properties of nanocrystalline metal films. In: MEMS/MOEMS components and their applications IV, vol 6464, p 64640C

Kim J, Plancher E, Tasan CC (2020) Hydrogenation-induced lattice expansion and its effects on hydrogen diffusion and damage in Ti–6Al–4V. Acta Mater 188:686–696

Korte S, Clegg WJ (2011) Discussion of the dependence of the effect of size on the yield stress in hard materials studied by microcompression of MgO. Phil Mag 91(7–9):1150–1162

Kulekci MK (2008) Magnesium and its alloys applications in automotive industry. Int J Adv Manuf Technol 39(9–10):851–865

Laplanche G, Bonneville J, Joulain A, Gauthier-Brunet V, Dubois S (2014) Mechanical properties of Al-Cu-Fe quasi crystalline and crystalline phases: an analogy. Intermetallics 50:54–58

Legros M, Gianola DS, Motz C (2010) Quantitative in-situ mechanical testing in electron microscopes. MRS Bull 35:354–360

Lü YZ, Wang QD, Ding WJ, Zeng XQ, Zhu YP (2000) Fracture behavior of AZ91 magnesium alloy. Mater Lett 44(5):265–268

Lugo M, Jordon JB, Horstemeyer MF, Tschopp MA, Harris J, Gokhale AM (2011) Quantification of damage evolution in a 7075 aluminum alloy using an acoustic emission technique. Mater Sci Eng A 528(22–23):6708–6714

Maire E, Zhou S, Adrien J, Dimichiel M (2011) Damage quantification in aluminium alloys using in situ tensile tests in X-ray tomography. Eng Fract Mech 78(15):2679–2690

Mathew S, Osterman M, Pecht M, Dunlevey F (2009) Evaluation of pure tin plated copper alloy substrates for tin whiskers. Circuit World 35(1):3–8

Michler J, Wasmer K, Meier S, Östlund F, Leifer K (2007) Plastic deformation of gallium arsenide micropillars under uniaxial compression at room temperature. Appl Phys Lett 90(4):043123

Muñoz-Palos JM, del Cristina MC, Adeva P (1996) Synthesis of Mg_2Si powder by mechanical alloying and its consolidation. Mater Trans Japan Inst Metals Mater 37(10):1602–1606

Östlund F (2011) Ductile-brittle transition in micropillar compression of GaAs at room temperature. Phil Mag 91(7–9):1190–1199

Östlundet F (2009) Brittle-to-ductile transition in uniaxial compression of silicon pillars at room temperature. Adv Func Mater 19 (15):2439–2444

Oswald LE (2003) Effects of microstructure on high-cycle fatigue of an Al-Zn-Mg-Cu Alloy (Al-7055). Masters thesis, School of Engineering, University of Pittsburgh, Pittsburgh, PA

Payne J, Welsh G, Christ RJ Jr, Nardiello J, Papazian JM (2010) Observations of fatigue crack initiation in 7075–T651. Int J Fatigue 32(2):247–255

Pearson S (1975) Initiation of fatigue cracks in commercial aluminium alloys and the subsequent propagation of very short cracks. Eng Fract Mech 7(2):235–240

Powell BE, Skove MJ (2004) Elastic strength of tin whiskers in tensile tests. J Appl Phys 36(4):1495

Proff C, Abolhassani S, Dadras MM, Lemaignan C (2010) In-situ oxidation of zirconium binary alloys by environmental SEM and analysis by AFM, FIB, and TEM. J Nucl Mater 404(2):97–108

Ragani J, Donnadieu P, Tassin C, Blandin JJ (2011) High-temperature deformation of the γ-$Mg_{17}Al_{12}$ complex metallic alloy. Scripta Mater 65(3):253–256

Sarvesha R, Ghori U-R, Chiu YL, Jones IP, Singh SS, Jain J (2020) Mechanical property evaluation of second phase particles in a Mg-8Al-0.5Zn alloy using micropillar compression. Mater Sci Eng A 775:138973

Sarvesha R, Chalapathi D, Yadava M, Singh SS (2021) *In-situ* studies on deformation and fracture characteristics of AZ91 Mg alloy. Materialia 18:101177. https://doi.org/10.1016/j.mtla.2021.101177

Schneider AS, Kiener D, Yakacki CM, Maier HJ, Gruber PA, Tamura N, Kunz M, Minor AM, Frick CP (2013) Influence of bulk pre-straining on the size effect in nickel compression pillars. Mater Sci Eng A 559:147–158

Singh SS, Sarkar R, Xie H-X, Mayer Rajagopalan CJ, Chawla N (2014) Tensile behavior of single-crystal tin whiskers. J Electron Mater 43 (4):978–982

Singh SS, Williams JJ, Hruby P, Xiao X, De Carlo F, Chawla N (2014) In-situ experimental techniques to study the mechanical behavior of materials using X-ray synchrotron tomography. Integr Mater Manuf Innov 3(1):109–122

Singh SS, Schwartzstein C, Williams JJ, Xiao X, De Carlo F, Chawla N (2014c) 3D microstructural characterization and mechanical properties of constituent particles in Al 7075 alloys using X-ray synchrotron tomography and nanoindentation. J Alloy Compd 602:163–174

Singh SS, Guo E, Xie H, Chawla N (2015) Mechanical properties of intermetallic inclusions in Al 7075 alloys by micropillar compression. Intermetallics 62:69–75

Singh SS, Williams JJ, Stannard TJ, Xiao X, Carlo FD, Chawla N (2016) Measurement of localized corrosion rates at inclusion particles in AA7075 by In-Situ three-dimensional (3D) X-ray synchrotron tomography. Corros Sci 104:330–335

Singh SS, Stannard TJ, Xiao X, Chawla N (2017) In Situ X-ray microtomography of stress corrosion cracking and corrosion fatigue in aluminum alloys. JOM 69(8):1404–1414

Slama MBH, Maloufi N, Guyon J, Bahi S, Weiss L, Guitton A (2019) In-Situ macroscopic tensile testing in SEM and electron channeling contrast imaging: pencil glide evidenced in a bulk β-$Ti_2$1S polycrystal. Material 12(15):2479

Song G, Kong T, Dusoe KJ, Canfield PC, Lee S-W (2018) Shear localization and size-dependent strength of YCd_6 quasicrystal approximant at the micrometer length scale. J Mater Sci 53 (9):6980–6990

Starke EA, Staley JT (2011) 24—application of modern aluminium alloys to aircraft. In: Lumley R (ed) Fundamentals of aluminium metallurgy. Woodhead Publishing, pp 747–783

Takeuchi S, Hashimoto T, Suzuki K (1996) Plastic deformation of Mg_2Si with the C1 structure. Intermetallics 4(Suppl. 1):S147–S150

Uchic MD, Dimiduk DM, Florando JN, Nix WD (2004) Sample dimensions influence strength and crystal plasticity. Science 305 (5686):986–989

Volkert CA, Donohue A, Spaepen F (2008) Effect of sample size on deformation in amorphous metals. J Appl Phys 103:083539

Wang L, Qin XY, Xiong W, Zhu XG (2007) Fabrication and mechanical properties of bulk nanocrystalline intermetallic Mg_2Si. Mater Sci Eng A 459(1–2):216–222

Weiland H, Nardiello J, Zaefferer S, Cheong S, Papazian J, Raabe D (2009) Microstructural aspects of crack nucleation during cyclic loading of AA7075-T651. Eng Fract Mech 76(5):709–714

Wisner B, Cabal M, Vanniamparambil PA, Hochhalter J, Leser WP, Kontsos A (2015) In-situ microscopic investigation to validate acoustic emission monitoring. Exp Mech 55(9):1705–1715

Xue Y, El Kadiri H, Horstemeyer MF, Jordon JB, Weiland H (2007) Micromechanisms of multistage fatigue crack growth in a high-strength aluminum alloy. Acta Mater 55(6):1975–1984

Yakubtsov IA, Diak BJ, Sager CA, Bhattacharya B, MacDonald WD, Niewczas M (2008) Effects of heat treatment on microstructure and tensile deformation of Mg AZ80 alloy at room temperature. Mater Sci Eng A 496(1–2):247–255

Zeng G, Xian JW, Gourlay CM (2018) Nucleation and growth crystallography of Al_8Mn_5 on B_2-Al(Mn, Fe) in AZ91 magnesium alloys. Acta Mater 153:364–376

Zindal A, Jain J, Prasad R, Singh SS, Cizek P (2017) Correlation of grain boundary precipitate characteristics with fracture and fracture toughness in an Mg-8Al-0.5 Zn alloy. Mater Sci Eng A 706:192–200

Zindal A, Jain J, Prasad R, Singh SS, Sarvesha R, Cizek P, Barnett MR (2018) Effect of heat treatment variables on the formation of precipitate free zones (PFZs) in Mg-8Al-0.5Zn alloy. Mater Charact 136:175–182

Exploring Carbon Surface Using Electron Microscopy: Applications to Energy, Environment, and Health

Priyanka Gupta and Nishith Verma

1 Introduction

Carbon is undoubtedly one of the most versatile elements known to mankind. The ability of the material to form a diverse hybridization and bonding with different elements gives rise to its excellent chemical and physical properties such as high thermal and chemical stabilities, good electrical and thermal conductivities, and a high surface area. Carbon can also bind with itself in different ways, forming various nanostructures. The unique and tuneable characteristics of carbon nanomaterials have provided us an opportunity to use them in many areas, for example, energy storage devices, wastewater remediation, biofertilizers, biosensors, biomedical devices, and air pollution control.

Carbon fibers are a relatively newer material and show various interesting morphologies at micron and nanoscales. In recent times, activated carbon microfiber (ACF) has drawn attention of research community because of the microporous structure of the material possessing a high surface area (1200–1800 m^2/g). Additionally, the narrow diameters (usually 10–20 μm) of the fibers exert a negligible external mass transfer diffusion resistance, when the material is used under practical (flow) conditions. Various functional groups such as ketonic, carboxylic, and hydroxyl present on the ACF surface are also responsible for the high catalytic activity of the material. Furthermore, the catalytic activity of ACF can be enhanced by functionalizing it with various metals.

Recent studies have introduced carbon nanofibers (CNFs) grown on the ACF substrate using catalytic chemical vapor deposition (CVD) (Yadav and Verma 2017; Kumar et al. 2020; Bairagi and Verma 2018; Ashfaq et al. 2017). The CNFs are cylindrical-shaped nanostructures with stacked graphene layers. Such nanostructures with extraordinary chemical and physical properties have been efficiently used as adsorbents and catalysts. The multiscale structured composite of ACFs and the graphitic CNFs has found applications in H_2-storage, plant growth, biosensors, and medical treatments.

Electron microscopy has emerged as a powerful tool for examining the material surface morphologies. Scanning electron microscopy (SEM) can provide information about the texture of carbonaceous materials, including macropores, shape of nanostructures, grain size, and the presence of metal nanoparticles (NPs) dispersed in the ACFs/CNFs. The high-resolution, and low and high magnification SEM images can be used for visually examining the samples. Transmission electron microscopy (TEM) is another analytical tool to examine the material surface, especially its internal texture. TEM can provide the size and shape of micro-nanofibers along with the other micro-nanostructures present in the material. High-resolution (HR) TEM can be used to provide information about the diffraction patterns, crystal planes, fringe width, graphitic characteristics, and different phases present in the carbonaceous materials. We first showcase the different applications of the ACF/CNF-based materials developed in our research laboratory and then discuss the material texture recorded using electron microscopy, and how the SEM/TEM images are extremely useful in understanding the carbon surface.

2 ACF/CNF as a H_2-storage Material

Recent research on energy has primarily focused on finding non-conventional sources of energy because of continuous depletion of fossil fuels globally. Hydrogen is a clean, renewable, and an abundantly available source of energy. Its efficient and safe storage is, however, a concern. Recently, Yadav and Verma (2017) have developed an efficient H_2-storage material based on the multiscale structured

P. Gupta · N. Verma (✉)
Department of Chemical Engineering and Centre for Environmental Science and Engineering, Indian Institute of Technology Kanpur, Kanpur, 208016, India
e-mail: nishith@iitk.ac.in

K. Biswas et al. (eds.), *Electron Microscopy in Science and Engineering*, IITK Directions 6,
https://doi.org/10.1007/978-981-16-5101-4_3

composite of ACF and CNF. The composite is dispersed with the nickel (Ni) and ceria (CeO_2) NPs. Briefly, the acid-pretreated ACF samples are impregnated using an aqueous solution of $Ni(NO_3)_2$ and $Ce(NO_3)_3$. The bimetals-impregnated ACFs are subjected to calcination and H_2-reduction, followed by CVD. The prepared Ni-CeO_2-ACF/CNF show a remarkable H_2-adsorption capacity of 1.36% (w/w) at 200 °C and 1 bar (Fig. 1). Furthermore, complete desorption of H_2 is possible at 300 °C, indicating regeneration of the proposed H_2 storage material to be energy-efficient.

3 Carbon Nanofibrous Beads for Desulfurization

Combustion of diesel, used as a fuel in transportation, generates a significant amount of SO_2, a major atmospheric air pollutants Decomposition of the sulfur (S) containing compounds, viz. thiophene and dibenzothiophene (DBT), also deactivates the catalyst used in the catalytic converters of automobiles, thereby decreasing its overall life (Ai et al. 2012). Recently, carbon nanofibrous beads have emerged as a promising material for the adsorptive desulfurization (ADS) process (Prajapati and Verma 2017). Micron-sized materials of ~0.8 mm size can serve as an efficient packed bed material, without channeling or maldistribution in flow of the liquid to be treated, unlike their counterpart powdery materials. The beads also allow an easy recovery and regeneration post-treatment. Prajapati and Verma (2017) have synthesized the activated carbon beads (ACBs) decorated with Ni-CNF as an efficient adsorbent for ADS. Figure 2 shows a schematics of the experimental setup used for ADS, along with the representative batch adsorption data for thiophene and DBT on NiO/ACBs and Ni-CNF/ACBs. The data shows dependence of the adsorption capacities of the materials on their pore volumes. Ni-CNF/ACBs show a higher adsorption capacity for thiophene, compared to NiO/ACBs. Ni-CNF/ACBs with small pore volume allow adsorption of the relatively smaller-sized thiophene molecules. On the other hand, adsorption of DBT is found to be higher in NiO/ACBs. The relatively small pore volume in Ni-CNF/ACB is inadequate for adsorption of the large-sized DBT molecules, whereas NiO/ACBs having a large pore volume show a high adsorption capacity for DBT.

4 Cu-CNF/ACF as an Adsorbent for Cr(VI) and Micronutrient for Plants

Agricultural fields and water bodies are gradually contaminated by industrial effluents despite stringent regulations in place globally. Toxic metals such as As(III), As(V), Cr(VI), Pb(II), and Cd(II) are common aqueous pollutants. Uptake of the metals from soil by plants can interfere with their physiological processes, adversely affecting their growth. A physical mixture of carbon micro- and nanofibers-based materials has been indicated to be an efficient adsorbent or scavenger of metals in soil, besides a good translocator of the micronutrients including Cu from soil to plant roots and shoots (Kumar et al. 2020; Bairagi and Verma 2018). Kumar et al. (2020) prepared Cu-CNFs grown over the ACFs to scavenge Cr(VI) in soil and simultaneously supply essential nutrients (Cu in this case) to the chickpea plant (Fig. 3). The prepared materials also increased root and shoot lengths significantly. As shown in the figure, Cu-CNF/ACF was ball milled to separate Cu-CNF from ACF. An aqueous dispersion of Cu-CNF and ACF was then mixed in a Cr-stressed medium for germination of chickpea seeds. Plant growth was monitored, and it was found that Cr(VI) was adsorbed on ACF, while the nanosized Cu-CNFs were translocated from soil to the plant roots and shoots, supplying essential micronutrients to the plants.

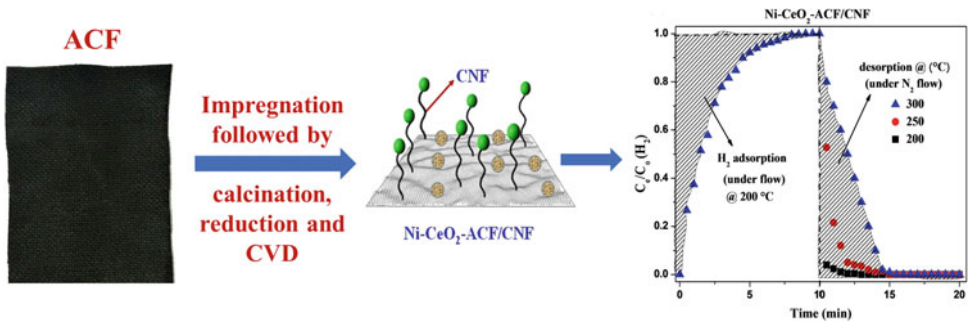

Fig. 1 Schematic representation of the Ni-CeO_2-ACF/CNF storage material and its H_2-adsorption/H_2-desorption characteristics under flow conditions (Yadav and Verma 2017)

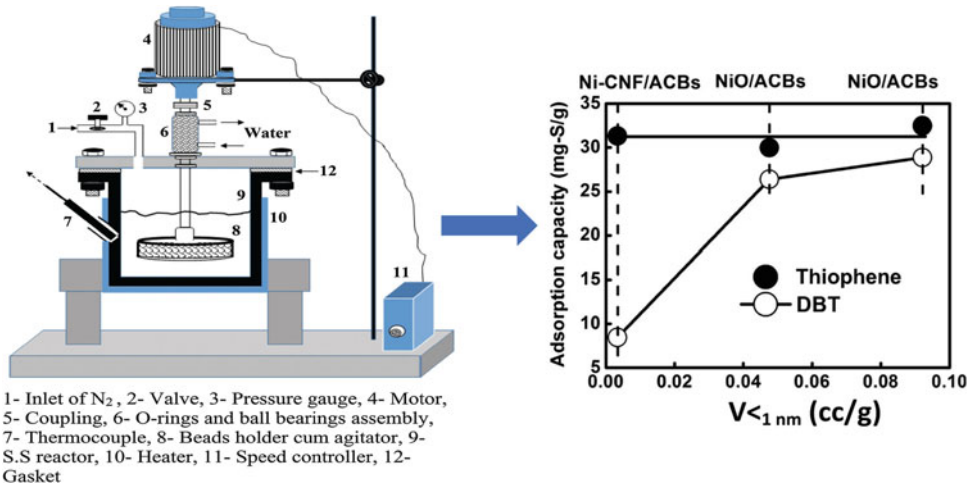

Fig. 2 Schematic illustration of the experimental setup used for the ADS tests and the adsorption capacities (mg S/g) of NiO/ACBs and Ni-CNF/ACBs determined for thiophene and DBT (Prajapati and Verma 2017)

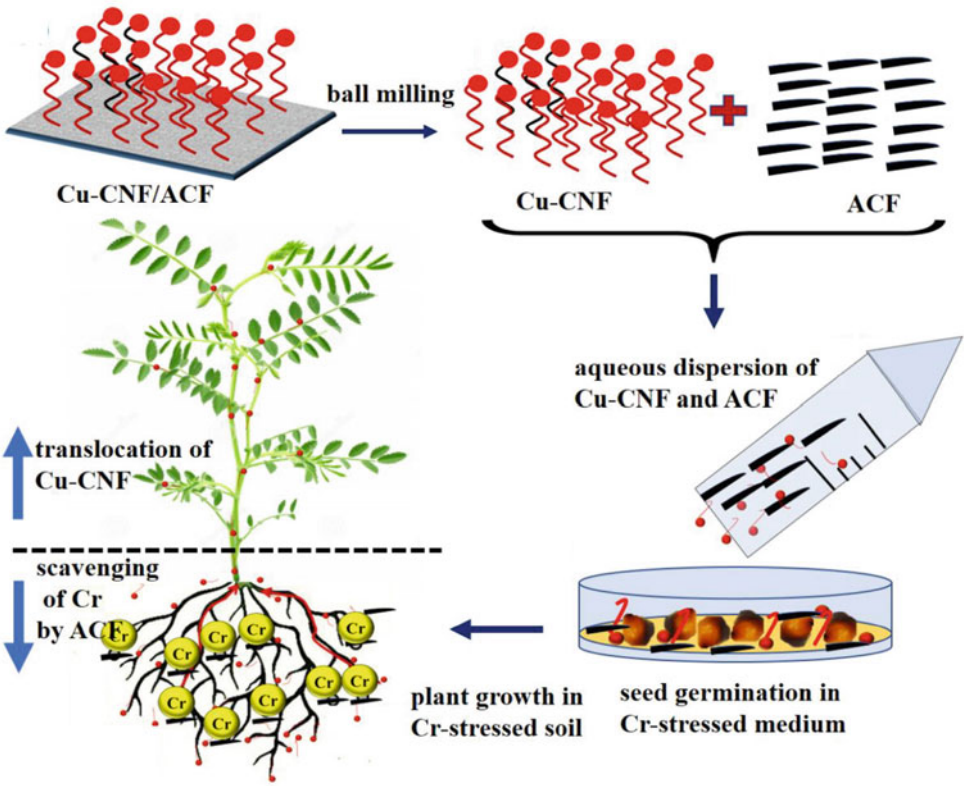

Fig. 3 Graphical representation showing the working principle of a physical mixture of Cu-CNF and ACF for growth of plants with simultaneous removal of Cr (VI) from aqueous soil (Kumar et al. 2020)

5 Cu/Ni-CNF as an Electrochemical Sensor for Cholesterol

Development of a sensor for detecting various biomarkers in blood, with a fast response, good reproducibility, and high sensitivity and selectivity is challenging (Li et al. 2010). Interestingly, Bairagi and Verma (2018) have successfully synthesized the dendritic nanofibers of polymethyl orange (PMO) over Cu/Ni-CNF, as the BMCP electrode, to measure cholesterol in human blood (Fig. 4). PMO, electropolymerized on BMCP using the methyl orange (MO) monomer, serves as the recognition element for cholesterol. Electropolymerization was performed using cyclic voltammetry from −1.0 to 1.0 V. Differential pulse voltammetry (DPV) was used to measure response of the prepared biosensor. The calibration plot (currents vs. cholesterol concentrations) showed a remarkable linearity (R^2 = 0.999) over a large concentration range (0.04–600 mg/dL).

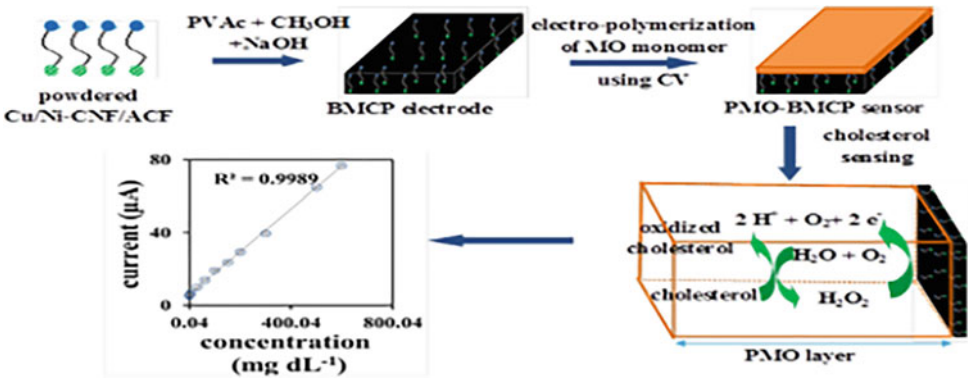

Fig. 4 Schematic illustration of the preparation steps for the BMCP sensor and the calibration plot for cholesterol sensing (Bairagi and Verma 2018)

6 Cu/Zn-ACF/CNF as a Wound Dressing Material

Growing resistance of wound bacteria toward clinical drugs has prompted the development of an effective and site-specific antibacterial therapy or dressing. The Cu and Zn metal NPs, well recognized for their antibacterial properties, can be used for wound treatment with effective deployment techniques. Ashaq et al. (2017) have prepared an efficient wound dressing biomaterial to cure bacterial infections caused by burn, surgery, and injuries. A polyvinyl alcohol (PVA) and cellulose acetate phthalate (CAP) precursor-based polymeric composite film was prepared using suspension polymerization. Cu/Zn-ACF/CNF was separately prepared. The ball-milled Cu/Zn-ACF/CNF was dispersed in an aqueous solution of CAP, and the prepared slurry was added to the polymerization reaction mixture of PVA at incipience of the gel formation (Fig. 5). The prepared polymer–metal–carbon (PMC) composite was mixed with DI water, and the mixture was cast on a Teflon sheet to prepare the dressing material. The material was found to be effective against bacterial dissemination by disrupting the bacterial cell membrane, besides enhancing platelet activation and the blood clotting abilities leading to rapid wound healing.

7 Materials Synthesis

The phenolic resin precursor-based ACF, procured from Kynol, Japan, is pretreated using 0.05 M HNO_3 at 80 °C for 2 h. The acid treatment removes impurities such as chlorides and nitrates, if any, from the ACF surface. The acid-treated ACFs are washed multiple times with DI water until pH of the ACF surface is ~7. Next, the ACF samples are dried in a vacuum oven at 200 °C for 12 h to remove moisture and any trapped gases. The ACFs are impregnated with the aqueous solutions of different metal salts, viz. $Ni(NO_3)_2$, $Ce(NO_3)_3$, $Cu(NO_3)_2$, and $Zn(NO_3)_2$, depending upon the applications. The salt-impregnated ACF samples are dried overnight at room temperature (~30 °C). The dried samples are calcined at 400 °C in an inert atmosphere (N_2) to convert the metal nitrates to metal oxides. The calcined samples are

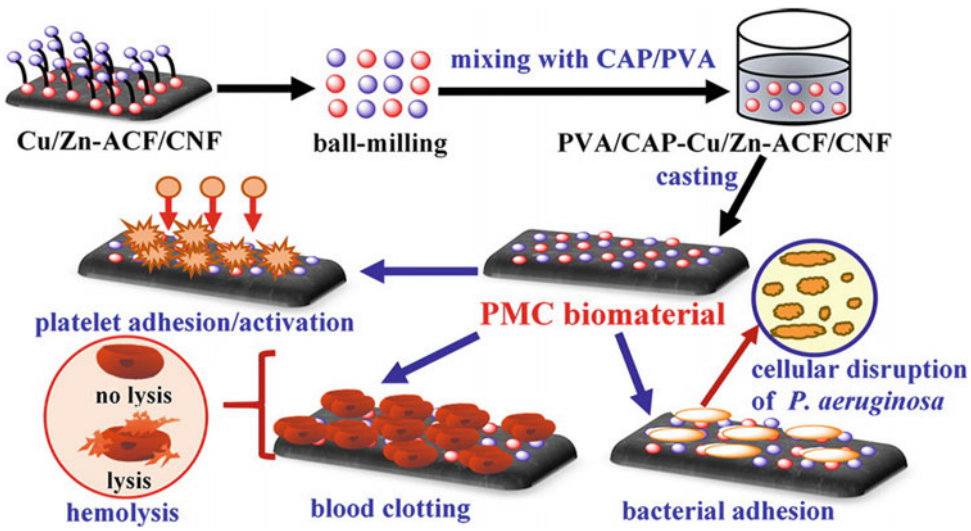

Fig. 5 Schematic representation of the preparation steps for the PMC wound dressing material and its application (Ashfaq et al. 2017)

subjected to the H_2-reduction at suitable temperatures, depending on the types of the impregnated metal salts. The reduction step results in conversion of metal oxides to their elemental form. CNFs are grown on the metal–ACF samples using CVD with acetylene as the carbon source and the metal NPs dispersed in the ACFs acting as the CVD catalyst.

The phenolic resin beads are synthesized using suspension polymerization. The reaction mixture includes 50 mL phenol as the monomer, 63 mL formaldehyde as the solvent, and 2 mL triethylamine (TEA) as the catalyst. Hexamethylenetetramine (HMTA) is used as the cross-linking agent, and PVA is added as the suspension stabilizing agent. The metal salts are added to the reaction mixture at incipience of the bead formation. The phenolic beads are subjected to carbonization and steam activation at 900 °C for 2 and 1 h, respectively, in N_2 atmosphere. The activation step creates porosity in the material. The activated beads are subjected to the H_2-reduction, and CNFs are grown over the porous activated beads by the CVD process. The detailed procedure is described in our study (Prajapati and Verma 2017).

8 Material Surface Characterization (SEM/TEM)

Surface morphology of the prepared materials was examined using the field emission scanning electron microscope (FE-SEM–MIRA3 series, TESCAN). The SEM images were captured using an in-lens detector at the accelerating voltage of 10 kV, filament current of 2.37 A, and working distance of 2–4 mm.

Figure 6 shows the SEM images of the materials tested for H_2-storage: ACF, Ni-CeO_2/ACF, and Ni-CeO_2-ACF/CNF. The low magnification image shows ACF fibers to be cylindrically shaped (Fig. 6a). Approximately uniform-sized micropores can be seen in the high magnification image (Fig. 6b). Figure 6 shows the shiny Ni and CeO_2 nanoparticles in the micropores of the ACF surface. An approximately uniform and dense growth of CNFs can be seen in Fig. 6c, c′. Shiny metal NPs located at the tips of CNFs corroborate the tip growth mechanism of the material (Zheng et al. 2004). The CNFs augment exposure of the metal NPs to the surrounding medium. The increased exposure enhances the H_2-adsorption capacity of Ni-CeO_2-ACF/CNF.

Figure 7 presents the HR-TEM images of Ni-CeO_2-ACF/CNF. The TEM image shows metal NP (dark spot) at the tips of CNFs (Fig. 7a). Figure 7b shows the selected area diffraction pattern of the Ni NP. The three distinct diffraction rings represent the (1 1 1), (2 0 0), and (2 2 0) crystal planes in the Ni NP. Crystallinity of the Ni NP and graphitic characteristics of the CNFs were confirmed by the presence of fringes (Fig. 7c). The fringe width was calculated to be 0.176 and 0.334 nm corresponding to the (2 0 0) crystal plane of Ni and (1 1 1) plane of carbon, respectively (Fig. 7d). The metal NPs catalytically dissociate H_2 to H atoms at the CNF edges, which migrate and diffuse into the porous carbon substrate. Therefore, the spillover effect results in the enhanced adsorption of H_2 in Ni-CeO_2-ACF/CNF (Kim et al. 2008).

The SEM images of Ni-CNF/ACB, used as an adsorbent in ADS, are presented in Fig. 8. Figure 8a shows an approximately dense and uniform growth of CNFs over the Ni-CNF/ACB bead. The average size of Ni-CNF/ACB is measured to be ∼0.8 mm. The CNFs are cylindrically shaped structures. The average diameter of the CNFs was measured to be 70 nm. Shiny dots at the tips of CNFs represent a Ni NP (Fig. 8b), which also indicates the tip growth mechanism during CVD. Ni NPs plays an important role in desulfurization via direct Ni-S interaction. A graphitic characteristic of CNFs enhances adsorption capacity of the material via π-π and/or hydrophobic interactions between the graphitic planes of CNFs and the thiophene molecules. The porous Ni-CNF/ACBs with an augmented exposure of Ni adsorb thiophene and DBT in diesel efficiently, with the adsorption capacities determined to be 62.3 and 8.1 mg S/g, respectively. Approximately dense growth of the CNFs over ACB and the location of Ni NPs at the tips of CNFs can be confirmed from the SEM analysis. Clearly, the images provide a visual understanding of how the CNFs augment the exposure of the Ni NPs, enhancing the interactions of the thiophene and DBT molecules with the Ni NPs.

Figure 9 shows the SEM images of Cu-CNF/ACF. As mentioned earlier, the material was used in its dual role: as a provider of the Cu micronutrient to plant and a scavenger of Cr(VI) in soil. Figure 9a corroborates the micron-sized ACF substrate containing micropores. Figure 9b corroborates an approximately uniform growth of CNFs on ACF using Cu as the CVD catalyst. The CNF growth using Cu as the CVD catalyst also followed the tip growth mechanism with the Cu NPs located at the tips of the CNFs, similar to the earlier case using Ni as the catalyst (Fig. 6c'). A small size and the negatively charged surface of CNFs facilitated their translocation in plant shoots through xylem. Broken cell compartments were clearly observed in the shoots of plant grown in Cr environment without providing any treatment (Fig. 9d). The intact cellular structure observed in Fig. 9e implies that ACF effectively scavenged Cr by adsorption and prevented it from disrupting the plasma cell membrane of plant. Figure 9f, g confirms that the CNFs and Cu NPs were efficiently translocated to the plant shoots, which acted as the micronutrient and promoted plant growth. Effectiveness of Cu-CNF and ACF can be directly gauged by monitoring plant growth, while the SEM analysis clearly provides an explanation for the plant growth on cellular level (Gupta et al. 2019).

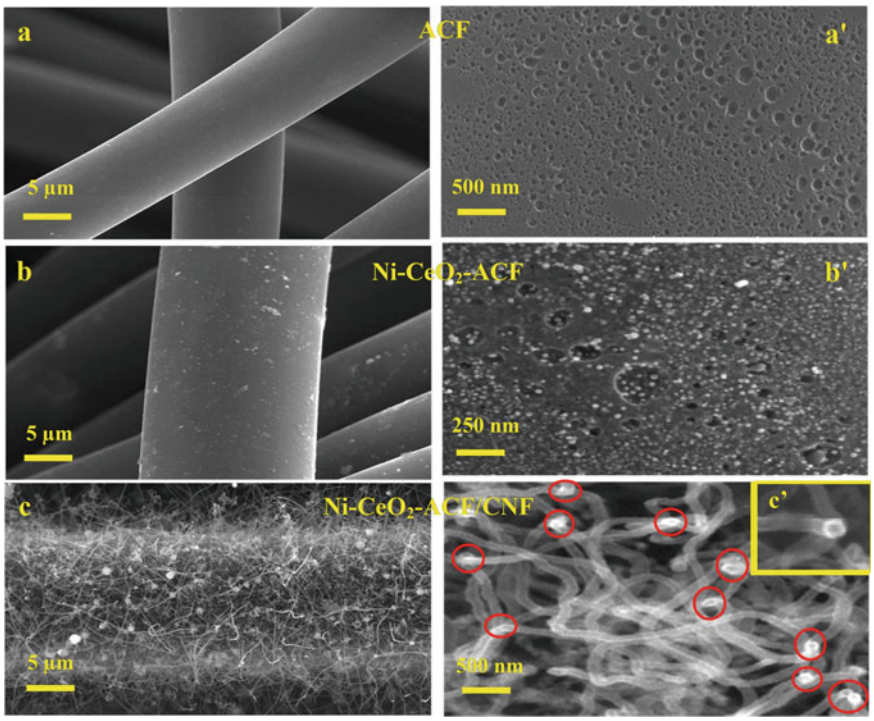

Fig. 6 SEM images at low and high magnifications of **a**, **a′** ACF, **b**, **b′** Ni-CeO_2/ACF, and **c**, **c′** Ni-CeO_2-ACF/CNF (Yadav and Verma 2017)

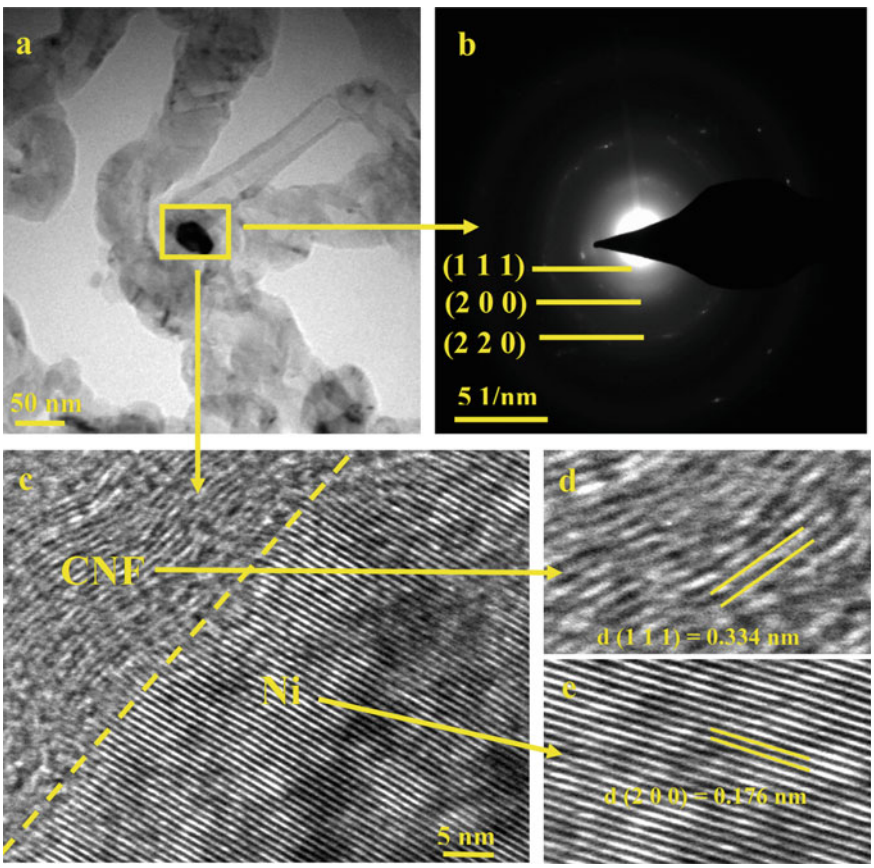

Fig. 7 **a** TEM image of CNF, **b** selected area diffraction pattern of Ni crystal, **c**, **d** fringes present in Ni NPs and CNFs and their corresponding fringe widths (Yadav and Verma 2017)

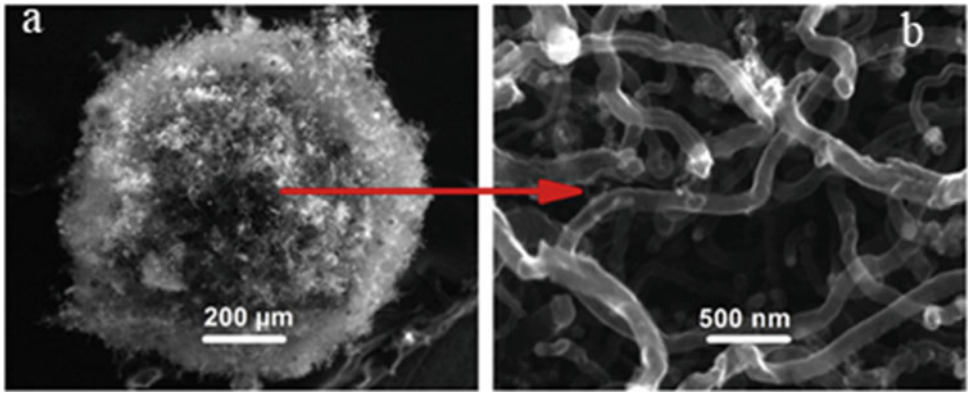

Fig. 8 SEM images of Ni-CNF/ACB at **a** low and **b** high magnifications (Prajapati and Verma 2017)

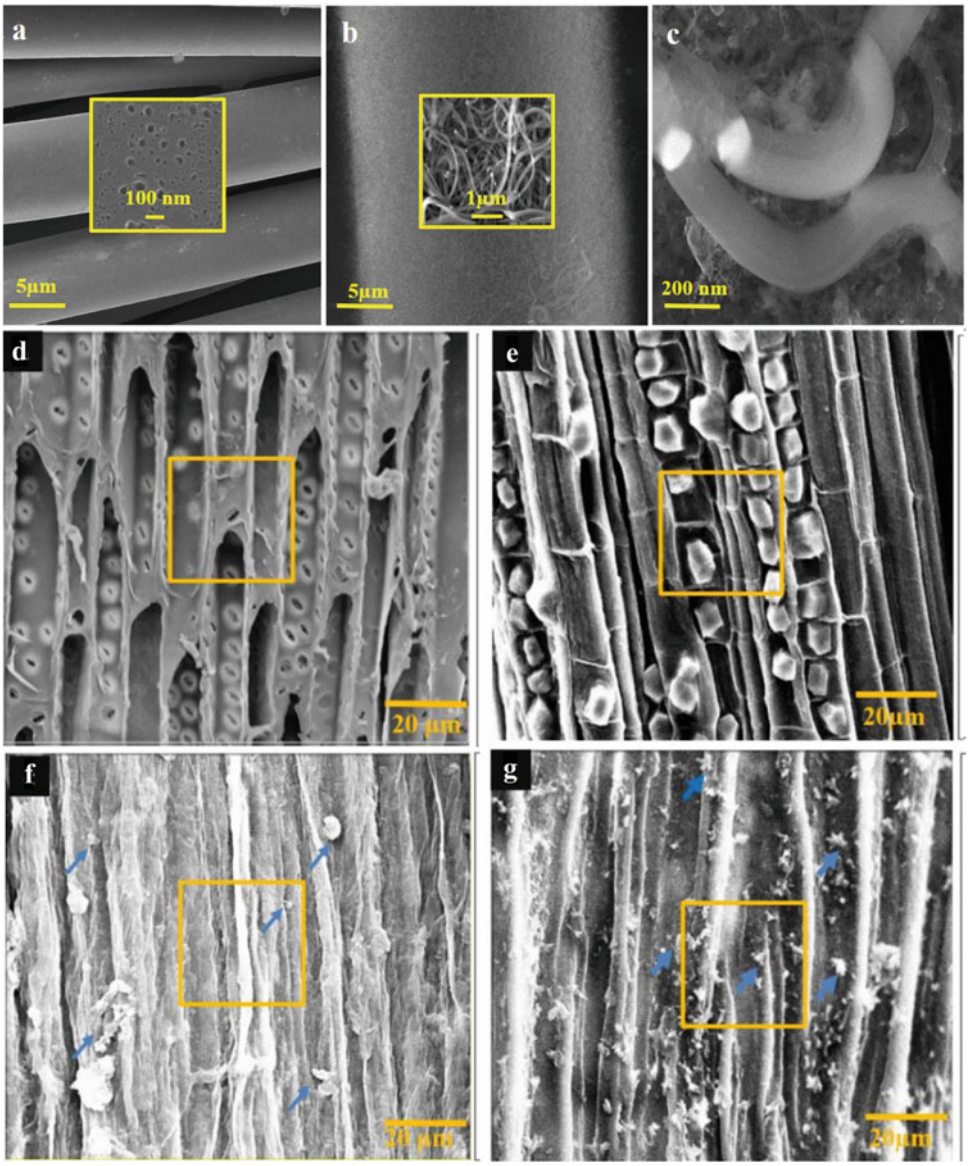

Fig. 9 SEM images at low and high (in inset) magnifications of **a** ACF, **b** Cu-CNF/ACF, **c** Cu-CNF; SEM images of plant shoots grown in Cr-stressed environment and treated with **d** control, **e** ACF, **f** Cu-CNF, and **g** mixture of ACF and Cu-CNF (the arrows point to CNFs) (Kumar et al. 2020)

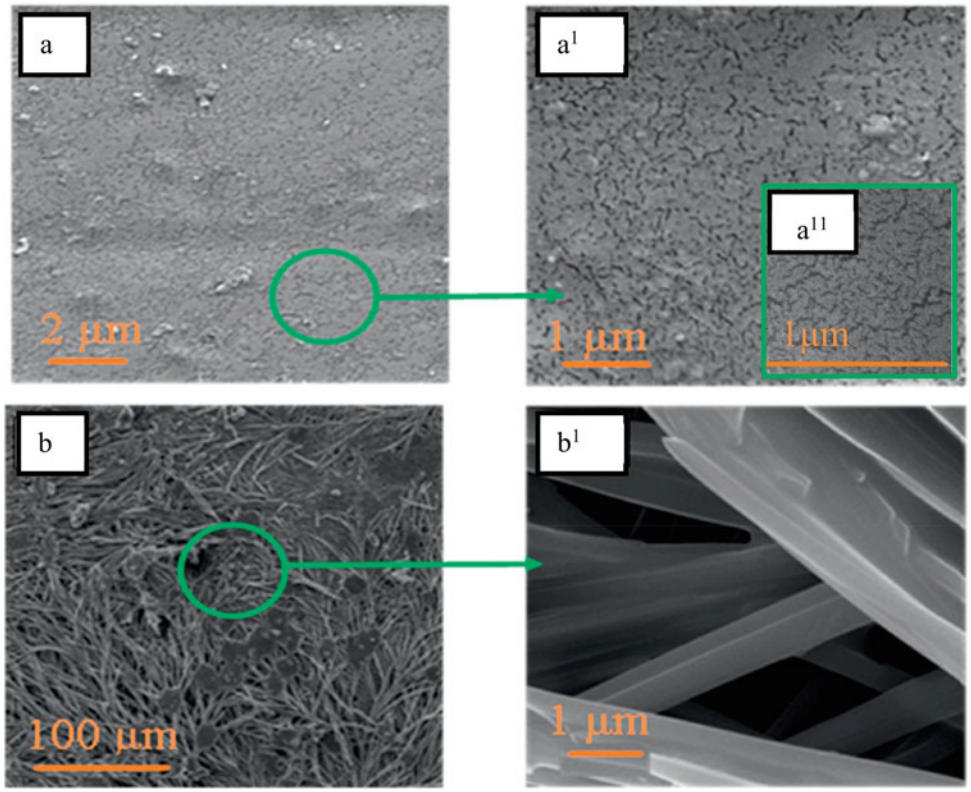

Fig. 10 SEM images at low and high magnifications of **a**, **a**$^{\mathbf{1}}$, **a**$^{\mathbf{11}}$ BMCP and **b**, **b**$^{\mathbf{1}}$ PMO-BMCP (Bairagi and Verma 2018)

Surface morphology of the BMCP cholesterol sensor can be examined using the SEM images shown in Fig. 10. A smooth surface of BMCP is clearly visible in the low magnification image, whereas roughness in the surface, caused by the CNF growth, can be seen in the high magnification image (Fig. 10a, a^{1}). The inset figure (a^{11}) confirms a uniform and dense growth of the CNFs in the PVAc polymeric matrix. The SEM images of the electropolymerized PMO over BMCP show a uniform growth of the dendritic PMO fibers (Fig. 10b). The high magnification image clearly shows the porous structure of PMO (Fig. 10b^{1}). The dendritic-like structure facilitates binding of the PMO recognition element with the cholesterol molecule and sensing of the analyte.

PMC exposed to red blood cells (RBCs), platelets, and bacterial strains was examined by observing any morphological change of the material surface, using the SEM images. During the synthesis stage, loading of Cu-Zn-ACF/CNF in the electrode material was optimized at a concentration level where the carbon fibers started protruding out of the film, creating a rough surface (Fig. 11a) that was suitable for adhesion of RBCs without causing any damage to the cells (Fig. 11b). The quiescent platelets resting on a silicon wafer are shown in Fig. 11b, which on exposure to PMC became activated with formation of a long-spider-like structure (Fig. 11b^{1}). A control sample of *P. aeruginosa* bacteria is shown in Fig. 11c. On exposure to PMC, the bacterial structure was observed to be distorted (Fig. 11c^{1}) confirming lysis of the bacteria. Thus, it was possible to gather critical information such as surface roughness of the dressing material, RBC adhesion, platelet activation, and bacterial lysis using the SEM analysis, which helped to optimize the synthesis conditions and determine suitability of the material for wound dressing.

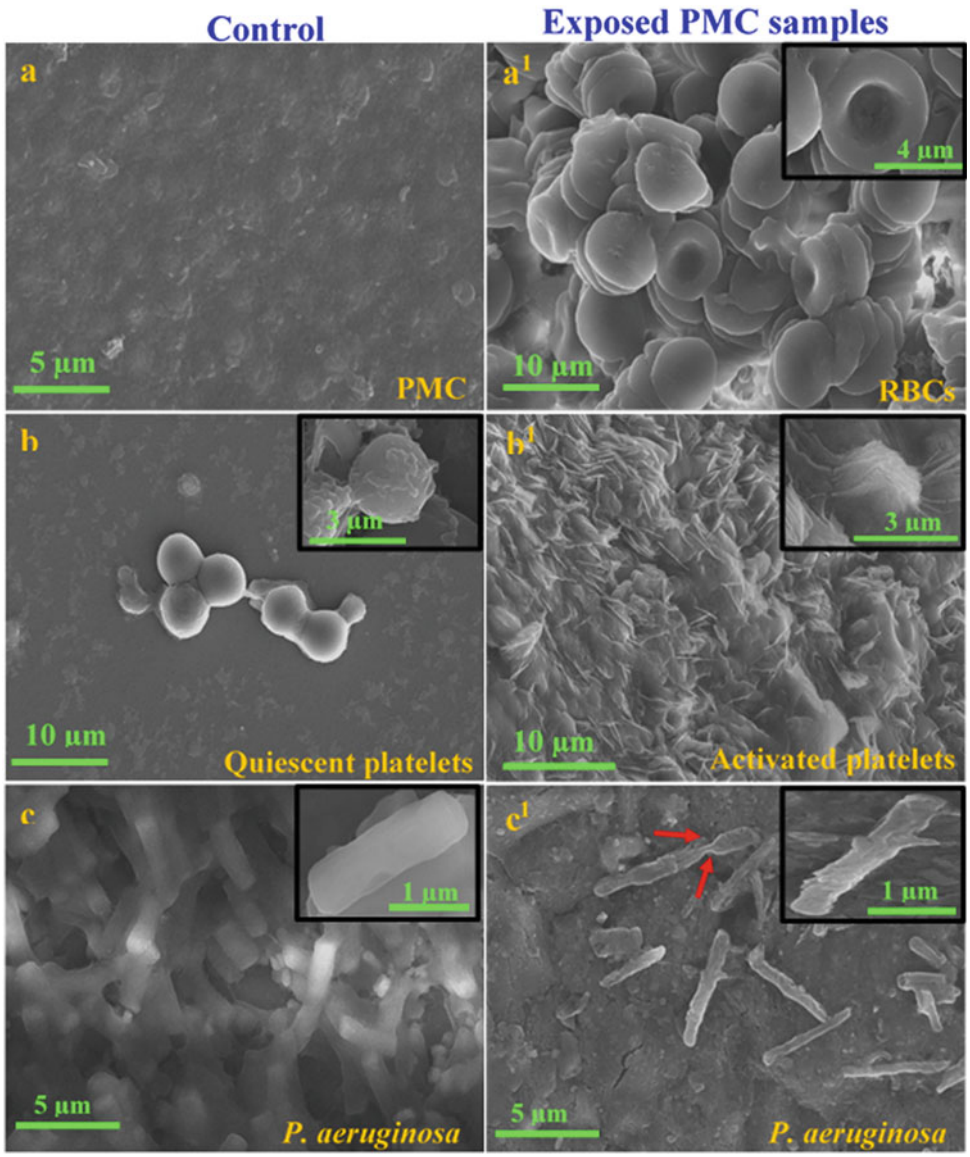

Fig. 11 SEM images of **a** PMC surface with optimized loading of fillers (Cu-Zn-ACF/CNF) as control, **a**[1] RBC-exposed PMC surface, **b** quiescent platelets on silicon wafer as a control, **b**[1] platelet-exposed PMC, **c** *P. aeruginosa* bacteria as a control, **c**[1] P. aeruginosa-exposed PMC (Ashfaq et al. 2017)

Acknowledgements The authors are thankful to the Centre for Environmental Science and Engineering, IIT Kanpur, for providing various research facilities. Contribution of the past and present graduate students studying various aspects of the carbon-based materials is highly acknowledged. Research grants from various government agencies including SERB (DST), DBT, and CSIR are also acknowledged.

References

Ai S, Sui H, Li H (2012) Ind Eng Chem Res 51:2337–2343
Ashfaq M, Verma N, Khan S (2017) Mater Sci Eng C 77:630–641
Bairagi P, Verma N (2018) J Electroanal Chem 814:134–143
Gupta GS, Kumar A, Verma N (2019) Env Sci Nano 6:1246–1258
Kim B-J, Lee Y-S, Park S-J (2008) Int J Hydrogen Energ 33:4112–4115
Kumar A, Gahoi P, Verma N (2020) Chemosphere 239:124760
Li Y, Bai H, Liu Q, Bao J, Han M, Dai Z (2010) Biosens Bioelectron 25:2356–2360
Prajapati YN, Verma N (2017) Fuel 189:186–194
Yadav A, Verma N (2017) Int J Hydrog Energ 42:27139–27153
Zheng G, Kouda K, Sano H, Uchiyama Y, Shi Y, Quan H (2004) Carbon 42:635–640

Electron Backscatter Diffraction Technique: Fundamentals to Applications

Shashank Shekhar, Nitin Kumar Sharma, Sandeep Sahu, and Santanu Misra

1 Introduction

Orientation imaging microscopy (OIM) has long been the quest of material scientists and microscopists, as it provides an immense amount of quantitative data about the microstructure of a material, which can then be related to its processing and also to the performance of the component. There are several techniques which can provide orientation information, some of which are electron channeling contrast imaging (ECCI) in SEM to convergent beam electron diffraction (CBED) and selected area diffraction (SAD) in transmission electron microscope (TEM). Each of these techniques is good in themselves in providing orientation; however, each of them is beset by some drawbacks which have subdued their utilization. A major limitation of these techniques is that they are not suitable for automation which allows to obtain orientation data from various points on a large scanned area. However, it must be pointed out that TEM-based EBSD has also now gained traction and it is gaining applicability among researchers.

In simple terms, electron channeling contrast is obtained due to difference in density of atoms along different directions, which results in varied intensity of backscattered electrons (BSEs) (Joy et al. 1982; Wilkinson and Hirsch 1997; Zaefferer and Elhami 2014). A schematic to explain this effect is shown in Fig. 1. If the electron beam is rastered in two-dimensional space of the sample surface, then one can expect that several lattice planes would together contribute to the electron contrast. One can expect high contrast from planes which are close to normal to the surface, while those away from the normal would show low contrast. Overall, backscattered beam would have a contrast in the form of bands, which carry information about orientation and lattice defects. The bands reflect the inherent symmetry of the orientation of the point, while local features reflect defects in the lattice. Coates was the first person to obtain patterns based on this technique (Coates 1967). This technique is not easy to automate because accurate and automated rocking of beam is not allowed in most electron microscopes. Moreover, the beam rocking process is very slow, and hence getting scans from a large number of points makes the process tedious (Kamaladasa and Picard 2010). Nonetheless, this process has been very successful in understanding lattice defects (Zaefferer and Elhami 2014; Ahmed et al. 1997).

In TEM, when thin foils are subjected to high-energy parallel beam, it leads to diffraction due to lattice points. If the beam illuminates a single crystal, then various planes of the crystal diffract to produce pattern of points. The symmetry and orientation of these points can be directly related to the orientation of the crystal and hence can be used for orientation imaging microscopy. A schematic of the process and the pattern obtained is shown in Fig. 2. Another related technique is convergent electron beam diffraction, which utilizes convergent beam, instead of parallel beam, and results in disks, instead of points in the diffraction pattern. This, too, can be used for understanding the orientation of the crystal.

Orientation recognition from SAD pattern has been commercialized, and it has also become a good tool for orientation imaging microscopy, particularly when the grains or precipitates are small in size.

S. Shekhar (✉) · S. Sahu
Grain Boundary Engineering Lab, Materials Science and Engineering, IIT Kanpur, Kanpur, UP 208016, India
e-mail: shashank@iitk.ac.in

N. K. Sharma
Chemical and Materials Engineering, University of Alberta, Edmonton, AB T6G 21, Canada

S. Misra
Department of Earth Sciences, IIT Kanpur, Kanpur, UP 208016, India

K. Biswas et al. (eds.), *Electron Microscopy in Science and Engineering*, IITK Directions 6,
https://doi.org/10.1007/978-981-16-5101-4_4

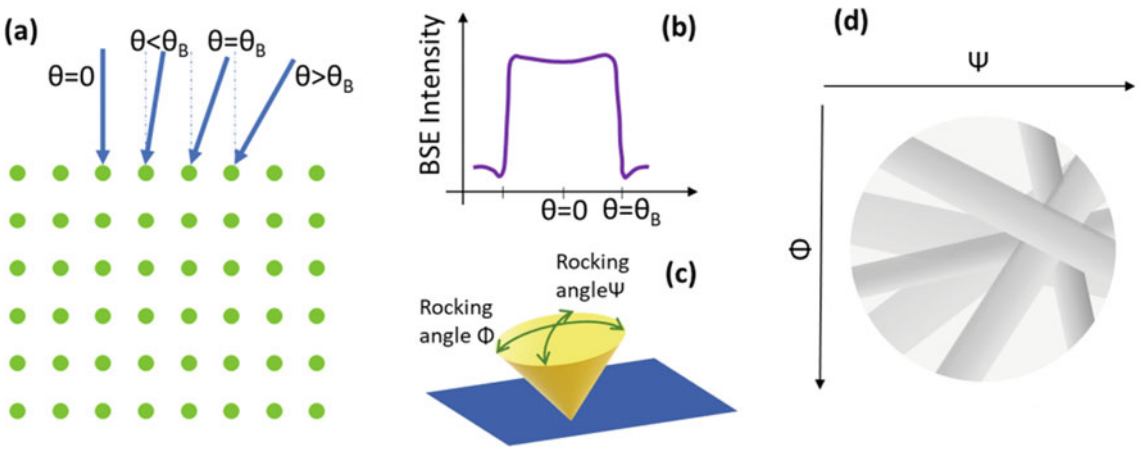

Fig. 1 **a** Orientation variation of incoming beam. **b** Its effect on BSE intensity. **c** Rocking of beam in 2 directions. **d** Schematic of the generated ECCI pattern. **a** and **b** adapted from Wilkinson and Hirsch (1997)

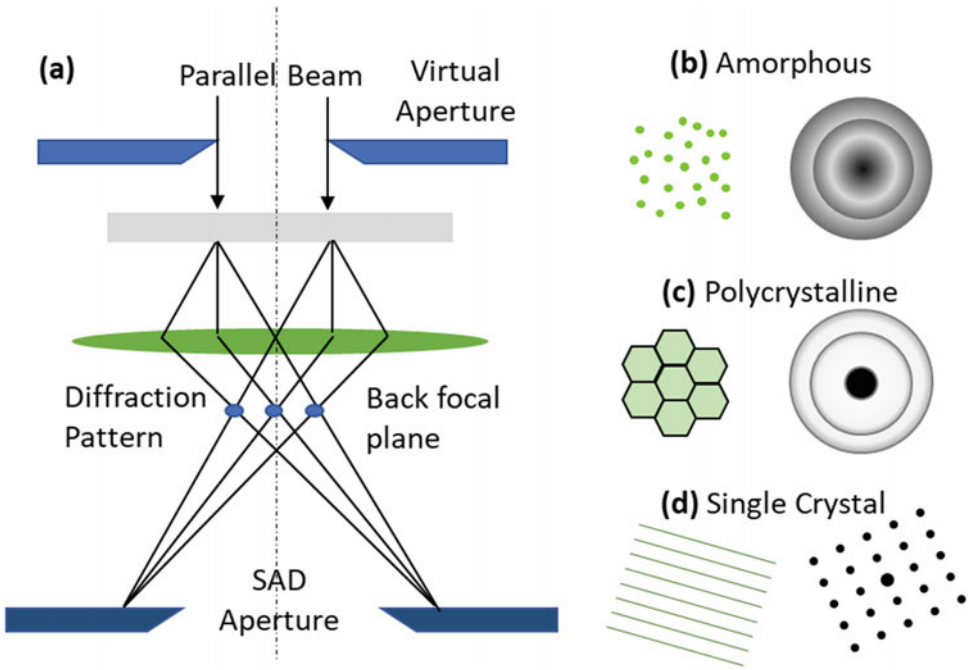

Fig. 2 **a** Schematic of the SAD pattern generation in TEM and the diffraction pattern corresponding to **b** amorphous material. **c** Polycrystalline material. **d** Single crystalline material

2 Origin of Kikuchi Pattern

Kikuchi pattern was first observed by S. Nishikawa and S. Kikuchi in 1928 during diffraction of cathode rays by calcite (Nishikawa and Kikuchi 1928a,b). In one of these publications, they presented transmission Kikuchi patterns (TKPs) (Nishikawa and Kikuchi 1928b), and in the other, they presented backscatter Kikuchi patterns (BKPs) (Nishikawa and Kikuchi 1928a). While most of the work in the early phase was concentrated on transmission Kikuchi diffraction (TKD), last three decades have seen a lot of attention being given to SEM-based backscatter Kikuchi diffraction, which has widely come to be known as electron backscatter diffraction (EBSD). It has further gained prominence due to automation and improvement in hardware which have accelerated acquiring and analyzing speed of these Kikuchi patterns (Kunze et al. 1993).

Kikuchi patterns are formed by the backscattered electrons that satisfy the diffraction condition for a given set of planes. A schematic of the same is shown in Fig. 3. When the electron beam falls on the material, interaction of electron and atoms takes place, and scattering of the incoming electrons occurs. The point of scatter becomes the source of secondary waves which has varying intensity at different orientations. Now, these secondary waves of electrons can

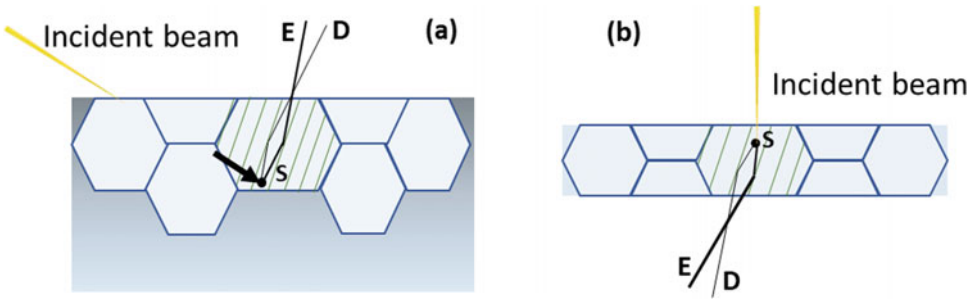

Fig. 3 Schematic showing generation of **a** backscatter Kikuchi diffraction in a bulk sample and **b** transmission Kikuchi diffraction in a thin foil ('S' is the scattering event which acts as source, 'D' is part of the defect cone, and 'E' is part of the excess cone)

further interact with the lattice points and result in diffraction, very similar to that in X-ray diffraction. One major difference with X-ray diffraction, however, is that wavelength of the electron waves is very small, leading to a very small Bragg's angle (θ) in Bragg's equation, $n\lambda = 2d\sin\theta$. For the sake of comparison, wavelength of K_α radiation originating from Cu source during *X*-ray diffraction is ~ 1.54 Å. On the other hand, wavelength of electron at 10 kV accelerating voltage is ~ 0.12 Å. Since the wavelength of these electron waves is an order of magnitude smaller than that of *X*-rays, Bragg's angles also come out to be much smaller than that obtained in X-ray diffraction.

Another major difference with X-ray diffraction is that since the 'source' of electrons is inside the material, diffraction may take place in 'forward' as well as 'backward direction,' as depicted in the schematic. Thus, in this diffraction, there is always a pair of diffracted cones. When these cones intersect with a planar detector, we observe a pair of hyperbolae. But due to the small values of Bragg angles, the curvatures of these hyperbolae are so small that they appear as parallel lines. These parallel lines are known as Kikuchi lines or Kikuchi bands. Because of the nature of its origin, one of the cones has higher intensity than the background, while the one which diffracted from the backward moving waves has intensity lower than the background. Thus, we obtain what are called as 'defect cone' and 'excess cone.' These cones and corresponding Kikuchi lines are formed in both transmission mode and backscatter mode. The geometry of the two modes is somewhat different and would be discussed in next section.

Since the Kikuchi patterns are formed by a fundamental phenomenon of diffraction, they show certain characteristics that help in understanding the structure and orientation of material. Each band in the Kikuchi pattern represents diffraction from a family of planes. Thus, each band has a one-to-one relation with family of planes. This, in turn, implies that intersection of these bands represents intersection of planes, viz. zone axes. Moreover, angle between the bands represents angle between planes. These characteristics of the Kikuchi pattern are exploited to identify the orientation of the individual point of the sample. In scanning electron microscope (SEM), the beam rasters over a region, moving from point to point in a serpentine fashion. Thus, one can obtain orientation of each of these points and recreate a micrograph representing the orientation map of the scanned region. Another important characteristic of these patterns is that the width of each of the bands is proportional to the spacing of the planes of that family. It can be easily shown that the angular separation between the two parallel lines of the Kikuchi band is twice the Bragg angle. From this, it can be extrapolated that if there are defects in the material which can cause variation in the average planar spacing, then it would reflect in the bands. This characteristic has also been exploited in EBSD to quantify the strain in the lattice (Wilkinson and Britton 2012).

3 Automated Indexing of Kikuchi Patterns

We pointed out earlier that application of EBSD has seen an exponential growth in last two decades. This is driven primarily by automation of pattern indexing across a selected grid in the scan area. This automation has allowed indexing of patterns from area as large as several 100 μm along both the directions. Automatic indexing has been achieved on the foundation of improvement in software as well as hardware capabilities. On the hardware front, there is a phosphor screen on which the Kikuchi patterns are formed, and the illuminated pattern is captured by a camera that is located behind this screen. The capabilities of the camera and screen have improved immensely over the years, so that the screen capturing rate has reached in excess of 2500 frames per second. Faster scanning rate has resulted in obtaining large maps in very short times. Once the images are captured, they are analyzed to identify the orientation and phase of the given point. In the next few paragraphs, we explain the method of recognition of Kikuchi pattern and indexing of the orientation of a given point from the obtained Kikuchi pattern.

Once the camera captures the Kikuchi pattern, identification of various lines from the Kikuchi pattern is carried out

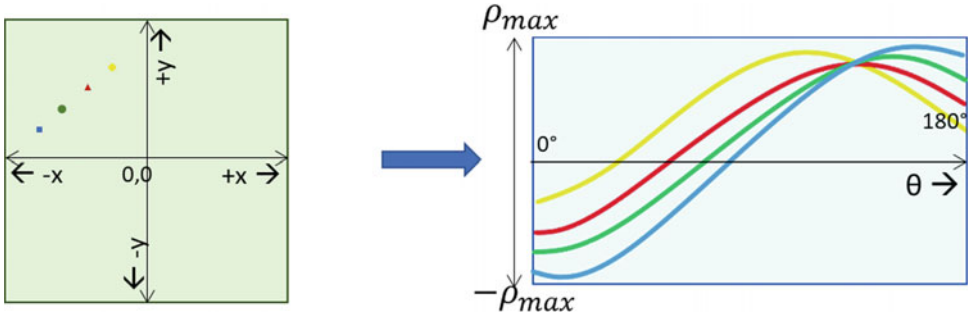

Fig. 4 Hough transformation translates each pixel in image space to a curve in the 'ρ–θ' space, and consequently, a line in the image space appears as an intersection of several of these curves in the 'ρ–θ' space

using Hough transform. In this technique, the line is transformed from Cartesian coordinate to a space where it is represented only by its length 'ρ' and angle 'θ'. To understand this, let us imagine a square image containing just one line. If we want to transform each pixel of this image space into 'ρ' and 'θ' parameter space, then each pixel on the image would transform to a sinusoidal curve in the 'ρ–θ' space. This is because each pixel can be imagined to be a part of infinite number of straight lines passing through it. Set of these straight lines would form a curve as represented in Fig. 4 (left). Now, wherever a line exists in image space, it will be represented as intersection of several of these sinusoidal curves at one point, as shown in Fig. 4 (right). This intersection point in the 'ρ–θ' space has value of 'ρ_i' and 'θ_i' which represents the given line in the image space. In the present context, 'ρ' varies from '$-\rho_{\max}$' to '$\rho_{\max}$' and 'θ' varies from 0 to 180°. Now, if we assign intensity value to each of these pixels in image space, then the intensity value of this particular 'ρ_i' and 'θ_i' would be much higher than that of its neighborhood. When all of Kikuchi pattern is transformed into 'ρ–θ' space, this is called Hough transformation. In the Hough transformed image, third direction represents the intensity, and each straight line in image space is represented by a 'Hough' or a mound, which has relatively higher intensity value compared to its neighbor. The bright lines can be easily identified by the relatively large peaks in the Hough transform space. Once these lines are identified, calculating the angle between the planes is much easier in this 'ρ–θ' space, as one can easily identify the equation for each and every line which is given as: $\rho_i = x\cos\theta_i + y\sin\theta_i$.

Kikuchi pattern is a set of bands with parallel lines, and each of these bands represents a family of planes of the crystal structure of the given phase. The centerline of each of these bands represents the trace of orientation of the given family of planes. Hence, by identifying the lines, as described in the previous paragraph, and by calculating the angle between any pair of bands, we are essentially calculating the angle between corresponding pair of family of planes. This angle between various sets of planes can be compared to the reference values of the crystal structure of the possible phases. At least 3 different sets of mutually intersecting lines and their corresponding angles must match, to uniquely identify the phase and define the crystal orientation of the point on the crystal. In general, 5 to 8 bands or reflectors need to be matched to get confidence in the result and to improve the accuracy of the orientation.

4 Geometry of EBSD Setup

In EBSD, it is very important to understand the geometry of the setup so that appropriate corrections can be made for the geometry during analysis. Intensity of the backscattered electrons has an angular distribution, and this angular distribution is also dependent upon the angle of incidence of the electron beam on the sample (Berger and Niedrig 1999). When the electron beam falls normally to the sample surface, highest intensity of the backscattered electrons lies normal to the plane. However, this distribution is very different when the electron beam has an acute incidence angle. A schematic of the angular density of the backscattered electrons in these two cases is shown in Fig. 5. In general, it is found that maximum intensity is found at an angle which is equal to the angle of incidence of the beam on the sample, as shown in the schematic (Berger and Niedrig 1999). Ideally, one would like to keep the sample normal and the detector right at the pole piece. However, due to constraints of space this is not feasible, and the next best configuration is to keep the sample oriented at some steep angle and keep the detector where one can get the maximum intensity of backscattered electrons. EBSD researchers have found that yield of the backscattered electron is highest at 70° tilt. The overall geometry of the sample with respect to the EBSD detector and the pole piece is shown in Fig. 6a. Figure 6b shows a typical Kikuchi pattern. This particular pattern was obtained from a single-phase material with FCC crystal structure at an accelerating voltage of 20 kV.

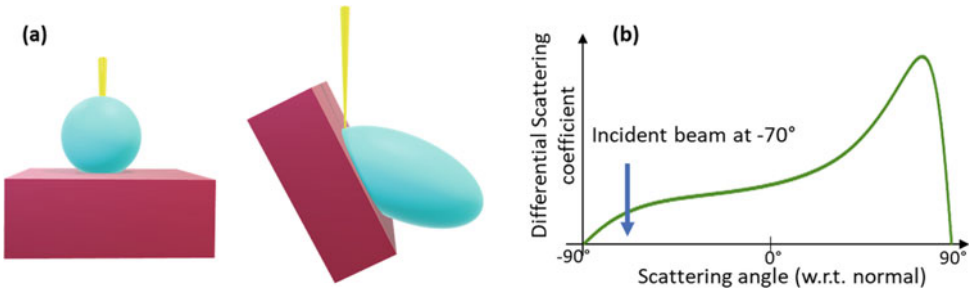

Fig. 5 **a** Schematic representation of the three-dimensional angular distribution of backscatter electrons. **b** Schematic representation of variation of differential scattering coefficient with scattering angle, assuming sample has a 70° tilt. Adapted from Berger and Niedrig (1999)

The tilted sample geometry has a significant role on the overall spatial resolution and also the fact that the lateral resolution is different from the longitudinal resolution of the scanned sample. Figure 7a shows the schematic interaction of the beam with the sample. The depth from which backscattered electrons can escape the surface to reach the detector is denoted by d_z. Its absolute value depends on the accelerating voltage and the atomic number of the given material. In general, its value ranges from 50 to 100 nm, which is a very small depth. This also implies that the surface must be polished and must be free of any asperities at least up to this depth. If there are any remnant strains or scratches due to polishing which are of this order, then obtaining Kikuchi pattern is not possible. This also explains why sample preparation is a very delicate and dedicated step for EBSD. There is dedicated equipment that has been designed in the past few decades, particularly for the preparation of the samples for EBSD. Some of the dedicated equipment is vibratory polishing machine and electropolishing machine.

In Fig. 7a, the largest cross section of the teardrop interactive volume represents the spatial resolution in lateral and longitudinal directions. It is obvious from the figure that this cross-sectional area is much larger than the spot size of the beam. A larger cross section also suggests that the yield of the backscattered electrons would be high. Secondly, it is also clear that due to the tilt of the sample, longitudinal resolution d_y is much larger (poorer) than the lateral resolution d_x. On a first order of approximation, it can be said that $d_y = d_x/\cos\theta$, based on the geometry of the sample, which is tilted at an angle θ from the direction of the electron beam. A schematic of the variation of lateral and longitudinal resolution with change in accelerating voltage is shown in Fig. 7b. The absolute values of resolution can range from 50 nm to few µm. By applying very low accelerating voltages, researchers have achieved resolution as low (good) as 10 nm (Dingley et al. 2005; Chen et al. 2011). This improvement is achieved as the interaction volume decreases with decrease in accelerating voltage.

The fact that resolution is dependent upon the geometry of sample and the interaction volume has been exploited for transmission Kikuchi diffraction in SEM. Here, like in TEM, a thin foil is used whose interaction volume is very small, and thus, the resolution is also small (better). A schematic of the same is shown in Fig. 8. In effect, the resolution is as good as the spot size of the beam falling on the sample can be obtained using this geometry. Resolution up to a few nm can be obtained using this technique (Wang et al. 2016).

5 Data Acquisition Parameters

Previous sections clearly outline the theory that lies behind EBSD-based OIM. Like any experimental technique, there are several other parameters related to hardware and software that need to be optimized in order to obtain good-quality data. In this section, we will discuss some of these important parameters and what points to keep in mind when acquiring data. First and foremost step in good-quality data acquisition is sample preparation. As pointed out earlier, during EBSD, data is acquired from only up to a depth of 50–100 nm from sample surface. This puts a huge obligation of preparing a surface that is free from any polishing artifacts up to a depth of few 10's of nm. However, we will not delve into sample preparation here, and readers are directed to read some of these in-depth studies on sample preparation for EBSD (Wang et al. 2016; Nowell et al. 2005; Michael and Giannuzzi 2007).

Once the Kikuchi patterns from a well-prepared sample are discernible, then the objectives of the users are to obtain high accuracy data and at high frame rate. High accuracy refers to high probability of getting correct identification of the orientation, and high frame rate refers to acquisition of a large number of frames and its analysis per unit time. Both these sets of objectives require different sets of parameters, and hence, there is a need to optimize them. The SEM operating condition should be set such that the current in the SEM is on the higher side. This is particularly true for FESEMs as the total

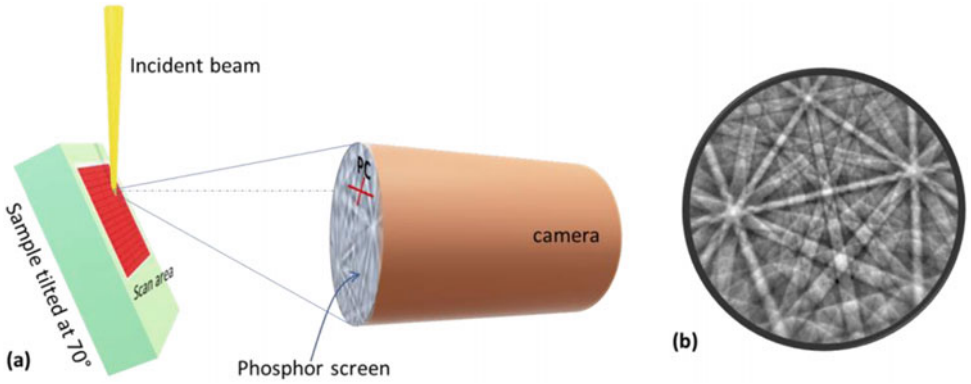

Fig. 6 **a** Geometry of the sample with respect to the incident beam and the EBSD detector (PC refers to pattern center). **b** A Kikuchi pattern obtained from a single-phase FCC crystal

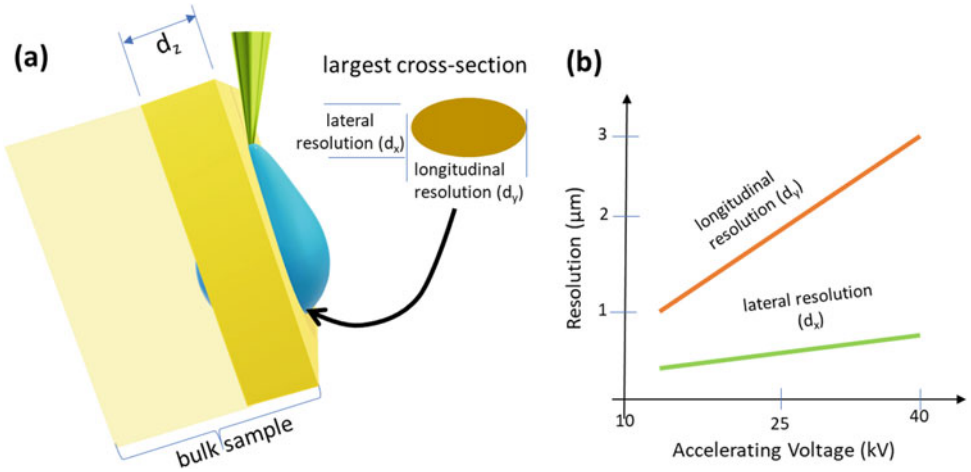

Fig. 7 **a** Schematic representation of interaction of beam with the sample in backscatter diffraction mode, also showing the largest cross section from which backscatter electrons escape. **b** Schematic of the variation of lateral and longitudinal resolution with change in accelerating voltage

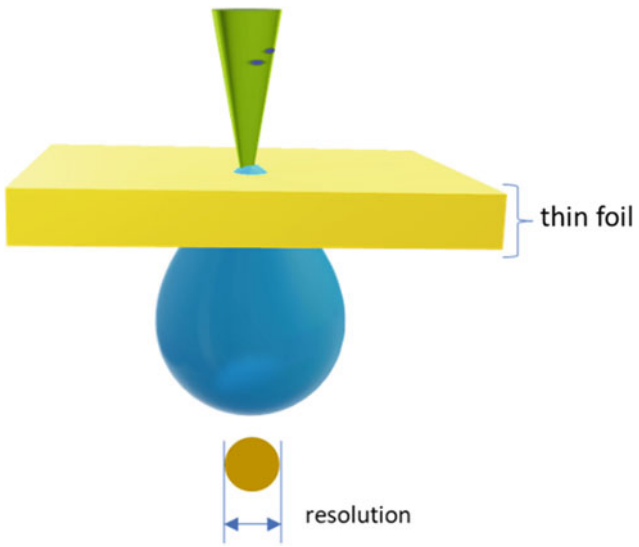

Fig. 8 Schematic representation of interaction of beam with thin foil in transmission Kikuchi diffraction mode. Also showing the large cross section, which represents the resolution of the geometry

current in field emission SEMs is quite low. Good current is necessary for obtaining high-contrast diffraction bands. The accelerating voltage has direct implication on the resolution of data, and it is usually kept at 10 kV. For resolving small particles, one may need to reduce the accelerating voltage to much lower values (Singh et al. 2018).

In the data acquisition window, we get to optimize the contrast of the patterns again, using gain and exposure time. Increasing the gain improves the signal, but the signal-to-noise ratio also deteriorates. On the other hand, increasing the exposure time improves signal as well as signal-to-noise ratio, but the acquisition rate goes down. Additionally, the gain needs to be just sufficient so that there is no saturation in the signal. Another important parameter that affects pattern quality and image acquisition rate is the binning size of the Kikuchi pattern. Usually, the Kikuchi pattern is obtained as a high-resolution image (e.g., 1024 × 1024 pixels). The binning size refers to the number of pixels that would be averaged when analyzing the Kikuchi pattern. Thus, a 1 × 1 binning would imply that all the 1024 × 1024 pixels (1,048,576 pixels) would be analyzed. However, a 4 × 4 binning would imply that only 65,536 pixels would be analyzed. This greatly reduces the analysis time, and hence, the acquisition rate increases drastically. The downside is that this also leads to reduced resolution of the Kikuchi pattern, and hence, it may

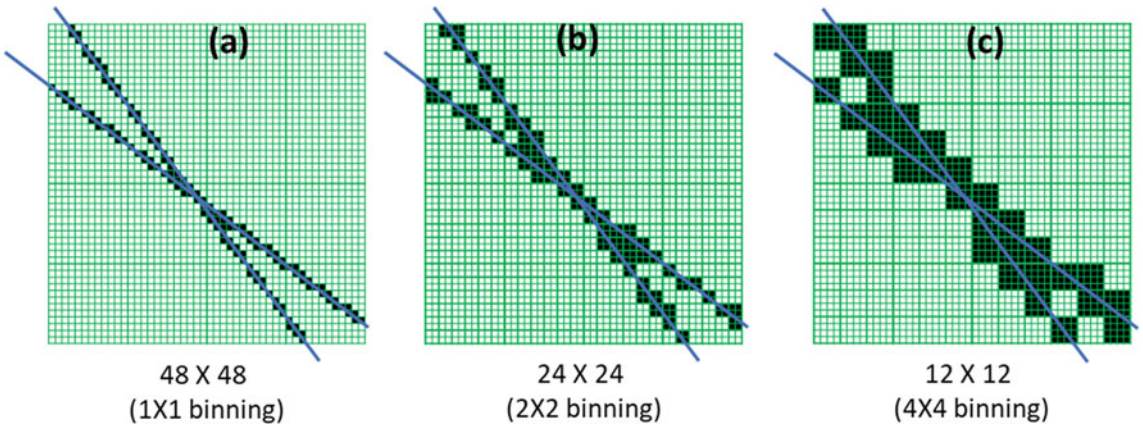

Fig. 9 Effect of binning size on the resolution of the image: Two straight lines are drawn on a grid of 48 × 48 at three different binning sizes. **a** 1 × 1 binning. **b** 2 × 2 binning. **c** 4 × 4 binning

deteriorate the accuracy. This is explained schematically in Fig. 9. Depending on the material and the polishing condition, one needs to identify the highest binning that can give accurate results and thus improve the acquisition rate. Data acquisition software also allows the user to improve the image contrast by subtracting background signal. Background signal refers to the signal being received from several other neighboring grains that can reduce the overall image contrast. By subtracting or dividing this background signal from the obtained signal, the contrast of the pattern obtained from the immediate point is improved significantly.

Once the pattern acquisition parameters are set, the user needs to define the step size for the scan area. Step size is the distance between two consecutive points from which orientation is obtained and thus defines the total number of points that will be acquired in a given scan area. If the step size is very small, one would be able to get very high-resolution micrograph with no visible jig-jag-type structure in the grain boundary; however, this also implies a significantly longer time to acquire the image. Usually, the electron beam inside the SEM has a gradual drift, and for very large scans, the total beam drift may be too large, and the OIM micrograph would yield elongated structures. On the other hand, using a very large step size takes very short time, albeit it sacrifices resolution. In fact, some very small grains may not get detected if the step size is too large. Hence, it is imperative to select an optimal step size. As a rule of thumb, step size should be taken as grain size divided by 10. This would yield on an average 100 points per grain, and the scan speed would also not be compromised. However, if the micrograph consists of very fine grains, then one has to ensure that all these grains are captured. Another rule of thumb is that at least 10 pixels should be present in a region for it to be defined as grain. So, this serves as another guide in selecting the step size. The users should also be aware of the smallest step size that yields meaningful result in their respective SEM. As a point of reference, the smallest step size that gives meaningful result using the Oxford Instruments' Nordlys EBSD detector installed in the FESEM JEOL JSM-7100F in the ACMS facility at IIT Kanpur is 50 nm. This would imply that the smallest grain that can be detected would have an area of 10 pixels × $(0.05\ \mu m)^2$, which is approximately $0.025\ \mu m^2$ or a square with ∼158 nm length.

6 Data Analysis

In the earlier sections, we discussed the theory of electron backscatter diffraction, and then we discussed the data acquisition process and the important parameters to keep in mind in order to obtain high-quality data at fast scan rates. Next, we need to understand how to interpret this data so that quantitative microstructural information can be extracted. Later, we will provide some case studies where these analyses are put in application. Data that is acquired from the EBSD acquisition software is simply the crystal orientation data for each and every point. Next few paragraphs will elaborate how this information alone is sufficient to extract quantitative information about several microstructural parameters. Some additional data is also collected at each point, which aids in analyzing and quantifying results. EBSD pattern at each point can also be saved, and these are used in special cases to analyze the results to a greater depth. First and foremost, we need to understand what is the mathematical form of these orientations and what is the reference frame with respect to which this orientation data is gathered.

6.1 Orientation Analysis

Orientation is always defined with respect to some reference coordinate. In this sense, orientation is the rotation from the

specimen coordinate system to crystal coordinate system. Mathematically, this can be described by rotation vector 'g'. A schematic is shown in Fig. 10a which represents orientation as rotation from specimen coordinate system to crystal coordinate system. Usually, the three primary orientations of sample coordinate system are denoted as 'rolling direction,' 'normal direction,' and 'transverse direction,' and three coordinates of the crystal are defined by $< 100 >$, $< 010 >$, and $< 001 >$. Another way of representing orientation or transformation is using the Euler angles, which is defined in terms of three angles $(\varphi_1, \emptyset, \varphi_2)$. These sets of angles are also called yaw, pitch, and roll and are explained in Fig. 10b. It can be readily shown that the rotation matrix 'g' and the Euler angles are related by the following equation:

$$g = \begin{vmatrix} \cos\varphi_1 \cos\varphi_2 - \sin\varphi_1 \sin\varphi_2 \cos\emptyset & \sin\varphi_1 \cos\varphi_2 + \cos\varphi_1 \sin\varphi_2 \cos\emptyset & \sin\varphi_2 \sin\emptyset \\ -\cos\varphi_1 \sin\varphi_2 - \sin\varphi_1 \cos\varphi_2 \cos\emptyset & -\sin\varphi_1 \sin\varphi_2 + \cos\varphi_1 \sin\varphi_2 \cos\emptyset & \cos\varphi_2 \sin\emptyset \\ \sin\varphi_1 \sin\emptyset & -\cos\varphi_1 \sin\emptyset & \cos\emptyset \end{vmatrix}$$

It is also possible to obtain the Euler angles from the rotation matrix 'g' (Herter and Lott 1993; Shoemake 1994). There are some more mathematical ways of representation of orientation and the misorientation between the points, e.g., Rodrigues vector and quaternions (Heinz and Neumann 1991; Morawiec and Field 1996). We will not get into details of other kinds of representation, and for now, it is sufficient to understand that orientations can be represented in mathematical form and that they can be stored in terms of the above-mentioned parameters. We should also realize that each of these representations is interchangeable, and one can get orientation parameters of one type of representation from other forms of representation.

With orientation data for each point of scan area, one can generate an orientation map giving unique color to each orientation. An easy way to define unique color to each orientation is by using a standard inverse pole figure (IPF) triangle of the crystal structure, with three primary colors (red, green, and blue) at three corners (Nolze and Hielscher 2016). The intermediate points are represented by a mix of these primary colors. Since the IPF represents all the possible orientations of a crystal, the colors provide an easy guide to the orientation of various points in the map. One such pseudo-colored orientation map, where each point was assigned a color based on the color of the corresponding orientation in the inverse pole figure (also shown), is depicted in Fig. 11a. An Inconel-718 sample was taken for this scan, which was found to be single phase. Usually, Inconel contains several precipitates, but this particular sample was processed such that it was mostly single phase. Regions or domains with similar colors depict points with similar orientation and hence represent one crystallite or one grain. Black dots represent points from where Kikuchi pattern could not be obtained or could not be indexed. This scan

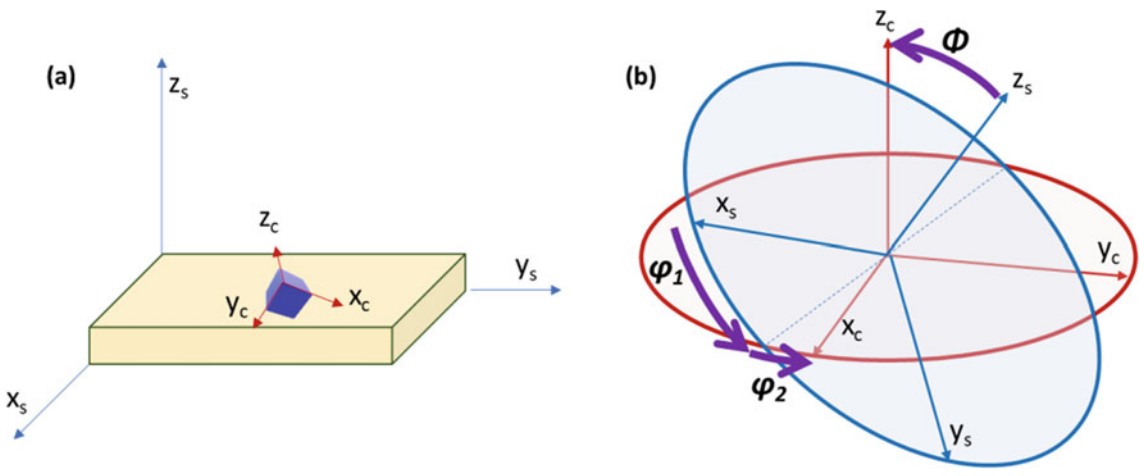

Fig. 10 Orientation of an individual crystal in a sample. **a** Crystal coordinate system (x_c, y_c, z_c) is described with respect to sample coordinate system (x_s, y_z, z_s). **b** This rotation can achieve three consecutive rotations, performed about the z_s-, x'-, and z"-axes by magnitude $\varphi_1, \emptyset$, and φ_2, respectively

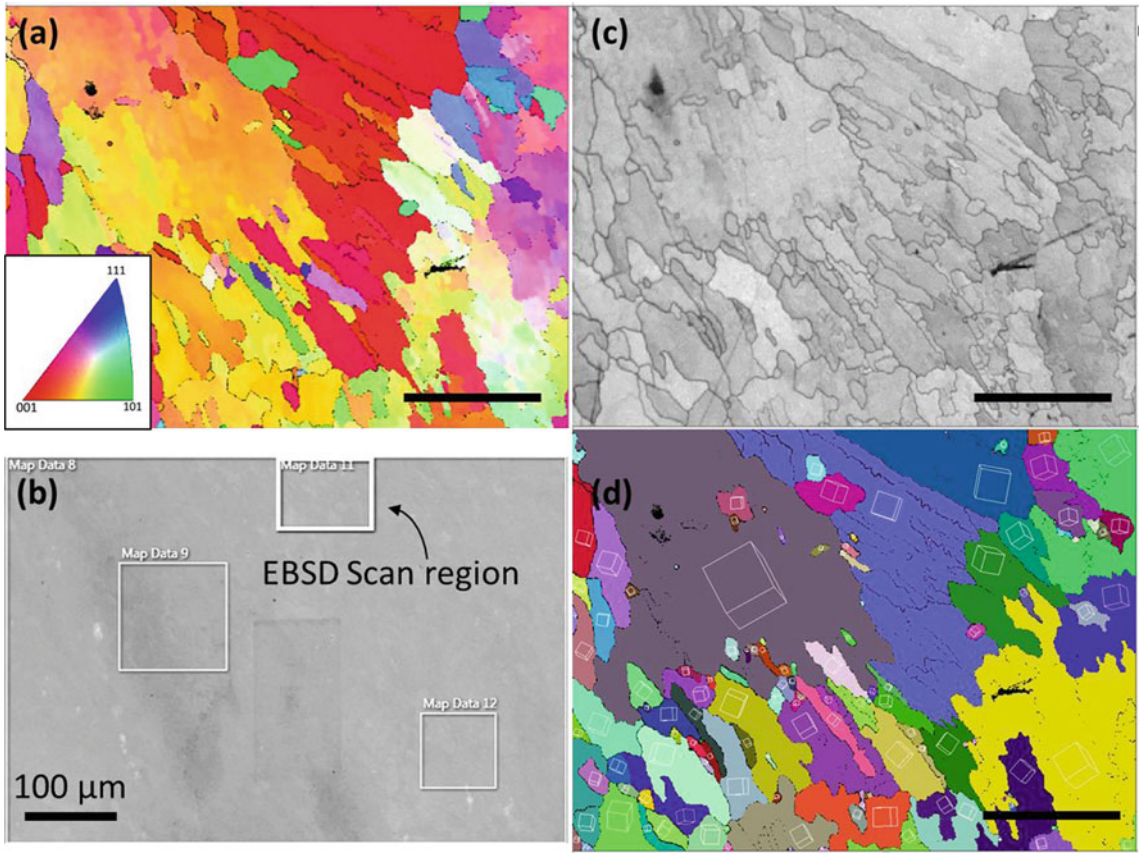

Fig. 11 EBSD of Inconel 718 sample. **a** Orientation map based on pseudo-colors of IPF (shown in inset). **b** SEM micrograph showing the region from where EBSD scan was taken. **c** Band contrast map. **d** Random colored grain map (scale bar = 25 µm, where not mentioned)

was taken with a step size of 150 nm over an area of 100 × 75 µm. This translates to 667 points along the horizontal direction and 500 points along the vertical direction, giving a total of 333,500 points to generate the orientation map. The reference inverse pole figure of cubic crystal structure with its color scheme is also shown in the inset. SEM micrograph of the material is also shown in Fig. 11b for reference, and the region from which scan was taken is marked on the SEM micrograph.

Another very useful map that is almost always generated using EBSD analysis tools is called band contrast map or pattern quality map, depending upon the manufacturer of the instrument. The primary information displayed in these maps is the contrast or average intensity of the Kikuchi bands for each and every point. If the sample is stress-free and generates good Kikuchi pattern, then these points will appear bright. On the other hand, points which are deformed or strained or cannot generate Kikuchi pattern for any other reason appear dark. The map so generated gives an idea about which regions contain defects and which regions are defect-free. Thus, this map can also be equated with the bright field image of TEM where defects usually appear darker relative to the brighter strain-free region. Band contrast map of the above-mentioned sample is also presented in Fig. 11c. Based on similar orientation, grains can be demarcated and random color is assigned to them. This is called random colored grain map, as shown in Fig. 11d.

In microstructural analysis, identification of grains, size, and morphology is a very important parameter. However, orientation map based on IPF color scheme is not sufficient to differentiate between grains. There is a possibility that two grains have similar normal orientation, but they differ in azimuthal orientation; thus, they will be assigned similar colors and hence may seem to be part of the same grain. An example from the EBSD map, discussed above, is shown in Fig. 12. In such cases, Euler maps can be used as a handy tool. Euler maps assign color to different points based on the value of one of the Euler angles. Since there are three different Euler angles to define an orientation, thus there are three different kinds of Euler maps that can be generated. These maps can be used in conjunction with IPF maps to differentiate between grains. However, Euler maps have their own limitations, and other means are needed to identify and quantify information about grains.

Since EBSD is able to extract information about points which have similar orientation and hence form a grain, its

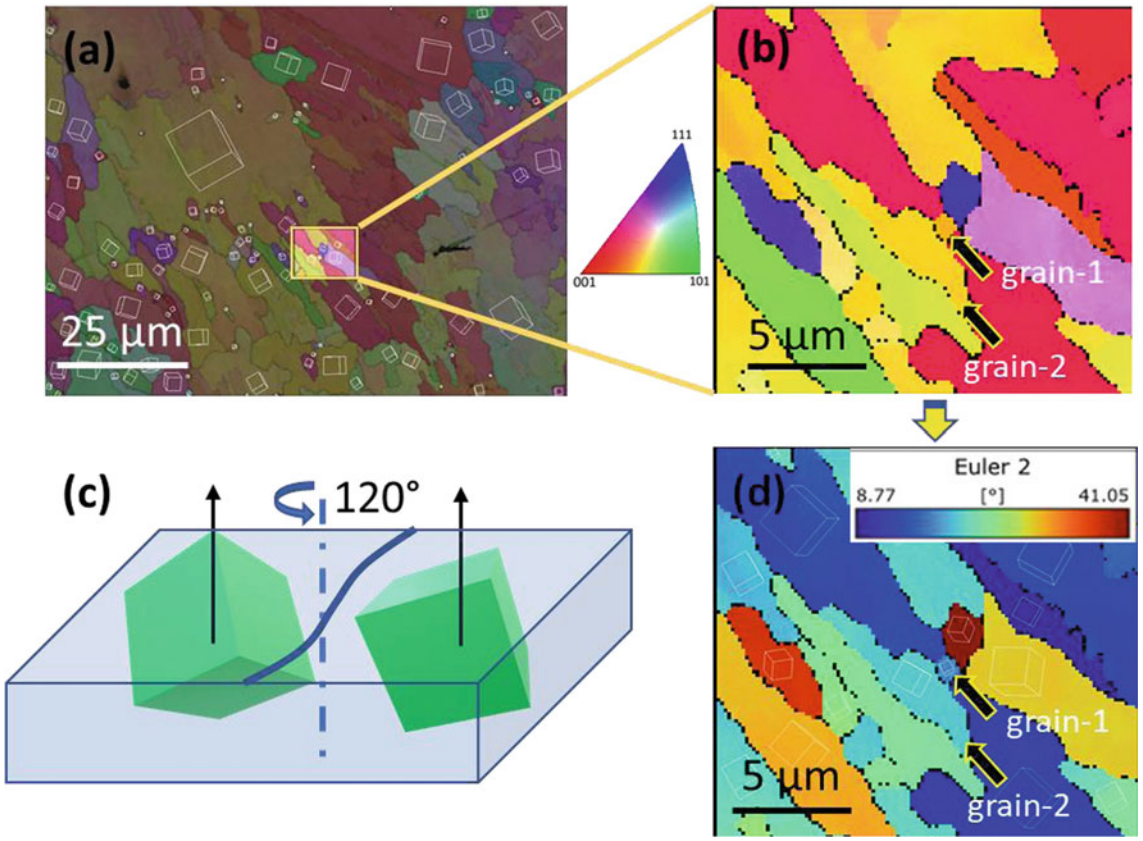

Fig. 12 **a** A small region from the orientation map is highlighted. **b** Orientation map of the highlighted region showing the two grains (grain-1 and grain-2) with similar color. **c** Two different grain scans have same IPF color because they may have same normal orientation, but different azimuthal angles. **d** Additional information from Euler map helps in differentiating between the grains

analysis engine can identify the grains and even add unique random color to each of them. It must be noted that this color is not based on the orientation of the grains or Euler angles, but a random unique color so as to be able to identify them easily. A map with grains in random color is also presented in Fig. 11d. Each of these grains has a particular orientation of the crystallite, and it has been superimposed on the map showing the grains. At this point, it is important to caution the readers that grains in EBSD are not exactly the same as grains understood in metallography. In EBSD, grains are defined mathematically, and hence, one has to define the cutoff misorientation between grains. As long as two neighboring points have misorientation below this critical value, they will be considered part of the same grain, and when they have misorientations greater than this cutoff value, then the two points will be considered as part of two different grains. Usually, this cutoff is taken as 10°, and the random grain map shown in Fig. 11d is based on this definition. A grain may also be composed of some 'sub-grains' where the misorientation between the different parts is less than 10°, and when the grain definition is changed to a small value, say 2°, some of these 'grains' may start to appear. Band contrast map of a selected region of the original map is shown in Fig. 13a. Figure 13b and c shows random grain maps with 10° grain definition and 2° grain definition, respectively. It is obvious from the figure that when the grain definition is reduced, lot more grains 'appear,' and some of these are highlighted in the figure. Grain statistics obtained from the analysis software show that there are 42 grains in Fig. 13b, while there are 83 grains in Fig. 13c. With all the requisite data for individual grains, grain-related parameters like grain size, grain morphology, grain area, etc., are easily quantified by the analysis engines.

Identification of crystal structure and its orientation also allows the EBSD analysis engine to differentiate between various phases. In some cases, where phase differentiation becomes difficult, another SEM-based technique, viz. energy-dispersive spectroscopy (EDS), is brought to use. EDS is another powerful tool which allows one to get quantitative information about composition of a given material along with its spatial distribution. This technique, combined with EBSD, can provide very accurate identification of various phases present in a given material system. Figure 14 shows EBSD maps for duplex steel, which contain both ferrite and austenite phase. Figure 14a shows the IPF map with grain boundaries, while Fig. 14b shows the

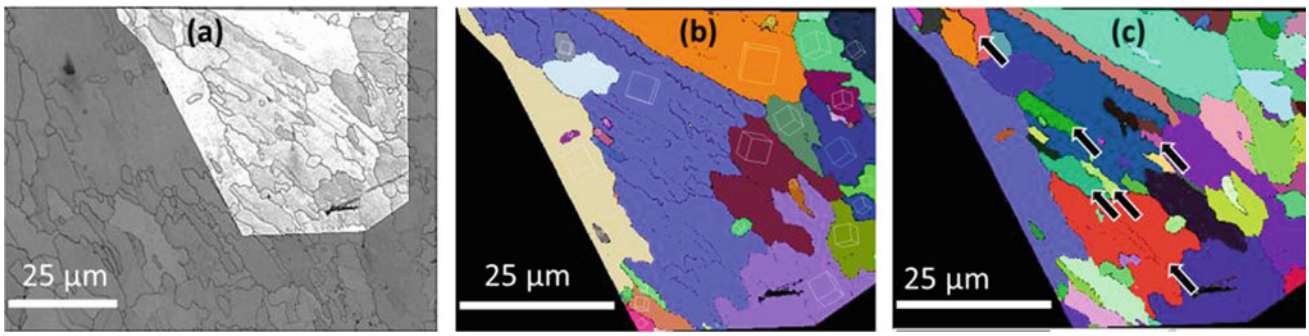

Fig. 13 **a** Region of interest from the original scan is highlighted. **b** Grain map with 10° grain definition. **c** Grain map with 2° grain definition, showing several 'new' grains which have been highlighted by arrow

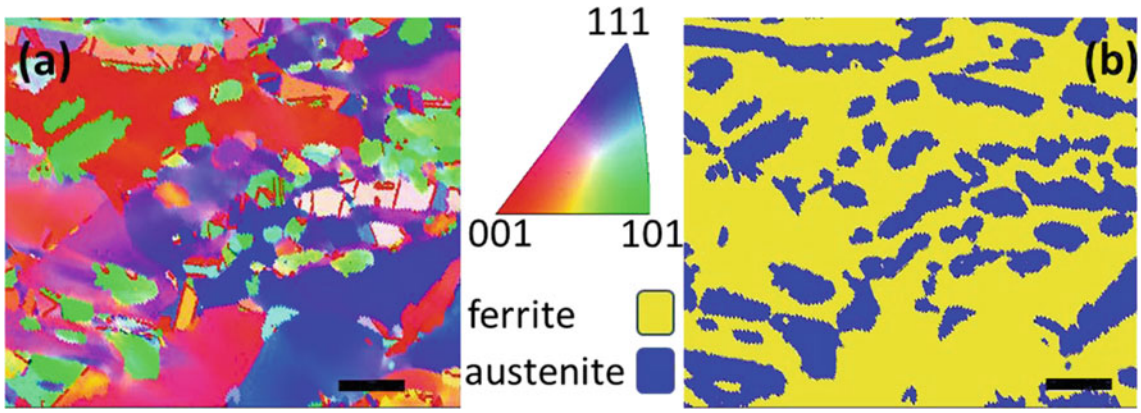

Fig. 14 Duplex steel. **a** Orientation map micrograph based on IPF color (shown here). **b** Corresponding phase map for duplex steel showing austenitic and ferritic phases (scale bar = 100 µm)

phase map of the same region, which differentiates between the two phases present in the material. Based on EBSD, it was determined that this material contained 34% austenite and 66% ferrite. This was also confirmed by ferrite scope study of the material.

6.2 Misorientation Analysis

Once we have the orientation information for each and every point or pixel in the scanned area, we can realize that most other microstructural parameters obtained in EBSD are just a derivative of this data. Since orientation is defined by the rotation matrix 'g', misorientation between two grains inside the same sample whose orientations are defined by rotation matrices 'g_1' and 'g_2', respectively, can be given by: $M = g_1^{-1} g_2$. Thus, misorientation data for any pair of points or pair of grains can be readily calculated. For data on grain boundaries or phase boundaries, misorientation data only from the neighboring points is considered and assigned as interface between the two points. The matrix form of representation of misorientation is very convenient for mathematical transformations and calculation, but misorientations are usually represented as axis–angle pair. Axis–angle pair are not unique, and depending on the symmetry of the crystal, one may obtain several sets of these axis–angle pairs. For instance, for cubic symmetry there are 24 symmetrically equivalent orientations, and this leads to 576 (=24 × 24) symmetrically equivalent misorientations. In such cases, the misorientation with the lowest angle is considered as the misorientation angle or also known as disorientation angle.

One of the simplest representations of misorientation data is the misorientation plot, which presents the frequency of occurrence of various misorientation angles between the neighboring grains of a particular microstructure (Randle et al. 2001). Misorientation plot for the Inconel sample is given in Fig. 15a. As stated earlier, misorientation angle is just one aspect of the misorientation data, and for a complete understanding of the interface between grains, one needs to also identify the misorientation axis and the boundary plane. In general, an interface between two grains is defined by five degrees of freedom. Three of these parameters are associated with misorientation and other two with the interface plane.

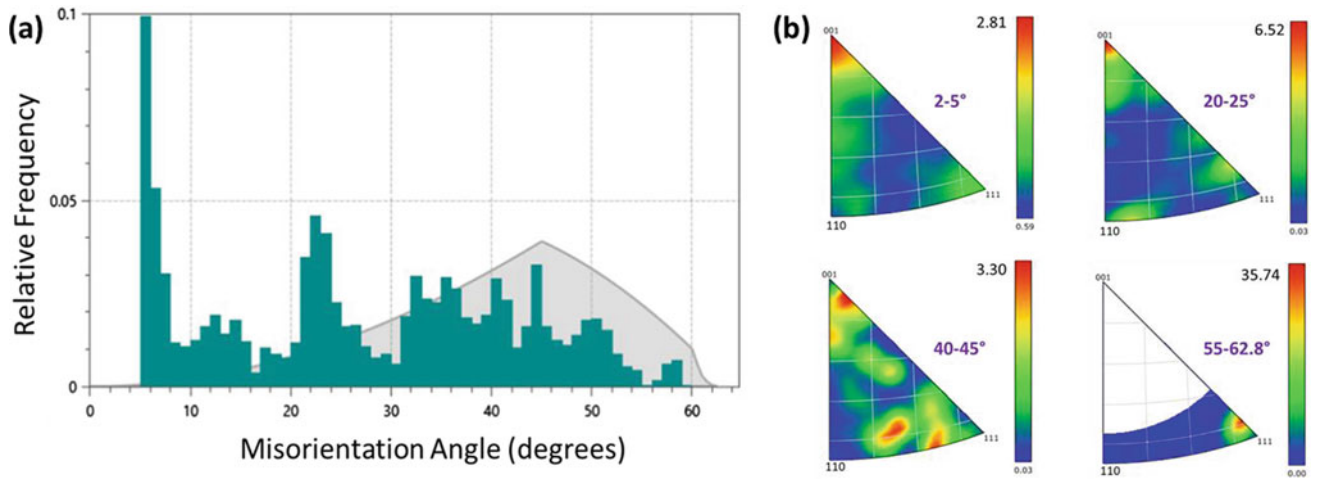

Fig. 15 **a** Misorientation distribution map for Inconel 718 sample. (Gray line indicates theoretical distribution of misorientation for a perfectly random polycrystalline material.) **b** Misorientation axis distribution of the Inconel 718 sample for four different angle ranges

For certain types of boundaries, misorientation angle is not sufficient, and they must be presented in terms of axis–angle pair. A set of axis–angle data obtained from Inconel 600, which is a single-phase material, is presented in Fig. 15b. This data shows the distribution of axis for various angle ranges. Another type of boundary of interest is coincident site lattice (CSL) boundaries, which have certain axis–angle pair that show distinct properties. These boundaries can also be extracted from the orientation and grain data and provide useful information to analyze the microstructure of the material. EBSD has come out as a powerful technique for this field of study, usually called grain boundary engineering. A case study has been provided for appreciation of the utility of EBSD in getting in-depth information about microstructure of material and thereby improving its characteristics.

6.3 Micro-strain Analysis

Residual strain inside the material is an important microstructural parameter that can also be extracted from EBSD data. Plastic strain in the material gets stored as an array of dislocations, which lead to misorientation inside the grain. These misorientations can be calculated in various ways to get different types of information. Some of the most widely used EBSD parameters to represent strain are kernel average misorientation (KAM), grain orientation spread (GOS), and grain reference orientation deviation (GROD). KAM is basically average misorientation of each point with respect to all its neighbors. This parameter is very useful in visualizing localized strains in a sample. Schematic representation of definition of KAM is shown in Fig. 16a.

GOS, on the other hand, represents average spread of the orientation of each grain. This is very useful in understanding average level of strains for individual grains and thus differentiating between the recovered and recrystallized grains from deformed grains. Grains with very low GOS value can be considered as recrystallized grain and free of any strains, while grains with very high GOS value can be considered deformed and still strained. Schematic representation of the definition of GOS and a GOS map for Inconel 718 is shown in Fig. 16b and d, respectively. Another data that is useful in understanding strains inside individual grains is intra-grain misorientation. One way to represent this is by using GROD, where the average misorientation of each point is calculated with respect to the mean orientation of the grain. This is very useful in bringing out the substructures inside a grain. KAM and GROD are similar in character and represent the deviation of individual pixels. The primary difference between the two parameters is that KAM is deviation calculated with respect to immediate neighbor orientations while GROD is deviation calculated with respect to the average orientation of the grain. A GROD map for Inconel 718 is shown in Fig. 16c. Some examples on the use of KAM and GOS to quantify the residual strain present in the material can be found in Sahu et al. 2019; Yadav et al. 2018; Yadav et al. 2019.

6.4 Micro-texture Analysis

We pointed out earlier that a complete understanding of orientation cannot be obtained from the orientation map or any other map for that matter. Maps represent only one parameter of the orientation (e.g., normal direction, Euler angle value, etc.), while orientation has at least three parameters (e.g., three perpendicular orientations or three Euler angles, etc.). It is possible to present the orientation data in three-dimensional space of the Euler angles, and this

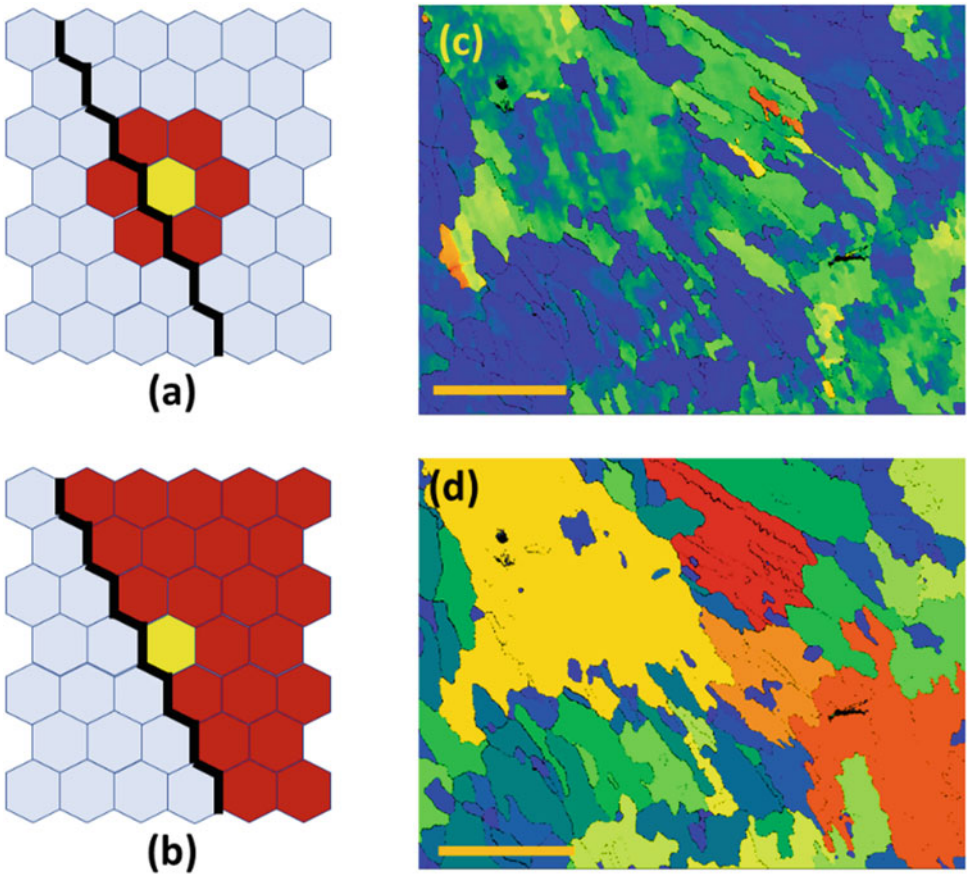

Fig. 16 Schematic explanation of the calculation of **a** KAM and **b** GOS. (Each hexagon represents individual point or pixel of EBSD map.) **c** GROD map and **d** GOS map of Inconel 718 sample

is called orientation distribution (OD). OD does not contain any information on spatial distribution of the pixels, and it only provides information related to density of pixels in this three-dimensional space. It is possible to obtain mathematical probability of orientation distribution, and in that case, it is called orientation distribution function (ODF) (Bunge and Haessner 1968; Bunge 2013). OD and ODF have served as powerful tools in texture analysis of materials. Occurrence of high density of crystal orientations in a particular Euler space denotes particular properties or phenomena in the material. A schematic of various texture components found in the cubic system in Euler space is shown in Fig. 17a (Humphreys 2001). Since plotting and analyzing a 3D information is difficult, this 3D space is cut into slices of 5° along the φ_2-axis. Hence, ODF is a 2D representation of Euler space. Orientation distribution (in 2D) of Inconel 718 sample is presented in Fig. 17b.

Another powerful tool for representation of texture is pole figures and inverse pole figures. Pole figure represents the orientation of a particular crystallographic plane with respect to sample coordinates. It basically shows the alignment of sample coordinates with the crystallographic pole. The term 'pole' refers to the normal of a given crystallographic plane intersecting a hemisphere and projected in two-dimensional plane (see Fig. 18). Pole figures can be generated for any particular crystallographic plane, but are meaningful only for certain low-index planes. Schematic of {111} pole figure of a cubic system giving rise to cube texture, copper texture, and brass texture is shown in Fig. 19. Here, RD, ND, and TD refer to the rolling direction, normal direction, and transverse direction, respectively, of the sample coordinate system. It is useful to recall that pole figures represent data with respect to the sample orientation, and hence, symmetry of the sample will also get reflected in the pole figure.

Inverse pole figure (IPF), as the name suggests, is an inverse representation of data. In IPF, all the crystallographic orientations are represented with respect to a particular sample direction (usually ND). Basically, IPF shows the alignment of crystallographic poles with a specified sample direction. Here too, crystal symmetry is reflected in the inverse pole figure. For cubic systems, we know that there are 24 symmetrically equivalent orientations, which are represented as 24 triangles in the stereographic projection (see Fig. 20a). Hence, for cubic crystal systems, representation of only one standard stereographic triangle is sufficient, shown in Fig. 20b. We can add unique colors to the orientations at the three corners of the triangle, leading to a mix of these colors for all other orientations, as shown in

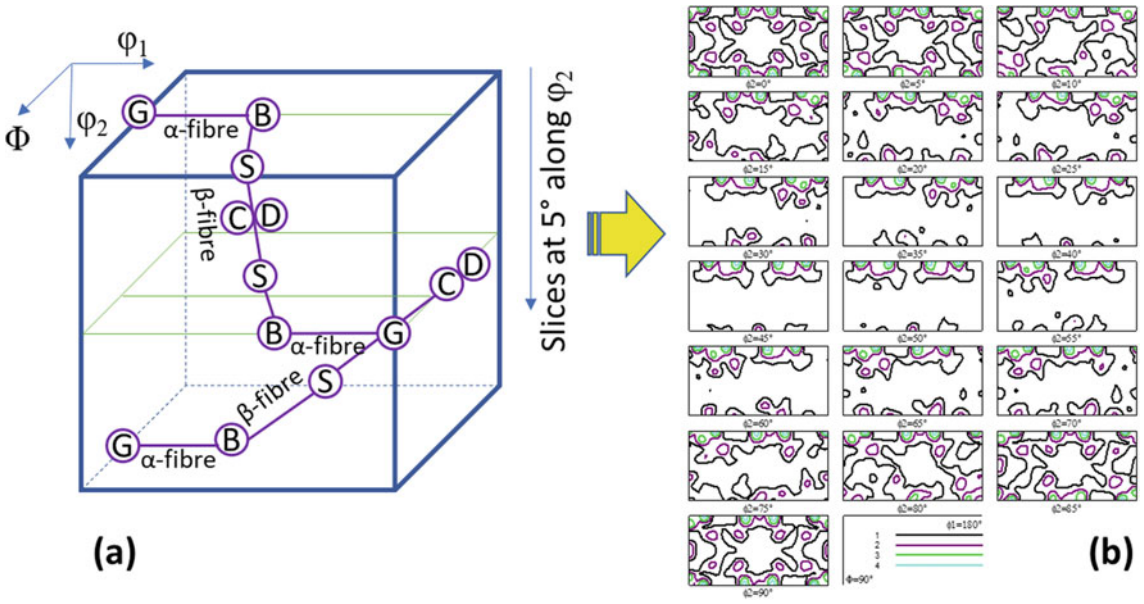

Fig. 17 **a** A schematic of various texture components found in cubic system in Euler space (adapted from ref Humphreys (2001)). **b** ODF map for Inconel 718

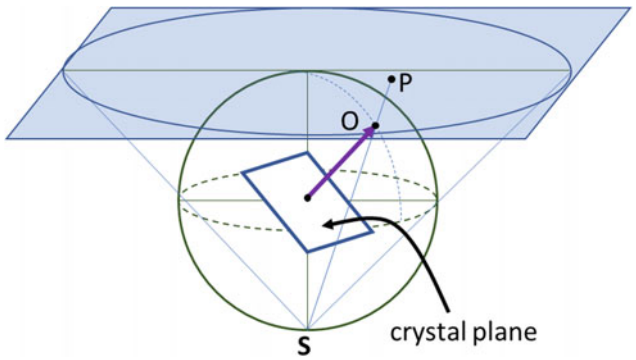

Fig. 18 Origin of pole figure: A crystal plane is shown whose normal intersects with the surface of positive hemisphere at point 'O'. 'S' is the light Source Which when passes through 'O' is projected in 2D plane at 'P', which is called the pole of the crystal plane. Adapted from ref Schwartz et al. 2009

Fig. 20c. This pseudo-colored IPF triangle is utilized for generating the pseudo-colored orientation maps shown earlier for Inconel 718, which has cubic symmetry. For lower symmetry crystal structures, there will be lesser number of the fundamental repeating unit from this stereographic projection, which can be used to add pseudo-color to the orientation map.

7 Case Studies

In the previous section, we gave a brief glimpse of various quantitative analyses that is possible from the data acquired using EBSD-based OIM. In this section, we will showcase some case studies where EBSD analysis is put in application

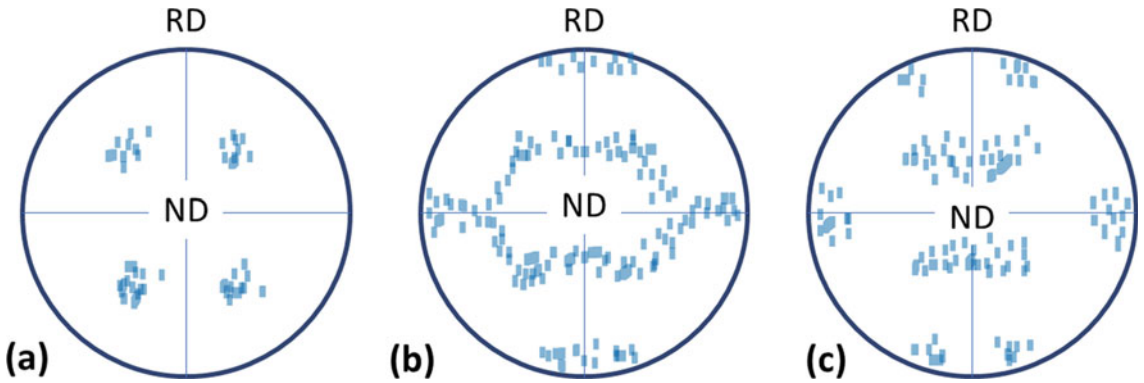

Fig. 19 Schematic of {111} pole figure of a cubic system giving rise to **a** cube texture, **b** copper texture, and **c** brass texture. (RD and ND refer to rolling direction and normal direction of the sample coordinate system.). Adapted from ref Schwartz et al. (2009)

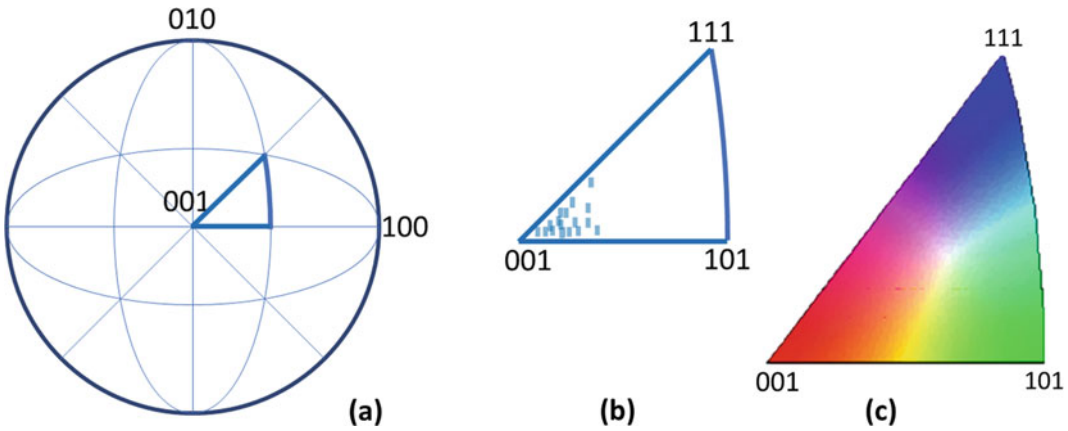

Fig. 20 **a** Stereo net for the representation of inverse pole figure and the standard stereographic triangle for the cubic system is highlighted. **b** Schematic of IPF triangle showing the cube texture. **c** IPF triangle with pseudo-colors which are used for orientation mapping

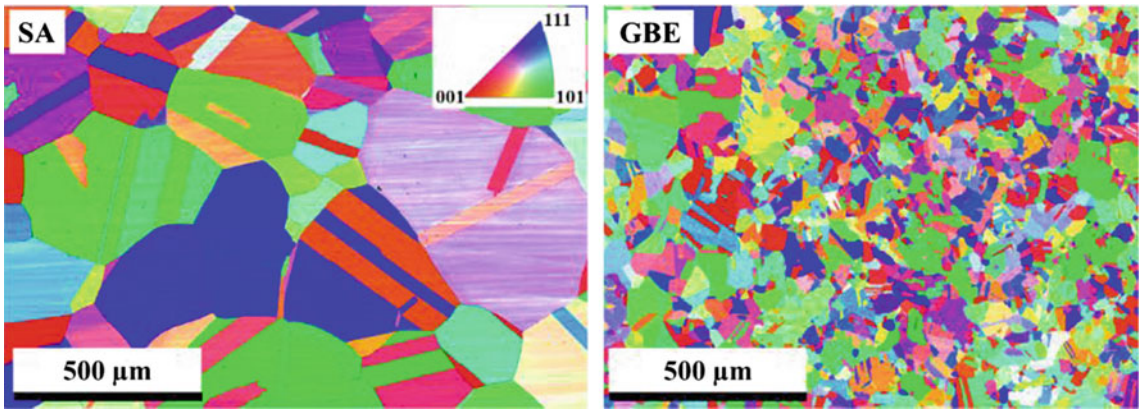

Fig. 21 IPF map of SA and GBE samples

to improve our understanding of the process–structure and structure–property correlation of material.

7.1 Study of Grain Boundary Engineering Using EBSD

EBSD technique is of particular interest, and in fact a necessity, in the field of grain boundary engineering (GBE) (Watanabe 1984; Randle 2004). Specifically, it helps to characterize various interfacial parameters like the fractions of low-Σ coincidence site lattice (CSL) boundaries, grain boundary misorientation deviation, triple junction distribution, and grain boundary connectivity.

The CSL model is used to explain the 'special' properties of some high-angle grain boundaries (HAGBs), which are highly resistant against intergranular degradation than random HAGBs. At some particular misorientation relationships, lattices of the two adjoining grains notionally coincide with each other and give rise to another three-dimensional sub-lattice, known as coincidence site lattice. The degree of coincidence is quantified by a symbol, 'Σ' (sigma), which indicates the reciprocal of the volume density of coinciding lattice sites, without consideration of the grain boundary plane (Brokman and Balluffi 1981). A deviation in the misorientation angle from the exact coincidence is allowed within which the properties of material do not vary much. The most commonly used criterion for the deviation is Brandon criterion (Brandon 1966), given as $\Delta\theta = \theta_m/\Sigma^{1/2}$ where $\Delta\theta$ is the maximum deviation angle allowed from the exact CSL misorientation and $\theta_m = 15°$. The value of low-Σ CSL is taken for $\Sigma \leq 29$, as $\Sigma > 29$ have only a negligible effect on grain boundary characteristics. Σ1 is the same as low-angle grain boundaries. Similar to grain boundaries, triple junctions may also affect intergranular characteristics. Gertsman and Tangri (1995) and Gertsman et al. (1996) classified different types of triple junctions (in 2D) into four kinds, represented as J_i ($i = 0$ to 3), depending upon the number of CSL boundaries they connect. Here, i represents the number of low-Σ CSL boundaries meeting at the triple

junction. Thus, junctions J_2 and J_3 are considered as special/secure junctions for their higher probability to arrest intergranular crack propagation. Junctions J_0 and J_1 are described as non-special/weak junctions for their lower ability in checking the propagation of intergranular degradation. The generation of special triple junctions is also necessary for the effective disruption of the connectivity of random HAGBs networks.

Here, we present a particular case study demonstrating the capabilities of EBSD for the GBE study. In this work, hot rolling and annealing were used as an industrially feasible GBE route to improve the grain boundary structure and, consequently, the functional property (viz. sensitization) of nickel-based superalloy, Alloy 600. Detailed information about this work can be found in Sahu et al. (2019, 2018).

7.1.1 Process–Structure Correlation

EBSD was used to understand the effect of thermomechanical processing on the evolution of microstructure and grain boundary structure. Figure 21 shows the IPF map of solution annealed (SA) and GBE sample conditions. It can be observed that thermomechanical processing leads to a large reduction in grain size by dynamic recrystallization. The variation of colors in the IPF maps in both the conditions indicates that there is no strong texture in either the SA condition or after the processing. The effect of processing on grain boundary structure has been quantified by measuring the fractions of special grain boundaries ($3 \leq \Sigma \leq 29$) and special triple junctions ($J_2 + J_3$), and it is shown in Fig. 22. It can be observed that the thermomechanical processing leads to an increase in not only the fraction of special boundaries but also the fraction of special junctions. In other words, this particular processing condition leads to grain boundary engineering as well as triple junction engineering in Alloy 600. This plot also distinguishes the characteristics of solution annealed and grain boundary engineered sample conditions. Even though ~60% special boundaries in the case of solution annealed sample are a fair fraction, a low fraction of special triple junctions makes it unsuitable to be called as grain boundary engineered condition. To further appreciate this effect, information regarding disruption of HAGBs network with the introduction of twin boundaries was collected with the help of twin-related domain (TRD) analysis (Reed and Kumar 2006; Gertsman 2001; Reed et al. 2004). TRD represents a cluster of grains, which are mutually connected by $\Sigma 3^n$ grain boundaries. Thus, a TRD much larger than the grain size would represent extensive multiple-twinning effects leading to high disruption of HAGBs network. The number of grains per TRD for SA and GBE condition has been shown in Fig. 22. This value is very high (15.9) for GBE sample condition in comparison with that of SA (5). Thus, grain boundary map

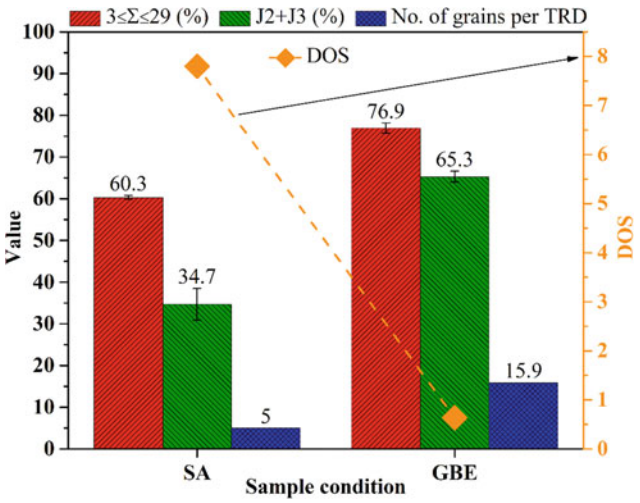

Fig. 22 Effect of thermomechanical processing on the evolution of grain boundary structure and consequently on DOS

of GBE condition can be expected to show disruption of grain boundaries, while SA condition would show a mutually connected HAGBs network. This is very well reflected in the grain boundary maps of these two particular conditions shown in Fig. 23.

7.1.2 Structure–Properties Correlation

After investigating the effect of thermomechanical processing on grain boundary structure, its correlation with functional property (in terms of sensitization effect) was studied. For it, these two samples were given sensitization heat treatment at 650 °C for 24 h, and the sensitization effect was studied with the help of double loop electrochemical potentio kinetic reactivation (DLEPR) test (Číhal Vr, Štefec R. 2001). Figure 22 shows the DOS values of the two particular conditions. As expected, a modified grain boundary structure after thermomechanical processing led to a sharp decrease in DOS value for GBE condition in comparison with that of SA sample.

The aforementioned results show an unambiguous correlation between grain boundary structure and sensitization effect; however, the role of individual boundaries on chromium carbide ($Cr_{23}C_6$) precipitation is not clear from this experiment. In order to analyze the role of individual boundaries, GBE sample was aged at 704 °C for various times between 0.5 and 100 h, and then, the precipitation of chromium carbides on individual boundaries was studied using EBSD-based OIM map and scanning electron microscopy (SEM) micrograph (showing the distribution of carbides) in the same regions. A typical subset of the EBSD map showing various kinds of boundaries and the corresponding SEM micrograph showing the precipitation of chromium carbides in 0.5 h aged GBE specimen have been demonstrated in Fig. 24. It can be seen that random HAGBs

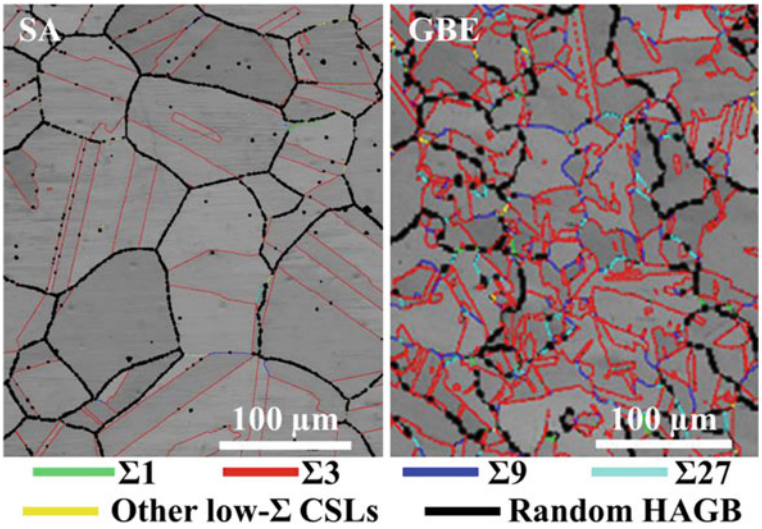

Fig. 23 Band contrast map overlaid with grain boundaries showing the effect of thermomechanical processing on the grain boundary connectivity

are very prone to the precipitation of carbides. On the other hand, low deviation Σ3 boundaries can be viewed to be void of any carbide precipitation. However, with an increase in misorientation deviation (shown by arrows in Fig. 24), even Σ3 boundaries start precipitating chromium carbides. Similarly, Σ9 boundaries are observed to have a low density of carbides.

Some more reports on the application of EBSD to study process–structure and structure–property correlation can be found in Yadav et al. 2016, 2018, 2019; Joham et al. 2017; Sharma and Shekhar 2017; Vaid et al. 2016. In conclusion, this case study showcases the capabilities of EBSD as a powerful quantitative characterization tool.

7.2 Study of Geological Materials Using EBSD

Quartz is one of the most common rock-forming silicate minerals, available in a wide range of crustal rocks, and is an important component to determine the rheology and overall dynamics of the crust. The mineral dominantly occurs in granite and granitoids, sandstones and shales, quartzites and schists. Quartz is also exclusively present in quartz veins and pegmatite dikes. Being a crystalline material, quartz deforms plastically following the laws of dynamic recrystallization under suitable pressure, temperature, and differential stress (Nicolas and Poirier 1976). A typical quartz crystal (right-handed) has several possible slip planes, activation of which is a function of temperature (Fig. 25). The systematic evaluations of such deformation, especially the study of microstructure and texture of the deformed quartz aggregates, provide a series of critical information. This information interprets the ambience, mechanisms, kinematics, and stress magnitude of the overall deformation (Bell and Etheridge 1976; Lloyd and Freeman 1994; Stipp and Tullis 2003; Twiss 1986; Halfpenny et al. 2012; Hunter et al. 2018). Quartz typically deforms maintaining three deformation regimes based on the ambient temperature (Hirth and Tullis 1992)—(i) low temperature (<300 °C); (ii) intermediate temperature (300–600 °C); and (iii) higher temperature (>600 °C). The strain rate is also a crucial factor, which generally decreases at elevated temperatures. Each regime has their characteristic set of microstructures and textures. Optical microscopy with or without universal stage attachment and automated electron backscattered diffraction (EBSD) are two of the most common and popular methods

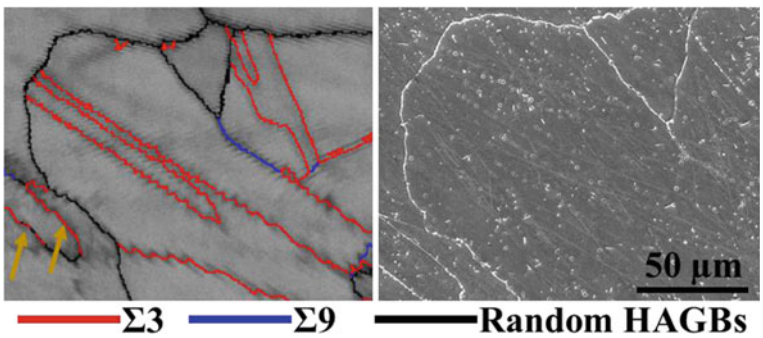

Fig. 24 (Left) Band contrast map and (right) SE image showing the effect of aging time on carbide precipitation on different kinds of boundaries

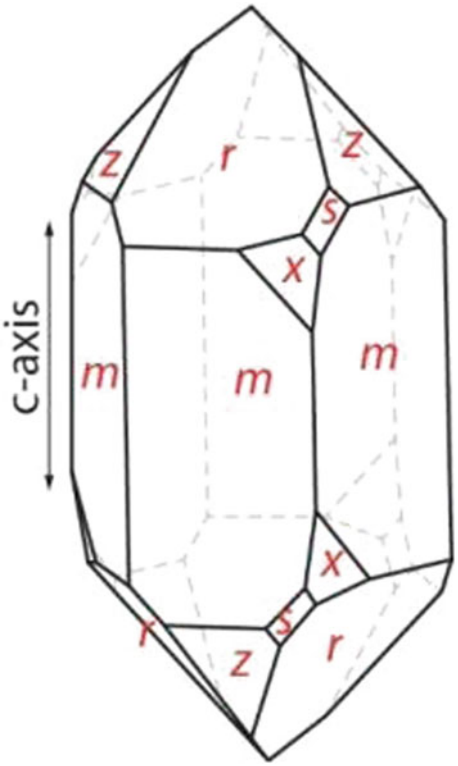

Fig. 25 A typical single quartz crystal (right-handed) showing the different slip planes. The orientation of the *c*-axis is shown by the arrow. The basal plane *a* is orthogonal to the *c*-axis

in order to study the qualitative and quantitative microstructures of quartz.

Here, we present the texture analysis of naturally deformed quartz aggregate. The samples were collected from southern granulite terrain (SGT) in India, and a rock suite underwent metamorphism up to granulite facies (Ghosh et al. 2004). SGT hosts high-grade rocks, like charnockites, khondalites, and other granulite facies metamorphic rocks. The concerned quartz unit typically occurs as discrete stratigraphic unit within the granulites as alternating layers of quartz and iron oxides (magnetite and hematite), popularly referred to as 'banded hematite quartzite' and 'banded magnetite quartzite.' The ultrahigh temperature and pressure granulite facies metamorphism (1000 ± 50 °C/5–9 kbar) in SGT dates back to 2.5 billion years (Raith et al. 1997; Janardhan 1999), which followed a counterclockwise *PTt* path and exhumation processes due to differential upliftment active in recent geological past.

Observations of the samples under a transmitted light optical microscope reveal that quartz (Qtz) grains are dominantly present as elongated thin micro-bands along with opaque minerals (iron oxides, IOx) and pyroxene (Pyx) grains (Fig. 26a). The quartz grains are dynamically recrystallized; in a few places, triple junctions along the grain boundaries are observed, and a large number of grains show undulose extinctions (Fig. 26b). Pyroxene grains remain as porphyroclasts and often show weak shear kinematics (Fig. 26a). Polished sections of the samples observed under the scanning electron microscope in backscatter electron (BSE) mode reveal equant shaped iron oxide grains occurring together in the stretched oxide segments (Fig. 26c).

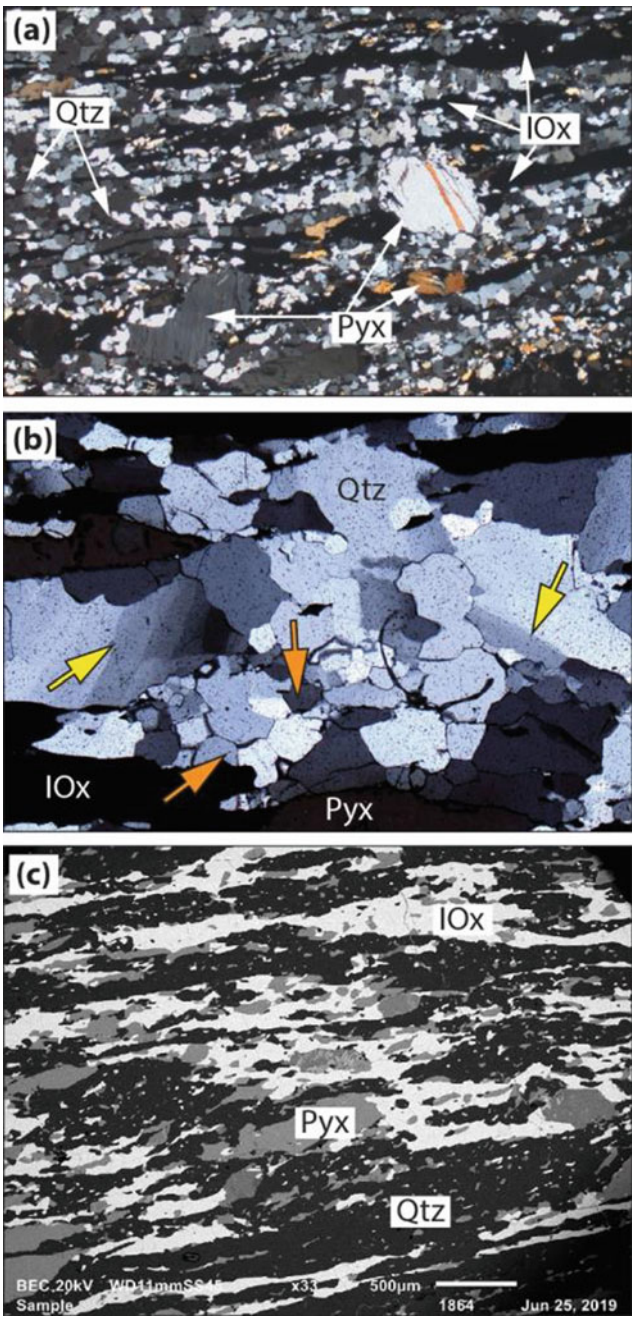

Fig. 26 Transmitted optical (**a**, **b**) and backscatter SEM images of the studied samples observed on the XZ plane of the bulk strain ellipse. In (**b**), the yellow and orange arrowheads point undulose extinctions and triple junctions, respectively, in the quartz grains. Qtz: Quartz; IOx: iron oxides; Pyx: pyroxene. The width of plates **a** and **b** is 10 and 2 mm, respectively

We performed EBSD analysis to study the texture of the quartz grains. A representative sample was cut along the XZ section of the bulk strain ellipsoid and prepared for the analysis following the standard protocols of the EBSD polishing. The EBSD analysis was performed using a field emission scanning electron microscope (JSM 7100F) equipped with an EBSD detector (Oxford Instrument NanoAnalysis, UK) keeping the scan surface of the samples tilted at 70°. The EBSD patterns were collected with 20 mm working distance, 2–5 μm step size, 20 kV accelerating voltage, and ~ 13 nA beam current. Data acquisition from the sample and crystallographic patterns were indexed automatically by Aztec Software (Oxford Instrument NanoAnalysis, UK). MTEX (Mainprice et al. 2011), an open-source MATLAB toolbox (version 5.1.1), was employed to post-process data. Data points with confidence index < 0.1 were removed using the software package. The critical misorientation angle to reconstruct individual quartz grains was chosen to be 10°. The data of the quartz grains is presented in phase map, grain orientation spread (GOS) map, kernel average misorientation (KAM) map, inverse pole figure (IPF) map, and pole figures.

We present the results of EBSD analysis in Fig. 27. The phase map shows that the quartz grains dominate the area with a few smaller hematite and magnetite grains (Fig. 27a). The GOS is noted to be within 5° (Fig. 27b). The IPF map reveals the fact that quartz grains are deformed, and in few, they also show sub-grain boundaries (Fig. 27c). The KAM for majority of the grains lies within 0.004, with few grains characterized by thin bands of high values (>0.016, Fig. 27d). One-point-per-grain pole figures (Fig. 27e–h) are calculated and presented using de la ValléePousin kernel and half width of 15°. The pole figures are contoured to multiples of uniform density (m.u.d). The ⟨c⟩-axis pole figure exhibits a well-defined central girdle. Its obliquity to the XY plane indicates top-to-left sense of shear (Fig. 27e). The cylindricity index (Larson 2018) was calculated to be 0.9, indicating that the quartz grains are highly strained/deformed. Moreover, the maxima of the ⟨c⟩-axis pole figure suggests both rhomb-⟨a⟩ and prism-⟨a⟩ planes were dominantly active, implying deformation within 400–500 °C (Passchier and Trouw 2005). The location of the maxima of the ⟨a⟩-axis pole figure (Fig. 27f) also confirms the same.

7.3 Study of the Effect of Machining Parameters on Subsurface Deformation Using EBSD

Machining is known to make structural changes to not only the surface, but also the subsurface of a machined component (Abolghasem et al. 2012; Shekhar et al. 2012; Wang et al. 2017). The strain, strain rate, and associated temperature rise and eventual microstructural changes in the chip and surface depend largely on the machining configuration. This microstructural transformation leads to change in the functional (Majumdar et al. 2015; Prakash et al. 2015a, b) as well as the mechanical response of the machined component (Gidla 2017; Verma 2014). Surface characteristics like roughness and hardness are known to have an impact on material failure that initiate from the surface such as fatigue failure, fretting fatigue, wear, and stress corrosion cracking as the surface is in contact with the environment (Yuri et al. 2003; Al-Samarai et al. 2012). The surface characteristics of a machined component are also resultant of the machining conditions used during the final shaping operation of the component. Thus, machining parameters affect the surface characteristics as well as the subsurface microstructure of the finished components, which in turn play an important role in deciding the mechanical and functional response of the material.

The overarching goal of this study was to optimize the machining parameters to improve surface characteristics and improve material performance. The specific objective of this work was to understand the effect of machining parameters on the subsurface microstructure and correlate it with surface characteristics. In this regard, simple orthogonal machining of SS316L using tungsten carbide tool was performed on CNC machine. We selected wear volume and hardness as our measure of surface characteristics and microstructure was characterized using EBSD technique. Steel rod was machined at two different speeds (30 and 180 mm/min) for two different feeds (0.05 and 0.2 mm/rev) at two different depths of cut (DOC) (0.1 and 0.5 mm) keeping tool parameters constant, i.e., rake angle (zero degree) and nose radius (0.4). 8-mm disks were taken from the rod, and overall, we had 8 sample conditions as listed in Table 1. Each of these samples was characterized for roughness using optical profilometry. Ball on disk method was used to conduct tribological studies. Tungsten carbide ball has 6-mm diameter, and the sample was made as the disk having diameter 55 mm and thickness 8 mm.

EBSD technique was utilized for characterizing the subsurface microstructure of the machined surface. Small samples from close to the machined surface were taken, and rectangular scans were taken on the transverse region from near the surface toward the inside of the sample. Orientation maps (overlaid on band contrast map and grain boundary map, shown in black) from an area of 120 μm × 40 μm for various sample conditions are presented in Fig. 28. The machined surface is shown by the direction of the arrow. Most of the samples show severe deformation near the surface. The black dots near the surface represent the un-indexed points, which point to some strain in the matrix. The extent of depth of these black dots indicates the extent of subsurface deformation. In some of the conditions, one

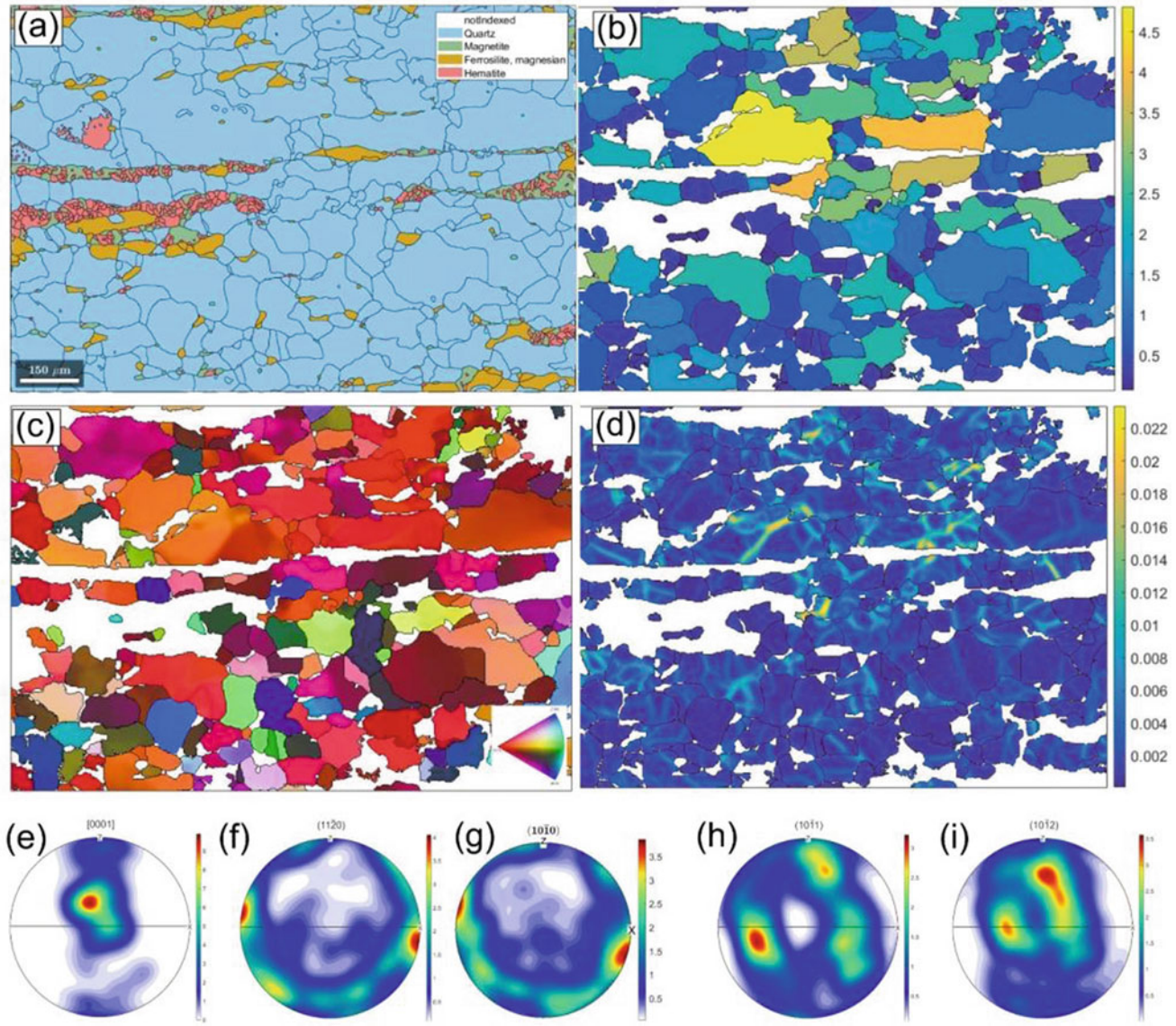

Fig. 27 Selected results of the EBSD analysis. **a** Phase map, **b** grain orientation spread (GOS) map, **c** inverse pole figure (IPF) map along with the key at the inset, **d** kernel average misorientation (KAM) map. One-point-per-grain pole figures of **e** ⟨c⟩-axes, **f** ⟨a⟩-axes, **g** {m}-planes, **h** {r}-planes, and **i** {z}-planes of the quartz grains. The scale is shown only for **a** so as to avoid repetition

Table 1 Details of machining parameters that were selected for machining of SS316L

Sample	Speed (mm/min)	Feed (mm/rev)	Depth of cut (mm)	Rake angle	Nose radius
S1F1D1	30	0.05	0.1	0	0.4
S1F1D2	30	0.05	0.5	0	0.4
S1F2D1	30	0.2	0.1	0	0.4
S1F2D2	30	0.2	0.5	0	0.4
S2F1D1	180	0.05	0.1	0	0.4
S2F1D2	180	0.05	0.5	0	0.4
S2F2D1	180	0.2	0.1	0	0.4
S2F2D2	180	0.2	0.5	0	0.4

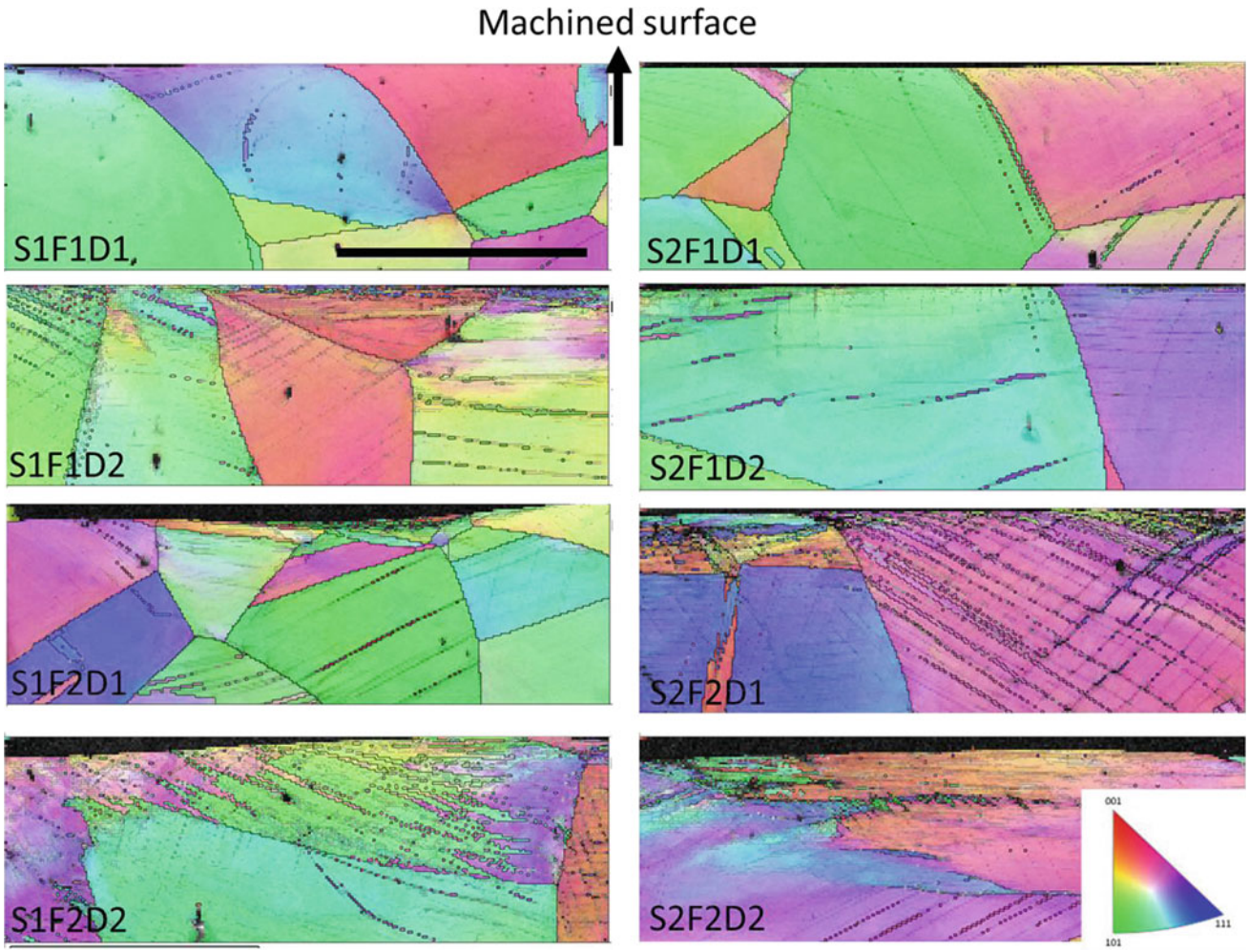

Fig. 28 Orientation maps (overlaid with band contrast map and grain boundary map shown in black) for samples machined under various conditions (scale bar = 50 μm; same for all micrographs)

can see some very refined grains very close to the surface, but it is not there in most of the other conditions. One can conclude that grain refinement, if it happened, was limited to few micrometers near the surface. However, the subsurface deformation does extend much below this. In order to get a better understanding of the subsurface deformation, GROD maps were generated from the EBSD data.

Roughness values and wear volume were plotted for various sample conditions along with the corresponding GROD map in Fig. 29. Here, one can very easily find a correlation between the smaller subsurface deformation and good (low values) roughness condition on the surface (S1F1D1 and S2F1D1). It is likely that subsurface deformation leads to massive slips on various planes, which leads to poor roughness (S1F1D2, S1F2D2, and S2F2D2). On the other hand, best wear resistance is obtained when we have very large subsurface deformation (S1F2D2 and S2F1D2). It is expected as subsurface deformation results in higher hardness near the surface, yielding better wear resistance. However, we found that some sample conditions yield good surface roughness as well as good wear resistance (S2F1D1 and S2F1D2). This most likely happens when there exists a very thin layer of subsurface deformation. A thin layer of subsurface deformation results in minimal upheaval on the surface while still resulting in high hardness for good wear resistance. A closer look at the data also suggests that roughness improves with an increase in speed, decrease in feed, and DOC.

This study clearly establishes that EBSD technique can provide a wealth of information about microstructure. In this work, we were able to relate the surface characteristics to the machining parameters and, in turn, to the subsurface microstructure. This improves our understanding in optimizing the machining parameters to obtain better microstructure as well as better surface characteristics.

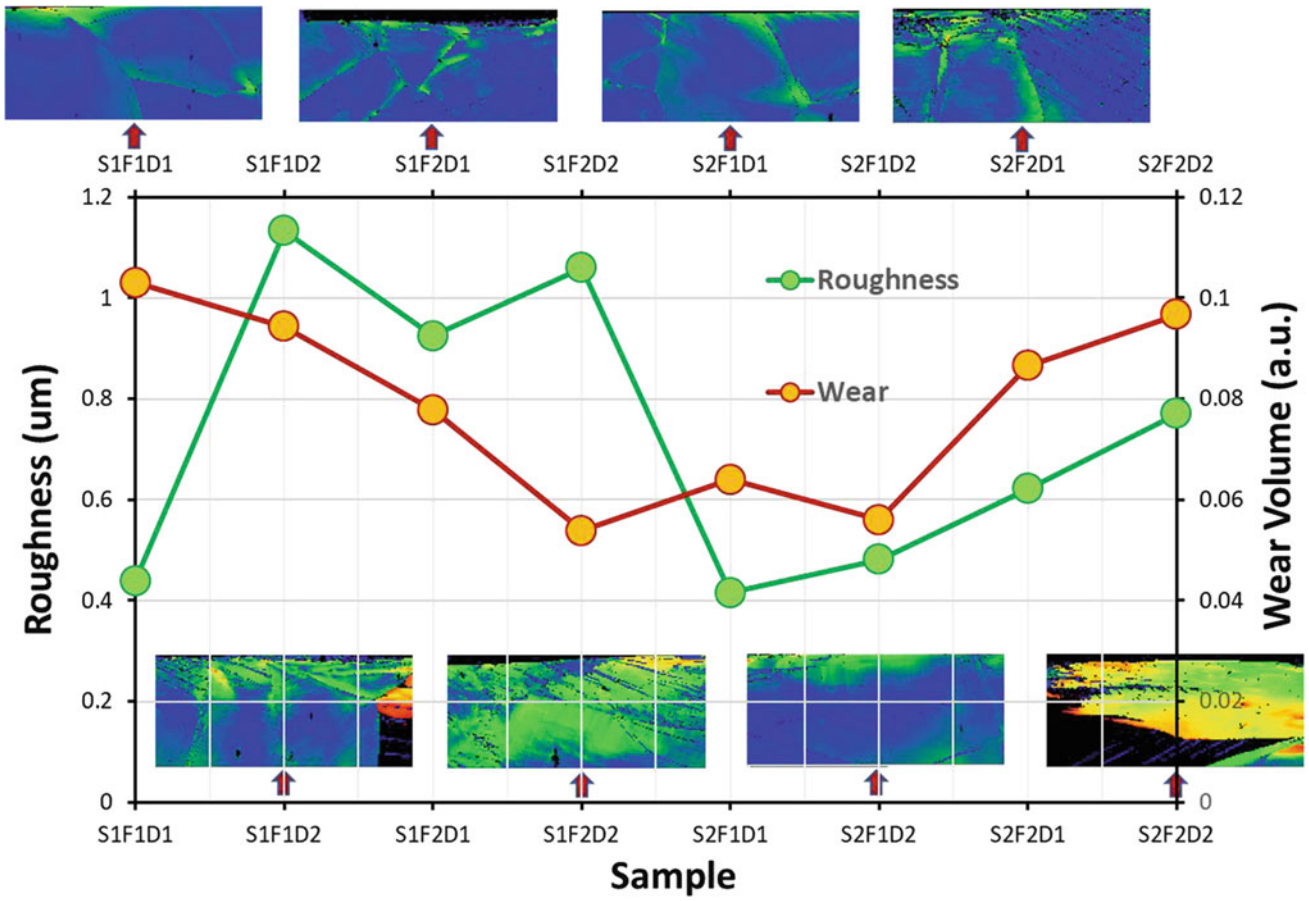

Fig. 29 Variation of roughness and wear volume for various sample conditions (machined surface is toward the top side of each micrograph)

8 Accuracy and Limitations of EBSD

The accuracy with which an absolute orientation of a crystallite can be measured using EBSD is typically ~1° (Humphreys 2001; Schwartz et al. 2009; Humphreys and Brough 1999). This value is dependent on the EBSD acquisition parameters, calibration of the EBSD system, and sample alignment conditions. Although the accuracy of the measurement of an orientation is an important factor in determining the usefulness of EBSD, applications of EBSD in the characterization of grain boundaries and their correlation with properties require very accurate measurement of the relative orientation between the neighboring pixels (Humphreys 2001; Humphreys et al. 1999). Accuracy in the relative orientation becomes even more critical in the case of low-angle grain boundaries, especially the interfaces between sub-grains in the deformed samples (Humphreys et al. 1999; Prior 1999; Wilson and Spanos 2001). Since this relative orientation, or misorientation, is calculated using the absolute orientation data, the accuracy of the measurement of misorientation is related to the precision with which the absolute orientation of individual crystallites can be obtained.

Ideally, all the absolute orientations within a same crystallite should be same, and there should not be any scatter in the orientation data. However, due to the inherent limitations of EBSD, there is a definite value of this orientation noise, ranging from 0.5 to 1° (Wilkinson 2001). These limitations include various factors such as accuracy of pattern solving using Hough transform, CCD camera settings, detector calibrations, accuracy of band detection, and sample alignment. This orientation noise also creates a scatter in the measured data of misorientation between the individual orientations. While this scatter in misorientation data is relatively smaller (~0.2° for misorientation angles higher than 2°) for higher angle grain boundaries, scatters even higher than the actual misorientation for low-angle grain boundaries make an accurate determination of small misorientation angles very difficult (Wilkinson 2001). This further inhibits the study of finer details of a microstructure using misorientation-based parameters like grain average misorientation (GAM), grain orientation spread (GOS), and kernel average misorientation (KAM). Similar to misorientation angles, accurate

Table 2 Typical angular resolution of EBSD in the form of scatter in the measured orientation data (Wilkinson 2001)

Scatter type	Average scatter	Maximum scatter
Absolute orientation	0.5°	1.4°

determination of the misorientation axis also poses certain challenges and is also dependent on the noise of absolute orientation data. Scatter in misorientation axis is not significant for higher misorientation angles. However, the measured misorientation axis for low misorientation angles (<5°) can cover almost complete inverse pole figure, hence making the accurate determination practically impossible (Wilkinson 2001).

Tables 2 and 3 provide a summary of the values of the scatter in the measured orientation and misorientation data, respectively. Average and maximum scatters in the measured orientation data are 0.5 and 1.4°. This scatter is a result of the low precision in the measurement of an individual orientation. As discussed earlier, this precision in the measurement of absolute crystal orientation becomes a limiting factor in the estimation of relative crystal orientation and hence in the characterization of very low-angle grain boundaries. It also makes the application of conventional EBSD potentially inadequate for the characterization of microstructures having deformation features.

Misorientation data is tabulated for 3 different actual misorientation angles, viz. 20, 2, and 0.2°. Maximum scatter in the data of misorientation angles is the standard deviation of the data for each case. It can be seen that for very small misorientation angles such as 0.2°, the scatter in misorientation angle is 0.4°, which is even higher than the actual misorientation angle, and hence, the accurate determination of small misorientation angle is very difficult. In the case of misorientation axis, angles between the measured misorientation axis and the actual misorientation axis are first calculated. Mean scatter and maximum scatter for the misorientation axis are then the mean and maximum value of this data set. Maximum scatter in the misorientation axis for very small misorientation angles reaches such a high value that it becomes practically indefinite, hence written as 'indefinite' in the table.

Improvement in the overall angular resolution of the EBSD technique requires the minimization of the scatter in misorientation data generated. This can ensure the routine and more reliable characterization of very small misorientation angles (<2°). One of the ways to minimize the scatter is either by statistically averaging the orientation data (Humphreys 2001; Wright et al. 2015) or by subtracting a Gaussian-type noise function (Humphreys 1999; Sharma and Shekhar 2018). Although this approach can lead to an improvement in misorientation angle distribution at smaller misorientation angles, improvement in the individual misorientation is not achieved. Changing the operating conditions such as probe current to enhance the quality of backscattered patterns is yet another way to improve the angular resolution (Humphreys and Brough 1999). However, this approach would lead to a decrease in the pattern collection speed and hence will be limited for very smaller area maps. Another approach is to improve the fundamental pattern detection, matching, and solving techniques, including cross-correlation (Bate et al. 2005; Brough et al. 2006; El-Dasher et al. 2003; Wright et al. 2017). These methods are essentially based on the recording of small changes in the absolute positions of similar features in the two patterns from adjacent pixels.

Since this method improves the angular resolution significantly, the EBSD technique with the improved pattern solving method is also known as high-resolution electron backscatter diffraction (HR-EBSD) (Schwartz et al. 2009). Table 4 shows the typical scatter values obtained using a routine HR-EBSD technique. It can be seen that maximum scatter in misorientation angle is only 0.02° even for misorientation angles as small as 0.2°. Maximum scatter in the misorientation axis is also lowered to a definite value of ~14°. This data shows that the EBSD technique with these improved pattern-solving capabilities can be confidently utilized for the routine characterization of deformation

Table 3 Typical angular resolution of EBSD in the form of scatter in the measured misorientation data (Wilkinson 2001)

Actual misorientation	20°	2°	0.2°
Misorientation angle (maximum scatter)	0.2°	0.25°	0.4°
Misorientation axis (mean scatter)	2°	15°	50°
Misorientation axis (maximum scatter)	5°	40°	-Indefinite-

Table 4 Typical angular resolution of HR-EBSD in the form of scatter in the measured misorientation data (Wilkinson 2001)

Actual misorientation	0.2°
Misorientation angle (maximum scatter)	0.02°
Misorientation axis (mean scatter)	5.7°
Misorientation axis (maximum scatter)	13.9°

constituents. This way, the HR-EBSD technique has proved to be pathbreaking in the characterization of localized strains with high resolution (Wilkinson et al. 2014).

It should also be noted that these methods are quite resource-intensive and require a lot of computer space for storing all the electron backscatter pattern (EBSP) data and, in turn, resulting in the increased cost for overall EBSD characterization. However, such limitations are gradually waning with the improvement in computing and storage capabilities.

9 Summary

It is clearly established that EBSD is a very powerful technique that can be applied to all types of crystallographic materials, ranging from metals to ceramics to semiconductors. We provided fundamentals on the origin of Kikuchi pattern and how this data is acquired by the hardware to identifying the orientation of a given material. We have also provided a glimpse of various fundamental analyses that can be carried out with the data extracted using EBSD. Analysis of the data can provide various in-depth understandings of the microstructure and its properties, and this was clearly brought out with the help of some of the case studies discussed here. Toward the latter part, we have also discussed the limitations of this instrument, particularly in terms of the accuracy of the data obtained. This must be kept in mind when interpreting the results and deriving conclusions. It should also be noted that there are several journal articles and books available on the topics listed above, which discuss at length each of these issues. The purpose of this article is to provide the beginners all the necessary information at one place, without getting distracted by great many details. Readers who are looking to gain an in-depth understanding of the subject are directed to the references cited in this article.

Acknowledgements All the EBSD data was generated using the facilities in the Advanced Centre for Material Sciences (ACMS) of IIT Kanpur. Mr. Sivakumar assisted in EBSD data acquisition for the Inconel 718 sample. EBSD of duplex steel was acquired by Prince Setia. Saquib Abdullah, Dripta Dutta, and R. Sarvesha assisted in the EBSD data acquisition and analysis of quartz in case study (B). A part of the work in case study (B) is supported by a DST Swarnajayanti Fellowship (DST/SJF/E&ASA-01/2015-16), awarded to Santanu Misra. Case study (C) is part of the project funded by BRNS, under sanction No. 36(2)/14/39/2016-BRNS/6047.

References

Abolghasem S, Basu S, Shekhar S, Cai J, Shankar M (2012) Mapping subgrain sizes resulting from severe simple shear deformation. Acta Mater 60(1):376–386

Ahmed J, Wilkinson AJ, Roberts SG (1997) Characterizing dislocation structures in bulk fatigued copper single crystals using electron channelling contrast imaging (ECCI). Philos Mag Lett 76(4):237–246

Al-Samarai RA, Haftirman KRA, Al-Douri Y (2012) The influence of roughness on the wear and friction coefficient under dry and lubricated sliding. Int J Sci Eng Res 3(4):1–6

Bate PS, Knutsen RD, Brough I, Humphreys FJ (2005) The characterization of low-angle boundaries by EBSD. J Microsc 220(1):36–46

Bell TH, Etheridge MA (1976) The deformation and recrystallization of quartz in a mylonite zone. Cent Aust Tectonophysics 32(3):235–267

Berger D, Niedrig H (1999) Complete angular distribution of electrons backscattered from tilted multicomponent specimens. Scanning 21 (3):187–190

Brandon D (1966) The structure of high-angle grain boundaries. Acta Metall 14(11):1479–1484

Brokman A, Balluffi RW (1981) Coincidence lattice model for the structure and energy of grain boundaries. Acta Metall 29(10):1703–1719

Brough I, Bate PS, Humphreys FJ (2006) Optimising the angular resolution of EBSD. Mater Sci Technol 22(11):1279–1286

Bunge HJ, Haessner F (1968) Three-dimensional orientation distribution function of crystals in cold-rolled copper. J Appl Phys 39 (12):5503–5514

Bunge HJ (2013) Texture analysis in materials science: mathematical methods. Elsevier

Chen D, Kuo J-C, Wu W-T (2011) Effect of microscopic parameters on EBSD spatial resolution. Ultramicroscopy 111(9):1488–1494

Číhal Vr, Štefec R (2001) On the development of the electrochemical potentiokinetic method. Electrochimica Acta 46(24):3867–3877

Coates DG (1967) Kikuchi-like reflection patterns obtained with the scanning electron microscope. Philos Mag: J Theor Exp Appl Phys 16(144):1179–1184

Dingley DJ, Wright SI, Nowell MM (2005) Dynamic background correction of electron backscatter diffraction patterns. Microsc Microanal 11(S02):528–529

El-Dasher BS, Adams BL, Rollett AD (2003) Viewpoint: experimental recovery of geometrically necessary dislocation density in polycrystals. Scripta Mater 48(2):141–145

Gertsman V (2001) Coincidence site lattice theory of multicrystalline ensembles. Acta Crystallogr A 57(6):649–655

Gertsman VY, Janecek M, Tangri K (1996) Grain boundary ensembles in polycrystals. Acta Mater 44(7):2869–2882

Gertsman VY, Tangri K (1995) Computer simulation study of grain boundary and triple junction distributions in microstructures formed by multiple twinning. Acta Metall Mater 43(6):2317–2324

Ghosh JG, de Wit MJ, Zartman RE (2004) Age and tectonic evolution of Neoproterozoic ductile shear zones in the Southern Granulite Terrain of India, with implications for Gondwana studies. Tectonics 23(3):TC3006

Gidla MR (2017) Effect of machining on mechanical, tribological and functional properties of mild steel, M.Tech. thesis at IIT Kanpur

Halfpenny A, Prior DJ, Wheeler J (2012) Electron backscatter diffraction analysis to determine the mechanisms that operated during dynamic recrystallisation of quartz-rich rocks. J Struct Geol 36:2–15

Heinz A, Neumann P (1991) Representation of orientation and disorientation data for cubic, hexagonal, tetragonal and orthorhombic crystals. Acta Crystallogr A 47(6):780–789

Herter T, Lott K (1993) Algorithms for decomposing 3-D orthogonal matrices into primitive rotations. Comput Graph 17(5):517–527

Hirth G, Tullis J (1992) Dislocation creep regimes in quartz aggregates. J Struct Geol 14(2):145–159

Humphreys FJ (1999) Quantitative metallography by electron backscattered diffraction. J Microsc 195(3):170–185
Humphreys FJ (2001) Review grain and subgrain characterisation by electron backscatter diffraction. J Mater Sci 36(16):3833–3854
Humphreys FJ, Brough I (1999) High resolution electron backscatter diffraction with a field emission gun scanning electron microscope. J Microsc 195(Pt 1):6–9
Humphreys FJ, Huang Y, Brough I, Harris C (1999) Electron backscatter diffraction of grain and subgrain structures—resolution considerations. J Microsc 195(3):212–216
Hunter NJR, Weinberg RF, Wilson CJL, Luzin V, Misra S (2018) Microscopic anatomy of a "hot-on-cold" shear zone: insights from quartzites of the Main Central Thrust in the Alaknanda region (Garhwal Himalaya). GSA Bull 130(9–10):1519–1539
Janardhan AS (1999) Southern granulite terrain, south of the palghat-cauvery shear zone: implications for India-madagascar connection. Gondwana Res 2(3):463–469
Joham R, Sharma NK, Mondal K, Shekhar S (2017) Low temperature cross-rolling to modify grain boundary character distribution and its effect on sensitization of SS304. J Mater Process Technol 240:324–331
Joy DC, Newbury DE, Davidson DL (1982) Electron channeling patterns in the scanning electron microscope. J Appl Phys 53(8): R81–R122
Kamaladasa R, Picard Y (2010) Basic principles and application of electron channeling in a scanning electron microscope for dislocation analysis. Microsc: Sci Technol Appl Educ 3:1583–1590
Kunze K, Wright SI, Adams BL, Dingley DJ (1993) Advances in automatic EBSP single orientation measurements. Textures Microstruct 20:589659
Larson KP (2018) Refining the structural framework of the Khimti Khola region, east-central Nepal Himalaya, using quartz textures and c-axis fabrics. J Struct Geol 107:142–152
Lloyd GE, Freeman B (1994) Dynamic recrystallization of quartz under greenschist conditions. J Struct Geol 16(6):867–881
Mainprice D, Hielscher R, Schaeben H (2011) Calculating anisotropic physical properties from texture data using the MTEX open-source package. Geolog Soc, London, Spec Publ 360(1):175–192
Majumdar P, Shekhar S, Mondal K (2015) Effect of machining parameters on oxidation behavior of mild steel. J Mater Eng Perform 24(1):484–498
Michael J, Giannuzzi L (2007) Improved EBSD sample preparation via low energy Ga + FIB Ion milling. Microsc Microanal 13(S02):926–927
Morawiec A, Field DP (1996) Rodrigues parameterization for orientation and misorientation distributions. Philos Mag A 73(4):1113–1130
Nicolas A, Poirier J-P (1976) Crystalline plasticity and solid state flow in metamorphic rocks. Jokn Wiley & Sons, London, p 444
Nishikawa S, Kikuchi S (1928a) Diffraction of cathode rays by calcite. Nature 122(3080):726–726
Nishikawa S, Kikuchi S (1928b) Diffraction of cathode rays by mica. Nature 121(3061):1019–1020
Nolze G, Hielscher R (2016) IPF coloring of crystal orientation data. Preprint Technische Universität Chemnitz
Nowell MM, Witt RA, True B (2005) EBSD sample preparation: techniques, tips, and tricks. Microsc Microanal 11(S02):504–505
Passchier CW, Trouw RA (2005) Microtectonics, 2nd edn. Springer, Heidelberg
Prakash M, Moon AP, Mondal K, Shekhar S (2015a) Effect of machining configurations on the electrochemical response of mild steel in 3.5% NaCl solution. J Mater Eng Perform 24(9):3643–3650
Prakash M, Shekhar S, Moon A, Mondal K (2015b) Effect of machining configuration on the corrosion of mild steel. J Mater Process Technol 219:70–83
Prior DJ (1999) Problems in determining the misorientation axes, for small angular misorientations, using electron backscatter diffraction in the SEM. J Microsc 195(3):217–225
Raith M, Karmakar S, Brown M (1997) Ultra-high-temperature metamorphism and multistage decompressional evolution of saphirine granulites from the Palni Hill Ranges, southern India. J Metamorph Geol 15(3):379–399
Randle V (2004) Twinning-related grain boundary engineering. Acta Mater 52(14):4067–4081
Randle V, Davies H, Cross I (2001) Grain boundary misorientation distributions. Curr Opin Solid State Mater Sci 5(1):3–8
Reed BW, Kumar M (2006) Mathematical methods for analyzing highly-twinned grain boundary networks. Scripta Mater 54 (6):1029–1033
Reed BW, Minich RW, Rudd RE, Kumar M (2004) The structure of the cubic coincident site lattice rotation group. Acta Crystallogr A 60 (3):263–277
Sahu S, Sharma NK, Patel SK, Mondal K, Shekhar S (2019) The effect of grain boundary structure on sensitization behavior in a nickel-based superalloy. J Mater Sci 54:1797–1818
Sahu S, Yadav PC, Shekhar S (2018) Use of hot rolling for generating low deviation twins and a disconnected random boundary network in inconel 600 alloy. Metall Mater Trans A 49(2):628–643
Schwartz AJ, Kumar M, Adams BL, Field DP (eds) (2009) Electron backscatter diffraction in materials science, 2nd edn. Springer, US, Boston, MA, pp 21–143
Sharma NK, Shekhar S (2017) Microstructure and property evolution for hot-rolled and cold-rolled austenitic stainless steel 316L. Trans Indian Inst Met 70(5):1277–1284
Sharma NK, Shekhar S (2018) Deconvoluting error in measurement of low angle misorientation distribution. Micron 107:28–34
Shekhar S, Abolghasem S, Basu S, Cai J, Shankar M (2012) Effect of severe plastic deformation in machining elucidated via rate-strain-microstructure mappings. J Manuf Sci Eng 134 (3):031008
Shoemake K (1994) III.5.—Euler angle conversion. In: Heckbert PS (ed) Graphics gems, vol 4. Elsevier Inc, London, pp 222–229
Singh S, Guo Y, Winiarski B, Burnett TL, Withers PJ, De Graef M (2018) High resolution low kV EBSD of heavily deformed and nanocrystalline Aluminium by dictionary-based indexing. Sci Rep 8 (1):10991
Stipp M, Tullis J (2003) The recrystallized grain size piezometer for quartz. Geophys Res Lett 30(21):2088
Twiss RJ (1986) Variable sensitivity piezometric equations for dislocation density and subgrain diameter and their relevance to olivine and quartz. Min Rock Deformation: Lab Stud, AGU Geophys Monogr 36:247–263
Vaid A, Mittal K, Sahu S, Shekhar S (2016) Controlled evolution of coincidence site lattice related grain boundaries. Trans Indian Inst Met 69(9):1745–1753
Verma M (2014) Effect of machining configurations on the mechanical properties of SS316L, M.Tech. thesis at IIT Kanpur
Wang YZ, Kong MG, Liu ZW, Lin CC, Zeng Y (2016) Effect of microscope parameter and specimen thickness of spatial resolution of transmission electron backscatter diffraction. J Microsc 264 (1):34–40
Wang Z, Saldana C, Basu S (2017) Subsurface microstructure and crystallographic texture in surface severe plastic deformation processes. In: International manufacturing science and engineering conference. American Society of Mechanical Engineers
Watanabe T (1984) An approach to grain boundary design for strong and ductile polycrystals. Res Mechanica 11(1):47–84
Wilkinson AJ (2001) A new method for determining small misorientations from electron back scatter diffraction patterns. Scripta Mater 44(10):2379–2385

Wilkinson AJ, Britton TB (2012) Strains, planes, and EBSD in materials science. Mater Today 15(9):366–376

Wilkinson AJ, Britton TB, Jiang J, Karamched PS (2014) A review of advances and challenges in EBSD strain mapping. IOP Conf Ser: Mater Sci Eng 55:012020

Wilkinson AJ, Hirsch PB (1997) Electron diffraction based techniques in scanning electron microscopy of bulk materials. Micron 28 (4):279–308

Wilson AW, Spanos G (2001) Application of orientation imaging microscopy to study phase transformations in steels. Mater Charact 46(5):407–418

Wright SI, Field DP, Nowell MM (2015) Post processing effects on GND calculations from EBSD-based orientation measurements. IOP Conf Ser: Mater Sci Eng 89:012049

Wright S, Nowell M, Basinger J (2017) Precision of EBSD based orientation measurements. Microsc Microanal 17(S2):406–407

Yadav PC, Sahu S, Subramaniam A, Shekhar S (2018) Effect of heat-treatment on microstructural evolution and mechanical behaviour of severely deformed Inconel 718. Mater Sci Eng, A 715:295–306

Yadav PC, Sharma NK, Sahu S, Shekhar S (2019) Influence of short heat-treatment on microstructural and mechanical inhomogeneity of constrained groove pressed Cu-Zn alloy. Mater Chem Phys 238:121912

Yadav PC, Sinhal A, Sahu S, Roy A, Shekhar S (2016) Microstructural inhomogeneity in constrained groove pressed Cu-Zn alloy sheet. J Mater Eng Perform 25(7):2604–2614

Yuri T, Ono Y, Ogata T (2003) Effects of surface roughness and notch on fatigue properties for Ti–5Al–2.5Sn ELI alloy at cryogenic temperatures. Sci Technol Adv Mater 4(4):291–299

Zaefferer S, Elhami N-N (2014) Theory and application of electron channelling contrast imaging under controlled diffraction conditions. Acta Mater 75:20–50

Application of Electron Backscatter Diffraction (EBSD) Method in Earth Sciences

Dripta Dutta, Vikram Maji, Saquib Abdullah, and Santanu Misra

1 Introduction

The electron backscatter diffraction (EBSD) has developed into a powerful tool for acquisition of micro-scale crystallographic information since its emergence in the 1970s. The applications of the EBSD are primarily in the field of material sciences (Schwarzer et al. 2009). Since early 1990s, the geoscientists, particularly from the field of rock deformation, geodynamics and seismic anisotropy, started using this technique as one of the essential tools and also contributing in the development and fine-tuning the method (Prior et al. 2009). Today, the application of texture analysis has considerably expanded due to an increasing diversity of high performance sources for electron, high-intensity X-ray and neutron diffraction, using field emission gun scanning electron microscopy (FEG-SEM), synchrotron and nuclear reactors, respectively.

Rocks are polycrystalline materials and consist of small crystals (grains) of varying compositions. The grains may or may not belong to the same crystallographic systems. The overall arrangement of the grains within the rocks also defines their characteristic microstructures. Under suitable temperature and differential stress, the individual crystals deform by bending and/or distorting their lattices following their rheology, compatibility constraints, and earlier deformation history (Vernon 2018). Such deformations give rise to typical textures of the deformed rocks, quantification of which provides information related to the prevailing conditions of deformation and underlying mechanisms (Fossen 2016). The texture encompasses the overall microstructures of the polycrystalline rocks and also the crystallographic preferred orientation (CPO). The intensity of CPO controls the first-order anisotropy of the rock aggregates, being isotropic for uniform orientation and close to the single-crystal anisotropy for a very strong preferred orientation (Almqvist and Mainprice 2017). The arrangements of the crystals and their shapes also have some influence of the material properties (Almqvist and Mainprice 2017; Passchier and Trouw 2005). Glide and climb of dislocations on slip systems are responsible for the CPO patterns exhibited by the minerals (Maitland et al. 2006). The activation of particular slip systems in a specific mineral is pressure and temperature-dependent. For example, in omphacite (a high-pressure silicate of pyroxene group), the mechanical twinning is identified on (100) and (001), and dislocation glide on the [001](100) slip system at low to intermediate temperatures and high strain rates (Boland et al. 1986). At high temperatures (T > 500 °C) and low strain rates, the mineral deforms with multiple slip systems [001](100), [001]{110}, 1/2 < 110 > {110} (Zhang et al. 2006). Microstructural characterization by EBSD on both naturally and experimentally deformed geomaterials can reveal different deformation mechanisms, viz. dynamic recrystallization, static recrystallization, and recovery (Prior et al. 2009). The data can also quantify the misorientations within and across the boundaries of the neighboring grains and differentiate between relict and recrystallized grains (Halfpenny et al. 2006). Additionally, calculations of elastic properties of the crystals are possible with the help of EBSD data. The elastic constants then are used to determine the seismic anisotropy, which originates from the anisotropic minerals (phyllosilicates, pyroxenes, olivine, serpentine, etc.) and their orientations in the crust and deep earth (Almqvist and Mainprice 2017).

EBSD is a scanning electron microscope (SEM)-based technique that provides quantitative microstructural, crystallographic, and textural information of the crystalline materials such as rocks, metals, alloys, semiconductors, and ceramics (Prior et al. 2009; Almqvist and Mainprice 2017). The post-processing of raw EBSD data yields quantitative information about the grains (size, shape, and crystallographic orientations), the grain boundaries (low- or

D. Dutta · V. Maji · S. Abdullah · S. Misra (✉)
Department of Earth Sciences, Indian Institute of Technology Kanpur, Kanpur, Uttar Pradesh 208016, India
e-mail: smisra@iitk.ac.in

K. Biswas et al. (eds.), *Electron Microscopy in Science and Engineering*, IITK Directions 6,
https://doi.org/10.1007/978-981-16-5101-4_5

high-angular contrast), and the crystal structures. The SEM system equipped with energy dispersive X-ray spectrometry (EDS) can also identify the different phases (minerals) in a rock sample (Prior et al. 2009; Almqvist and Mainprice 2017). However, the method has its limitation for minerals with solid solutions, which are structurally identical (i.e., the unit cell parameters are same), but they are compositionally different (Prior et al. 2009). In general, for earth scientists, the EBSD technique is an excellent and quick tool to investigate the crystal-scale mechanisms of ductile deformation, which dominates at mid-lower crustal levels, and the upper mantle (Prior et al. 2009).

In this article, we present a comprehensive review of the EBSD techniques and its applications in Earth Sciences. Brief discussions on the working principles of the EBSD instrument, followed by data acquisition, processing and analysis, sample preparation methods for geological samples are presented at the beginning. We then discuss in detail the applications of EBSD in Earth Sciences and how the processed grain-scale data could be utilized in understanding the large-scale geodynamics.

2 Background of EBSD Analysis

2.1 Acquisition Protocol and Background Physics

EBSD is a powerful non-destructive tool for quantifying crystallographic information from a small volume of material using an additional charge coupled device (CCD) camera and detector in a scanning electron microscope (SEM) set up (Karato et al. 2008). High energy stationary electron beam is projected on the prepared sample surface (Fig. 1a), which is kept inclined ($\sim$70° to horizontal) toward the detector. Such an arrangement enhances the quality of the diffraction pattern (Cao et al. 2013). The electrons either interact with the nucleus (high angle scattering) or interact with the inter-nucleic electron cloud (low angular deviation) (Venables and Harland 1973). The diameter (1 nm, lowest) of the incident electron beam ensures all possible combinations of interactions.

Part of the incident electrons, after one or more scattering events at varying depths (mostly $\sim$ 20–40 nm), exits the sample and constitutes the back scattered electron (BSE) source (Fig. 1b). The BSEs then encounter a scintillator/phosphor screen ($\sim$5 cm in diameter and kept $\sim$ 2 cm away from the specimen), coupled with a lens (sometimes with fiber-optic bundle) that converts the projected BSEs into light. Subsequently, the light energy is captured and processed by a photon-sensitive imaging detector, typically a CCD camera. The diffracted pattern, also known as the Kikuchi pattern (Alam et al. 1954), is the 'gnomic projection' of the lattice planes on to the screen. It consists of linear Kikuchi bands, which are the edges of the two diffracted cones (Fig. 1c, d). The angular width of any Kikuchi band is twice the Bragg angle, and thus related to the interplanar lattice distance of the crystal by Bragg's law. The intensity of the Kikuchi pattern is inversely proportional to the square of the distance between the specimen and the phosphor screen. Intersecting Kikuchi bands form a bright spot and correspond to a zone axis (Fig. 1e), surrounded by higher-order Laue zone (HOLZ) lines.

2.2 Data Processing and Analysis

Electron backscatter patterns (EBSP), captured by the camera, are transferred to the processing computer for further reconstruction. The width, contrast, and sharpness of the Kikuchi bands are primarily controlled by the accelerating voltage (in kV) used for the acquisition (Loretto 2012). Polychromatic source and variations in BSE intensities associated with varying scattering angles introduce significant background component in the data set. Such background noises are typically normalized using a filter of adequate geometry by assigning mean value in the central pixel (Nishikawa and Kikuchi 1928). EBSP with poor contrast can further be enhanced and fine-tuned after background signal subtraction or division from the total signal. This protocol is particularly useful for materials with low atomic numbers.

Crystallographic orientations at the source point are estimated using ESBP of known materials or minerals by indexing. In practice, Hough transform algorithm (Hough 1962) is extensively used for transforming the Kikuchi bands from lines to points (Fig. 2). This step is important for identification of crystallographic orientation, as points can easily be spotted in the Hough space. The peak locations are restored in a sequence of interplanar angles and are compared with the look up table for matching of expected angles to identify the phases present in the sample. The complexity associated with indexing often leads to misorientation of reference points than the actual solution within the error window—generally a degree—of indexing protocols (Schwarzer et al. 2009). *Misindexing* refers to the points in the EBSD map (Fig. 3) with incorrect orientation information. '*Non-indexed*' points are the ones without any optimum solution. The problems associated with indexing are eminent for geomaterials than metals due to low signal level and the fact that minerals with lower symmetry emits continuous spectrum of inter-band angles. This typical property of minerals makes it difficult to find the exact match from the pre-calibrated library as the signal can correspond to more than one set of lattice planes (Prior et al. 2009). Positioning of the camera close to the sample for producing high-quality

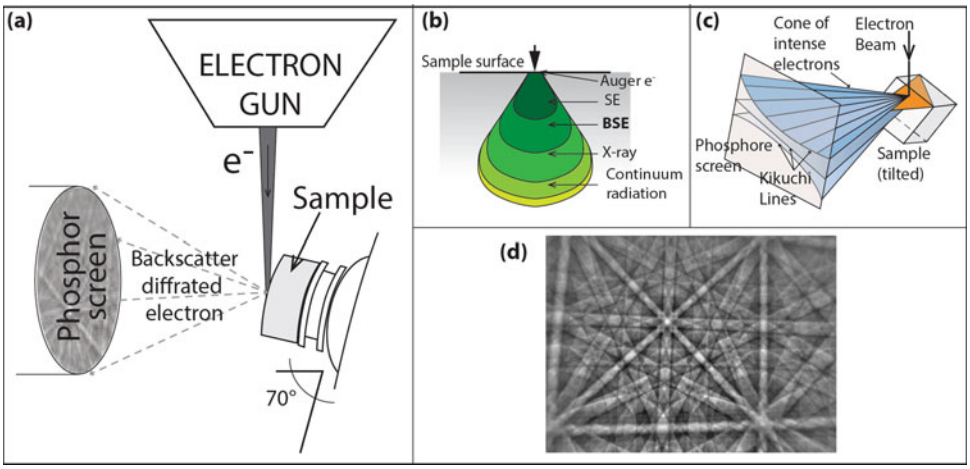

Fig. 1 Various components of the EBSD acquisition method are shown along with the background mechanisms and final outcome. **a** Illustration showing the electron source, sample, and detector with phosphor screen. **b** Diagram, showing the interaction of the electron beam with the sample. The depth of penetration determines the characteristics. **c** Three-dimensional (3D) illustration for formation of diffraction cone when electron beam interacts with a lattice plane to produce Kikuchi lines. **d** EBSP showing Kikuchi bands formed after BSE interact with the detector screen (image from Oxford Instruments)

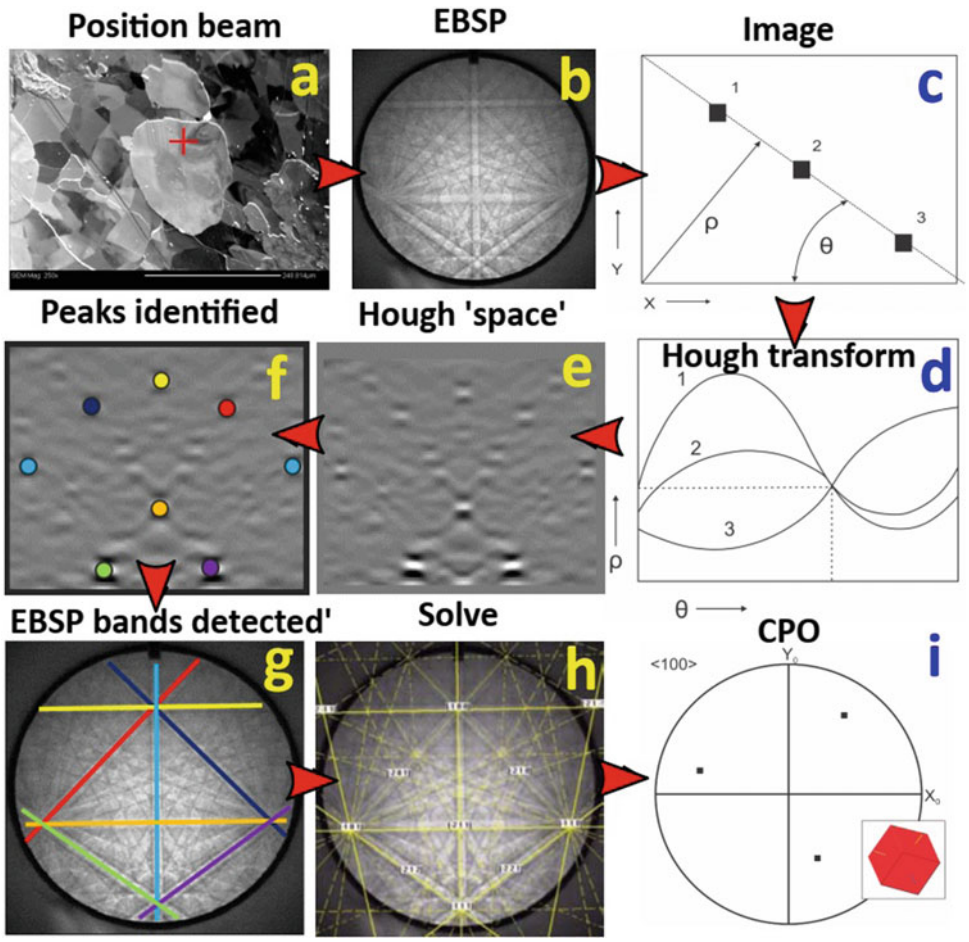

Fig. 2 Different stages of indexing method are shown to identify CPO from EBSP. **a** SEM image with a cross mark showing the location of incident electron beam. **b** EBSP showing Kikuchi bands. **c** and **d** illustrates Hough transformation from a straight line into a point. **e** Hough 'space' as simplified in (**d**). **f** The peaks are identified as points in Hough 'space.' **g** and **h** The Kikuchi bands shown in (**b**) are identified with their actual crystallographic orientation. (i) CPO of the material at incident point (**a**) with the figure in inset showing the orientation in 3D. *Source* Oxford Instruments

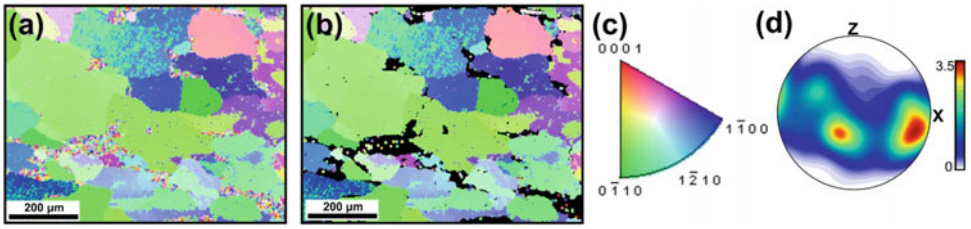

Fig. 3 Typical **a** and **b** orientation maps, the corresponding **c** color key, and **d** pole figure plot. The poorly indexed data points in (**a**) were removed to produce the map in (**b**). This was done in EDAX OIM v8. The pole figure is an equal area, lower hemisphere stereographic projection that is contoured to multiples of uniform density using MTEX v5.2. The sample is a gneiss from the Trans-Himalayan terrane, near Puga (Ladakh Union Territory, India). All the grains in **a** and **b** are of quartz

patterns and maintaining reasonable numbers of index points are often useful to reduce the indexing-induced glitches. Enhanced beam current and longer acquisition time are also good practice to improve the ESBP quality. Modern acquisition systems are capable of EBSP capturing and indexing very rapidly (~100 s of EBSPs per second), and reproducing EBSD map with detailed information on crystal types, orientations, etc.

Once the acquisition and the necessary corrections are performed, and the artifacts are minimized, the processed data can then be further analyzed using both commercially available and open-source software packages. Among them, MTEX (Bachmann et al. 2010) is an open-source user-friendly MATLAB toolbox. The EBSD data is normally visualized based on the orientations and shape of the crystals, phase contrasts, grain boundary contrasts (boundaries are defined with deviation in orientation angles) for both mono-and poly-mineralic assemblages. The CPO is generally displayed as pole figures which consist of poles of lattice planes on a stereonet that corresponds to the sample reference frame. The realtive differences in the orientations of the structural elements (e.g., lineation and/or foliation) and the crystallographic reference axes can also be inferred from inverse pole figures (IPF). Individual crystallographic orientations are plotted as single points using orientation distribution function (ODF) method (Bunge 1981).

2.3 Sample Preparation

There are no definite guidelines with suitable information for adequate sample preparation, and therefore, though the principles remain same, the protocols vary for specific geological sample and available instruments. A deformed sample is generally observed along the *XZ* plane of the strain ellipsoid, where *X* represents the stretching direction (equivalent to rolling direction, RD), identified by the lineation and *Z*-direction is orthogonal to the foliation plane (equivalent to normal direction, ND) (Fig. 4). A careful observation, sample collection and cutting the samples along

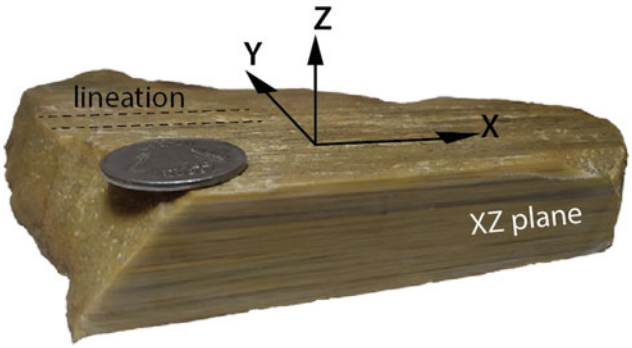

Fig. 4 Illustration to show the sections at which the EBSD data should be collected from a deformed rock. The sample is a naturally sheared quartzite, collected from Singhbhum Shear Zone, India. The top surface is parallel to the foliation plane (*XY*), and *X* is the stretching direction which is identified by the lineation observed on the *XY* plane. The cut surface (*XZ* plane) is the key surface, which should be processed to collect the EBSD data. (The sample is from the personal collection of S. Misra)

the *XZ* plane, are very important for extracting representative EBSD data (Fig. 4). Standard mechanical processes of initial grinding and polishing are the primary starting points but often damages the soft minerals at the sample surface. One has to take special care for soft and flaky minerals, while polishing. For porous and/or fragile samples, resin impregnation in vacuum is recommended. After the initial polishing, a combination of chemical–mechanical polishing (colloidal silica, electropolishing, ion milling, and chemical or plasma etching) ensures damage-/scratch-free surface for common rock forming minerals (Koll et al. 2011). After the final polishing, the quality of the polishing can be checked with a reflected light microscope. It is worthwhile to have a quick, manual 'point and click' investigation with the sample in the SEM chamber to ensure good-quality polishing; otherwise, preparation procedures may possibly require revisiting. After the satisfactory level of polishing, the nonconductive (non-metallic) samples are lightly sputter coated with carbon, unless the samples are being analyzed in low vacuum. A conductive circuit must be ensured between the sample and the stage.

Backscatter and/or secondary electron imaging are useful guidelines for selection of initial area and the step size to be used. However, the selection of step size is objective dependent. For instance, if overall texture estimation is the primary aim, then using relatively coarse step size is relevant, whereas for investigating localized/intragranular deformation, a finer step size is recommended.

3 Applications in Earth Sciences

Although EBSD had emerged as a useful technique back in the 1970s, it was not until the 1990s when geologists started utilizing it. A common and useful technique before the EBSD era was fitting a universal-stage (*U*-stage) attachment in the transmitted light microscope, the data processing of which used a FORTRAN-based program (Mainprice 1990) at the later times. A number of pioneering work unraveled the deformation mechanisms and CPOs of quartz from various tectonic settings (Schmid et al. 1986). Although *U*-stage measurements for quartz are easier to obtain, the presence of strong undulose extinctions in the crystals can distort the results, and hence, necessary precautions must be taken beforehand. Moreover, it can only measure *c*-axis orientations, which are sufficient in most of the cases but not always (Passchier and Trouw 2005). Automated microscopic fabric analyser (MiFA) is also another useful instrument, which measures the orientation of the *c*-axis of the crystals; limited again for uniaxial minerals (Wilson et al. 2007). Geologists also used few other instruments in order to determine the crystallographic orientations, including *X*-ray goniometry (Schmid et al. 1986) and computer-integrated polarization microscopy (CIP) (Heilbronner and Tullis 2006). Even though, the outcomes from the methods are well comparable with each other, but have certain advantages and disadvantages.

The SEM-based EBSD remains the most widely used method to extract crystallographic information from the minerals to date. In comparison with the other techniques, listed above, the advantages include higher spatial and angular resolution, ability to determine the complete CPO including Dauphine twins and faster speed of data acquisition (Peternell et al. 2010). There has been a surge in EBSD-centric articles since the late 1990s (Prior et al. 2009), and these works were not restricted only to quartz. The results discussed CPOs of important earth forming minerals, such as feldspar (Prior and Wheeler 1999), olivine (Zhang et al. 2000), garnet (Mainprice et al. 2004), pyroxene (Tommasi et al. 2006), mica (Abdullah et al. 2020; Lloyd et al. 2009), calcite (Barnhoorn et al. 2004), amphibole group of minerals (Abdullah et al. 2020; Ko and Jung 2015), and chromite (Ghosh et al. 2017). EBSD, along with numerical modeling, simulations, and deformation experiments at elevated pressure and temperature, has significantly improved our understanding of the physical processes and deformation mechanisms prevailing in the Earth's interior.

The EBSD technique is primarily used by structural geologists and solid earth geophysicists to infer the (i) deformation mechanism and slip system (Passchier and Trouw 2005), (ii) deformation temperature (Law 2014), (iii) shear kinematics (Passchier and Trouw 2005), and (iv) kinematic vorticity number (Xypolias 2010), to name a few. Crystallographic vorticity axis (CVA) analysis (Michels et al. 2015) and seismic anisotropic studies (Almqvist and Mainprice 2017) are some of the recent applications of EBSD in geosciences. Moreover, if the EBSD data is integrated with *X*-ray energy dispersive spectroscopy (XEDS), the phases present in the sample can also be differentiated based on their chemical composition. In the following sections, we discuss some of the applications of EBSD in geosciences.

3.1 Deformation Sense, Mechanism, and Temperature

When rocks undergo plastic deformation, the lattices of the constituent grains are distorted and their corresponding crystallographic axes tend to align themselves in accordance to the deforming forces. This is called crystallographic preferred orientation or CPO (Schmid et al. 1986). The obliquity of the central girdle of the mineral CPO (particularly quartz) plots on the pole figures has been widely used to infer the sense of shear (Fig. 5, Passchier and Trouw (2005)). Moreover, this also provides a qualitative estimate about the amount of non-coaxiality. The CPO fabric skeleton reflects the active slip system, which in turn depends upon the temperature at which those grains deformed (Fig. 6, Passchier and Trouw (2005)). The opening angle (*OA*, in degrees) of the quartz CPO fabric (Hunter et al. 2018) also varies with temperature, and thus acts as a proxy for the same (Law 2014). Also, (Faleiros et al. 2016) reported two mathematical equations depicting the relationship between the opening angle and the deformation temperature (*T*):

$$T(^{\circ}\mathrm{C}) = 6.9 \times OA + 48 (OA \leq 87^{\circ}) \quad (1)$$

$$T(^{\circ}\mathrm{C}) = 4.6 \times OA + 258 (OA \geq 87^{\circ}) \quad (2)$$

3.2 Kinematic Vorticity Number

Understanding the kinematics of deformation is crucial to decipher the geodynamic evolution of a terrain. Natural deformations are never perfectly coaxial or non-coaxial, but

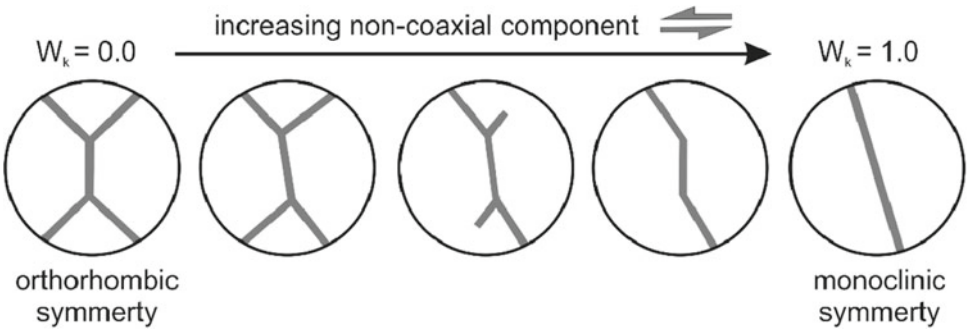

Fig. 5 Schematic illustration showing the variation in quartz CPO fabric skeleton with increasing simple shear component of deformation. Shear sense: sinistral. Modified after Fig. 1c of (Hunter et al. 2018). W_k = Kinematic vorticity number

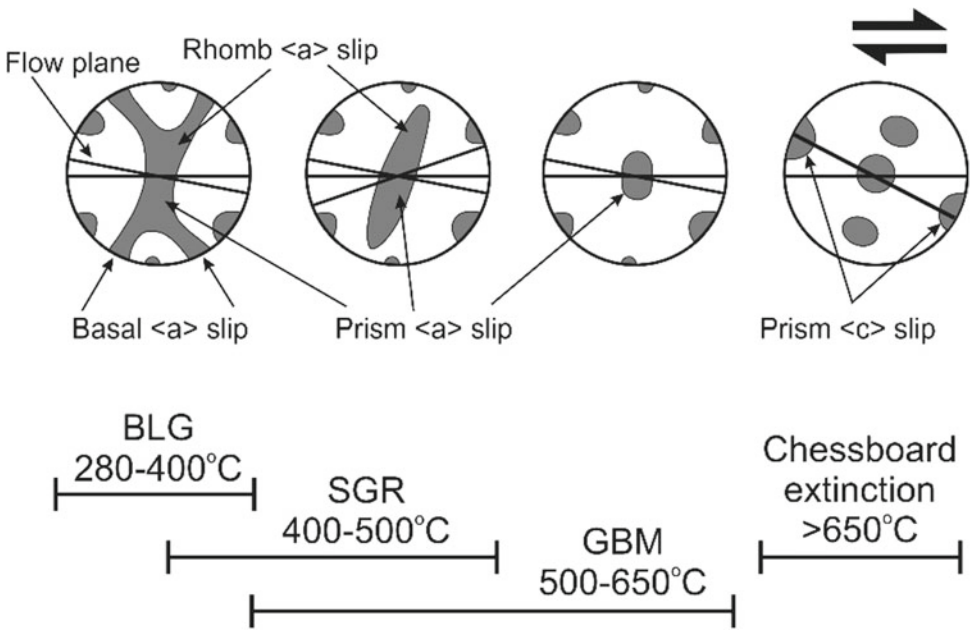

Fig. 6 Temperature dependency of quartz CPO fabric. Reproduced from Passchier and Trouw (2005). BLG: Bulging recrystallization, SGR: Sub-grain rotation, GBM: Grain boundary migration

are combinations of the two aforementioned extremities. The proportion of each component is quantified by the kinematic vorticity number (KVN or W_k), and the number may vary within a single terrain or shear zone (Tikoff and Fossen 1995). Over the years, several techniques have been reported to derive the KVN (Xypolias 2010). EBSD-derived quartz petrofabric data is also useful in this regard and has been utilized by several geologists (Xypolias 2010). This technique is also known as the R_{XZ}/δ method, wherein R_{XZ} is the strain ration and δ is the angle between the foliation and the perpendicular to the central girdle in the quartz CPO (Fig. 7).

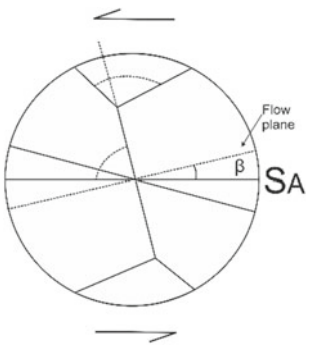

Fig. 7 Schematic illustration of a CPO fabric with the foliation (SA) and the angle β. The dotted line marks the perpendicular to the central girdle. Adopted after (Sarkarinejad et al. 2010)

3.3 Crystallographic Vorticity Axis Analysis

Plastic deformation rotates minerals with respect to an axis called the bulk vorticity axis (BVA). Consequently, all the intragranular crystallographic axes get reoriented such that they lie along a girdle in a stereoplot. The pole to the girdle denotes the vorticity axis for that particular grain. Michels et al. (2015) utilized this concept and applied rotational statistics on a deformed grain population to deduce the orientation of BVA from EBSD-based petrofabric data. The

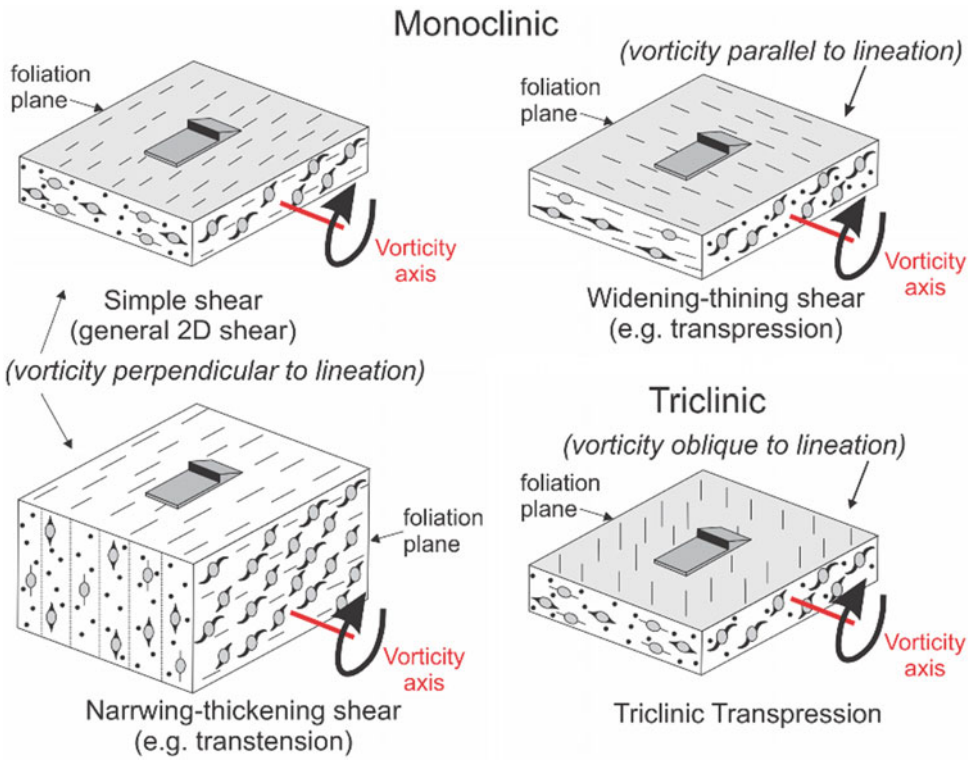

Fig. 8 Schematic figure illustrating types of kinematic flows and the angular relationships between the meso-fabrics to the vorticity axes. Reproduced from fig. DR1 of (Michels et al. 2015)

outcome when compared with the meso-fabric (e.g., lineation and foliation) orientations helps to comment on the symmetry (monoclinic or triclinic, Fig. 8) nature of deformation (transpressional or transtensional; Díaz-Azpiroz et al. (2019)). Once the orientation of the BVA is estimated, one can derive the same for the vorticity normal section (VNS) that is normal to the BVA. The VNS may not be parallel to the lineation (Díaz-Azpiroz et al. 2019) and is the most appropriate section to determine the kinematics of the deformation (Passchier and Trouw 2005).

3.4 Seismic Anisotropic Studies

While the heterogeneity is a crucial factor in controlling the subsurface dynamics, mechanical, thermal, and seismic anisotropy play significant role to manifest the deep-earth mechanisms at surface. Anisotropy in rocks results from a regular arrangement of atomic bonds in a crystal or, at a larger scale, the repetition of layers of rocks with different compositions or structures and varying elastic properties (Mainprice 1990). Though elastic anisotropy develops at crystal scale, its affects can pass on to larger scales when the anisotropic objects are arranged in a systematic way. Anisotropy of physical properties is a 2nd rank tensor and changes the characteristic strain fields produced by an applied stress, since some directions are easier to deform than others. It may therefore localize strain, the mechanism that initiates plate tectonics (Bercovici 2003). The term 'seismic anisotropy' refers to the directional variation in seismic velocities, which in turn depend on the elastic properties of the crystals (Almqvist and Mainprice 2017). Deformation-induced preferred alignment of crystallographic axes is considered to be one of the reasons for such elastic anisotropies, which could also be imparted due to the presence of melt networks, fractures, or variations in chemical compositions (Almqvist and Mainprice 2017; Almqvist et al. 2015). Fouch and Rondenay (2006) reported the upper crust to be seismically anisotropic. However, previously (Hirn et al. 1987) had advocated the opposite.

The effect of crystallographic arrangement on the velocity was noted in the 1940s. However, it was the work of Hess (1964), where the shear-induced olivine CPO was reported to be the cause of seismic anisotropy in the upper mantle. Since 1970s, several research works have been published on predicting seismic properties from the CPO data (Peselnick et al. 1974; Mainprice 2007). The FORTRAN script in Mainprice (1990) is one of the most widely used codes to deduce seismic anisotropies and plot the pole figures. Recently, these codes have been rewritten in the MATLAB programming language and included into the MTEX toolbox package. Although majority of the seismic anisotropic studies have been carried out on olivine CPOs from peridotites and serpentinites (Ben Ismail , Mainprice 1998), interests in subduction zone geodynamics have led geoscientists to study seismic properties of exhumed eclogites too (Mainprice et al. 2004; Abdullah et al. 2020; Almqvist et al. 2015).

4 Future Directions

Future research with the EBSD data may include comparative studies of the seismic properties derived from the petrofabric data obtained through the field geophysical measurements, ultrasonic laboratory experiments of the rock samples, and/or well-logs. Techniques to identify vorticity normal sections (VNS) from oriented drill cores have also been developed recently (Blenkinsop et al. 2015). We believe this could further help in deriving elastic properties from the same core using different techniques.

Moreover, the applications of machine learning (ML) and artificial neural network could also be implemented on EBSD data. A few very recent works showed that material scientists have embarked on that journey already (Kaufmann et al. 2020a, b). Furthermore, the link between petrofabric data and deformation could also be evaluated and approached utilizing ML techniques that would include training the algorithm using published database. These algorithms could then serve to predict outcomes from future data sets.

5 Summary and Conclusions

The article briefly reviews the working principles of the EBSD technique and its major applications in Earth Sciences. The EBSD technique had developed back in the 1970s, but geoscientists started to implement the method since 1990s onwards. *U*-stage, MiFA, X-ray goniometry, CIP were some of the instruments extensively used in the pre-EBSD era. Kikuchi patterns are the primary outcome of the EBSD method when BSEs interact with the detector/phosphor screen. Hough's algorithm is the key fundamental transformation used for extracting the indexing information of crystals from the Kikuchi patterns. During the reconstruction phase, different case-specific protocols are followed to eliminate the background noise. The major challenges encountered during post-processing of the EBSD data are the misindexing- and nonindexing-induced errors. The post-processing is performed using commercially available software packages; however, numerous researchers are now using the open-source MTEX toolbox that can be run on the MATLAB platform.

Deformation temperatures can be estimated from the opening angles derived from the pole figures and also by identifying the slip systems from inverse pole figures. The obliquity of CPO skeleton to the foliation can be utilized to infer the shear sense and calculate the KVN. Recently devised CVA analysis can help in estimating the orientation of the bulk vorticity axis from the EBSD-derived petrofabric data. Anisotropy in seismic velocities in the crust and upper mantle is primarily controlled by the elastic properties of the constituent material phases, and significant breakthroughs were established by assessing olivine CPOs from peridotites and serpentinites specimens. Future research in this field may incorporate the applications of machine learning, big data analytics, and artificial neural networks for faster processing of data and better accuracy of the results.

Acknowledgements The authors thank the editors for an invitation to write this article. The financial supports from SERB (ECR/2016/001988) and DST Swarnajayanti Fellowship (DST/SJF/E&ASA-01/2015-16) are greatly acknowledged.

References

Abdullah S, Misra S, Sarvesha R, Ghosh B (2020) Resurfacing of deeply buried oceanic crust in Naga Hills Ophiolite, North-East India: petrofabric, microstructure and seismic properties. J Struct Geol 139. https://doi.org/10.1016/j.jsg.2020.104141

Alam MN, Blackman M, Pashley DW (1954) High-angle Kikuchi patterns. Proc R Soc Lond Ser Math Phys Sci 221:224–242. https://doi.org/10.1098/rspa.1954.0017

Almqvist BS, Mainprice D (2017) Seismic properties and anisotropy of the continental crust: predictions based on mineral texture and rock microstructure. Rev Geophys 55:367–433. https://doi.org/10.1002/2016RG000552

Almqvist BSG, Misra S, Klonowska I et al (2015) Ultrasonic velocity drops and anisotropy reduction in mica-schist analogues due to melting with implications for seismic imaging of continental crust. Earth Planet Sci Lett 425:24–33. https://doi.org/10.1016/j.epsl.2015.05.039

Bachmann F, Hielscher R, Schaeben H (2010) Texture analysis with MTEX – free and open source software toolbox. Solid State Phenom 160:63–68. https://doi.org/10.4028/www.scientific.net/SSP.160.63

Barnhoorn A, Bystricky M, Burlini L, Kunze K (2004) The role of recrystallisation on the deformation behaviour of calcite rocks: large strain torsion experiments on Carrara marble. J Struct Geol 26:885–903. https://doi.org/10.1016/j.jsg.2003.11.024

Ismail WB, Mainprice D (1998) An olivine fabric database: an overview of upper mantle fabrics and seismic anisotropy. Tectonophysics 296:145–157. https://doi.org/10.1016/S0040-1951(98)00141-3

Bercovici D (2003) The generation of plate tectonics from mantle convection. Earth Planet Sci Lett 205:107–121. https://doi.org/10.1016/S0012-821X(02)01009-9

Blenkinsop T, Doyle M, Nugus M (2015) A unified approach to measuring structures in orientated drill core. In: Richards FL, Richardson NJ, Rippington SJ et al (eds) Industrial structural geology: principles. Geological Society of London, Techniques and Integration, pp 99–108

Boland JN, Tullis TE (1986) Deformation behavior of wet and dry clinopyroxenite in the brittle to ductile transition region. In: Hobbs BE, Heard HC (eds) Geophysical monograph series. American Geophysical Union, Washington, D. C., pp 35–49

Bunge HJ (1981) Fabric analysis by orientation distribution functions. Tectonophysics 78:1–21. https://doi.org/10.1016/0040-1951(81)90003-2

Cao Y, Jung H, Song S (2013) Petro-fabrics and seismic properties of blueschist and eclogite in the North Qilian suture zone, NW China: implications for the low-velocity upper layer in subducting slab, trench-parallel seismic anisotropy, and eclogite detectability in the subduction. J Geophys Res Solid Earth 118:3037–3058. https://doi.org/10.1002/jgrb.50212

Díaz-Azpiroz M, Fernández C, Czeck DM (2019) Are we studying deformed rocks in the right sections? best practices in the kinematic analysis of 3D deformation zones. J Struct Geol 125:218–225. https://doi.org/10.1016/j.jsg.2018.03.005

Faleiros FM, Moraes R, Pavan M, Campanha GAC (2016) A new empirical calibration of the quartz c-axis fabric opening-angle deformation thermometer. Tectonophysics 671:173–182. https://doi.org/10.1016/j.tecto.2016.01.014

Fossen H (2016) Structural geology, 2nd edn. Cambridge University Press, Cambridge, United Kingdom

Fouch MJ, Rondenay S (2006) Seismic anisotropy beneath stable continental interiors. Phys Earth Planet Inter 158:292–320. https://doi.org/10.1016/j.pepi.2006.03.024

Ghosh B, Morishita T, Ray J et al (2017) A new occurrence of titanian (hydro) andradite from the Nagaland ophiolite, India: Implications for element mobility in hydrothermal environments. Chem Geol 457:47–60. https://doi.org/10.1016/j.chemgeo.2017.03.012

Halfpenny A, Prior DJ, Wheeler J (2006) Analysis of dynamic recrystallization and nucleation in a quartzite mylonite. Tectonophysics 427:3–14. https://doi.org/10.1016/j.tecto.2006.05.016

Heilbronner R, Tullis J (2006) Evolution of c axis pole figures and grain size during dynamic recrystallization: results from experimentally sheared quartzite. J Geophys Res 111:B10202. https://doi.org/10.1029/2005JB004194

Hess HH (1964) Seismic anisotropy of the uppermost mantle under oceans. Nature 203:629–631

Hirn A, Damotte B, Torreilles G, Party ES (1987) Crustal reflection seismics: the contributions of oblique, low frequency and shear wave illuminations. Geophys J Int 89:287–296. https://doi.org/10.1111/j.1365-246X.1987.tb04421.x

Hough PVC (1962) Method and means for recognizing complex patterns

Hunter NJR, Weinberg RF, Wilson CJL, Law RD (2018) A new technique for quantifying symmetry and opening angles in quartz c-axis pole figures: implications for interpreting the kinematic and thermal properties of rocks. J Struct Geol 112:1–6. https://doi.org/10.1016/j.jsg.2018.04.006

Karato S, Jung H, Katayama I, Skemer P (2008) Geodynamic significance of seismic anisotropy of the upper mantle: new insights from laboratory studies. Annu Rev Earth Planet Sci 36:59–95. https://doi.org/10.1146/annurev.earth.36.031207.124120

Kaufmann K, Maryanovsky D, Mellor WM et al (2020a) Discovery of high-entropy ceramics via machine learning. Npj Comput Mater 6:1–9. https://doi.org/10.1038/s41524-020-0317-6

Kaufmann K, Zhu C, Rosengarten AS et al (2020b) Crystal symmetry determination in electron diffraction using machine learning. Science 367:564–568. https://doi.org/10.1126/science.aay3062

Ko B, Jung H (2015) Crystal preferred orientation of an amphibole experimentally deformed by simple shear. Nat Commun 6:6586. https://doi.org/10.1038/ncomms7586

Koll L, Tsipouridis P, Werner EA (2011) Preparation of metallic samples for electron backscatter diffraction and its influence on measured misorientation. J Microsc 243:206–219. https://doi.org/10.1111/j.1365-2818.2011.03495.x

Law RD (2014) Deformation thermometry based on quartz c-axis fabrics and recrystallization microstructures: a review. J Struct Geol 66:129–161. https://doi.org/10.1016/j.jsg.2014.05.023

Lloyd GE, Butler RWH, Casey M, Mainprice D (2009) Mica, deformation fabrics and the seismic properties of the continental crust. Earth Planet Sci Lett 288:320–328. https://doi.org/10.1016/j.epsl.2009.09.035

Loretto MH (2012) Electron beam analysis of materials. Springer Science & Business Media

Mainprice D (1990) A FORTRAN program to calculate seismic anisotropy from the lattice preferred orientation of minerals. Comput Geosci 16:385–393. https://doi.org/10.1016/0098-3004(90)90072-2

Mainprice D (2007) Seismic anisotropy of the deep earth from a mineral and rock physics perspective. In: Vol 2: Mineral Physics. Elsevier, pp 437–491

Mainprice D, Bascou J, Cordier P, Tommasi A (2004) Crystal preferred orientations of garnet: comparison between numerical simulations and electron back-scattered diffraction (EBSD) measurements in naturally deformed eclogites. J Struct Geol 26:2089–2102. https://doi.org/10.1016/j.jsg.2004.04.008

Mainprice D, Hielscher R, Schaeben H (2011) Calculating anisotropic physical properties from texture data using the MTEX open-source package. In: Prior DJ, Rutter EH, Tatham DJ (eds) Deformation mechanisms, rheology and tectonics: microstructures. Geological Society of London, Mechanics and Anisotropy, pp 175–192

Maitland T, Sitzman S (2006) Backscattering Detector and EBSD in Nanomaterials Characterization. In: Zhou W, Wang ZL (eds) Scanning microscopy for nanotechnology. Springer, New York, New York, NY, pp 41–75

Michels ZD, Kruckenberg SC, Davis JR, Tikoff B (2015) Determining vorticity axes from grain-scale dispersion of crystallographic orientations. Geology 43:803–806. https://doi.org/10.1130/G36868.1

Nishikawa S, Kikuchi S (1928) Diffraction of cathode rays by Calcite. Nature 122:726–726. https://doi.org/10.1038/122726a0

Passchier CW, Trouw RAJ (2005) Microtectonics, 2nd edn. Springer, Berlin, Heidelberg

Peselnick L, Nicolas A, Stevenson PR (1974) Velocity anisotropy in a mantle peridotite from the Ivrea Zone: application to upper mantle anisotropy. J Geophys Res 79:1175–1182. https://doi.org/10.1029/JB079i008p01175

Peternell M, Bitencourt MdeF, Kruhl JH, Stäb C (2010) Macro and microstructures as indicators of the development of syntectonic granitoids and host rocks in the Camboriú region, Santa Catarina, Brazil. J South Am Earth Sci 29:738–750. https://doi.org/10.1016/j.jsames.2009.11.006

Prior DJ, Wheeler J (1999) Feldspar fabrics in a greenschist facies albite-rich mylonite from electron backscatter diffraction. Tectonophysics 303:29–49. https://doi.org/10.1016/S0040-1951(98)00257-1

Prior DJ, Boyle AP, Brenker F, Cheadle MC, Day A, Lopez G, Peruzzi L, Potts G, Reddy S, Spiess R, Timms NE, Trimby P, Wheeler J, Zetterstrom L (1999) The application of electron backscatter diffraction and orientation contrast imaging in the SEM to textural problems in rocks. Am. Mineral. 84(11–12):1741–1759. https://doi.org/10.2138/am-1999-11-1204

Prior DJ, Mariani E, Wheeler J (2009) EBSD in the earth sciences: applications, common practice, and challenges. In: Schwartz AJ, Kumar M, Adams BL, Field DP (eds) Electron backscatter diffraction in materials science. Springer, pp 345–360

Sarkarinejad K, Samani B, Faghih A et al (2010) Implications of strain and vorticity of flow analyses to interpret the kinematics of an oblique convergence event (Zagros Mountains, Iran). J Asian Earth Sci 38:34–43. https://doi.org/10.1016/j.jseaes.2009.12.015

Schmid SM, Casey M (1986) Complete fabric analysis of some commonly observed quartz C-axis patterns. In: Hobbs BE, Heard HC (eds) Geophysical monograph series. American Geophysical Union, Washington, D. C., pp 263–286

Schwarzer RA, Field DP, Adams BL, et al (2009) Present state of electron backscatter diffraction and prospective developments. In: Schwartz AJ, Kumar M, Adams BL, Field DP (eds) Electron backscatter diffraction in materials science. Springer, pp 1–20

Tikoff B, Fossen H (1995) The limitations of three-dimensional kinematic vorticity analysis. J Struct Geol 17:1771–1784. https://doi.org/10.1016/0191-8141(95)00069-P

Tommasi A, Vauchez A, Godard M, Belley F (2006) Deformation and melt transport in a highly depleted peridotite massif from the Canadian Cordillera: implications to seismic anisotropy above subduction zones. Earth Planet Sci Lett 252:245–259. https://doi.org/10.1016/j.epsl.2006.09.042

Venables JA, Harland CJ (1973) Electron back-scattering patterns—a new technique for obtaining crystallographic information in the scanning electron microscope. Philos Mag J Theor Exp Appl Phys 27:1193–1200. https://doi.org/10.1080/14786437308225827

Vernon RH (2018) A practical guide to rock microstructure, 2nd edn. Cambridge University Press, Cambridge, United Kingdom

Wilson CJL, Russell-Head DS, Kunze K, Viola G (2007) The analysis of quartz c-axis fabrics using a modified optical microscope. J Microsc 227:30–41. https://doi.org/10.1111/j.1365-2818.2007.01784.x

Xypolias P (2010) Vorticity analysis in shear zones: A review of methods and applications. J Struct Geol 32:2072–2092. https://doi.org/10.1016/j.jsg.2010.08.009

Zhang S, Karato S, Gerald JF et al (2000) Simple shear deformation of olivine aggregates. Tectonophysics 316:133–152. https://doi.org/10.1016/S0040-1951(99)00229-2

Zhang J, Greenii H, Bozhilov K (2006) Rheology of omphacite at high temperature and pressure and significance of its lattice preferred orientations. Earth Planet Sci Lett 246:432–443. https://doi.org/10.1016/j.epsl.2006.04.006

Electron Probe Micro-Analyzer: An Equipment for Accurate and Precise Micro-Composition Analysis

Kaustubh N. Kulkarni, Aparna Tripathi, Abhinav Varshney, Jyoti Chandra, Siva Kumar, Sandeep Sangal, Debajyoti Paul, and Kallol Mondal

1 Introduction

An electron microscope is probably the most versatile characterization equipment that a materials scientist is blessed with. The generation of several different types of signals from the interactions of the primary electron beam with the sample gives access to analysis of multitude of the sample characteristics. Two most important of them are the topographical imaging and the micro-composition analysis; the latter being the topic of focus here. An electron probe micro-analyzer (EPMA) is essentially an electron microscope dedicated mainly for micro-compositional analysis, and it is equipped with certain additional features to serve this purpose. Examples of such additional features are the multiple channels for separating and counting specifically chosen characteristic X-rays, and an electron beam optics designed to give much higher beam stability and beam currents than usually available with typical electron microscopes. Depending upon the way X-ray signals are analyzed, micro-compositional analysis can be classified into two types, namely energy dispersive spectroscopy (EDS) and wavelength dispersive spectroscopy (WDS). In the former, the characteristic X-rays generated from the sample are collected all together, and their counts are recorded based on their energies. In the latter, user-selected characteristic X-rays are collected and counted; all other X-rays are filtered out as they are made incident on a pre-set Bragg diffractor. Thus, WDS is a batch-processing technique that analyzes desired X-ray wavelengths one by one. Although most EPMAs can be fitted with an EDS detector, the EPMA is meant primarily for WDS. Hence, in this article, we will focus on WDS, with EDS being discussed elsewhere in this book.

EPMA is probably the most accurate and precise tool for micro-composition analysis. However, the user needs to be aware of the right procedures of operation and data analysis in order to fetch the desired accuracy from the tool. This combined with inherent slow nature of the batch processing of X-rays often leads to long analysis times. Hence, EPMA often remains an under-utilized instrument despite of its unmatched accuracy and precision as well as its potential of usage in diverse applications. Hence, the main objective of this article is to introduce EPMA to a general materials researcher interested in accurate and precise compositional analysis on microscale. In order to keep it simple, to serve this purpose, detailed review of various concepts is intentionally avoided, and the stress is given more on explaining in simple language the important technical aspects of WDS analysis including the way various corrections are applied to the raw intensity data collected from the instrument.

The article starts with a brief history of EPMA followed by a discussion of its working principle. This is followed by a very short description of construction of EPMA. The various corrections applied to the raw data collected and their application procedures are then explained in some details. At the end, several case studies are discussed based on the state-of-the art research published from IIT Kanpur that essentially involved major usage of EPMA. It is expected that this discussion along with the various case studies will encourage many more researchers to find applications of EPMA in their research.

K. N. Kulkarni (✉) · A. Tripathi · A. Varshney · S. Sangal · K. Mondal
Department of Materials Science and Engineering, IIT Kanpur, Kanpur, India
e-mail: kkaustub@iitk.ac.in

A. Varshney
Department of Mechanical Engineering, Maulana Azad National Institute of Technology, Bhopal, 462003, India

J. Chandra
CSIR—National Geophysical Research Institute, Hyderabad, Telangana 500 007, India

J. Chandra · D. Paul
Department of Earth Sciences, IIT Kanpur, Kanpur, India

S. Kumar
Advanced Center for Materials Sciences, IIT Kanpur, Kanpur, India

K. Biswas et al. (eds.), *Electron Microscopy in Science and Engineering*, IITK Directions 6,
https://doi.org/10.1007/978-981-16-5101-4_6

2 A Brief History of EPMA

The first instrument making use of electron probe for compositional analysis was reported by Hillier and Baker in 1944 (Hillier and Baker 1944). In their instrument, they measured the energy lost by the primary electrons due to inelastic collisions with the atoms of the specimen being analyzed. The energy lost was correlated with the characteristic X-rays of the elements present. The first EPMA based on the analysis of characteristic X-rays generated due to collisions of primary electrons with sample atoms is credited to Raymond Castaing who developed this equipment as a part of his Ph.D. thesis (Castaing 1952). Castaing and Guinier first presented the concept of EPMA in an Electron Microscopy conference held in Delft in 1949 (Cosslet 1948). In 1953, they presented the first application of EPMA by point-by-point analysis of the diffusion profiles between copper and zinc (Caistaing and Guinier 1953). Castaing also established the approximation of proportionality between the intensity of characteristic X-rays emitted by an element and its concentration in the alloy sample after accounting for the matrix effects. CAMECA manufactured the first commercial EPMA prototype in the year 1956. Several manufacturers later came up, but currently, to the authors' knowledge, there are only two other commercial manufacturers of EPMA in addition to CAMECA, viz. JEOL and Shimadzu. Improvement in technology and analytical framework has been going on since then. Detection limits are continuously being improved due to higher probe currents (up to $10\mu A$), counting times, and larger surface of the analyzing crystal along with better background correction strategies. With more upcoming challenges, developments in EPMA will continue in coming years as well.

3 Working Principle of EPMA

When an electron beam irradiates a sample, a variety of signals are generated, some of which are characteristic X-rays, secondary electrons, backscattered electrons, and cathodoluminescence. These signals can be used to characterize the sample in terms of its composition and microstructure. The electron from the primary beam (incident beam) interacting inelastically with the sample can knock off an electron from the inner most orbitals of a sample atom resulting in its ionization. The unstable atom can return back to the ground state only after an electron from an outer shell falls into the inner shell, releasing the energy in the form of a characteristic X-ray photon. This energy is the difference between the energy levels of the two orbitals involved and is unique to an element. This characteristic X-ray photon can be used to identify the element present in an unknown sample. Energy and wavelength of the characteristic X-rays are related by

$$\lambda = \frac{12.3985}{E} \tag{1}$$

where λ is in Angstrom, and the energy E has the unit of keV. The X-ray generated due to falling of an electron from L-shell to K-shell is denoted as K_α whereas that due to transition of an electron from M-shell to K-shell is denoted as K_β. Similarly, falling of an electron from M-shell to L-shell gives rise to an L_α and from N-shell to L-shell gives rise to an L_β X-ray. Transition from N-shell to M-shell would generate an M_α X-ray and so on.

An EPMA is equipped with multiple spectrometers each of which can be preset to collect the desired wavelengths of X-rays and record their intensities. The X-rays are emitted from the sample in all the directions. Only small fraction of X-rays with a certain take-off angle can enter a given WDS spectrometer for detection. For WDS analysis, all the X-ray wavelengths other than the selected one should be filtered out before reaching the detector. For this purpose, each spectrometer channel can have one or more analyzing crystals, called Bragg diffractors or reflectors, each with a particular interplanar spacing d. At a given angle of incidence θ, a crystal will diffract X-rays of a specific wavelength when Bragg's law of diffraction is satisfied:

$$n\lambda = 2d \sin\theta \tag{2}$$

In order to reflect the sufficient intensity of the X-rays onto the detector, area of the specimen under observation, the reflector, and the detector (proportional counter) all should lie on one circle of a fixed radius called Rowland circle. Since sample remains fixed in its position, motion of the remaining two components, the reflector and the detector, should be synchronized so as to focus the desired wavelength onto the detector by satisfying the Bragg's law, Eq. (2). A typical arrangement of the reflector and the detector with respect to the stationary source (i.e., the sample here), called Johannsson geometry, is schematically illustrated in Fig. 1. Each crystal in a spectrometer channel moves on a linear trajectory inside the channel (shown by the blue dashed line in Fig. 1) and at the same time be tilted by certain angle so that θ can acquire a range of values and the crystal can diffract a range of wavelengths. This is the reason why in usual EPMA communications, the specific X-rays to be detected with a given crystal are identified with a macro-linear dimension (on the linear trajectory of the reflector) rather than in the form of its wavelength in nm or energy in keV. Due to the predefined coordinated movements of the reflector and the detector, it is easy to convert these linear dimensions to the wavelength or energy by knowing the geometry of the particular spectrometer.

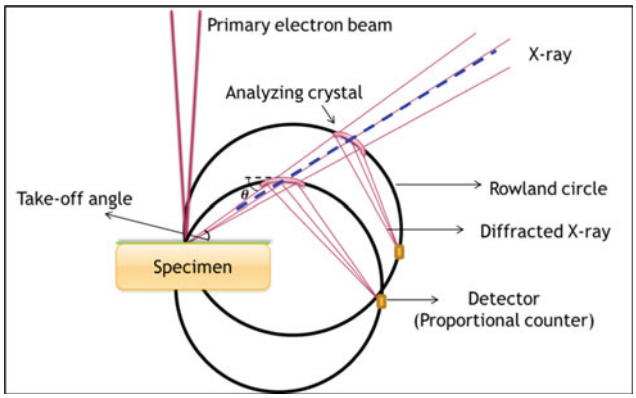

Fig. 1 Working principle of WDS spectrometer showing the observation field of the specimen, the reflecting crystal, and the detector lying on a common Rowland circle

The EPMAs typically give the options to represent the obtained WDS spectra in the form of intensity versus the linear dimension or, versus wavelength or energy.

Upon diffraction, the X-rays of the selected specific wavelength enter the detector, which is a proportional counter filled with either Xenon or Argon inert gas along with methane. The gas ionizes upon interacting with incident X-rays and releases photoelectrons. This signal is further sent to amplifiers and analog-to-digital converter for recording the X-ray intensity. Corrections for dead time and background have to be applied to the raw intensity data before further processing. Matrix corrections are applied to the X-ray counts using established algorithms, the basics of which are covered in a later section. Finally, the corrected intensities are converted to concentration of the element present in the unknown sample which is displayed on screen.

WDS has the capability to detect composition of elements present in trace amounts (as low as 100 ppm). Energy resolution (5 eV) is also better than that by EDS technique (about 100 eV). With reduced beam size, spatial resolution in an EPMA can reach below $1\mu m$.

4 Basic Construction

The basic functioning of an EPMA is similar to a scanning electron microscope (SEM) in that a focused high energy electron beam is bombarded onto the sample being studied and the various signals generated from the interactions of the electron beam with the samples are analyzed for imaging and micro-composition analysis. Hence, the EPMA and SEM share most of the components. However, since EPMA is primarily meant for WDS analysis of X-rays, multiple spectrometer channels are provided to serve this purpose. The main components of the EPMA thus include a source for primary electron beam, magnetic lenses for focusing and guiding the electron beam onto the sample, an optical microscope for accurate positioning of the sample, and the WDS spectrometers housing the Bragg reflectors and X-ray detectors.

4.1 Emission Source (Reed 2005; Akhtar et al. 2018)

W-filament, lanthanum hexaboride (LaB_6) or field emission gun (FEG) can be used as a source of primary electron beam. The first two emitters work on the principle of thermionic emission, in which the electron source is heated to a temperature that is high enough for the electrons to overcome work function of the material. FEG which is a tungsten rod with very sharp tip (<100 nm) does not require heating and is therefore referred to as cold cathode. Electrons are extracted by applying a high voltage of 3–5 kV near the tip. Due to nonthermal functioning, FEG guns have a longer lifetime (1–5 years) as compared to the other two sources. Moreover, much larger current density ($1,00,000A/cm^2$) or brightness can be obtained in FEG as compared to tungsten filament ($3A/cm^2$). This results in higher current in the same beam size or the same current at a smaller beam size (submicron) for FEG filament. Therefore, FEG gives increased spatial resolution and signal-to-noise ratio as compared to *W*-filament. FEG has a disadvantage of being very expensive as compared to LaB_6 or *W*-source. FEG also requires ultrahigh vacuum to prevent poisoning of cathode from trace elements in the chamber (10^{-10} torr). Vacuum requirement for LaB_6 is 10^{-7} torr while that for *W* is 10^{-5} torr. Other than cold cathode, FEG can be Schottky type which requires both heat and external electric fields to overcome the potential barrier. Long-term current stability of thermionic emitters is much better. For comparison, a *W*-based EPMA gives the beam current deviation of less than $\pm 0.05\%/hr$ and $\pm$ 0.3%/12 h, whereas Schottky-based FEG gives about $\pm$ 0.3%/hr and $\pm$ 1%/12 h [*from JEOL data for JXA-iSP100 and JXA-iSP200F*]. LaB_6 gives the beam stability performance that is in between the two. This is the reason why tungsten filaments are preferred source for microanalysis which essentially requires current to be stable for longer times rather than high image resolution. W-filament can also be heated and cooled quickly as compared to LaB_6 filament but at the cost of lower brightness and spatial resolution. FEG is more suited for low voltage applications providing low interaction volume at the same time ensuring good strength of the signal for EDS and WDS analysis. This has specific applications in studying thin films, multilayer assemblies, coatings, and small-sized inclusions (Rinaldi and Llovet 2015).

4.2 Column (Reed 2005; Akhtar et al. 2018)

The column in an EPMA consists of condenser lens, scanning coils, objective lens, apertures, and stigmator coils. Condenser lenses are electromagnetic lenses which converge the electron beam and align it along the optic axis. Current in the lens controls the probe diameter. Smaller the spot size better will be the spatial resolution of the sample. Scanning coils raster the beam on the sample for elemental mapping or imaging. Slow scanning results in a good signal-to-noise ratio and vice-versa. Current in the scanning coil controls the magnification of the image. Objective lenses are closest to the object and are used to focus probe on to the sample. Stigmator coils are used to correct the x and y deflection of the beam to produce beam with rounder shape and clearer image. Apertures are micron size holes in a metal disc which help in reducing the diameter of the beam and sample charging. Choice of aperture size depends completely on the requirement of the sample. The entire column is evacuated typically up to 10^{-5} torr if W-filament is used to avoid electron dispersion and cathode contamination.

4.3 EDS and WDS Spectrometer Channels

An EPMA usually has one to five WDS channels and can also be mounted with an EDS detector. Each WDS spectrometer channel houses one or more Bragg reflectors and a detector. All the channels are usually mounted symmetrically so that the take-off angle remains the same. Multiple wavelength dispersive spectrometers help in parallel analysis of many elements at a time and thus reduce the analysis time for multicomponent samples. For energy dispersive spectrometry, silicon drift detector (SDD) is used to count X-ray signals having an energy resolution of 120 eV, being very close to the theoretical limit. For WDS, gas proportional counter with P10 gas (a mixture of 10% methane and 90% argon) is used as a detector. Argon is ionization gas, while methane acts as a quenching gas to reduce the dead time of the counter. As compared to SDD, energy resolution is much higher in WDS (<10 eV) resulting in precise elemental identification.

The JEOL JXA 8230 EPMA at IIT Kanpur is equipped with one EDS and four WDS channels which facilitate quick as well as accurate compositional analysis. Each of the four spectrometers house two single crystals as given below:

1. Channel 1: LiFH and PETH
2. Channel 2: LDE2 and TAP
3. Channel 3: LiF and PETJ
4. Channel 4: LiF and PETJ.

This EPMA is based on W-gun that gives the highest beam stability and high beam currents (up to 10 μA) for better statistics. If higher resolution is desired, W can be replaced with LaB_6 but at the cost of slightly reduced beam stability and current.

4.4 Optical Microscope

As described in an earlier section, the sample, the reflector, and the detector should lie on a common Rowland circle. Since the spectrometer collects the X-rays at a fixed take-off angle, any slight change in the height of the sample may result into the sample being out of the circle and the subsequent loss of intensity. Hence, for precise and accurate measurement of concentrations, it is necessary to align the sample surface exactly with its position on the Rowland circle. An optical microscope (OM) is invariably used for this purpose due to its very narrow depth of field (less than 1 micron). OM is placed coaxially to the electron beam. The shallow depth of field of the OM helps in accurately aligning the height of the area under observation, and thus, OM is one of the most crucial components of an EPMA for ensuring accuracy and precision of the measurements.

5 WDS Analysis Methodology

The composition analysis with WDS by EPMA can be classified into two types, viz. qualitative analysis and quantitative analysis. Qualitative analysis, as the name suggests, deals with only the identification of elements present in a sample whose composition is unknown. The detectors scan the entire range of elements (in our case boron to uranium), and the elements present in the sample are identified based on the various peaks of characteristic X-ray energies collected by the detectors. Since the entire range of peaks has to be scanned, qualitative analysis usually takes a long time, but the advantage is that it does not miss any elements, which is due to high resolution of WDS. Qualitative analysis is frequently useful for geological samples and minerals.

In quantitative analysis, the composition of a sample is determined in terms of weight fractions of various elements present in the sample. Since WDS is a standard-based analysis technique, one has to a priory know all the elements present in the sample. For composition analysis of a completely unknown sample, i.e., in the absence of a complete knowledge of elements present in the sample, it has to be first subjected to qualitative analysis for identifying the various elements. Once the elements are identified, the

appropriate standards can be selected, and the quantitative analysis can be then carried out on the sample. It should be noted here that EPMA characterizes the elements based on their characteristic X-ray energies or wavelengths and hence, it is incapable of identifying the chemical states of the elements present. This is not an issue in the analysis of metals and alloys, in which it is typically required to know only the weight fractions of individual elements. In case of compounds, as usually encountered in minerals and geological samples, calibration and quantification are usually done based on the knowledge of the oxidation states of the elements or stoichiometry of the compound. EPMA is most frequently used for quantitative analysis. Hence, we will look into the details of the quantitative analysis using WDS.

5.1 Quantitative Analysis by WDS

As mentioned earlier, WDS analysis is a standard-based analysis. Hence, it is first necessary to perform calibration step, in which a reference sample with known concentration is analyzed for each of the elements present in the sample to be characterized. Let us call the sample whose composition has to be quantified as 'unknown sample'. A 'standard' is a sample that contains one or more elements present in the unknown sample and whose composition is already known. Each of the elements present in the unknown sample has to be calibrated with at least one standard. In the analysis of metals and alloys, pure elements are most commonly used as standards, whereas in the analysis of geological samples and minerals, pure compounds or their mixtures are used as standards.

The first step in the analysis is to decide upon the particular characteristic X-ray (K_α, L_α, M_α, etc.) that will be analyzed for each of the elements. The various factors that need to be considered during the selection of the X-ray line are energy of the particular X-ray, intensity of the X-rays desired, possible overlap with peaks of the other elements present in the unknown sample, the accelerating voltage to be used, and the range of scan available on the spectrometer to be used. Out of the five factors, the first three are fundamental in nature, whereas the latter two are more practical, dependent on the equipment being used. Although it is desirable to select K_α lines due to their large intensities, their energies for heavier elements maybe too high to be excited by the given accelerating voltage. A typical rule of thumb is that for using a particular X-ray, numerical value of its energy (in keV) has to be lower than half the accelerating voltage (in kV). Thus, for analyzing copper under 20 kV accelerating voltage, one can use Cu K_α radiation which has an energy of 8.046 keV. However, if the accelerating voltage has to be restricted to below 10 kV, for example, for enhancing the spatial resolution of the image, then one has to analyze Cu L_α with energy of 0.928 keV. Most EPMAs work with highest possible accelerating voltage of 30 kV, and hence, for heavy elements (Yttrium and beyond) one has to settle for L_α or lower energy X-rays. Lower intensities in such cases can be addressed with longer accumulation times to improve the statistics. During the calibration step, each of the standards is first subjected to excitation under fixed accelerating voltage and probe current for sufficient amount of time, and intensity of the desired X-ray from the standard sample (I_{Std}) is recorded in terms of counts per second. Then, the unknown sample is exposed to the same exciting conditions as the standard and the intensity of the desired X-rays collected from the unknown sample (I_{ukn}) are recorded. As per Castaing's first approximation (Castaing 1952), the ratio of the concentrations of an element in the unknown sample to that in the standard is taken as the ratio of intensities of the corresponding X-ray 'generated directly from the primary electrons' in the unknown sample to that in the standard. However, in reality, the intensities of 'collected' signals are modified due to various factors, and a correction coefficient has to be applied for each of these factors. The various corrections to be applied include background correction, atomic number correction (Z), absorption correction (A), and fluorescence correction (F). Of course, the measured intensities are corrected after taking into account the dead time during counting. If I_{Std} and I_{ukn} are the intensities of the X-ray in standard and unknown sample after applying respective background corrections, and if C_{Std} is the concentration (in weight fraction) of the element in the standard, then the concentration (wt. fraction) of the element in the unknown sample (C_{ukn}) is given by

$$C_{\text{ukn}} = C_{\text{Std}} \cdot \frac{I_{\text{ukn}}}{I_{\text{Std}}} \cdot Z \cdot A \cdot F \tag{3}$$

Z, A, and F are commonly referred to as 'matrix corrections' or ZAF corrections (Philibert and Tixier 1968) as they depend upon the type of matrix being analyzed. The various corrections applied to the collected raw intensities are briefly described in the following few sections.

5.1.1 Background Corrections

It is well known that production of any characteristic X-ray is also accompanied by production of a continuous spectrum of X-rays called as Bremsstrahlung. Although the intensity of the Bremsstrahlung is typically low, they do tend to increase the collected intensity of the desired characteristic X-ray, and hence, they add to the background noise. Moreover, the intensity of background is different in different samples including in standard and unknown samples. Hence, the background noise has to be subtracted from the obtained intensity of the characteristic X-ray, before it is

processed further. The background intensity is typically measured at a position, which is sufficiently away from the characteristic peak under consideration so that a part of the peak itself does not get counted in the background. It should be made sure that no other peak from other elements of the sample is at or in the vicinity of the background-collection position. If the background is continuously varying across the peak, the background collections are done at two positions, one lower than the peak position and the other higher than the peak position. The background count at the peak position is then taken as the mean of the two background counts. It is necessary to collect and apply background to standard and unknown samples individually.

5.1.2 Atomic Number Correction (Z)

The depth to which the primary electron beam can penetrate into the sample depends upon the occurrence of inelastic scattering events of the primary electrons as these events tend to slow down and eventually stop the electrons. The spatial distribution of the primary electrons will be guided by the elastic scattering events that tend to deflect the electrons without much loss in their energies. The total interaction volume of primary electrons in the sample depends upon the average atomic number of the sample and the accelerating voltage. The interaction volume in a lighter matrix is higher than that in a heavier one. For example, the interaction volume of the primary electrons in pure aluminum will be much higher than in an alloy of Cu-10 wt% Al. If we are analyzing concentration of aluminum with pure Al as standard, then the production of Al K_α X-rays in pure aluminum standard will be from much higher volume than in Cu-10 wt % Al. Hence, the obtained ratio of intensities of Al K_α in the unknown sample to that in the standard sample will be lesser than 0.1. Moreover, some of the primary electrons would be lost due to their backscattering and subsequent exit from the sample. The backscattering effect also depends upon the average atomic mass. Thus, the energy available for production of X-rays is different in the unknown sample than in the standard (Henrich 1991). Hence, a correction factor has to be applied to account for different interaction volumes and backscattering events in the standard and the unknown samples. This is called atomic number correction, denoted as *Z*.

Atomic number correction (Z_i) for an element *i* depends upon two aspects; first, the penetration of the electron into the matrix, which is basically governed by the stopping power (P_i) of the matrix and second, the backscattering of the electron (R_i). The parameters R_i and P_i further depend upon the composition of the alloy, over voltage ratio, i.e., the ratio of accelerating voltage (E_0) to *K*-shell excitation energy (E_K) of the element, average atomic number of the matrix, and the average atomic weight of the matrix. The *Z* correction for an element *i* can be given in terms of stopping power factor (P_i) and backscattering factor (R_i) as

$$Z_i = \frac{R_i^{\mathrm{Std}}}{R_i^{\mathrm{Unk}}} \times \frac{P_i^{\mathrm{Unk}}}{P_i^{\mathrm{Std}}} \tag{4}$$

Since only the energies within accelerating voltage (E_0) and the desired excitation energy (E_{Ki}) are of concern, only the ratio E_0/E_{Ki}, also known as overvoltage potential (U_i), is of significance in evaluating atomic number correction. An expression for the penetration factor (P_i) as derived by Love et al. (Love et al. 1978) for an *n*-component sample can be given as

$$P_i = \frac{1}{M}\left[1 + 16.05\left(\frac{J}{E_{Ki}}\right)^{1/2}\left(\frac{U_i^{1/2} - 1}{U_i - 1}\right)^{1.07}\right] \tag{5}$$

where *J* is the mean ionization potential of the sample, and *M* is evaluated as

$$M = \sum\nolimits_{j=1}^{n} \frac{C_j Z_j}{A_j} \tag{6}$$

J for an *n*-component system can be evaluated as

$$J = \frac{1}{M}\sum\nolimits_{j=1}^{n}\left(\frac{C_j Z_j}{A_j}\ln J_j\right) \tag{7}$$

The average ionization potential of a pure element *j* (J_j) is approximately proportional to the atomic number (Bloch 1933), and experimentally, a constant value for the ratio of *J*/*Z* of 11.5 eV has been obtained for aluminum (Wilson 1941). More accurate expression for J_j as proposed by Berger and Seltzer (Berger and Seltzer 1964) for $Z \geq 13$ is

$$J_j = 9.76Z_j + 58.8 \cdot Z_j^{-0.19} \tag{8}$$

The backscattering factor (*R*) is the fraction of ionization remaining in the target after accounting for loss due to backscattering of primary electrons. It is related to the backscatter coefficient (η) of the electron, which is the fraction of the incident electrons that are backscattered. If all backscattered electrons retain their original energy, then $R = 1-\eta$. However, the BS electrons possess a range of energies as they undergo some inelastic collisions on their way out. As shown by Duncumb and Reed (Duncumb and Reed 1968) based on the data on backscatter coefficients (η) reported by Bishop (Bishop 1967), the backscattering factor (*R*) can be expressed as a simple function of atomic number (*Z*) and overvoltage ratio ($U_i = E_0/E_{K(i)}$). Ducumb and Reed (Duncumb and Reed 1968) have tabulated the data for *R* as function of *Z* and $1/U_i$. In a multicomponent sample, the backscatter coefficient (R_{ji}) for a given X-ray *i* of energy $E_{K(i)}$ in a matrix *j* can be calculated simply by interpolation of

the data with an interpolation error of less than 0.2% (Duncumb and Reed 1968). One equation for R_{ji} obtained by least square method as given in the JEOL's user manual for JXA-8230 (JXA-8230) can be written as

$$\begin{aligned} R_{ji} = {} & 1 - X_j V_i \left[-0.187204 + 1.67366V_i - 1.51187V_i^2 + 0.707063V_i^3\right] \\ & + X_j\left(3.63547 - 1.9914V_i - 1.6539V_i^2 + 0.477246V_i^3\right) \\ & + X_j^2\left(-4.04514 - 4.11268V_i + 9.26509V_i^2 - 2.79199V_i^3\right) \\ & + X_j^3\left(1.54054 - 3.43134V_i - 5.22007V_i^2 - 1.23353V_i^3\right) \end{aligned} \tag{9}$$

where $X_j = Z_j/100$ and $V_i = 1 - 1/U_i$.

The total backscatter factor for i (R_i) in the sample is then evaluated as

$$R_i = \sum_{j=1}^{n} C_j R_{ji} \tag{10}$$

5.1.3 Absorption Correction (A)

X-ray emitted by an atom i in a sample maybe absorbed by another atom j whose absorption edge lies close to the wavelength of the characteristic X-ray of i that we are measuring. There will be continuous mass absorption of the X-ray signals as they are traveling through the sample, which depends upon the mass absorption coefficient (μ/ρ). The X-rays generated at lower depths are more likely to escape and reach the detector than those generated at higher depths. Also, the X-rays traveling at lower angles are less likely to escape than those traveling at higher angles. Thus, the intensity of the X-rays of i observed would be lower than those actually generated because of the absorption effects. Hence, a correction factor needs to be applied to correct for the signals of i lost due to the absorption, which is different in the sample than in the standard. In a multicomponent alloy, the absorption factor for i is most commonly evaluated based on simplified form of Philibert's formula (Philibert 1963), extended to multicomponent system as follows:

$$f_i = \frac{1 + h_i}{\left[1 + \frac{X_i}{\sigma_i}\right]\left\{1 + h_i\left(1 + \frac{X_i}{\sigma_i}\right)\right\}} \tag{11}$$

where h_i is the factor depending upon atomic number and atomic weight of i given by Philibert 1963

$$h_i = 1.2\frac{A_i}{(Z_i)^2} \tag{12}$$

X_i is the factor depending upon mass absorption coefficient for the wavelength being considered, and the take-off angle is given by

$$X_i = \left(\mu/\rho\right)^i_{\text{Specimen}} \operatorname{cosec}(\theta) \tag{13}$$

and for a multicomponent sample, X_i can be evaluated as (Private communication with JEOL EPMA experts 2019)

$$\left(\mu/\rho\right)^i_{\text{Specimen}} = \sum_j C_j \left(\mu/\rho\right)^i_j \tag{14}$$

and σ_i is Lenard's coefficient, which according to Heinrich and Yakowitz (Heinrich and Yakowitz 1975) can be given as

$$\sigma_i = \frac{4.5\text{x}10^5}{E_0^{1.65} - E_{Ki}^{1.65}} \tag{15}$$

Once the factors for standard (f_i^{Std}) and the unknown sample (f_i^{Ukn}) are known, the absorption correction factor for an element i in the sample is given by

$$A_i = \frac{f_i^{Std}}{f_i^{Ukn}} \tag{16}$$

5.1.4 Fluorescence Correction (F)

If the energy of a characteristic X-ray of an element j lies at an absorption edge of the element i, the later would fluoresce by the former. If the fluoresced X-ray is being measured, the apparent intensity would be higher than originally generated by direct excitation. The fluorescence factor for excitation of i by j is given by Reed (2005, 1965)

$$\gamma_{ij} = C_j \cdot J_i \cdot D_{ij} \cdot \frac{\left(\mu/\rho\right)^j_i}{\left(\mu/\rho\right)^j_{\text{Specimen}}} \cdot \left\{\frac{\ln\left(1 + u_{ij}\right)}{u_{ij}} + \frac{\ln\left(1 + v_{ij}\right)}{v_{ij}}\right\} \tag{17}$$

$$D_{ij} = \left(\frac{U_j - 1}{U_i - 1}\right)^{1.67} \tag{18}$$

$$u_{ij} = \frac{\left(\mu/\rho\right)^i_{\text{Specimen}}}{\left(\mu/\rho\right)^j_{\text{Specimen}}} \cdot \operatorname{cosec}(\theta) \tag{19}$$

$$v_{ij} = \frac{\sigma_i}{\left(\mu/\rho\right)^j_{\text{Specimen}}} \tag{20}$$

and J_i is the coefficient depending upon absorption edge jump ratio of i and the fluorescence yield of j. The values of J_i are tabulated by Reed (Reed 2005, 1965). The fluorescence correction factor is then given by

$$F_i = \frac{1 + \sum_j \gamma_{ij}^{STD}}{1 + \sum_k \gamma_{ik}^{Unk}} \tag{21}$$

5.1.5 Determination of ZAF Corrections

As can be seen from Eqs. (5), (10), (14), and (17), each of the correction factors Z_i, A_i, and F_i is dependent on all the elemental concentrations that we are trying to determine. Hence, the correction factors have to be determined by using iterative algorithms. First the raw intensity ratios (K'_{raw}) are determined for all the elements after correcting the intensities for background and dead time. As a first approximation, the concentration of each element is taken as normalized raw intensity ratio for that element:

$$K_i = \frac{K'_{raw,i}}{\sum_{j=1}^{n} K'_{raw,j}} = C_i \tag{22}$$

The concentrations C_i are then used for evaluating the three correction factors (Z_i, A_i, F_i) for each element. The new set of concentrations are then obtained by applying the ZAF correction factors based on Eq. (3). In the next iteration, the new concentrations are used to evaluate the set of (Z_i, A_i, F_i), and this process is repeated until all the concentrations converge.

5.1.6 Phi-Rho-Z Correction Method

Castaing in his original work (Castaing 1952) had suggested the expression for intensity of a characteristic X-ray of an element A generated in a sample as

$$I_A^{Unk} = \theta C_A \int_0^{\infty} \phi_s(\rho z)\exp\left(-\mu_S^A \cdot \rho z \cdot \text{cosec}\psi\right)\text{d}(\rho z) \tag{23}$$

where C_A is the concentration of A in the sample (in weight fraction), ρ is the density of the sample, z is the depth, μ_S^A is the mass absorption coefficient of the X-ray in the sample, ψ is the take-off angle, and θ is a constant depending upon instrumental parameters. ρz is commonly referred to as mass-depth parameter and the function $\phi_s(\rho z)$ is the 'ionization distribution' that gives the number of X-rays generated as a function of penetration of primary electron into the sample.

Similar expression can be written for intensity generated in a pure elemental standard, and since the constant θ is dependent on instrumental parameters, it cancels out upon taking the intensity ratios if the instrumental parameters are kept constant. Thus, the intensity ratio can be written as

$$K_A = C_A \frac{\int_0^{\infty} \phi_s(\rho z)\exp\left(-\mu_S^A \cdot \rho z \cdot \text{cosec}\psi\right)\text{d}\rho z}{\int_0^{\infty} \phi_A(\rho z)\exp\left(-\mu_A \cdot \rho z \cdot \text{cosec}\psi\right)\text{d}\rho z} \tag{24}$$

where $\phi_A(\rho z)$ is the ionization distribution function in pure A and μ_A is the mass absorption coefficient of the X-ray in pure A. The distribution function $\phi(\rho z)$ is usually determined by tracer method in which a thin layer of element A is sandwiched inside B at a depth z from the surface. $\phi(\rho z)$ for X-rays of A in B is then defined as "the intensity generated by the thin layer of A at the depth z, relative to that generated in an isolated layer of A of the same thickness" (Reed 2005). Packwood and Brown (Packwood and Brown 1982) showed that the $\phi(\rho z)$ function can be accurately modeled with a Gaussian type of function, which combined the atomic number and absorption correction in a single expression (Brown and Packwood 1982). Fluorescence corrections have to be calculated separately. Phi-Rho-Z correction method has been commonly used for analysis of light elements, silicates, and oxides.

5.1.7 Calibration Curve Method

Ziebold and Ogilvie (Ziebold and Ogilvie 1964) empirically observed that intensity ratio versus concentration plots for most binary systems can be fitted with the following relation:

$$\frac{1 - K_i}{K_i} = \alpha_{ij}\frac{1 - C_i}{C_i} \tag{25}$$

where, C_i is the concentration of i in mass fraction and K_i is the ratio of intensity of characteristic X-ray of i in the sample to that in pure i, after applying the background and dead time corrections. α_{ij} is the fitting constant for the relation for i in binary system i-j. They also proposed that this relation can be extended to multicomponent systems, in which case the fitting parameter for the relation (α_i) can be expressed as

$$\alpha_i = \frac{\sum_{j \neq i} \alpha_{ij} C_j}{\sum_{j \neq i} C_j} \tag{26}$$

Thus, for multicomponent systems, one needs to know the α_{ij} parameters for each of the binary pair i-j of the system.

The calibration curve method is especially useful while analyzing low concentrations of elements such as carbon in steels. For this, samples of known concentrations are analyzed in a small range typically encountered in the alloys. In such small concentration ranges, the intensity versus concentration can be simply related linearly as

$$I_i = A_i C_i + B_i \tag{27}$$

where I_i is the absolute intensity for i at a concentration C_i and A_i and B_i are fitting constants. Once the fitting constants are determined over a small concentration range of interest, any sample with C_i lying in the desired range can be determined by just determining the intensities and applying Eq. (27).

The main advantage of calibration curve method is that the application of the complicated ZAF corrections is not required separately.

6 Case Studies

Various case studies in which EPMA has been used as an essential characterization tool are presented in this section. Although the various cases presented here are taken from already published works from our research groups, the focus here is to bring out the relevance of EPMA studies in these research works. Solid–solid diffusion couples are often used in determining interdiffusion coefficients in multicomponent systems. In a diffusion couple, two alloys of different compositions are placed in contact with each other and isothermally annealed at the desired temperature for sufficient time to develop measurable concentration profiles in the diffusion zone. After diffusion annealing, the couple is quenched in order to retain the microstructure and concentration profiles developed at high temperature to room temperature. The quenched couple is then sectioned parallel to the diffusion direction and metallographically polished to observe the microstructure developed across the initial weld plane (the plane at which the two terminal alloys were in contact at the beginning). The concentration profiles developed in a single-phase diffusion couple (the couple having the same phase in the diffusion zone as well as in the two terminal alloys with no phase interface) are further analyzed for obtaining interdiffusion coefficients. Thus, accurate and precise measurements of the concentration profiles are key in determination of interdiffusion coefficients. The diffusion profiles are typically a few hundreds of microns in width. To get a good profile, one needs to measure concentration of each diffusing species at every one or two microns. One may afford to determine concentrations at larger intervals toward the terminals as the concentration profiles tend to become flatter near the terminals. However, determining the entire concentration profiles by such point-by-point analysis takes a few hours of time. Moreover, the intensities of selected X-ray peaks have to be determined first on the standards before starting the analysis of the diffusion profiles. The standard calibration adds to the time of the analysis. However, all this analysis is essential in obtaining accurate and precise concentration profiles using WDS. One of the main advantages of using EPMA is the high stability of the electron beam current that the instrument is designed to give, which is essential to get consistent statistics of the X-rays over the longer length of time. Hence, EPMA is often used in the analysis of the diffusion couples. Two case studies are presented below that illustrate the use of EPMA data for determining interdiffusion coefficients; one in a ternary system and another in a quinary system.

Multiphase diffusion couples are characterized by development of planar or non-planar interfaces and multiphase diffusion zones in the couples. If a planar interface exists between two single-phase regions, local equilibrium can be assumed at the interface. It means that the concentrations on the two sides of the interface correspond to the equilibrium compositions of the phases. Thus, the concentration profiles are characterized by discontinuities at the planar interfaces. By extrapolating the concentration profiles from either side of the interface, one can obtain information of a tie-line. Thus, an accurate determination of concentration profiles can help in determining phase diagrams. One of the case studies presented below illustrates the use of EPMA analysis on multiphase diffusion couples in determining quaternary isotherm of Fe–Ni-Co–Cu system.

The microstructure developed across a joint is crucial in determining the properties and performance of mixed-material joints. Hence, it is important to understand the concentration profiles developed across a joint during the joining process and post-joining heat treatments. Thus, EPMA can be an important tool in studying mixed-material joining. Study of the effect of alloying elements on joining of aluminum alloy to steel is also presented as one of the case studies.

Understanding the partitioning of carbon and other alloying elements in various phase transformations that occur in steels is critical in continual development of new grades of steels. Especially, carbon concentration in steels is typically very low, between 0 to 2 wt%. In this range, use of elemental standard does not yield accurate carbon concentration. Hence, calibration curve method is most often used for microanalysis of carbon contents in steels. This method is illustrated with a case study of development of a new grade of steel.

EPMA is also very critical in analyzing geological samples. Hence, one case study is presented on analysis of geological samples. In the end, a case study on WDS analysis on a Ni-based superalloy is presented, and application of mapping and point-by-point analysis on solidified microstructure is illustrated. The classic case of peak overlaps, and advantage of EPMA in resolving such peaks is also illustrated with this superalloy that contains nine elements.

6.1 Determination of Interdiffusion Coefficients in Ternary Ti–Al-Nb System (Tripathi et al. 2018)

Ti-based alloys are potential lightweight alternatives for steels and other heavy materials used for components in automobile, aerospace, and bio-implant industry. However, their cost is the biggest hurdle in their widespread use. The recent development in extraction of titanium in powder form has enabled the availability of titanium powder at a very low cost (Sachdev et al. 2012). This has led to a rise in interest from industrial and research communities in developing

titanium parts with blended elemental powder metallurgy (BEPM) techniques (Sachdev et al. 2012). For developing and controlling such BEPM processes, in which alloying takes place by solid state diffusion during sintering itself, understanding of diffusion in Ti-based alloys is critical. Hence, our research group has been focusing on investigating interdiffusion in various titanium systems including Ti–Al-Nb (Tripathi et al. 2018), Ti–Al-Mn (Tripathi et al. 2020), and Ti–Al-Mo (Chauhan and Kulkarni 2021). The study in Ti–Al-Nb system is briefly illustrated below.

In this study (Tripathi et al. 2018), several ternary diffusion couples between various Ti–Al-Nb alloys were prepared and isothermally annealed at three different temperatures of 1060, 1100, and 1170 ºC for 48 h. The concentration profiles developed within the diffusion zones of the couples were analyzed by point-by-point analysis technique in EPMA using WDS. Two example concentration profiles, one for the diffusion couple between Ti-35Nb and Ti-10Al-8Nb and the other for the couple between Ti-15Al-29Nb and pure Ti (concentrations in at%), both obtained using the JEOL JXA-8230 EPMA in ACMS, IIT Kanpur, are presented in Fig. 2a–b.

Both the couples were diffusion annealed at 1170 ºC for 48 h. The profiles shown in Fig. 2a–b were obtained by employing an accelerating voltage of 20 kV and a probe current of 20 nA. The characteristic X-rays used for the analysis were K_α for titanium and aluminum and L_α for niobium. The X-ray intensities were calibrated using pure elemental standards. The collected intensities for both the standards as well as the diffusion couples were corrected by applying ZAF correction algorithm, which is provided by JEOL as a user-selectable inbuilt procedure in the JXA-8230 EPMA.

Based on Kirkaldy's method (Kirkaldy et al. 1963), to determine ternary interdiffusion coefficients at one composition, one needs to set up two independent diffusion couples with their diffusion paths intersecting at least at one composition, i.e., the composition at the intersection point is common to the diffusion zones of both the couples. One can determine the set of four ternary interdiffusion coefficients at this common composition by setting up four independent equations based on the experimental penetration curves of the couples and the interdiffusion fluxes determined from these curves. In Ti–Al-Nb system, several diffusion couples were having their diffusion paths intersecting with other diffusion couples, and hence, the ternary interdiffusion coefficients could be determined in the beta (BCC) phase of the Ti–Al-Nb system at several compositions at the three temperatures studied. The ternary interdiffusion coefficients so determined in the beta (BCC) phase of Ti–Al-Nb system are listed in Table 1. The strong diffusional interactions existing in the Ti–Al-Nb system are highlighted by the large

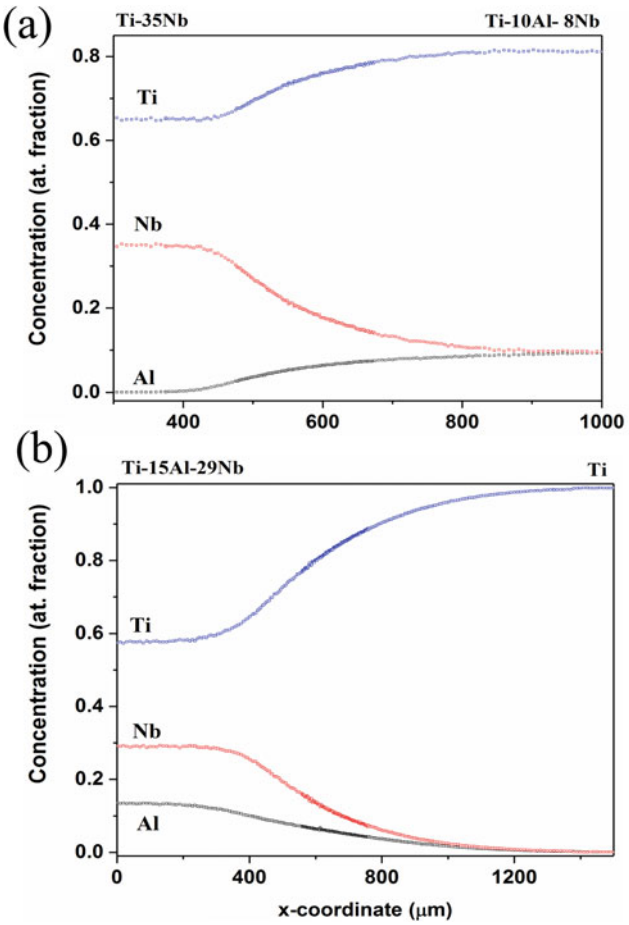

Fig. 2 Experimental concentration profiles developed in the diffusion zones of two Ti–Al-Nb diffusion couples annealed at 1170 ºC for 48 h and obtained using point-by-point analysis using WDS in EPMA (Tripathi et al. 2018). **a** Diffusion couple between Ti-35Nb and Ti-10Al-8Nb and **b** Diffusion couple between Ti-15Al-29Nb and pure Ti (concentrations in at%)

magnitudes of cross-interdiffusion coefficients as seen from Table 1. The cross-coefficient $\tilde{D}^{Nb}_{TiAl}$ is negative and comparable in magnitude with the main coefficient, $\tilde{D}^{Nb}_{TiTi}$ which implies that the interdiffusion of titanium is retarded down the concentration gradient of aluminum, while it is enhanced up the gradient of aluminum.

6.2 Interdiffusion in Quinary Fe–Ni-Co-Cr-Mn High-Entropy Alloy (Verma et al. 2020)

High-entropy alloys (HEAs) are emerging as a promising class of new materials due to the various combinations of properties that they offer (Miracle and Senkov 2017). Presence of sluggish diffusion in HEAs has been the most debated topic in the field of HEA materials (Divinski et al. 2018). As far as interdiffusion is considered, flux of a

Table 1 Interdiffusion coefficients in β (BCC) Ti–Al-Nb system experimentally determined at various temperatures and compositions (Tripathi et al. 2018)

Temperature (ºC)	Composition (at %)			Interdiffusion Coefficients (10^{-14} m^2/s)			
	Ti	Nb	Al	$\tilde{D}^{Nb}_{TiTi}$	$\tilde{D}^{Nb}_{TiAl}$	$\tilde{D}^{Nb}_{AlTi}$	$\tilde{D}^{Nb}_{AlAl}$
1060	80	14	6	4.2	−2.1	−0.7	5.7
	77	16	7	3.2	−4	−0.7	4.7
	72	20	8	2.6	−2.6	−0.7	3.2
	76	21	3	1.5	−1.4	−0.1	2.0
	73	23	4	1.6	−1.7	−0.3	2.1
	70	24	6	1.6	−2.1	−0.4	2.1
	70	26	4	0.8	−1.0	−0.1	1.3
	69	26	5	0.9	−1.3	−0.3	1.4
	62	27	11	2.1	−0.3	−0.9	1.1
	62	28	10	2.4	0.2	−0.7	1.4
1100	74	22	4	2.5	−2.8	−0.5	3.7
	71	23	6	2.8	−2.8	−0.6	3.9
	77	17	6	4.6	−3.3	−1.0	6.2
	76	21	3	2.7	−2.4	−0.3	3.4
	78	18	4	3.5	−2.3	−0.1	4.8
1170	70	26	4	3.0	−2.9	−0.5	4.4
	73	22	5	4.5	−4.6	−0.9	6.8
	78	15	7	12.9	−18.3	−3.1	16.2

component can be retarded or amplified depending upon the diffusional interactions of the other components, which are in turn guided by the cross-interdiffusivities and relative concentration gradients. In an earlier study conducted in our lab, the significance of diffusional interactions in driving such interdiffusion effects was established through appropriately designed quinary diffusion couples in Fe–Ni-Co-Cr-Mn system (Verma et al. 2017). In order to quantitatively determine the diffusional interactions, however, the knowledge of multicomponent interdiffusion coefficients was necessary. In principle, one could extend Kirkaldy's approach for ternary interdiffusion, to an n-component system. However, it would require preparing $(n-1)$ diffusion couples with their diffusion paths intersecting at one composition. Preparing such a set of diffusion couples was unfeasible until recently when Morral (Morral 2018) proposed a 'body diagonal diffusion couples' approach to possibly get a set of required number of diffusion couples having at least one common composition in their diffusion zones. We reported, for the first time in the literature, the entire sets of quaternary and quinary interdiffusion coefficients by applying the body diagonal diffusion couple approach in Fe-Ni-Co-Cr and Fe-Ni-Co-Cr-Mn systems (Verma et al. 2020). In this case study, we shall consider only the quinary Fe-Ni-Co-Cr-Mn system.

One needs sixteen interdiffusion coefficients to define interdiffusion at a given composition of a quinary system. If one can obtain four independent diffusion couples whose diffusion paths intersect at one point in the four-dimensional quinary composition space, the sixteen interdiffusion coefficients could be determined at the composition of the intersection. As per body diagonal diffusion couple approach, we prepared diffusion couples with the terminal alloys selected from ends of body diagonals of a hyper-cube formed in the quinary composition space. For this particular set of couples, the mean composition used was equimolar composition (i.e., 20Fe-20Ni-20Co-20Cr-20Mn), and the composition difference employed was 6 at%. Four such diffusion couples, BD-1–BD-4, annealed at 1000 ºC for 100 h were found to have diffusion paths intersecting at one common composition with an uncertainty of less than 1 at%.

The experimental composition profiles for the four quinary diffusion couples are presented in Fig. 3a–d.

These concentration profiles were obtained using WDS analysis in JEOL JXA-8230 EPMA. Accelerating voltage of 25 kV and a probe current of 20 nA were employed for the WDS analysis, which was carried out with pure elemental standards. The intensities of K_α X-rays determined for each of the elements (Fe, Ni, Co, Cr, and Mn) in the couples as well as on standards were corrected by applying ZAF corrections by JEOL's inbuilt program. The concentration profiles were then fitted and analyzed for interdiffusion fluxes by using *Multi*DiFlux program (Day et al. 2005). Sixteen equations were set up at the common compositions

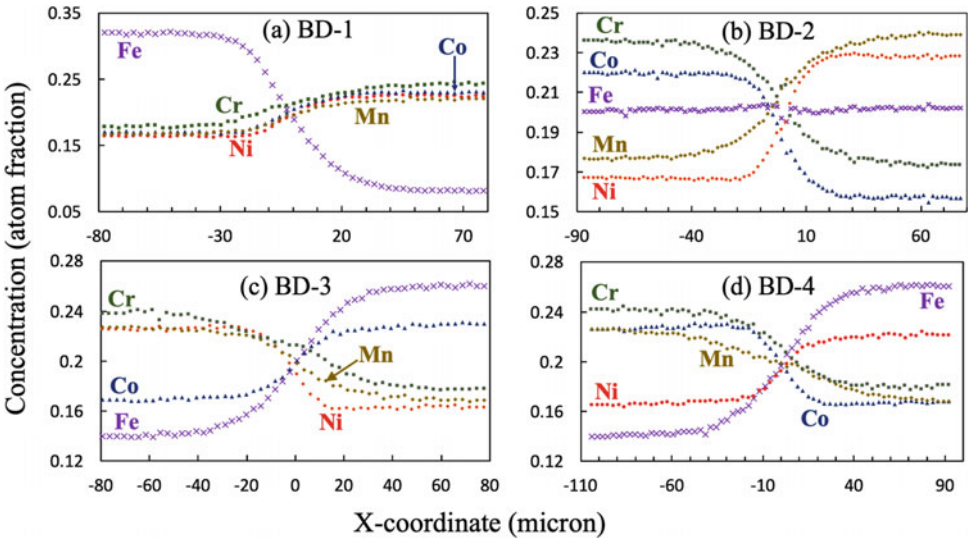

Fig. 3 Experimental concentration profiles developed in the diffusion zones of four quinary diffusion couples annealed at 1000 ºC for 100 h, obtained by point-by-point analysis using WDS in EPMA (Verma et al. 2020)

Table 2 Set of sixteen quinary interdiffusion coefficients experimentally determined at the equimolar composition of Fe-Ni-Co-Cr-Mn system at 1000 ºC (Verma et al. 2020). The interdiffusion coefficients are reported in 10^{-16} m^2/s

$\tilde{D}^{Cr}_{CoCo}$	$\tilde{D}^{Cr}_{CoFe}$	$\tilde{D}^{Cr}_{CoMn}$	$\tilde{D}^{Cr}_{CoNi}$	$\tilde{D}^{Cr}_{FeCo}$	$\tilde{D}^{Cr}_{FeFe}$	$\tilde{D}^{Cr}_{FeMn}$	$\tilde{D}^{Cr}_{FeNi}$
3.2	0.8	−0.1	1.5	2.8	5.5	−1.0	4.1
$\tilde{D}^{Cr}_{MnCo}$	$\tilde{D}^{Cr}_{MnFe}$	$\tilde{D}^{Cr}_{MnMn}$	$\tilde{D}^{Cr}_{MnNi}$	$\tilde{D}^{Cr}_{NiCo}$	$\tilde{D}^{Cr}_{NiFe}$	$\tilde{D}^{Cr}_{NiMn}$	$\tilde{D}^{Cr}_{NiNi}$
−0.5	−0.3	9.1	−3.3	1.4	0.6	−1.9	3.3

based on the four independent fluxes and four independent concentration gradients measured in each of the couples. The equations were then solved simultaneously to get the set of sixteen quinary interdiffusion coefficients at the common composition, which happens to be the equimolar composition within experimental error. The quinary interdiffusion coefficients so determined at the equimolar composition of the Fe-Ni-Co-Cr-Mn system are presented in Table 2.

The values of cross-interdiffusion coefficients in Fe-Ni-Co-Cr-Mn system as listed in Table 2 corroborate the proposed "existence of strong diffusional interactions in HEA" in our earlier studies (Verma et al. 2017). Especially significant are the cross-coefficients $\tilde{D}^{Cr}_{FeNi}$ and $\tilde{D}^{Cr}_{NiMn}$. The former being positive indicates that the interdiffusion of iron is retarded up the concentration gradient of nickel and enhanced down its gradient, whereas the negative value of the latter indicates that the interdiffusion of nickel is enhanced up the gradient of manganese and retarded down its gradient.

6.3 Determination of Quaternary Isotherm of Fe-Ni-Co-Cu at 950 ºC (Krishna and Kulkarni 2018)

As mentioned earlier, multiphase diffusion couples can give valuable information about phase diagrams. There are abundant studies reporting experimental phase diagram determination in binary and ternary systems. In a first of its kind study in the literature, we have determined a significant part of the quaternary isotherm of Fe-Ni-Co-Cu system at 950 ºC with multiphase diffusion couple experiments (Krishna and Kulkarni 2018). The ternary Fe-Ni-Cu system exhibits a large miscibility gap separating Cu-rich FCC-1 and Fe-rich FCC-2 at 950 ºC (Gupta 1990). This miscibility gap is expected to extend into the quaternary Fe-Ni-Co-Cu system, and the purpose of this work (Krishna and Kulkarni 2018) was to determine this quaternary miscibility gap at 950 ºC. Since Fe-Ni-Co ternary system is expected to show almost complete miscibility at 950 ºC (Guillemet 1989), the diffusion path of a diffusion couple prepared between a ternary Fe-Ni-Co alloy as one terminal and pure copper as another terminal most probably would pass through the miscibility gap. Hence, eleven diffusion couples were prepared between ternary Fe-Ni-Co alloys and pure copper. All 11 couples developed planar interfaces between Cu-rich FCC-1 phase and Fe-rich FCC-2 phase. The concentration profiles in all the couples were determined by point-by-point analysis in WDS mode with JEOL JXA-8230 EPMA using K_α X-rays and pure elemental standards for each of the elements Fe, Ni, Co, and Cu. The micrograph of diffusion zone and the concentration profiles for one of the couples assembled between 10Co-40Fe-50Ni and pure copper are presented in Fig. 4a–b, respectively. The planar interface

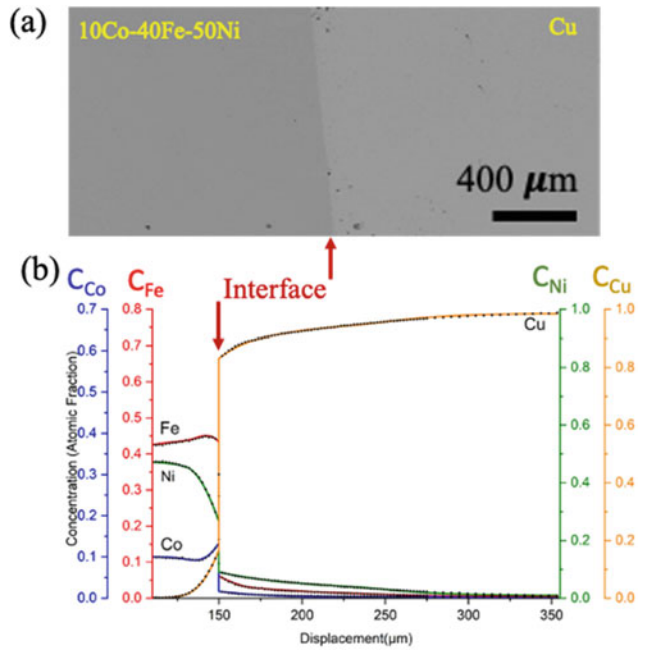

Fig. 4 **a** Microstructure around the interface and **b** concentration profiles in the diffusion zone developed in a diffusion couple between 10Co-40Fe-50Ni and pure copper annealed at 950 ºC for 72 h. The interface position on the micrograph as well as the concentration profiles is marked by red arrows

between FCC-1 and FCC-2 is clearly evident from and marked by the discontinuity in the concentration profiles.

The experimental concentration profiles for all the couples were fitted by interpolation with Cubic Hermite polynomials using *Multi*DiFlux program (Day et al. 2005). It should be noted that if WDS analysis is carried out exactly at a sharp interface, the X-ray signals are generated from both sides of the interface due to large interaction volume (1–2 microns) of primary electrons. Hence, it is recommended to get the concentration data only up to about 2 microns on either side of the interface. The concentrations of the two phases exactly at the interface should then be found out by extrapolation of the concentration profiles from both sides onto the interface position. The equilibrium concentrations of all the constituent elements in both phases at the interface were determined using multiphase module of the *Multi*-DiFlux program for each of the couples studied. Due to long diffusion annealing of the couples, local equilibrium can safely be assumed at the interface. Thus, the extrapolated compositions represent the compositions of the two phases which are in equilibrium at the interface. This enabled not only the determination of the surface enclosing the two-phase region FCC-1 + FCC-2 on the quaternary isotherm of Fe-Ni-Co-Cu system at 950 ºC but also the fixing of tie lines in this two-phase region. For details of the graphical representation of the isotherm and its mathematical equation, the work of A. B. Krishna and K. N. Kulkarni (Krishna and Kulkarni 2018) is referred to.

6.4 Mixed-Materials Joining (Dangi et al. 2018)

With increasing demand for lightweighting, 'mixed-material' or 'hybrid' structures have become need of the hour for automobile industry (Jiangqi et al. 2008; Jennings and Gould 2008). For making the hybrid structures a reality, joining of dissimilar metals becomes essential. However, formation of intermetallics (IM's) at the joint interface is the biggest issue in most of the dissimilar metals joining. Particularly in joining of steel to aluminum alloys, the brittle aluminide-based IM's reduce the performance and life of the joints. As these IMs form by diffusion process, diffusional and thermodynamic interactions among the various elements play a crucial role in deciding the nature and growth rate of the IMs. This case study (Dangi et al. 2018) was undertaken in order to understand the effect of alloying elements that are generally present in commercial steels on the growth rate of IM at the iron/aluminum alloy interface. For this study, various Fe–X alloys (where X = Mn, Ni, and Si) were dipped in liquid AA 6061 alloy at 750 °C for various times (Dangi et al. 2018). The growth rates of IMs formed at the interface were measured and compared with those formed at the interface of pure Fe and AA 6061 alloy with similar experiments. The micrographs of the IMs developed for various Fe–X alloys are shown in Fig. 5a–d. The growth constants of the IM layer for pure Fe, Fe–Mn, Fe–Ni, and Fe-Si as determined from the experiments done for various

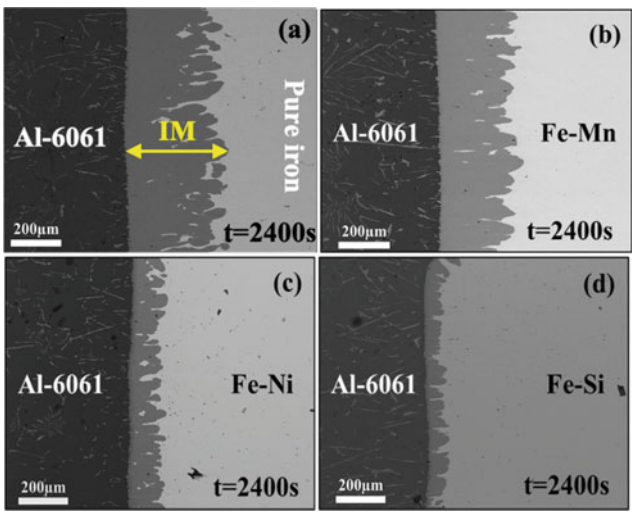

Fig. 5 SEM micrographs of the interfaces developed for various Fe–X alloys dipped in liquid aluminum alloy AA 6061 at 750 °C for 2400 s. **a** pure Fe, **b** Fe-2%Mn, **c** Fe-2%Ni, **d** Fe-2%Si (Dangi et al. 2018)

times were found to be (in 10^{-11} m^2/s) 6.1, 3.3, 0.8, and 0.4, respectively (Dangi et al. 2018). Thus, the presence of each of the three alloying elements in iron helps in reducing the IM growth. However, effect of Si is the strongest followed by Ni and Mn. These effects have been explained based on the diffusional and thermodynamic interactions (Dangi et al. 2018).

Validity of these results for Mn was also obtained by comparing the IM growths observed in the spot welds of IF steel and HSLA 340 with AA 6022 (Tripathi et al. 2017). The joints of IF steel having negligible Mn content (~0.097wt%) display higher IM thickness than that of HSLA having Mn content of 0.7 wt% (Tripathi et al. 2017).

In order to understand the effect of various alloying elements on the IM growth, concentration profiles were determined in the diffusion zones of the LS couples by point-by-point EDS analysis conducted in JEOL JXA-8230 EPMA. The advantage of using EPMA even for EDS analysis in determining these concentration profiles was that the stable beam current could be obtained in EPMA during the entire duration of the long analysis. Concentration profiles of Fe, Al, and Si developed in LS couple formed by dipping pure iron in liquid AA6061 alloy at 750 ºC for 1200 s are shown in Fig. 6a. The various phase interfaces developed in the diffusion zone are indicated by dotted lines labeled as IF-1, IF-2, and IF-3 for the interface between Fe and Fe_2Al_3, that between Fe_2Al_3 and $FeAl_3$, and that between $FeAl_3$ and AA6061, respectively. In all other LS couples' studies, same phase regions were developed although with different widths. Figures 6b–d present the concentration profiles of element *X* in LS couples formed by immersing Fe–X alloy in liquid AA6061 at 750 ºC for 2400 s where *X* stands for Mn, Ni, and Si, respectively. It can be seen that the concentration gradient of Si is the steepest in the Fe_2Al_3 layer followed by Ni, whereas Mn has almost zero slope in the layer. This indicates that Si is the slowest and Mn is the fastest diffusing species in Fe_2Al_3 layer. Based on this, it could be said that the effect of silicon in restricting the IM growth across the steel/AA6061 interface is due to the reduced diffusivities in the IM layer due to the presence of silicon (Dangi et al. 2018).

6.5 Carbon Concentration in Steel by Calibration Curve Method (Varshney et al. 2016a)

This case study on steels highlights the utility of calibration curve method in determining carbon concentration in steels at micro-level. There are various convenient methods available for accurately determining the carbon concentration in steels at a macro-level. However, macro-level composition is not a true representative of local micro-level composition due to the presence of multiple number of finely distributed phases in the steel. Knowledge of carbon distribution in various phases is of prime significance while

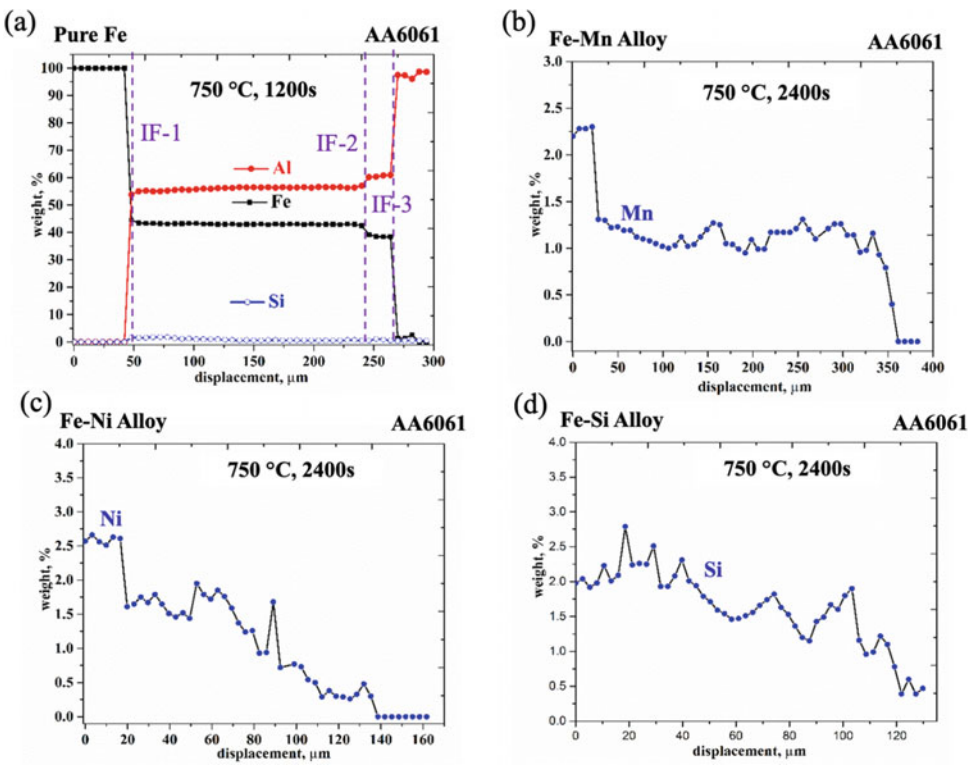

Fig. 6 Experimental concentration profiles developed in various liquid–solid (LS) couples formed by immersing Fe–X alloy in liquid AA6061 alloy at 750 ºC. **a** Profiles of Fe, Al, and Si in LS couple of pure iron and AA6061, **b** Mn profile in LS couple of Fe–Mn alloy and AA6061, **c** Ni profile in LS couple of Fe–Ni alloy and AA6061, **d** Si profile in LS couple of Fe-Si alloy and AA6061 (Dangi et al. 2018)

designing various heat treatments. The following discussion presents an example of how EPMA analysis helped in understanding the role of carbon distribution in phase transitions and resultant properties.

A medium carbon high silicon steel with composition 0.61C-1.71Si-0.86Mn (wt%) was austenitized at 1040 °C followed by air cooling for various times from 0 to 40 s. At the end of the air cooling, the steel was austempered at various temperatures of 300, 350, and 400 °C for 10 min followed by quenching in water to room temperature. The purpose of the heat treatment was to design a microstructure comprising multiple phases with varying mechanical properties and to retain large amount of austenite at room temperature so that the best combination of strength and ductility can be obtained in a low alloyed steel. Purpose of the air cooling during heat treatment was to nucleate pro-eutectoid ferrite at the prior austenitic grain boundaries. Temperature of the sample during air cooling (recorded using an Arduino-based data acquisition system) was in the intercritical temperature range, i.e., in ($\alpha + \gamma$) phase field. Due to a large difference in the maximum solubility limit of *C* in ferrite or α (0.02wt.%) as compared to austenite or γ (2.1 w.%), *C* is expected to partition from α to γ during air cooling, resulting in *C*-enriched austenite (γ'). Austempering was then carried out to transform γ' to bainitic ferrite. Due to the presence of high silicon in steels, the inhibition of carbide formation was anticipated. Carbon that could have been utilized in carbide formation would now enrich and stabilize the untransformed austenite, which would then get retained in the microstructure after quenching to room temperature. Thus, after the completion of heat treatment, the microstructure of the steel was expected to comprise pro-eutectoid ferrite at the grain boundaries along with bainite and carbon-enriched retained austenite inside the grains resulting in a multiphase microstructure.

Microstructure of the samples austempered at 350 °C after air cooling for 10–40 s is shown in Fig. 7. Pro-eutectoid ferrite at the grain boundaries and the bainitic ferrite inside the grain can be easily observed in all the samples. In the samples cooled for 30 and 40 s, some pearlite can also be observed. Investigations of mechanical properties of the heat treated steels showed an excellent combination of strength and ductility. The high tensile strength was due to the presence of hard bainite in the microstructure, whereas the high tensile ductility was due to the presence of soft pro-eutectoid ferrite along with the retained austenite (Varshney et al. 2016a).

Content of retained austenite in the present case, as measured from X-ray diffraction analysis, was observed to have reduced after the tensile test. Scanning electron microscopic analysis of gauge lengths of the tensile specimens post-tensile test revealed the presence of martensite in the microstructure (Varshney et al. 2016a, b). Retained austenite under the application of strain tends to transform to martensite which delays necking by suppressing the localized deformation and increasing the work hardening rate resulting in both high ductility and strength (Varshney et al. 2016b, 2017). This is known as the transformation-induced

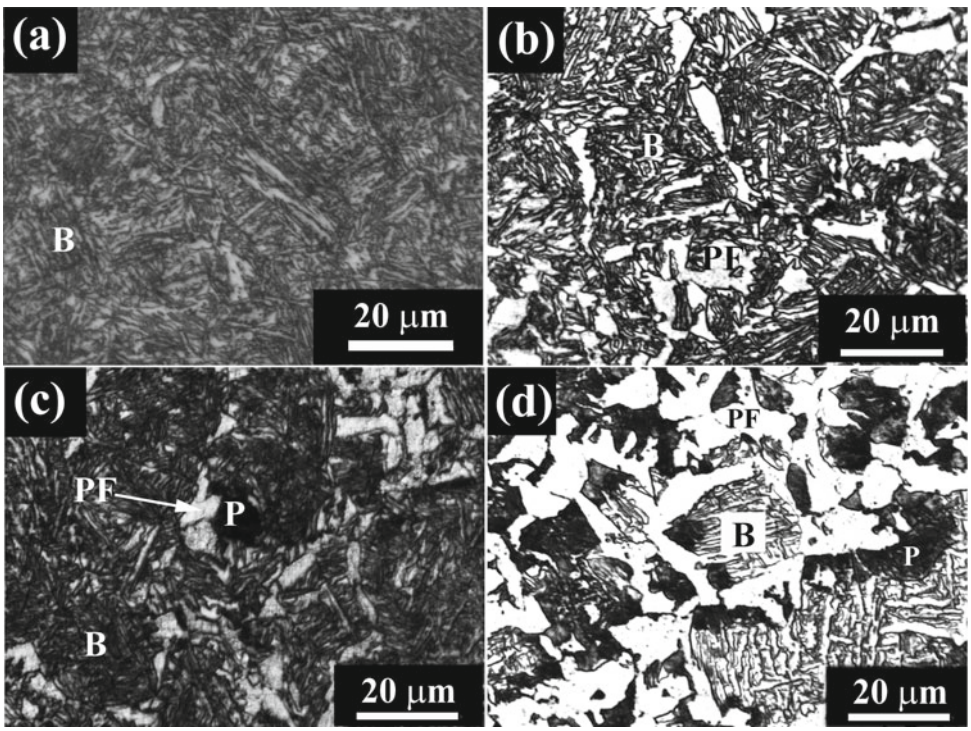

Fig. 7 Optical microstructure of the samples austempered at 350 °C after air cooling for **a** 10 s, **b** 20 s, **c** 30 s, and **d** 40 s. White etched region is the pro-eutectoid ferrite (PF), gray etched region is bainite (*B*), and black etched region is pearlite (*P*) (Varshney et al. 2016a)

plasticity (TRIP) phenomenon. The Ludwigson equation, which accurately predicts the flow behavior of metastable austenitic stainless steels, was found to closely represent the flow behavior of the steels austempered at 350 and 400 °C in this study (Varshney et al. 2016b). Both depletion of austenite during tensile straining and large extent of fitting of the true stress–strain data to the Ludwigson equation indicate that strain-induced transformation of austenite is playing an important role in the deformation of steels. The susceptibility of retained austenite to transform to martensite under the application of strain depends on its M_s (martensitic start) temperature. One of the primary factors that influences the M_s temperature is the carbon content of austenite.

Detailed microstructural examination revealed the presence of carbides in the microstructure of the samples austempered at 350 and 400 °C after air cooling for 30 s (Varshney et al. 2017). Presence of carbides in spite of the large amount of Si content in steels (1.71 wt.%) was surprising. Previous literature suggests high chances of carbide precipitation during austempering when the amount of carbon in the parent austenite is high. As discussed above, bainite transformation in this study initiated in γ'. Thus, it was very important for the investigators to determine the amount of carbon in austenite after air cooling (i.e., in γ') as well as in the retained austenite. Knowledge of the carbon content in γ' may be helpful in understanding the reason for carbide precipitation during austempering, while knowledge of the amount of carbon in retained austenite may aid in explaining the susceptibility of the austenite to undergo the TRIP phenomenon.

Energy dispersive spectroscopic (EDS) analysis determines inaccurate *C* content because of low atomic weight of *C*. Wavelength dispersive spectroscopy (WDS) provides a unique feature to accurately determine the amount of *C* content in submicron region of the specimen. WDS installed in a JEOL make EPMA (JXA-8230) at ACMS, IIT Kanpur, was used to determine the carbon content by generating a calibration curve.

To determine carbon content in the desired phase, the machine was first calibrated with five steel samples of known compositions. Fe-**0.1C**-0.28Si-1.8Mn-1.75Ni-0.3Al-0.027Nb-0.08 N, Fe-**0.41C**-0.313Si-0.750Mn-0.129Cr-0.0038 V-0.119 N, Fe-**0.61C**-1.65Si-0.86Mn-0.1Cr, Fe-**1.03C**-0.215Si-0.408Mn-1.04Cr-0.009Mo-0.06Ni-0.09Cu, and Fe-**2C**-0.481Si-0.375Mn-1.26Cr-0.07Ni-0.016Co-0.012Cu-0.013Ti-0.08 N were the five standard steel specimens used for the study. The compositions of all the standard samples were determined with SPECTROMAXx optical emission spectrometer, which itself was calibrated with certified reference materials provided by MBH Analytical Ltd., England. Uniform martensitic microstructure was obtained in all the standard specimens used for calibration by water quenching the steel sample upon suitable austenitization prior to calibration procedure. This was done to ensure homogenous composition in a single-phase matrix in the standards. For each specimen, intensities of carbon K_α X-Rays were recorded at the probe condition of 20 kV and 20 nA. A calibration curve was generated by plotting intensities versus carbon content as shown in Fig. 8. Under the similar conditions in which the calibration curve was generated, desired regions of the samples with unknown carbon content were analyzed. The X-ray count from the selected region was noted, and with the help of the previously generated calibration curve, shown in Fig. 8, amount of carbon was determined.

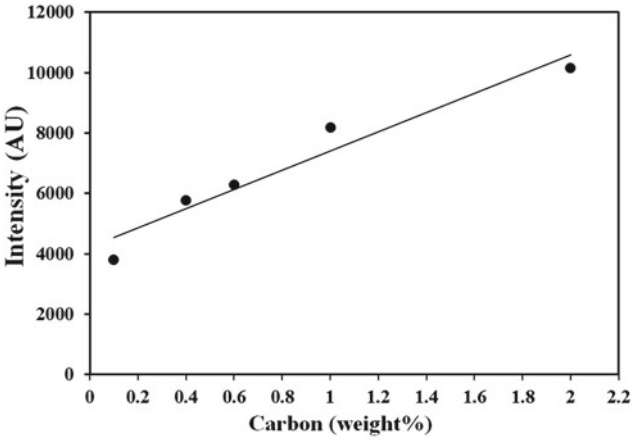

Fig. 8 Calibration curve generated by using various steel compositions of known carbon content (Varshney et al. 2016a)

To determine the amount of carbon in γ' after continuous cooling for various durations, the samples air cooled for 0 to 40 s were directly quenched in water to retain the amount of carbon partitioned in austenite during air cooling. The microstructure of the steel samples obtained after water quenching are shown in Fig. 9. Pro-eutectoid ferrite (*F*) and martensite (*M*) can be clearly observed in the microstructures. Due to the fast diffusionless transformation, martensite will have similar carbon content as that in prior austenite after respective air cooling duration. Under the similar conditions in which the calibration curve was determined, X-ray count in the martensitic region of the water quenched sample was measured by impinging the electron beam onto it. X-ray counts measured from the small region were compared with the calibration curve in Fig. 8, and the carbon content of the region was determined.

The variation in carbon content in the untransformed austenite (martensite) with air cooling duration has been shown in Fig. 10. Increase in the carbon content in martensite with increase in air cooling duration till 30 s can be observed. The increase is clearly due to more amount of carbon getting partitioned into austenite, which in turn resulted from increased content of pro-eutectoid ferrite during air cooling. A slight decrease in the carbon content in

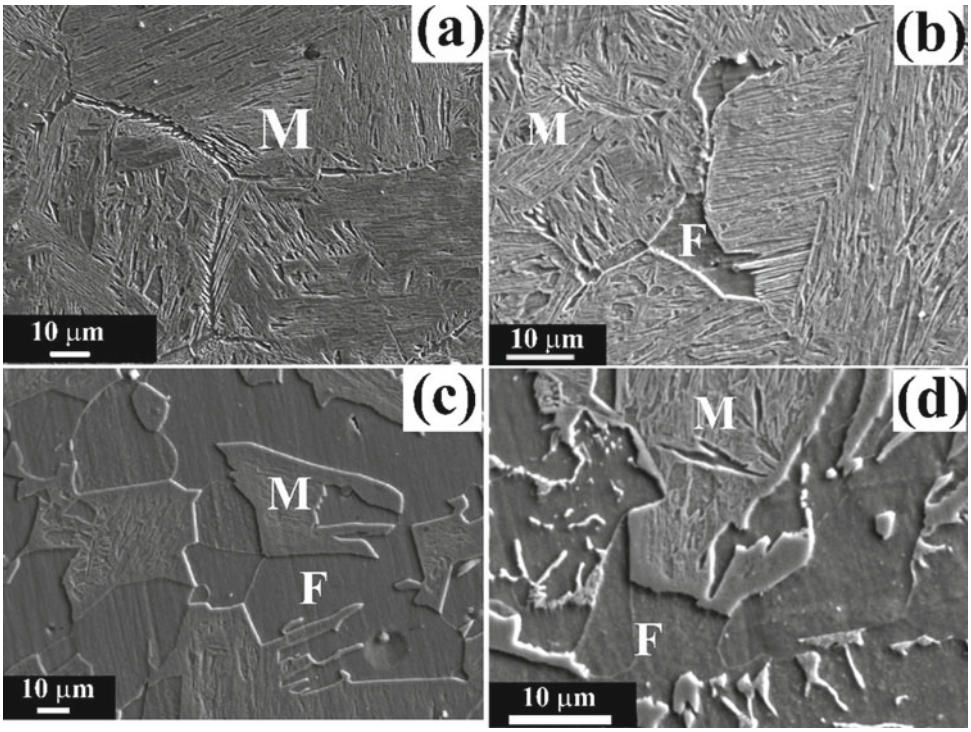

Fig. 9 Microstructure of the water quenched samples air cooled for **a** 10 s, **b** 20 s, **c** 30 s , and **d** 40 s. pro-eutectoid ferrite at the grain boundaries and martensite inside the untransformed austenitic grains can be observed

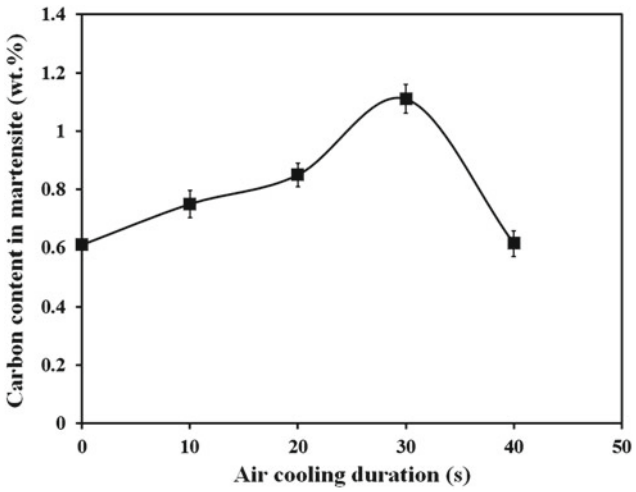

Fig. 10 Variation of carbon content in the martensitic regions with continuous cooling duration (Varshney et al. 2016a)

the samples air cooled for 40 s might be due to nucleation of pearlite in the microstructure. Carbides in pearlite would have consumed some carbon and then reduced the amount of the carbon in the untransformed region.

Previous extensive microstructural examinations revealed the presence of carbides in the samples air cooled for 30 s and austempered at 350 and 400 °C. In the samples air cooled for 0, 10, and 20 s, carbides were not found to be present (Varshney et al. 2017). From Fig. 10, it is clear that high carbon content in austenite in the samples cooled for 30 s led to the precipitation of carbides during austempering. Takahashi and Bhadeshia (Takahashi and HKDH Bhadeshia. 1990) in their theoretical study on the effect of carbon content in parent austenite on the precipitation of carbides in bainite established that probability of the precipitation of carbides inside bainitic ferrite lath increases with increase in the carbon in parent austenite. Thus, measurement of carbon content in austenite after air cooling with EPMA helped to understand the reason for carbide precipitation taking place in spite of high Si content of the steels.

6.6 Application of EPMA in the Field of Earth Sciences/Geosciences

EPMA is an essential research tool routinely used in complex mineralogical and petrological studies of geological (rocks and minerals including ore minerals) and planetary materials. It is routinely used for nondestructive quantitative geochemistry—to precisely determine major oxides and trace element abundances—of in-situ mineral phases such as olivine, pyroxenes, apatite, monazite, uraninite, and thorite, or tiny inclusions in a mineral, at a scale of few microns on the surface of solid samples. Therefore, it is also widely used in experimental petrology with an objective of characterizing phase changes and partition behavior of elements during melting, etc. For petrological investigation, a geological

sample must be in the form of either a thin-polished section mounted on a glass slide (predominantly used) or polished sample in a resin block.

The main advantage of EPMA is its capability to acquire the chemical composition of a targeted small spot (1–2 microns) within a (primary, secondary, or accessory) mineral grain, employing WDS technique. The main applications of EPMA in Earth Sciences/Geology can be summarized as follows.

1. This technique is mainly used to precisely analyze the chemical (major oxides and trace constituents) composition of the mineral grains in geological samples such as rocks, minerals, and glasses by wavelength dispersive spectrometry in a nondestructive way. Many times, the variation in elemental concentrations within a single mineral grain can be determined from the rim to the center, which are used to estimate the temperature and the pressure under which the mineral formed. Detailed mineral chemistry of all mineral phases, particularly tiny melt inclusions, helps to obtain the parental magma composition, which in turn can be linked to the origin of such magma.
2. Chemical composition of small-sized spots (1–2 microns) can be analyzed, which is particularly beneficial in analysis of fluid inclusions or small glass globules trapped within small mineral grains.
3. Elemental mapping, showing false color images characterizing spatial distribution of elements in a sample of interest, is done to identify chemical zoning within a mineral grain, as well as to identify mineral phases.
4. Different images prepared by EPMA technique, particularly, secondary electron images, backscattered electron images (BSE) and cathodoluminescence images reveal the textural (shape, size and orientation of grains, and their relationship) aspects of a geological sample that aid in drawing inferences on magma cooling. For example, high-resolution BSE images of the sample combined with micro-composition analysis obtained from EPMA help to study micro-textures in detail, in-situ characteristics, and resolve complex chemical variations within individual mineral phases; these are often difficult to achieve using an optical microscope.
5. The primary and secondary (or altered) nature of the mineral grain can be determined using probe data, e.g., mantle-derived mineral or crustal-derived mineral, reaction rims, hydrothermal alteration, etc. The presence and identification of mantle and crustal xenoliths (foreign fragments) within the rock sample can be easily identified at a microscopic level.
6. EPMA is useful to analyze the elemental components of sedimentary rocks, including B, Ga, Ba, Sr, Co, V, Cr, Mn, Fe, and Ni. This information helps to evaluate the effect of redox conditions, depth of water column, and salinity on the formation of sedimentary rock in a basin.
7. This technique has been used for geochronology, particularly for U-Th age of monazite, uraninite, thorite, and xenotime minerals. Monazite dating by EPMA is a reliable and powerful dating technique and widely used in the geochronological study of monazite-bearing rocks that does not require measurement of isotope ratios.

A Case Study: Apatite from the Amba Dongar Carbonatite Complex

The Amba Dongar Carbonatite Complex, Gujarat, is a type locality for occurrence of carbonatite rocks (containing more than 50 modal% carbonate minerals) as well as alkaline rocks such as nephelinites. In general, carbonatite has high economic significance, particularly for the rare earth elements (REE), Nb, and phosphates (Simandl 2015). Globally, carbonatite complexes are well known for the largest source of REE deposits (Harmer and Nex 2016); REE-bearing phases are bastnaesite, britholite, and monazite. The mineral apatite (phosphate-bearing phase) commonly occurs as an accessary mineral in both carbonatites and the associated nephelinite rocks. In this regard, apatite chemistry obtained via EPMA analysis can be used to understand genetic relationship between the carbonatites and nephelinites, as well as the origin of the parental magma(s). Chandra et al. (Chandra et al. 2018) reported the mineral chemistry of apatites from three different calciocarbonatites and one nephelinite. The electron probe data for major and trace element compositions of apatite was obtained using a CAMECA SXFive electron probe micro-analyzer (EPMA) at IIT Bombay. Targeted apatite in thin-polished samples were excited with a primary electron beam sourced from lanthanum hexaboride (LaB_6) and operated at 15 kV and 20 nA with a beam of 1 μm diameter. Calibration was done using both natural and synthetic minerals and elemental glass (apatite (F, P), diopside (Ca), albite (Na), $SrSO_4$ (Sr), NaCl (Cl), Th-glass (Si), La-glass (La), Ce-glass (Ce), Pr-glass (Pr), and Nd-glass (Nd).

Considerable compositional variation is observed in the analyzed major oxide and selected trace element compositions of apatites from three calciocarbonatite samples and a nephelinite sample (Chandra et al. 2018). Apatites from both rocks show similar F and FeO contents and REE abundances except for La. These similarities in the elemental abundances indicate a common parental magma and support a genetic relationship between the calciocarbonatites and the associated nephelinite rocks. Also, apatites in carbonatites contain up to 0.4 wt% Na_2O, which indicates a comparatively more volatile content in the original parental carbonate magma. This volatile content of the original parental carbonate

magma might have been lost to the country rocks (or host rock) causing wide spread fenitization, a process of chemical alteration (mainly alkali metasomatism) of country rocks in the form of aureole around carbonatite intrusion by mantle fluids containing Na, K, F, Cl, CO_2, etc.

Backscattered electron images of apatites in calciocarbonatites and nephelinite are presented in Fig. 11a–d. Apatite cumulate in calciocarbonatites has higher CaO content as compared to other forms of apatites. Apatite cumulate is an early formed mineral phase than other forms of apatites identified using these images. Apatite shows various textural features in calciocarbonatites: (1) scattered or disseminated apatites in calcitic groundmass (Fig. 11a), (2) clusters of apatites near calcite boundaries (Fig. 11b), and (3) apatite cumulates (Fig. 11c). Nephelinite contains apatites of varying size and habit (Fig. 11d). Petrography of calciocarbonatites reveals that apatite cumulate is the second most fractionated mineral phase after calcite.

These forms of apatite reflect continuous apatite fractionation with accompanying physicochemical changes during calciocarbonatite formation from the rising carbonatite melt (Chandra et al. 2018). EPMA analyses constrain the composition of SiO_2 (0.01–0.34 wt%) and SrO (0.58–0.95 wt%) contents of apatites in calciocarbonatites, which are comparatively lower than the apatites in nephelinite (SiO_2, 0.69–1.10 wt%; SrO, 1.32–2.6 wt%). In contrast, the P_2O_5 (39.9–41.3 wt%) and Na_2O (0.1–0.38 wt%) contents of apatites in calciocarbonatite are distinctly higher than those in nephelinite (P_2O_5, 38.6–39.6 wt%; and Na_2O, 0.06–0.13 wt%). These variations in major oxides suggest that apatite crystallization may have continued after immiscible separation of the carbonatite melt and the silicate melt from a common parental carbonated silicate magma.

6.7 Microstructure Study of Ni-Based Superalloy

Ni-based superalloys are widely used in aero-engine applications, such as in turbine blades and vanes, due to their exceptional high temperature strength (Schafrik and Sprague 2004; Pollock and Tin 2006). This class of alloys is mainly based on Ni as the principal element, and they obtain their strength on account of the coherent Ni_3Al-based phase having $L1_2$ crystal structure. The refractory alloying elements such as W, Nb, and Mo are added for solid solution strengthening of the matrix (γ) phase, whereas the elements such as Ti, Nb, and Ta assist in the formation and strengthening of the precipitate (γ') phase (Pollock and Tin 2006). In general, Ni-based superalloys contain a large number (8–10) of alloying elements, and their distribution and partitioning during solidification significantly affect the properties of the alloys in as-cast as well as post-processed conditions. EPMA is the most useful tool for experimental investigations of distribution of various alloying elements in a Ni-based superalloy.

Figure 12 presents a BSE micrograph of a directionally solidified Ni-based superalloy provided by GE Research—Bangalore. The dendritic structure is clearly highlighted by light gray contrast (Arrows labeled 1 on Fig. 12), whereas the interdendritic $\gamma + \gamma$' eutectic regions are highlighted by dark gray contrast (Arrow labeled 2 on Fig. 12). The precipitates containing Ti and the refractory elements Ta, W,

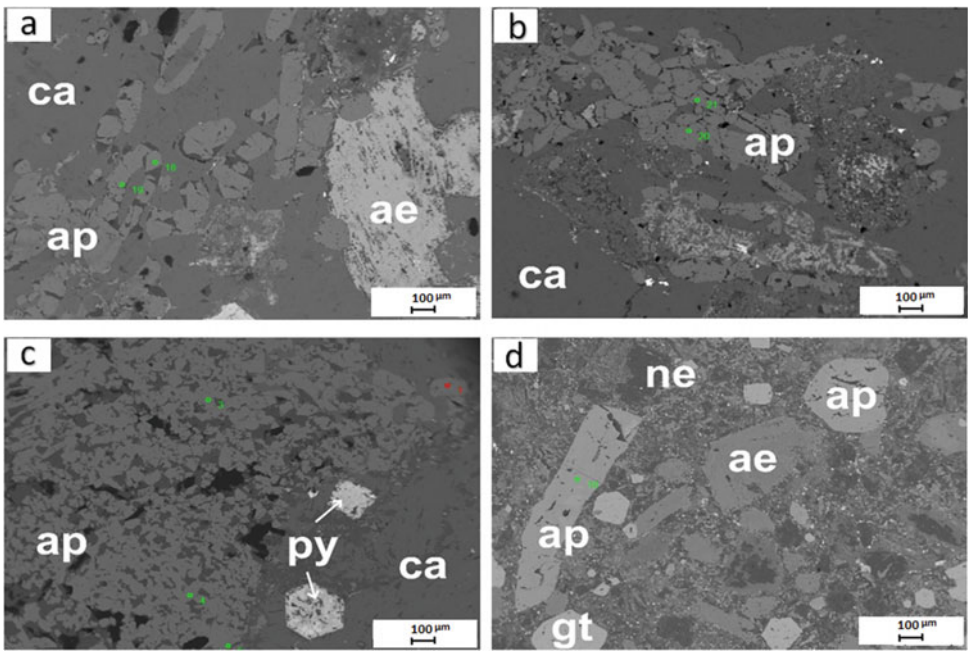

Fig. 11 Photomicrographs of backscattered electron images of various apatite forms from three calciocarbonatites: (a–c) and one nephelinite (d) from the Amba Dongar Carbonatite Complex (Chandra et al. 2018). **a** size variations in apatites with calcitic groundmass, **b** apatite clusters along the boundaries of calcite crystals, **c** apatite cumulate, **d** apatite crystals in nephelinite. Locations of microprobe spots are shown by green dots. Symbols are ca: calcite, ap: apatite, ae: aegirine, py: pyrochlore, ne: nepheline, and gt: garnet

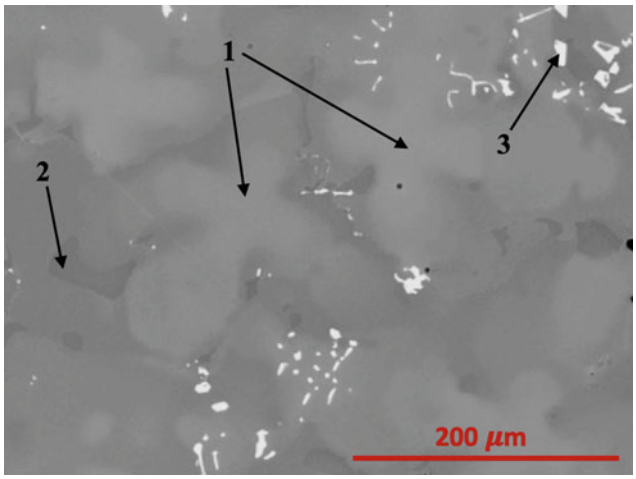

Fig. 12 BSE micrograph of a solidified nickel-based superalloy. Dendritic regions, interdendritic regions, and refractory element-rich precipitates are marked by Arrows 1, 2, and 3, respectively

and Nb are the bright regions on the micrograph (Arrow labeled 3 on Fig. 12).

The areas rich in various elements can be nicely captured in elemental maps prepared by WDS. As examples, the elemental maps collected for Ti (K_α), Ta (L_α), W (L_α), and Mo (L_α) are presented in Fig. 13a–d, respectively. In the Ti-map shown in Fig. 13a, the dendrites are clearly highlighted due to the enrichment of titanium in the interdendritic regions and its gradual deprival toward the center of the dendrite. Maps of Ti and Ta shown in Fig. 13a–b correctly highlight the precipitates rich in them, whereas Fig. 13c–d shows more or less uniform distribution of tungsten and molybdenum in the dendritic regions. Enrichment of interdendritic regions with tungsten and depletion with molybdenum are also clearly visible. The intensity of each pixel in the map can be converted into concentration after applying appropriate ZAF corrections at each pixel, and the intensity maps can be converted into composition maps. Quantitative analysis at each pixel can also be obtained in a tabular form. Such quantitative data is very useful in validating the various solidification models used for simulation of microstructure of as-cast superalloys. Such simulations are routinely performed in industry for design and control of various processing routs, and availability of such quantitative maps from EPMA can be a very valuable resource in such developments.

In order to get an idea about how concentration distribution of various elements varies across a dendrite arm, point-by-point quantitative analysis was conducted across a dendritic arm shown by a yellow dotted line on Fig. 13a. The analysis was carried out using pure elemental standards and with the probe conditions of 25 kV and 20 nA. The X-ray lines used for the WDS analysis were Ni-K_α, Al-K_α, Co-K_α, Cr-K_α, Ti-K_α, Nb-L_α, Mo-L_α, Ta-L_α, and W-L_α. The concentration profiles obtained across the dendritic arm are presented in Fig. 14.

It can be seen that Ti gradually increases from center of the dendrite toward the outer and the interdendritic regions are characterized by higher amount of titanium. Ni and Al are seen to partition in the same way, whereas Co and Cr are partitioning exactly opposite to Ni and Al. Ta, Mo, and Nb seem to be segregated only on the MC intermetallics. Such quantitative data on concentration profiles of a microstructure is essential for modeling certain processes such as homogenization annealing.

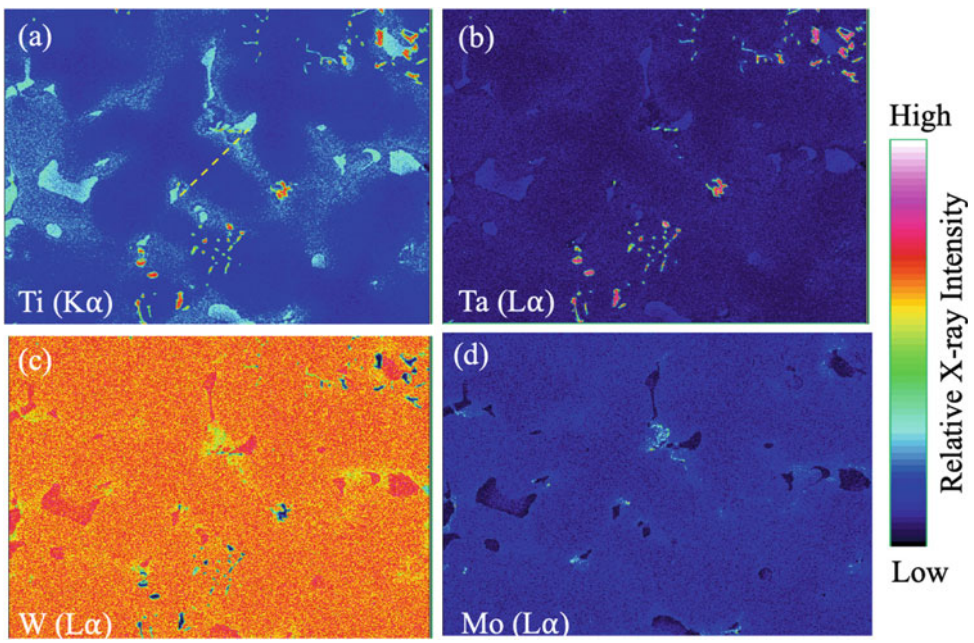

Fig. 13 Elemental maps produced by WDS for **a** Titanium. **b** Tantalum. **c** Tungsten, and **d** Molybdenum

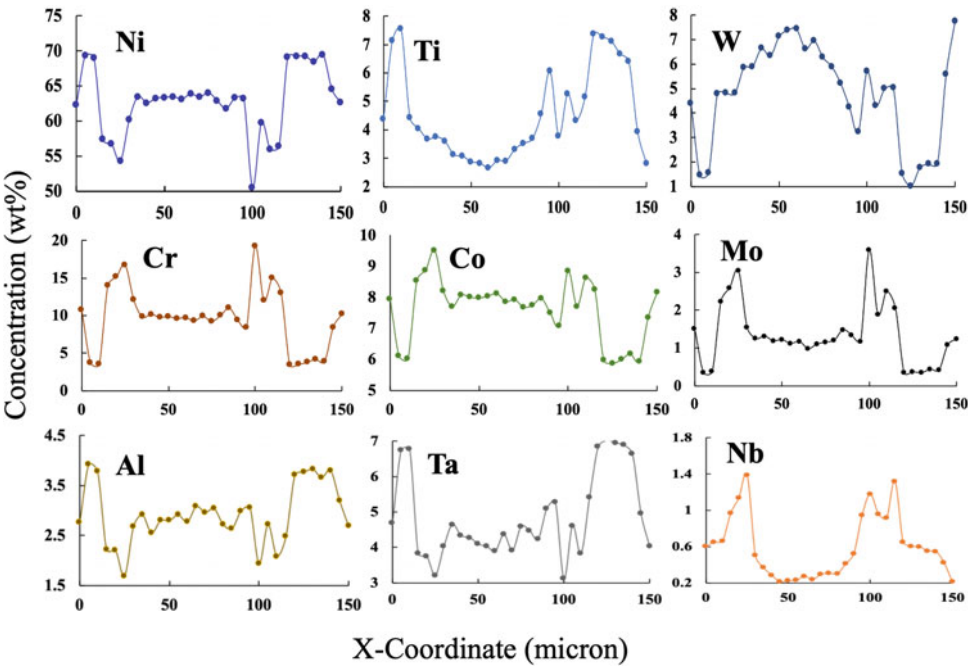

Fig. 14 Concentration profiles of all elements in the Ni-based superalloy analyzed by WDS across a dendritic arm

It should be noted here that while analyzing Ni-based superalloys, there maybe overlap of several peaks from various alloying elements, and hence, WDS with higher energy resolution should be a better choice than EDS. For example, the part of spectra obtained by WDS and EDS on the superalloy used in the present study is presented in Fig. 15a–b. It can be seen that Ni-K_β (8.267 keV), Ta-L_α (8.146 keV), and W-L_α (8.398) peaks are very close to each other. These peaks are overlapping in the EDS spectrum. However, they are clearly resolved in the WDS spectrum. Such a high resolution obtained by WDS increases the accuracy of the quantitative analysis manifold over that done by EDS. Similarly, Ni-K_α (7.48) and Co-K_β (7.649) are very close to each other such that they are not resolved in the EDS spectrum (Fig. 15b) but can be clearly resolved by the WDS spectrum (Fig. 15a).

For quantitative analysis with 25 kV, Ta-L_α (8.146 keV) and W-L_α (8.398) lines can be used. However, the precaution has to be taken while collecting the background intensities, which are usually collected from positions that are close enough to the peak position so as to properly represent the background of the peak and at the same time slightly away enough so as to avoid the interference from the peak width. In case of Ta-L_α and W-L_α, since Ni-K_β is very close to both the peaks, one also has to make sure that the positions for their background collections are not interfered by the peak width of Ni-K_β. Thus, it is necessary to quickly assess the peak positions of all possible characteristic X-rays generated from the sample as they may interfere with the measured peak or background intensities even though these X-rays are not going to be under consideration for analysis.

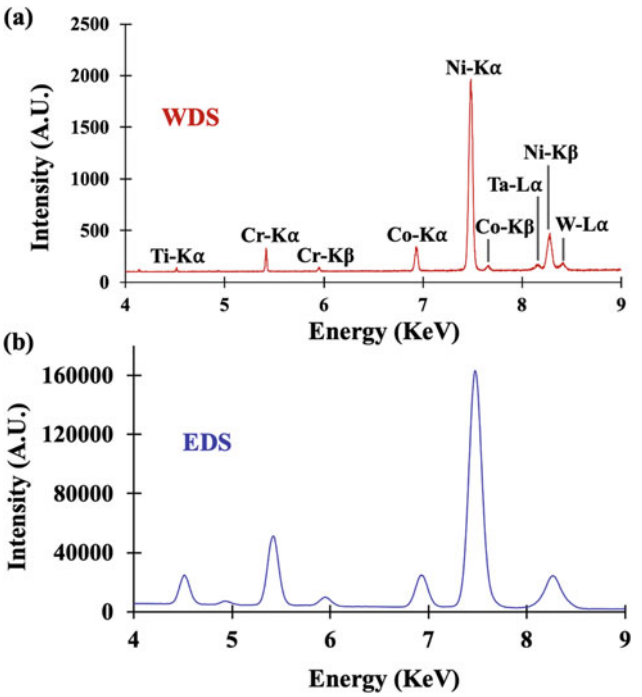

Fig. 15 Part of the X-ray energy spectra obtained by **a** WDS and **b** EDS on the Ni-based superalloy illustrated in the present study

7 Summary

Electron probe micro-analyzer (EPMA) is one of the most accurate and precise tools for micro-composition analysis of multicomponent samples. EPMAs are equipped with an EDS

and multiple WDS channels. However, WDS, due to its better accuracy and energy resolution, should be the preferred choice for both qualitative and quantitative analysis wherever high accuracy and precision are needed. Although the intensities of X-rays collected by detectors are significantly affected by the sample's matrix effects, the various correction methods including ZAF, Phi-Rho-Z, or calibration curves essentially yield quite accurate analysis with the help of standards. The various case studies were discussed that covered the EPMA applications in range of materials including steels, titanium alloys, nickel-based superalloys, high-entropy alloys, and geological materials. The various applications covered in these case studies included determination of interdiffusivities and phase equilibria, understanding of phase transformation during heat treatments, gathering the quantitative microstructure-composition map data for model validation, and understanding the genetic relationship between the geological rock samples. Although only limited cases could be covered in the present article, the utility of EPMA is essentially boundless whenever and wherever accurate and precise micro-composition analysis is desired.

Acknowledgements The authors are grateful for the generous support from various funding agencies and organizations with which the discussed case studies have been conducted: Indian Space Research Organization, General Motors USA, GE Research—Bangalore, GOALI grant from NSF and IIT Kanpur. Thanks to GE Research—Bangalore for providing the Nickel-based superalloy for the case study. The authors are also thankful to JEOL's EPMA experts for useful discussions.

References

Akhtar K, Khan SA, Khan SB, Asiri AM (2018) Scanning electron microscopy: principle and applications in nanomaterials characterization. In: Sharma SK (ed) Handbook of materials characterization. Springer International Publishing AG, pp 113–146

Berger MJ, Seltzer SM (1964) Tables for energy losses and ranges for electrons and positrons. Natl Acad Sci Natl Res Counc Publ 1133:205–268

Bishop HE (1967) Optique des Rayons X et Microanalysis. Hermann, Paris

Bloch F (1933) Bremsvermogen von Atomen mit mehreren Elektronen. Zeitsehrift Fiir Physik. 81:363–376

Brown JD, Packwood RH (1982) Quantitative electron probe microanalysis using Gaussian curves. X-Ray Spectrom 11(4):187–193

Caistaing R, Guinier A (1953) Point-by-point chemical analysis by X-ray spectroscopy: electronic microanalyzer. Anal Chem 25 (5):724–726

Castaing R (1952) Application des sondes electroniques a une methode d'analyse ponctuelle. Office National d'Estudes et Recherches Aeronautiques, paris, France

Chandra J, Paul D, Viladkar SG, Sensarma S (2018) Origin of the Amba Dongar carbonatite complex, India and its possible linkage with the Deccan Large Igneous Province. Geological Society, London, Special Publications, Geological Society of London vol 463. pp 137–169

Chauhan GPS, Kulkarni KN (2021) Investigations of ternary interdiffusion in β (BCC) phase field of Ti-Al-Mo system. Metall Mater Trans A 52A:413–425

Cosslet VE (1949) Conference on electron microscopy. Nature 164:481–483

Dangi B, Brown TW, Kulkarni KN (2018) Effect of silicon, manganese and nickel present in iron on the intermetallic growth at iron-aluminum alloy interface. J Alloys Compd 769:777–787

Day KM, Dayananda MA, Ram-Mohan LR (2005) Determination and assessment of ternary interdiffusion coefficients from individual diffusion couples. J Phase Equilib Diffus 26:579–590

Divinski SV, Pokoev AV, Esakkiraja N, Paul A (2018) A mystery of sluggish diffusion in high-entropy alloys: the truth or a myth. In: Mehrer H (ed) Diffusion foundations, vol 17. pp 69–104

Duncumb P, Reed SJB (1968) The calculation of stopping power and backscatter effects in electron probe microanalysis. In: Heinrich KFJ (ed) Quantitative electron probe microanalysis, vol 298. NBS Special Publication, pp 133–154

Guillemet A (1989) Assessing the thermodynamics of the Fe-Co-Ni system using a CALPHAD predictive technique. CALPHAD; 13 (1):1–22

Gupta KP (1990) The Cu-Fe-Ni (Copper-Iron-Nickel) system. In: Phase diagrams of ternary nickel alloys, Part 1. Indian Institute of Metals, Kolkata, pp 290–315

Harmer RE, Nex PAM (2016) Rare earth deposits of Africa. Episodes 39:381–406

Heinrich KFJ, Yakowitz H (1975) Absorption of primary X Rays in electron probe microanalysis. Anal Chem 47(14):2408–2411

Henrich KF (1991) Strategies of electron probe data reduction. In: Henrich KFJ, Newbury DE (eds) Electron probe quantitation. Springer Science+Business Media, New York, pp 9–18

Hillier J, Baker RF (1944) Microanalysis by means of electrons. J Appl Phys 15:663–675

Jennings J, Gould J (2008) A new road for automotive architectures. Welding J 87(10):26–30

Jiangqi L,Fengchong L, Jiqing C (2008) New technology of lightweight and steel-aluminum hybrid structure car body. Chin J Mech Eng 6:6

JEOL User Manual for JXA-8230

Kirkaldy JS, Lane JE, Mason GR (1963) Diffusion in multicomponent metallic systems: VII solutions of the multicomponent diffusion equations with variable coefficients. Can J Phy 41(12):2174–2186

Krishna AB, Kulkarni KN (2018) Experimental determination of quaternary isotherm of Fe-Ni-Co-Cu at 950 °C by diffusion couple technique. Materialia 4:549–552

Love G, Cox MG, Scott VD (1978) A versatile number correction for electron-probe microanalysis. J Phys D Appl Phys 11:7–21

Takahashi MM, Bhadeshia HKDH (1990) Model for transition from upper to lower bainite, Mater Sci Technol 6:592

Miracle DB, Senkov ON (2017) A critical review of high entropy alloys and related concepts. Acta Mater 122:448–511

Morral JE (2018) Body-diagonal diffusion couples for high entropy alloys. J Phase Equilib Diffus 39:51–56

Packwood RH, Brown JD (1981) A Gaussian expression to describe curves for quantitative electron probe microanalysis. X-Ray Spectrom 10(3):138–146

Philibert J (1963) A method of calculating the absorption correction in electron probe microanalysis. In: Pattee HH, Cosslett VE, Engstrom A (eds) X-ray optics and X-ray microanalysis. Academic Press, New York, pp 379–392

Philibert J, Tixier R (1968) Some problems with quantitative electron probe microanalysis. In: Heinrich KFJ (ed) Quantitative electron

probe microanalysis. NBS Special Publication 298, National Bureau of Standards, Washington, DC, pp 13–34

Pollock TM, Tin S (2006) Nickel-based superalloys for advanced turbine engines: chemistry, microstructure and properties. J Propul Power 22(2):361–374

Private communication with JEOL EPMA experts (2019)

Reed SJB (1965) Characteristic fluorescence corrections in electron-probe microanalysis. Br J Appl Phys 16

Reed SJB (2005) Electron microprobe analysis and scanning electron microscopy. Cambridge University Press, Cambridge

Rinaldi R, Llovet X (2015) Electron probe microanalysis: a review of the past, present, and future. Microsc Microanal 21(5):1053–1069

Sachdev AK, Kulkarni K, Fang ZZ, Yang R, Girshov V (2012) Titanium for automotive applications: challenges and opportunities in materials and processing. JOM 64:553–565

Schafrik R, Sprague R (2004) Saga of gas turbine materials part II. Adv Mater Process 162(4):27–30

Simandl GJ (2015) Carbonatites and related exploration targets. In: Simandl GJ, Neetz M (eds) Symposium on Strategic and Critical Materials Proceedings 13–14 November 2015; Victoria, British Columbia. British Columbia Ministry of Energy and Mines, British Columbia Geological Survey Paper, vol 3. pp 31–37

Tripathi S, Verma V, Brown TW, Kulkarni KN (2017) Effect of small amount of manganese on the interdiffusivities in Fe-Al alloys. J Phase Equilib Diffus 38:135–142

Tripathi A, Middleton S, Lavernia EJ, Sachdev AK, Kulkarni KN (2018) Ternary interdiffusion in β (BCC) phase of the Ti-Al-Nb system. J Phase Equilib Diffus 39(6):841–852

Tripathi A, Kulkarni A, Kulkarni KN (2020) Interdiffusion in β (BCC) phase of Ti-Al-Mn system at 1100 °C. Metall Mater Trans A 51A:1789–1798

Varshney A, Sangal S, Kundu S, Mondal K (2016a) Super strong and highly ductile low alloy multiphase steels consisting of bainite, ferrite and retained austenite. Mater Des 65:75–88

Varshney A, Sangal S, Kundu S, Mondal K (2016b) Superior work hardening behavior of moderately high carbon low alloy super strong and ductile multiphase steels with dispersed retained austenite. Mater Des 99:439–448

Varshney A, Sangal S, Mondal K (2017) Exceptional work-hardening behaviour of medium-carbon high-silicon low-alloy steels. Metall Mater Trans 48:589–593

Varshney A, Sangal S, Gouthama, Pramanick AK, Mondal K (2017) Microstructural evidence of nano-carbides in medium carbon high silicon multiphase steels. Mater Sci Eng A 708:237–247

Verma V, Tripathi A, Kulkarni KN (2017) On interdiffusion in FeNiCoCrMn high entropy alloy. J Phase Equilib Diffus 38(4):445–456

Verma V, Tripathi A, Venkateswaran T, Kulkarni KN (2020) First report on entire sets of experimentally determined interdiffusion coefficients in quaternary and quinary high entropy alloys. J Mater Res 35(2):162–171

Wilson RR (1941) Range and ionization measurements on high speed protons. Phys Rev 60(11):749–753

Ziebold TO, Ogilvie RE (1964) An empirical method for electron microanalysis. Anal Chem 36(2):322–327

Nanosciences and Advanced Imaging Centre: Unravelling Attributes by Electron Microscopy

Rajneesh Kumar Prajapati, Manish Kulkarni, Prabhat K. Dwivedi, and Sri Sivakumar

1 Introduction

The microscope has been emerged as the most fundamental tool for research in diverse fields of science and engineering, owing to limited resolving power of human eye. Resolving power or resolution of an unaided human eye is about 0.2 mm, which refers to the minimum distinguishable distance between two points. In order to see the points closer than that, a lens or a microscope, which is essentially the assembly of lenses is required to magnify the object. Since the dawn of science, there has been a lasting thrust among researchers to get the intricate details of their specimen in increased magnification, which offered substantial impetus to craft a microscope with enhanced resolution.

While relentless efforts for better resolution, it was realized that the resolving power of light microscope was not only limited by the number and quality of the lenses but also by the wavelength of the visible light used for illumination, thus precluding atomic scale imaging. A major breakthrough occurred in 1920s, when de Broglie discovered that accelerated electrons in vacuum behaves as light wave and exhibit wavelength thousands times shorter than that of visible light. Moreover, it was realised that these electrons have similar effect of electric and magnetic field as glass mirrors and lenses have on visible light. It didn't take long to translate these insights in to a microscope based on accelerated electron beam and in 1932 Knoll and Ruska proposed the term electron microscope. They developed the idea of electron lenses in to practical reality and later in 1986 received noble prize for this crucial discovery[1]. Since the development of first transmission electron microscope (TEM), enormous improvements in resolution have occurred over the past few decades which enabled advanced TEM to offer resolution close to 0.1 nm or better. In modern era, TEM has become an indispensible tool for establishing attributes such as particle size, crystalline habit, elemental composition and many more. While, *insitu* TEM provides a deeper insight to material sample under varying heating condition; *cryo* TEM opened newer paradigms towards imaging of diverse biological and other beam sensitive samples. Moreover, recent developments in tomography and quantitative scanning TEM (STEM) have further expanded the abilities of TEM by allowing three-dimensional (3D) reconstructions at nanoscale instead of only two-dimensional (2D) projections.

In this diverse and fast changing arena of nanosciences and nanoengineering, an analytical facility equipped with advanced electron microscopes and specimen preparation tools is highly desirable for sustainable research. In this milieu, Nanosciences (CNS) and Advanced Imaging Centre (AIC) at IIT Kanpur, has been established to disrupt the stratification of discipline in the characterization of materials (Fig. 1).It is among the eight centres supported by the Department of Science and Technology (DST) across India with the objectives of providing state of the art imaging facility and resources for research and development activities. These centres offer a critical mass and outstanding expertise in the wide range of electron microscopy techniques available for materials characterisation down to atomic scale. This facility is intended to bring together multidisciplinary expertise to drive synergy and amplify our characterization capabilities which support continuous fundamental research, innovations, brain storming and global interactions with academia as well as industry. Over the past few years Nanosciences and Advanced Imaging Centre has became the materials characterization hub for the academic institution, research centre and industry.

2 Electron Microscopes at CNS and AIC

Nanosciences and Advanced Imaging Centre offers two main types of electron microscope, namely, the transmission electron microscope (TEM) and the scanning electron

R. K. Prajapati · M. Kulkarni · P. K. Dwivedi · S. Sivakumar (✉)
Center for Nanosciences and Advanced Imaging Center,
IIT Kanpur, Kanpur, UP 208016, India
e-mail: srisiva@iitk.ac.in

K. Biswas et al. (eds.), *Electron Microscopy in Science and Engineering*, IITK Directions 6,
https://doi.org/10.1007/978-981-16-5101-4_7

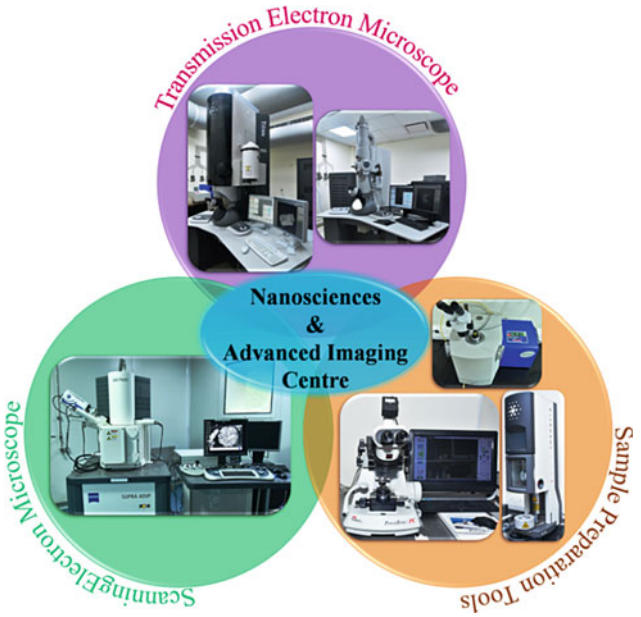

Fig. 1 Schematic overview of imaging facilities at nanosciences and advanced imaging centre

microscope (SEM). A transmission electron microscope produces an image by passing a high voltage electron beam through a very thin specimen that is transparent/semi-transparent to electrons. The beam that is transmitted through the specimen carries structural information about the specimen, which can then be magnified by the microscope. In stark contrast, a scanning electron microscope detects secondary and backscattered electrons that arise from the surface as a result of excitation by the original electron beam.[2]

The scanning electron microscope does produce lower resolution images than the transmission electron microscope, but since it uses surface electron interactions, it can image bulk samples which enable scientists to achieve 3D information about the physical features of the specimen.

Additionally, Scanning transmission electron microscopy (STEM) invoked the technology of both the scanning electron microscope and the transmission electron microscope. Major advantage of STEM imaging is that the signal is generated by the electrons scattered out at high angles and collected by high-angle annular dark field detector (HAADF), known for its intuitive atomic number contrast (Z-contrast imaging), which led to characteristic elemental mapping of the specimen (Fig. 2). Moreover, similar to TEM, STEM also requires very thin samples, as the technique mainly involves looking at the electron beam transmitted through and emerging from the specimen.

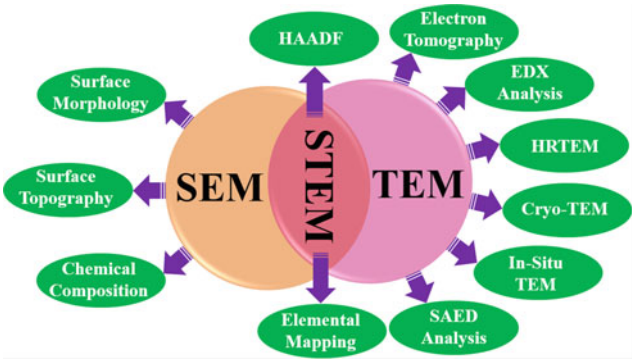

Fig. 2 Schematic representation of analytical abilities of SEM and TEM at nanoscience and advanced imaging centre IIT Kanpur

3 Scanning Electron Microscope

Center for Nanosciences (CNS) offers Zeiss Supra 40VP Field Emission Scanning Electron Microscope (FESEM), suitable for observing structures as small as 1 nm on the surface of the material with three-dimensional appearance. It is equipped with a field emission cathode as electron source and three different detectors namely In-lens SE, SE2 detectors and variable pressure secondary electrons detector (VPSE). In order to be observed with an SEM, objects are preferably made conductive for currents. This could be achieved by coating them with an extremely thin layer (1.5–3.0 nm) of gold or gold–palladium by using sputter coater available at the centre (Fig. 3).

4 Transmission Electron Microscope

TEM facility is present at Advanced Imaging Centre, comprised of two transmission electron microscopes, operating at different acceleration voltage and is meant for imaging diverse samples ranging from nanomaterials to biological samples.

4.1 FEI-Titan G2 60–300 kV TEM

The FEI Titan G2 60–300 scanning transmission electron microscope (STEM/TEM) is an advanced analytical field emission scanning transmission electron microscope for the characterization and chemical analysis of wide range of materials and nanostructures, down to the atomic level. It is equipped with a high-brightness Schottky-field emission electron source, a high-resolution Gatan Imaging Filter

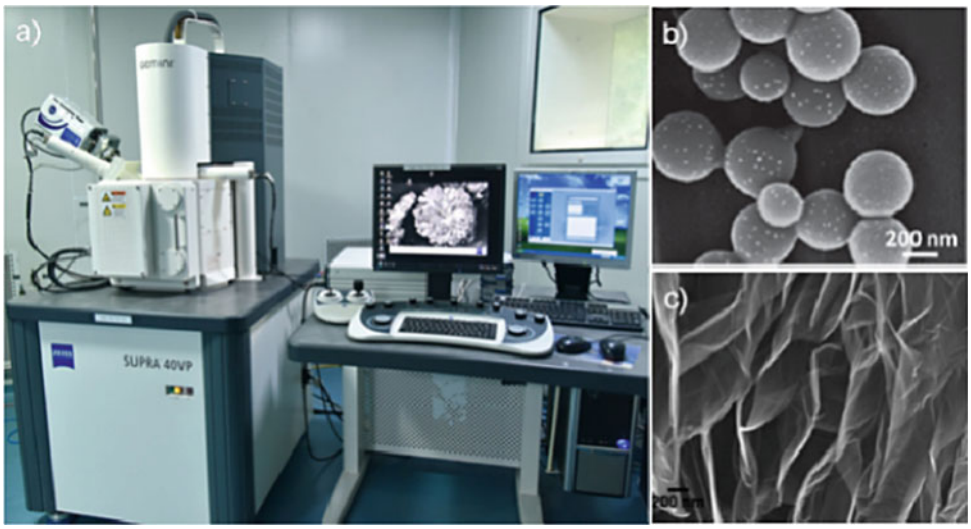

Fig. 3 **a** FESEM at the centre for Nanosciences; SEM image of **b** peptide soft structure decorated with Au nano particles(Reproduced from ref. 3 with permission from The Royal Society of Chemistry); **c** Graphine sheets (Reproduced from ref. 4 with permission)

(GIF), and X-ray energy dispersive spectrometer (EDS) for elemental and chemical analysis of materials at high spatial resolution. The microscope system also includes a high angle annular dark field detector (HAADF) for scanning transmission electron microscopy (STEM) and for chemical analysis of very small volumes. This instrument permits access to get critical information during imaging by exploiting diverse range of analytical, heating, cooling, and double tilt specimen holders (Figs. 4 and 5).

4.2 FEI-Tecnai G2 12 Twin 120 kV TEM

The Tecnai is an efficient and easy operation microscope with excellent analytical capabilities. It uses LaB_6 filament as electron source and could be exploited for the analysis of wide variety of samples ranging from materials to soft biological samples at room temperature as well as cryo-temperature. Moreover, it is compatible with tomography which could be useful in determining localization, orientation, shape and distribution.

5 Sample Preparation Lab

Unlike SEM, TEM does not offer a lot space for specimen. Additionally, specimen needs to be very thin so that electron can penetrate from the sample and form an image. This requires critical efforts to prepare quality samples for TEM as the results are strongly influenced by the quality of thin specimen.The imaging and analytical facilities at AIC are complimented by extensive sample preparation facilities for TEM and the preparation equipment covers a wide range of techniques to handle the large variety of samples brought

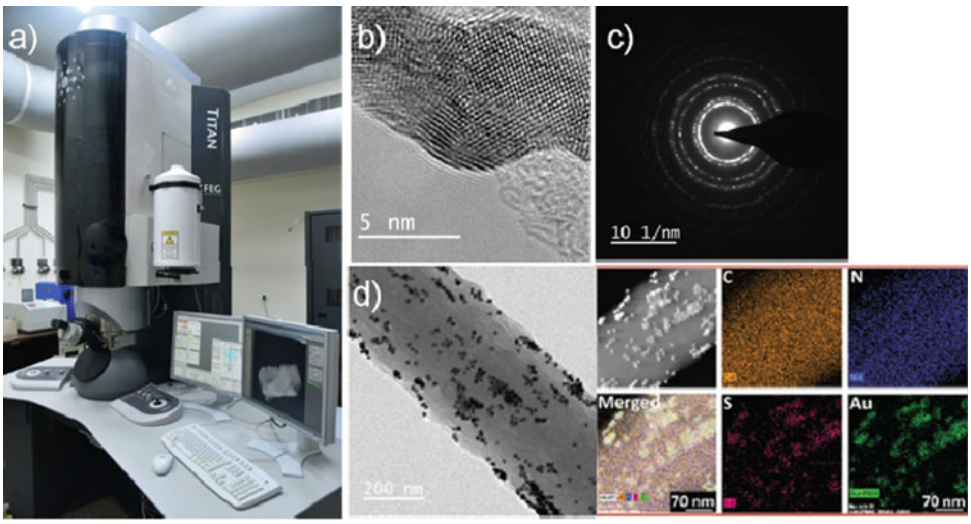

Fig. 4 **a** FEI-Titan G2 60–300 kV TEM, **b** HRTEM image, **c** SAED pattern of standard gold cross grating sample, **d** Elemental mapping of gold coated nanofibres (Reproduced from ref. 5 with permission from The Royal Society of Chemistry)

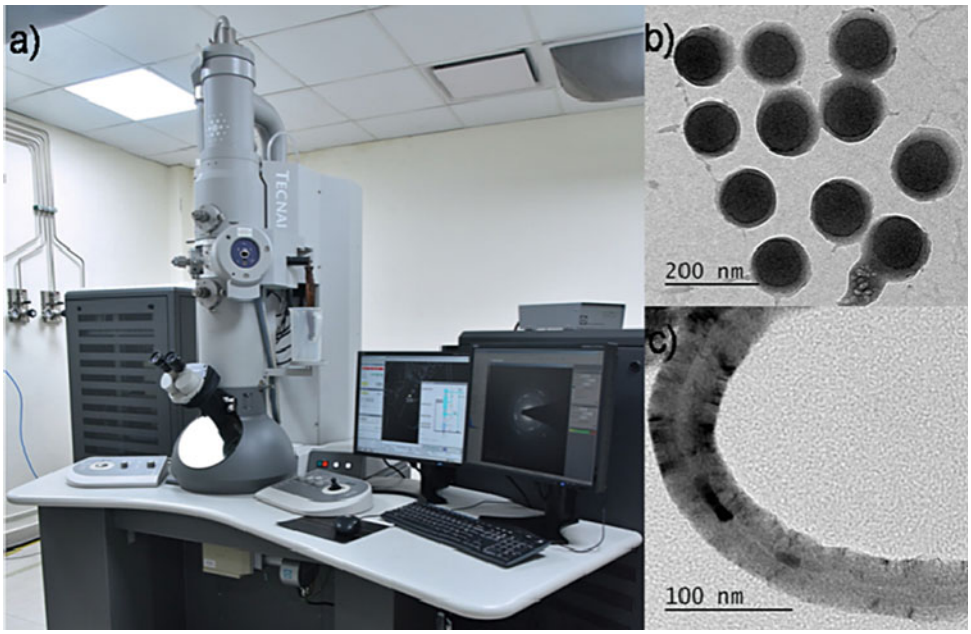

Fig. 5 **a** FEI-Tecnai G2 12 Twin 120 kV TEM; **b** TEM image of paint samples with core–shell structure; **c** TEM image of carbon nanotube

into the facility.While powdered sample can be dissolves/dispersed in an appropriate solvent followed by drop-casting over a supporting copper grid of 3 mm width; bulk samples require specific tools for cutting, grinding, dimpling, electropolishing and ion milling. For SEM preparation, there are carbon and gold sputter coaters, which can also be used for replica techniques. Moreover, centre is equipped with instruments required to proceed with soft material samples as well as biological samples, both at room and cryo temperature. Detailed description of tools available at the center has been discussed.

6 Precision Low Speed Saw

The TechCut-4 is a compact, multipurpose precision low speed saw designed to cut wide variety of small or delicate samples which cannot sustain at elevated temperature generated due to friction caused by high speed sectioning. The pivoting cutting arm has adjustable weights to apply or counterbalance downward force to the sample during sectioning. Cutting fluid is drawn from the reservoir by the blade to cool the sample. Samples up to 2`` thickness can be sectioned by using a 3' to 6`` blade range.

7 Variable Speed Polisher/Grinder

The MetPrep-1 grinding/polishing machine is excellent for polishing delicate samples using handheld tools with lapping films (Fig. 6b). It features digital control of all operations including run/stop, platen speed, platen direction and coolant flow. It includes 8' or 10`` platens with rotation speed ranges from 5–350 RPM, in either clockwise or counterclockwise direction, with smooth, consistent low-end torque.

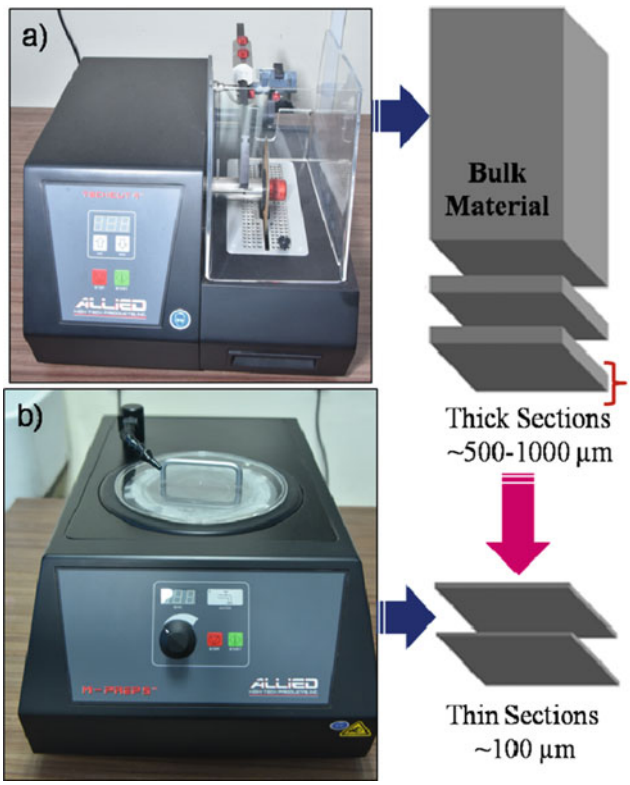

Fig. 6 **a** precision low speed saw; **b** Variable speed polisher and grinder and schematics of their capabilities

8 Ultrasonic Disk Cutter

The Ultrasonic Disk Cutter readily cuts transmission electron microscopy (TEM) specimens from hard, brittle materials without mechanical or thermal damage. It produces disk specimens as thin as 10 µm or cylindrical rods up to 10 mm length from bulk samples or rectangular wafers, which are subsequently being used in the preparation of cross-section TEM specimens. The cutting tool movement is governed by the excitation of lead zirconate titanate crystals oscillating at a frequency of 26 kHz. The cutting medium is abrasive slurry of either boron nitride or silicon carbide.

9 Dimpling Grinder

Dimpling Grinder is a state-of-the-art mechanical grinder required for prethining of specimens for ion milling while preparing electron microscopy samples. Dimpling is a rapid technique that involves rotating both the grinding wheel and the specimen, produces a specimen with only its central area reduced to a thickness of a few microns. The dimpling grinder features grinding rate control, a precise indication of specimen thickness, and an easy-to-use interface. The specimen can be accurately positioned using an optical microscope with transmitted and/or reflected light. The final specimen thickness is readily programmed for accurate, unattended operation (Fig. 7).

10 TEM Mill

TEM Mill is a sophisticated ion milling and polishing system offering reliable, high performance specimen preparation. It is compact, precise, and consistently produces high-quality transmission electron microscopy (TEM) specimens with large electron transparent areas from a wide variety of materials. It is equipped with two independently adjustable TrueFocus ion sources working over a wide range of operating energies (100 eV to 10 keV) and adjustable milling angle range of −10 to + 10°. These variables could be exploited for the rapid milling and slow specimen polishing of TEM specimens (Fig. 8).

11 PowerTome PC Ultramicrotome

PowerTome Ultramicrotome (including Cryo-ultramicrotome) is a computer controlled ultramicrotome used for the preparation of ultrathin/semi-thin sections as well as very flat

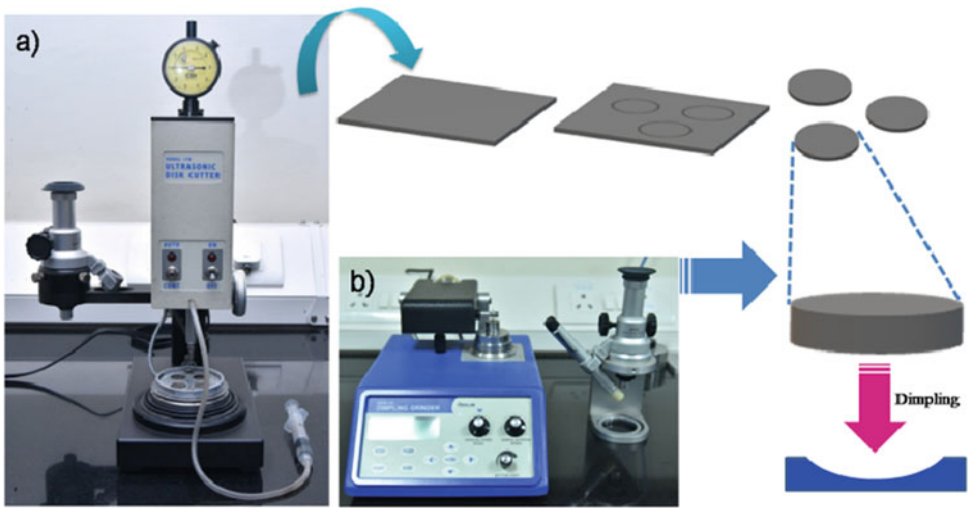

Fig. 7 **a** ultrasonic disc cutter; **b** Dimpling grinder and workflow scheme

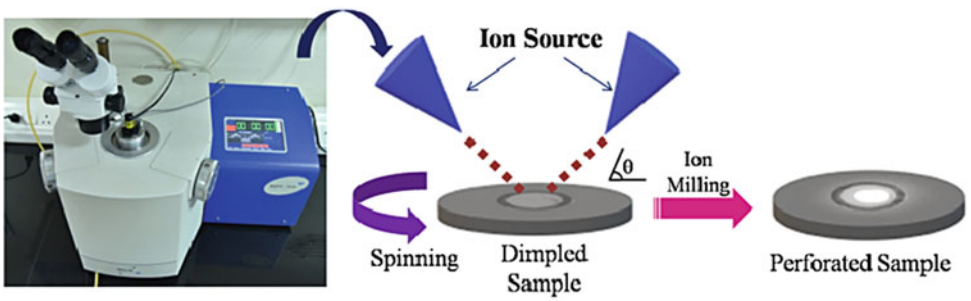

Fig. 8 Ion milling and its working scheme

surfaces of plastics, biological and biomedical objects for various microscopic investigations. This machine offers automatic sectioning range from 5 nm to 15 µm with cutting speed range from 0.1 to 100 mm/sec and there is a digital section counter and feed totaliser.

12 Vitrobot

The Vitrobot is a semi automated device for vitrification (plunge freezing) of aqueous samples. Critical vitrification parameters, such as temperature, relative humidity, blotting pressure and time, can be precisely controlled. A simple touch-screen user interface and programmable process control allow for consistent and high-yield sample output (Fig. 9).

13 Plasma Cleaner

Plasma cleaner automatically and quickly removes organic contamination (hydrocarbon) from electron microscopy specimens and specimen holders. A low energy, reactive gas plasma cleans without changing the specimen's elemental composition or structural characteristics. The Plasma Cleaner features easy-to-use front panel controls and an oil-free vacuum system for optimal processing.

14 Automatic Twin-Jet Electropolisher

Electrolytic thinning of conductive materials is an effective method of quickly producing specimens for transmission electron microscopy (TEM) without any induced artifacts. In Twin-Jet Electropolisher, twin jets simultaneously polish both sides of the sample, creating electron transparent specimens within a few minutes. The electropolisher features easily adjustable electrolyte flow, polishing voltage, termination detection sensitivity, and jet and specimen holder positions (Fig. 10).

15 Conclusions

In the current era of scientific research where chemistry, biology, material science, engineering, medicine and other disciplines are converging, comprehensive material characterization facility are essential to overcome the delay in

Fig. 9 **a** Vitrobot for plunge freezing, **b** Ultramicrotome for sectioning of samples

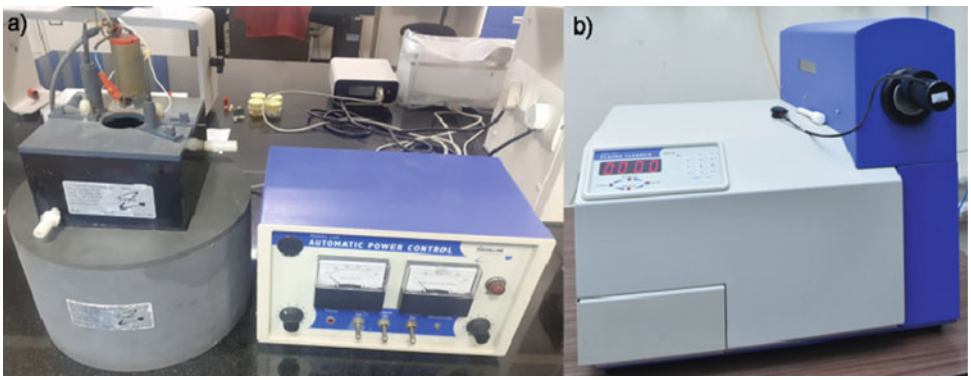

Fig. 10 **a** Automatic Twin-Jet Electropolisher; **b** Plasma cleaner

scientific discoveries. From the past few years, Nanosciences and Advances Imaging Centre are operating as a central facilities with users from inside the institute as well as access to local industry and outside universities.We are the centre which evolved as expert base breaking through the current characterization limitations in nanotechnology, medicine, environmental science, energy materials, and beyond.

Acknowledgements We gratefully acknowledge IITK grant for establishing electron microscopy facilities and providing infrastructural and recurring support for maintenance of the facilities. All authors are specially thankful to Profs. Ashutosh Sharma and Sandeep Verma for their efforts in establishment of CNS and AIC facilities.

Notes and References

Williams DB, Carter CB (1996) Transmission electron microscopy: a textbook for materials science. Plenum Press, New York

Zhou W, Wang ZL (eds) (2006) Scanning microscopy for nanotechnology. Springer, New York

Barman AK, Verma S (2010) Chem Commun 46:6992–6994

Naqvi TK, Srivastava AK, Kulkarni MM, Siddiqui AM, Dwivedi PK (2019) Silver nanoparticles decorated reduced graphene oxide (rGO) SERS sensor for multiple analytes. Appl Surf Sci 478:887–895

Saravanan RK, Naqvi TK, Patil S, Dwivedi PK, Verma S (2020) Purine-blended nanofiber woven flexible nanomats for SERS-based analyte detection. Chem Commun (Camb) 56(43):5795–5798

In-Situ Transmission Electron Microscopy Investigation of Phase Transformation Behavior of Alloy Nanoparticles

Khushubo Tiwari and Krishanu Biswas

1 Introduction

In every basic nanoscale science, research and commercial production of nanotechnologies entirely rely upon the potential of instruments and methodologies to determine, fabricate, sensitize, and manipulate the system at the nanoscale. Over the past decades, microscopy has gained advantages as compared to other characterization tools. Since it is more descriptive, the producing micrographs of objects that are directly associated to their morphology, shape, structure, and composition and thus it reveals spatial heterogeneities (Sinclair 2013). Recently, high-resolution transmission electron microscopy (TEM) is routinely utilized to acquired lattice high-resolution images of nanocrystalline materials through conventional TEM optics. However, in recent times, the state of the art has to turn to the sub-Angstroms high-resolution imaging and investigation attained using the images or examine aberration-corrected TEM instrument (Urban 2009; Krivanek et al. 2010).

Observing the physical process 'on-site' as they are arising and under many external stimuli is the dominant goal of the *in-situ* time-resolved technique. *In-situ* transmission electron microscopy (TEM) recently has drawn extraordinary attention from several fields ranging from chemistry, biology, and material science (Dehm et al. 2012; Banhart 2008). Since *in-situ* TEM is an essential and powerful tool for the nanomaterial depiction, it provides significant opportunities to probe the dynamic change in chemical composition, size, shape, and interface structure of nanoscale materials. At present, it is possible to acquire images at the atomic scale of materials in real time under several external stimuli to assessing relevant properties. Different kinds of *in-situ* TEM holders have been developed with the potential of capturing images and measurements under stress, optical excitation, heat, magnetic, and electric fields (Zewail 2010; Butler and Hale 1981).

Further, the advancement of environmental cells permits an investigation to be performed in different liquid and gaseous environments (Boyes and Gai 1997). Besides, the processing system and data acquisition improved temporal resolution and are capable of handling extensive data set generation. In the recent time, the motivation of *in-situ* TEM is to match scientific challenges, e.g., explaining synthesis route, nanoscale property, chemical activity measurement of nanoparticle, and mechanism of atomic scale failure; all these lead to the establishment of more explicit fabrication/synthesis–structure relationship properties (as shown in Fig. 1).

In this present article, we will illustrate some of the interpretation and understanding that has been attained by examples depicted from our work and experimental investigations of nanoalloy materials.

2 *In-Situ* TEM Instrumentation and Operation

In the past few years, various developments and modifications have been carried out in the dedicated design of electron microscopy columns. The vast advancement of auxiliary attachments, for example, stages, *in-situ* reaction process. At present, accessories and instruments for *in-situ* microscopy are not limited only for laboratory-made purposes but also crucial in commercially available. In this part of the section, a brief review of the modern or advance instrumentation for *in-situ* TEM will be discussed.

Typically, the microscope and specimen requirement for performing *in-situ* TEM or STEM (Scanning Transmission Electron Microscopy) experiments rarely not different from conventional TEM of STEM operation. Only the significant change is in the ability to employ external conditions and a few methods of analyzing as well as recording the resulting

K. Tiwari · K. Biswas (✉)
Department of Material Science and Engineering, Indian Institute of Technology, Kanpur, 208016, India
e-mail: kbiswas@iitk.ac.in

K. Biswas et al. (eds.), *Electron Microscopy in Science and Engineering*, IITK Directions 6,
https://doi.org/10.1007/978-981-16-5101-4_8

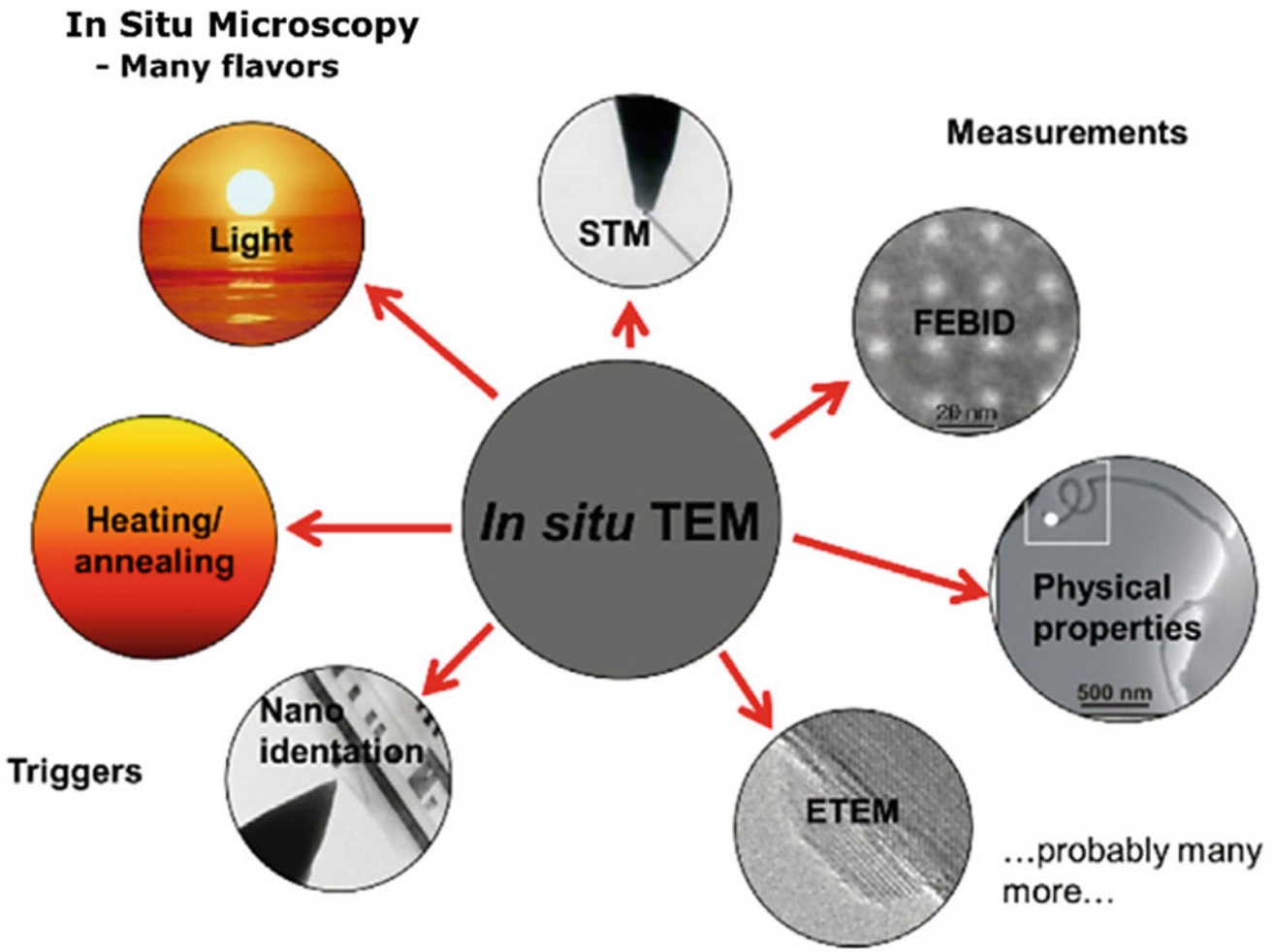

Fig. 1 External stimuli currently used for *in-situ* observations on TEM platform (Sinclair 2013)

dynamic reactions. Nowadays, the majority of the TEM systems are connected with charge-coupled devices (CCDs), which can function at ultrafast rates and with the television (TV) rate cameras. These attachments can record images within tens of milliseconds. Few significant drawbacks have been observed while recording images like considerable drift, tilting, and bending of the specimen. Thus, it is utmost to optimize the stability of the sample, stage, holder, and electron optics to the most satisfaction of our ability. These limitations can be reduced by recording images at ultrafast acquisition rates as inside the ultrafast electron microscope (UFEM). The operation and various examples of employing UFEM, including many benefits of using aberration-corrected TEM optics, for exploring nano-millisecond dynamics of many experiments have already been described and reviewed in the literature (LaGrange et al. 2008; Zewail and Thomas 2010). It is worth mentioning that this technique establishes an exciting opportunity of studying reactions and transformations that occur at the femtosecond time scale.

2.1 *In-Situ* Stages and Holders

In recent years, custom-made stages or modified sample arm has received a lot of attention due to the possibility to change materials by utilizing external influences inside the TEM (Han et al. 2007; Chen and Peng 2011). There are several types of TEM sample holders' ability of heating/cooling, specimen arms, evaporation/deposition of materials, and straining and lasing that are commonly available commercially or easily can be manufactured without much problem in the laboratory. In this section, we will briefly only discuss two modes of operations we widely used for our investigation.

I. ***Heating Stages:*** Many phenomena such as transformation or reactions such as recrystallization, growth, and phase transformation in materials occur at increasing temperature. *In-situ* heating holders for TEM are generally incorporated of the specimen arm and employ accurate Joule heating and heat dissipation

to acquire stable and tuneable samples at elevated temperatures. Gatan has manufactured the *in-situ* heating holder employed at IIT Kanpur with model number 652. This holder can be used up to a temperature of 1000 °C in the Tantalum furnace. The specimen is secured inside the holder using a beryllium hex ring mechanism and can be tilted up to $\alpha = \pm 45°$ and $\beta = \pm 30°$. The mechanical link between the heater and the stage of this model is made of a material with a near-zero coefficient of expansion to minimize thermal drift. Moreover, the temperature at the specimen holder tip is maintained near the heat of the specimen stage using a water-cooled specimen rod, thereby allowing for the least thermal loss. Figure 2 shows a schematic diagram of a Gatan single tilt heating holder that can adapt a 3-mm disk sample and can go 1000 °C while using a Tantalum furnace (https://www.gatan.com/products/tem-specimen-holders/heating-situ-holders; Idrees 2013).To perform high-resolution imaging at high temperatures, it is substantial to obtain stability at high temperatures and extremely low specimen drift. But these factors are difficult to attain due to a large specimen stage that has large thermal mass and thus contribute to gradual temperature response. To overcome these issues, the microfabricated heating holder has been assembled and is commercially available by DENs solution (https://www.denssolutions.com/en/our-products/sample-heat-ing-systems) and Protochips Inc. (http://www.protochips.com/products/aduro.html). Figure 3 shows the photograph of the *in-situ* heating holder of the Gatan model no. 652 available at the advance imaging center of IIT Kanpur. In these particular holders, integrated circuitry is commonly used to develop localized resistive heating instantly on the specimen support. These stages depict very low thermal mass and extremely high thermal stability that permits high-resolution imaging at high temperatures.

II. ***Cooling Stages:*** TEM cooling holders are used for applications which necessitate low-temperature observations of *in-situ* phase transformations and to reduce contamination due to carbon migration. They can also be used to reduce unwanted thermal effects in various analytical techniques such as energy-dispersive X-ray spectroscopy (EDS) by reducing contamination and mass loss. Typically, such holders are cooled via a well-insulated, bubble-free cryogen dewar. The high mechanical stability of the dewar helps to minimize drift during use. Precise temperature control of the specimen is achieved through a conductor rod connecting the specimen holder to the cryogen dewar, which contains an electric heater to control the specimen temperature. The temperature of the holder is monitored by a calibrated silicon diode that provides a sensitive response for precise temperature control of the specimen. The holder also provides a robust mechanism for tilting the sample with the β-tilt maximum of ± 30°. Figure 4 presents the photograph of the *in-situ* cooling stage (Gatan Inc.) available at IIT Kanpur for investigation.

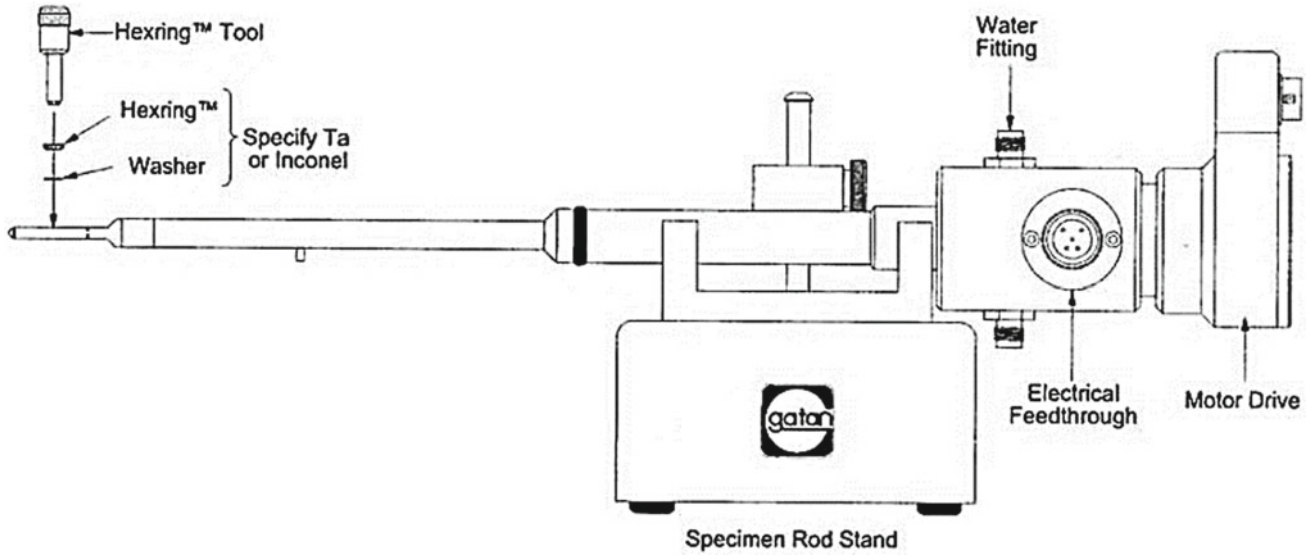

Fig. 2 Schematic figure of the Gatan single tilt heating holder (https://www.gatan.com/products/tem-specimen-holders/heating-situ-holders)

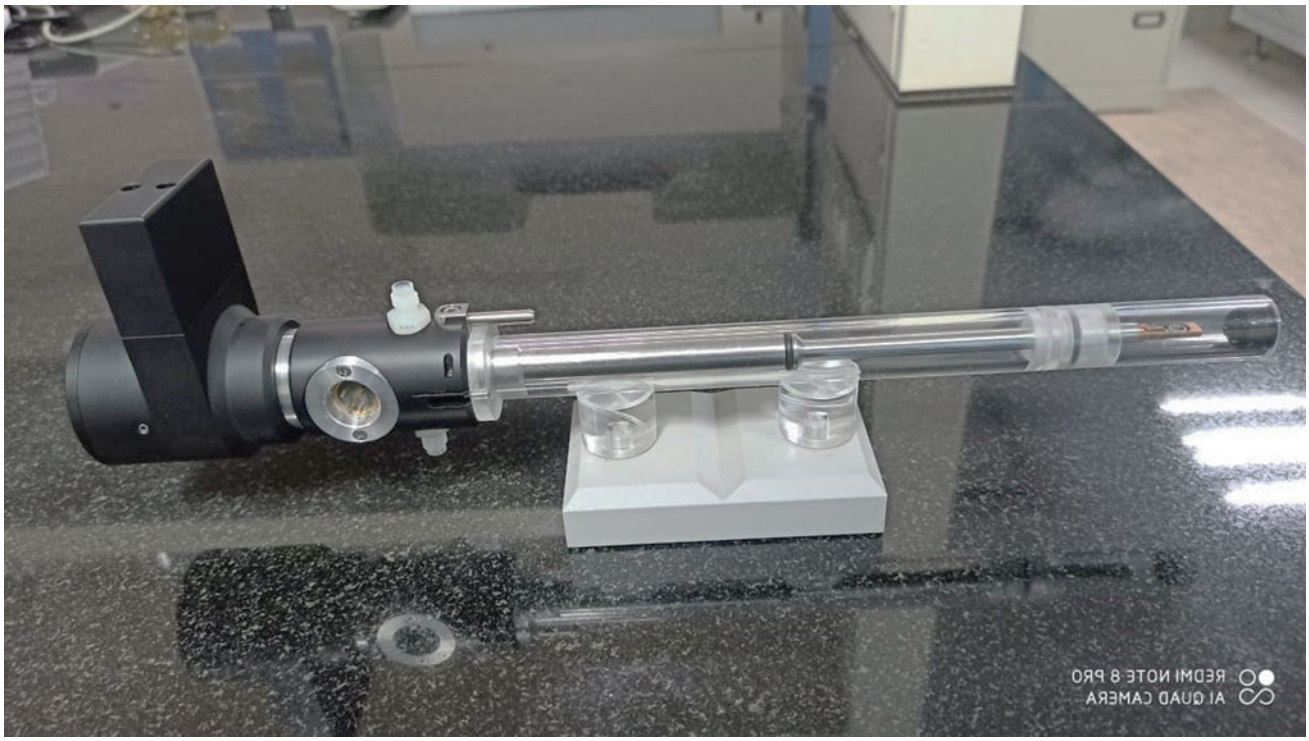

Fig. 3 Photograph of the *in-situ* heating holder of the Gatan model no. 652 available at advance imaging centre of IIT K

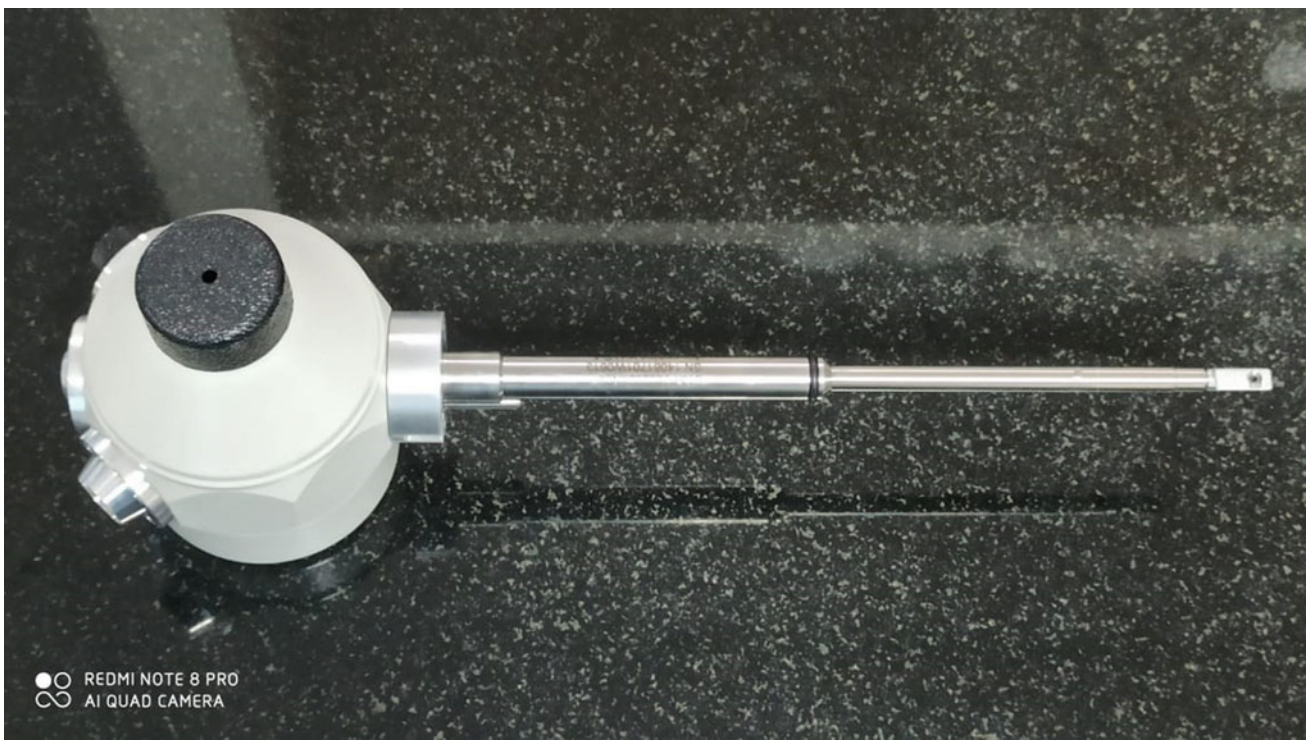

Fig. 4 Photograph of the *in-situ* cooling holder (Gatan Inc.) available at advance imaging centre of IIT K

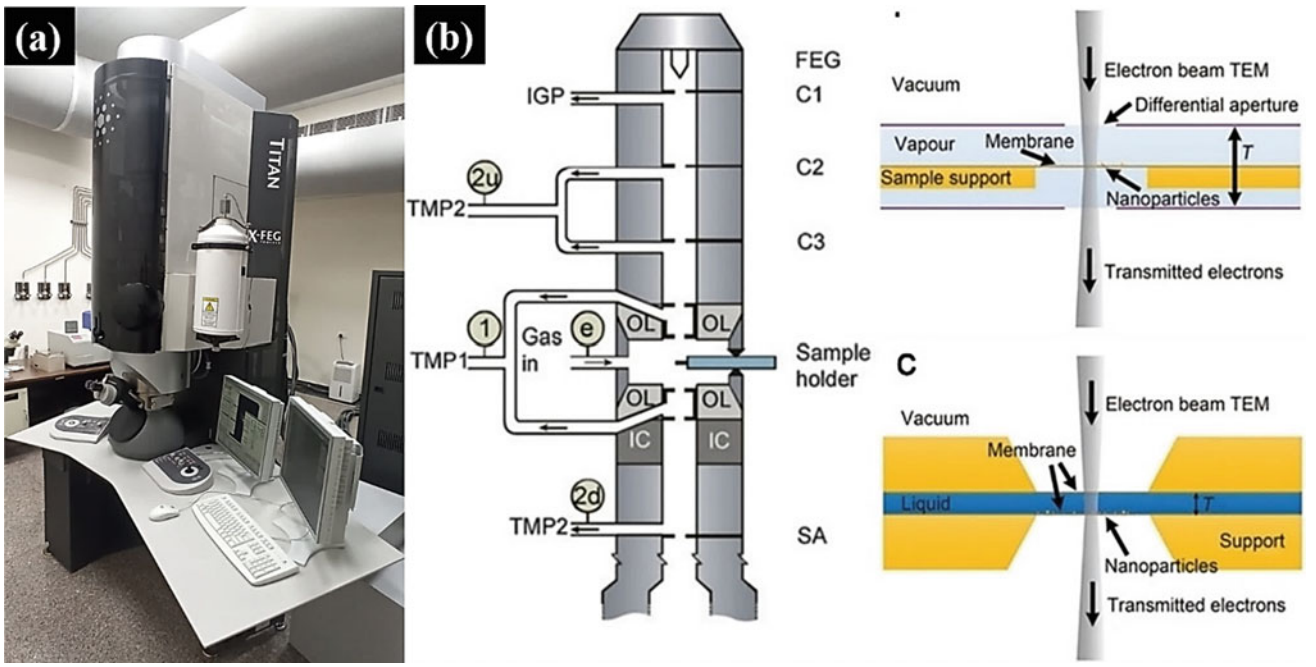

Fig. 5 **a** Photograph of FEI Titan 80–300 field emission scanning transmission electron microscope (**b**). **a** A diagram of a typical in-situ TEM with a differential pumping system, indicating the ultra-HV system, the pressure-limiting apertures and two sets of the differential pumping systems (He et al. 2020)

2.2 Advanced Transmission Electron Microscopy

The FEI Titan 80–300 STEM is an advanced analytical field emission scanning transmission electron microscope competent of atomic-level imaging and analysis on a wide range of materials and nanostructures (as shown in Fig. 5a–b) (He et al. 2020). The Titan is equipped with an electron energy loss spectrometer and X-ray energy-dispersive spectrometer for elemental and chemical analysis of materials at high spatial resolution. The microscope system comprises a scanning module and a high-angle annular dark-field detector for scanning transmission electron microscopy (STEM) and chemical analysis of minimal quantities. Aberration-corrected STEM/TEM is proficient at producing images with 0.07 nm resolution with Cs correction. It is equipped with a high-brightness Schottky field emission electron source with a high maximum beam current (>100 mA), a high-resolution Gatan imaging filter (GIF) Tridiem energy filter, and with third-order spectrometer aberration correctors. The imaging aberration corrector can entirely correct for coherent axial aberrations up to third order and partially compensates for fourth- and fifth-order aberrations. The microscope has two 2048 × 2048 slow-scan CCD cameras; one is bottom-mounted, and one is the GIF camera. The maximum tilt angle for the STEM with a double-tilt holder is ± 40°, whereas the maximum tilt angle with tomography holder is ± 80°.

3 Phase Transformations in Nanostructured Materials Using *In-Situ* Electron Microscopy

Nanotechnology has become a rapidly emerging field in recent times. Nanomaterials often show an effective and drastic change in physical, chemical, mechanical, electronic properties as compared to their bulk counterparts (Calvo 2013). The most typical characteristic observed in nanosized materials is the size dependence of several properties, including electrical, catalytic, magnetic, thermal, and optical (Jellinek 2008; Ferrando et al. 2008). It reveals that these properties strongly depend on grain size or crystallite size. Therefore, extraordinary and novel properties showed by the nanomaterials have attracted the researchers. From the last two decades, nanoalloys have developed as a unique field to enhance the properties of the materials. In general, nanoalloys are commonly referred to as multimetallic nanoparticles, without chemical ordering inside the alloy (Calvo 2015). Considerable researches have been reported in the literature based on the various properties and structural complexity originating due to shape, size, and composition effects (Calvo 2015; Ferrando 2016). The principle of phase transformation of nanoalloys necessitates being investigated to comprehend the size-dependent effect in the properties of nanoalloys, e.g., melting temperature, the thermal stability of different phases, alloying at the nanosized particle, order–

disorder transformation, etc. These nanomaterials can be in the form of free-standing (without matrix) or embedded (encapsulated in the matrix) nanoparticles. In free-standing nanoparticle, the surface energy is created due to the large surface area, which dominates the total free energy of the system. On the other hand, in the embedded nanoparticle, the additional interfacial energy is created due to the formation of an interface between particle and matrix. This interfacial energy can be altered by embedding the nanosized particle in different matrices (Chattopadhyay and Bhattacharya 2004; 2003).

From the last two decades, the phase transformation study of pure metal nanoparticles embedded in amorphous, crystalline, and quasicrystalline matrices has been extensively investigated (Mei and Lu 2007; Chattopadhyay and Goswami 1997). From these extensive studies led to a fair understanding of the phase transformation (i.e., melting and solidification) behavior and morphological evolution of nanoparticle embedded in various matrices. The alloy nanoparticles can be further classified based on their morphology into two distinct categories: single and multiphase alloy nanoparticles (shown in Fig. 6). In the case of multiphase nanoalloy particle forms, additional interfaces between phases exhibit in the alloy nanoparticle as compared to the single-phase nanoalloy particle and pure metal nanoparticle (Chattopadhyay and Bhattacharya 2004). Biphasic alloy nanoparticle comprises two different phases, and triphasic alloy can have three distinct phases (shown in Fig. 6 with a research example). The existence of an additional interface constitutes between phases that are the same for both the free and embedded alloy nanoparticles. Interfacial energy comprises both chemical and structural contributions.

From the last two decades, extensive researches have been carried out on the phase transformation of single-phase nanoalloys (Khan and Biswas 2015; Siem* and Johnson 2005). Recently, multiphase alloy nanoparticle has gained tremendous attention due to their distinct properties as compared to pure metal or single phase. The majority of the research work focused on multiphase nanoalloy particles embedded in various matrixes. From these studies, it has been categorically indicated that the interface between matrix and nanoparticle plays a vital role in the melting behavior and thermal stability of nanoalloys (Chattopadhyay and Bhattacharya 2004, 2003,2009). It is also noted that the effect of matrix on the melting and solidification behavior of embedded nanoparticles cannot be decoupled. This limits the possibility of understanding the intrinsic phase transformation behavior of alloy nanoparticle.

3.1 *In-Situ* Transmission Electron Microscopy of Multiphase Alloy Nanoparticle

In this section, we will dwell on different aspects of phase transformation of multiphase nanoalloy particles. In particular, melting and solidification of free and embedded multiphase alloy nanoparticle will be discussed. In the following, we will discuss some of the investigations achieved from our research work carried out in our laboratory at IIT Kanpur.

3.2 Method and Materials

It is important to note that in general, the behavior is often shown by free nanoparticles are not same what observed in embedded nanoalloy particle. The properties altogether depend on the methodology that has been utilized to prepare the nanomaterials. In the following section, we will first briefly discuss the synthesis route of nanoparticle.

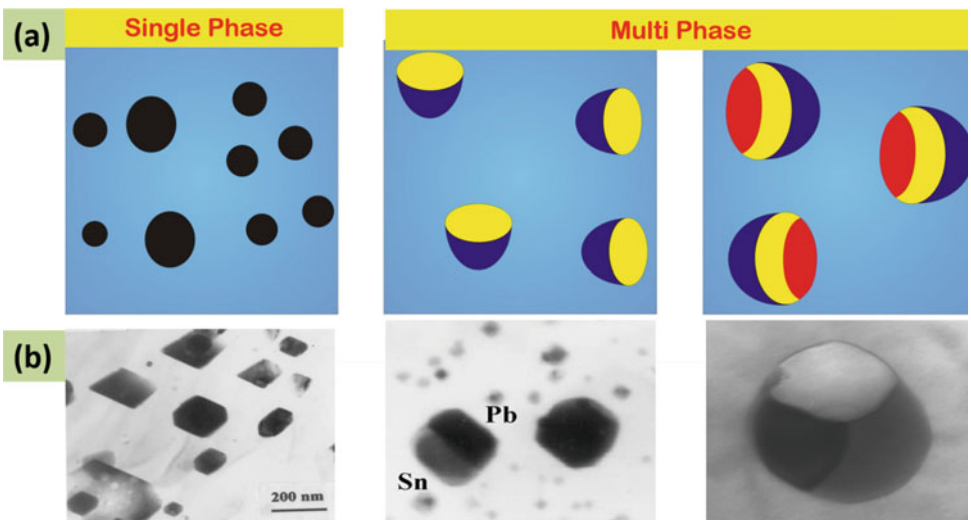

Fig. 6 **a** Schematic representation of distinct categories of alloy nanoparticles: single and multiphase **b** the examples of each category from the research work

I. ***Synthesis of free alloy nanoparticles***

To synthesize the free alloy nanoparticle, several facile chemical synthesis routes have been adopted. The chemical route has been reported to be an effective route due to the controlled synthesis of the particle with desirable shape, size, and composition. Several routes have been employed to synthesize free nanoalloy particles. In this section, we will only discuss the most popular route in the trend for preparing these nanomaterials.

First is the solgel process; this route is widely used to synthesize free alloy nanoparticles. The solgel process has two approaches: hydrolysis and condensation. This process is initiated with the formation of a concentrated mixture containing hydroxide or metallic oxide by hydrolysis (Jones 1990; Brinker and Scherer 2013). The next route is micro-emulsion method or reverses micellar route; in this route, hydrophilic head and hydrophobic tailor of the surfactant are conducted inward and outward, which ensues into the formation of the internal core holding water (Garcia Esparza 2011). Therefore, reverse micelle is regarded to be the nanoreactors because the reaction occurs in its inner core. In addition to this route, the solvothermal or hydrothermal method is very commonly used for preparing free nanoparticle. The fundamental principle of this route is that when the solvent is heated in a closed vessel, the temperature increases much above the ideal boiling point, which further leads to self-generated pressure exceeding higher than the ambient pressure, and this raises the boiling point of the solvent much above the vital temperature and pressure. Later, the solvent behaves like a supercritical liquid (Byrappa and Adschiri 2007).

II. ***Synthesis of nanoembedded particles***

In recent times, the most popular synthesis route for preparing embedded nanoparticle is melt spinning (rapid solidification route) and ion implantation. These processes are very competent when the embedded nanoparticle makes the immiscible system with the matrix. Rapid solidification is associated with a distinctive cooling rate of the order of 10^6K/s, in which the cooling rate is attained by a conductive heat transfer process (Suryanarayana 1991). On rapid cooling a melt by an immiscible realm, the liquid phase separates and makes an emulsion of clear liquids. Later on, the significant fraction of melts solidifies as the matrix, thereby developing a distribution of small packet liquid particle dispersed in the matrix. Eventually, the liquid particles get solidified to provide final nanomaterials, whereas, in the case ion implantation process, high-energy ions generate the energy contributed to local altering or disordering of the matrix of the materials (Ziegler 2012). This process encounters in the solid state and is substantially dominated by the crystal orientation of the matrix. Therefore, it often observes an epitaxial orientation relationship between the matrix and nanoparticles. Further, the mechanical alloying route is also utilized for the formation of nanoembedded particles, which includes breaking down both embedded nanoparticle and matrix by continuous fracturing and re-welding process in the solid state (Suryanarayana 2001).

3.3 Results and Discussion

In the following section, the experimental results on several alloy systems will be deliberated and discussed. Primary interest will be given to the melting of the alloy nanoparticles. We will start presenting with the melting behavior of free nanoalloy, followed by the embedded nanoparticle.

In order to understand the intrinsic melting behavior of an alloy nanoparticle, the nanoalloy should not be confined by matrix; i.e., the nanoparticle needs to be free surfaces. In this respect, some studies have been carried out on free single and multiphase nanoalloy particles (Khan and Biswas 2015; Bhattacharya and Chattopadhyay 2007; Johnson et al. 2000; Khan et al. 2015). Recently, we have attempted an effort to investigate the size effect on the melting behavior of the multiphase Pb-Sb alloy nanoparticle by extensive use of *in-situ* TEM. From the equilibrium phase diagram, the binary system Pb-Sb shows a two-terminal solid solution of FCC (Pb) and rhombohedral (Sb) and exhibits eutectic reaction at the temperature of 251.4 °C for the composition of Pb-17.5 at.%Sb (Massalski 1992). The composition was chosen for study the multiphase free alloy nanoparticle was Pb-17.5 at.%Sb. Free nanoalloy particles were synthesized by the solvothermal route (Devi and Biswas 2015; Devi et al. 2019). During *in-situ* studies, a sequence of video of the heating experiment was recorded and further analyzed to acquire the melting behavior of individual nanoalloy particles. Thermocouple made up of a Chromel–Alumel was attached to the specimen holder to record the temperature, and the temperature was calibrated (± 2 °C). Figure 7 indicates the heating sequence of the two-phase alloy nanoparticle. Up to the temperature of 234 °C, no considerable change in the shape of nanoparticle has been observed, whereas the relative area fractions and their facets of phases present in the nanoparticle undergo alteration while heating. As the temperature rises and reaches 239 °C, an abrupt change appeared at the triple junction of the outer surface and interface between (Pb)/(Sb), which suggests the initiation of melting. The onset melting temperature of Pb-Sb alloy nanoparticle (239 °C) is lower (13.5 °C) than the

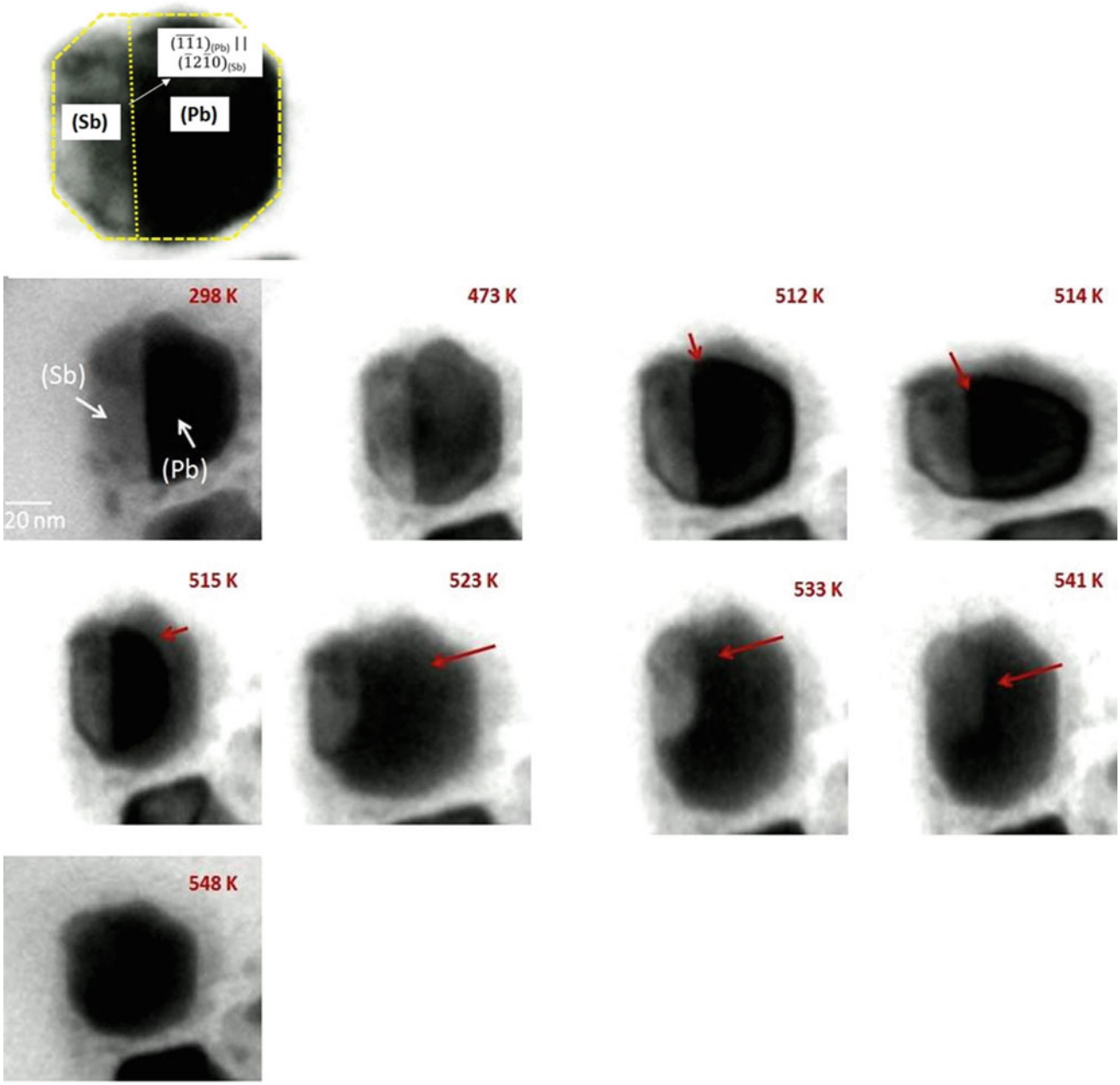

Fig. 7 A series of TEM micrographs showing melting within a Pb-Sb nanoparticle during the in situ heating experiment (Devi et al. 2019)

equilibrium eutectic temperature (252 °C). As the temperature rises further, initially, the liquid front spread along the (Pb) surface boundary instead of spreading along with the interface between (Sb)/(Pb). At the temperature of 250 °C, the (Pb) phase entirely melts; subsequently, the liquid front propagates along (Sb) phase, and the whole nanoparticle became molten (at 275 °C).

As we have stated earlier, the embedded nanoparticle can constitute multiple phases having different shapes and sizes, with a common interface. In the case of two-phase embedded nanoparticle, they comprise three interfaces: the interphase interface between two phases and interfaces among matrix and two phases of the nanoparticle. These interfacial energies have a key role in determining the phase transformation behavior of multiphase embedded nanoparticles. Therefore, it provides lots of opportunities to change the interface between the phases in the nanoalloy particle and matrix (Chattopadhyay and Bhattacharya 2004; Chattopadhyay 2005). In this regard, we have investigated to understand the phase transformation of multiphase embedded Pb–Sn nanoalloy particles *via* a melt spinning route. Earlier extensive investigations have been reported on

literature (Bhattacharya et al. 2002; Fecht and Perepezko 1989; Fecht et al. 1989; Johnson et al. 2001). Johnson et al. depicted the formation of a single phase of (Pb) solid solution before the melting of the nanoalloy particle embedded in the Al matrix prepared by ion implantation (Johnson et al. 2001). Subsequently, Bhattacharya et al. performed an *in-situ* heating experiment to probe the melting behavior of Pb–Sn (1:1) nanoparticle embedded in the Al matrix via melt spinning (Bhattacharya et al. 2002). Therefore, it shows some ambiguity in the understanding of the melting behavior of the Pb–Sn nanoalloy particle. Thus, to investigate the existence of exact melting behavior, an attempt has been made to carry out an in-depth investigation of $Pb_{26.1}Sn_{73.9}$nanoparticles embedded in two different matrices: Al (crystalline) and Al-Cu-Fe (quasicrystals) via melt spinning. While the presence of Pb–Sn nanoinclusions in the Aluminium matrix, synthesized through rapid solidification route, leads to the formation of two-phase nanoparticles consisting of (Pb) (FCC) and β-Sn (Tetragonal). Taking this into account, a detailed investigation has been carried out on the melting and solidification behavior of the Pb–Sn biphasic embedded alloy inclusions using *in-situ* TEM investigation tools. The subsequent discussion involves the phase transformation behavior of biphasic Pb–Sn alloy nanoparticles embedded in the crystalline (aluminum) and the quasicrystalline ($Al_{65}Cu_{20}Fe_{15}$) matrices. Particularly, $Pb_{26.1}Sn_{73.9}$ alloy undertakes eutectic solidification ($L \rightarrow Pb + \beta\text{-}Sn$) through regular lamellar morphology at 183 °C. Detailed in-situ heating stage experiment has been performed inside the TEM column in both cases. The evolution of the melting event is depicted by a set of dark-field images (as shown in Fig. 8a–g). Preliminary heating (much below 171 °C) changes the area of the illuminated (Pb) phase. This shows that there is the tuning of the volume fraction of (Pb) and β-(Sn) phases in the nanoparticle as a function of the temperature. The assessment *via* the dark-field images indicates that the relative volume fraction of (Pb) declines as the temperature rises. However, Sn from (β-Sn) segment dissolves into the (Pb) segment at 171 °C. It can be clearly seen that the biphasic particle changes into metastable single-phase FCC (Pb) at the corresponding temperature followed by the melting of the particle at about 182 °C, which is almost the bulk melting temperature (183 °C) of the alloy particles. This is the first such clear indication showing transformation during an in-situ TEM study. The results of the in-situ cooling of an alloy nanoparticle embedded in the QC matrix from the liquid state are shown in Fig. 9b. The bright field micrograph of the biphasic particle is shown in Fig. 9a, showing β-(Sn) and (Pb) regions. The figure illustrates the completely molten state of the particle. The figure shows that a small portion of the particle has been solidified. In-depth diffraction experiment shows the solidified portion as FCC (Pb). At about 150 °C (Fig. 9d), complete solidification occurs for the particle into metastable FCC (Pb). Upon subsequent cooling while in the solid state, the metastable phase separates into (Pb) and (Sn) lamellae. The particle achieves a morphology similar to a eutectic particle consisting of FCC (Pb) and BCT β-(Sn) at room temperature.

Since multiphase embedded nanoalloys are noticeably different and complex in comparison with single-phase nanoalloys, the total Gibbs free energy increases due to the presence of additional interface within the nanoparticles. This sequentially can change the melting and alloying behavior of nanoparticles. Hence, an in-depth understanding of the thermal stability of the multiphase embedded nanoparticles is imperative. To investigate the thermal stability of the multiphasic nanoparticles, triphasic alloy nanoparticles have been selected. It becomes more cumbersome to understand the triphasic embedded alloy nanoparticles because of the presence of three distinct phases and a large number of interfaces between matrix and phases in addition to the internal interphase interface within the nanoparticles. Nevertheless, the embedded triphasic alloy nanoparticles offer the best possible scenario to understand the nanoscale alloying. Thus, to understand the melting behavior of triphasic nanoparticles, we have chosen Bi-In-Sn alloy nanoparticle embedded in the icosahedral quasicrystalline (IQC) matrix (Tiwari et al. 2020). The calculated phase diagram demonstrates the two invariant eutectic reactions E1 and E2 at the temperature of 76.08 and 58.73 °C, respectively. For the present investigation, a ternary eutectic reaction (E1) present in the bismuth-rich region of the phase diagram has been selected. The eutectic reaction is associated with the transformation of liquid to three solid phases; (Bi), BiIn, and (β-Sn). Triphasic $Bi_{44}In_{32}Sn_{23}$ nanoalloy embedded in IQC ($Al_{65}Cu_{20}Fe_{15}$) matrix was synthesized *via* the melt spinning route. An *in-situ* heating experiment has been performed inside the TEM column for a detailed investigation of the melting behavior of the nanoparticles. Figure 10a shows the sequence of the micrographs, revealing the melting of the nanoparticle. A set of bright field images depicts the progression of the melting event. Initially, the heating up to 40 °C shows no substantial change in the nanoparticle. At 45 °C, the transformation of (γ-Sn) to (β-Sn) and at 70 °C, the whole (γ-Sn) region completely transforms into (β-Sn). Concurrently, there is an initiation of melting at the triple junction of BiIn, (Bi), and IQC matrix. BiIn melts at 77 °C and melts transverse along with the interphase interface. As the temperature increases, the propagation of the melt front initiates along (β-Sn), and the matrix interface and (Bi) phase melt abruptly once the temperature reaches 100 °C. The schematic illustration of the melting of triphasic Bi-In-Sn embedded nanoparticle is shown in Fig. 10b.

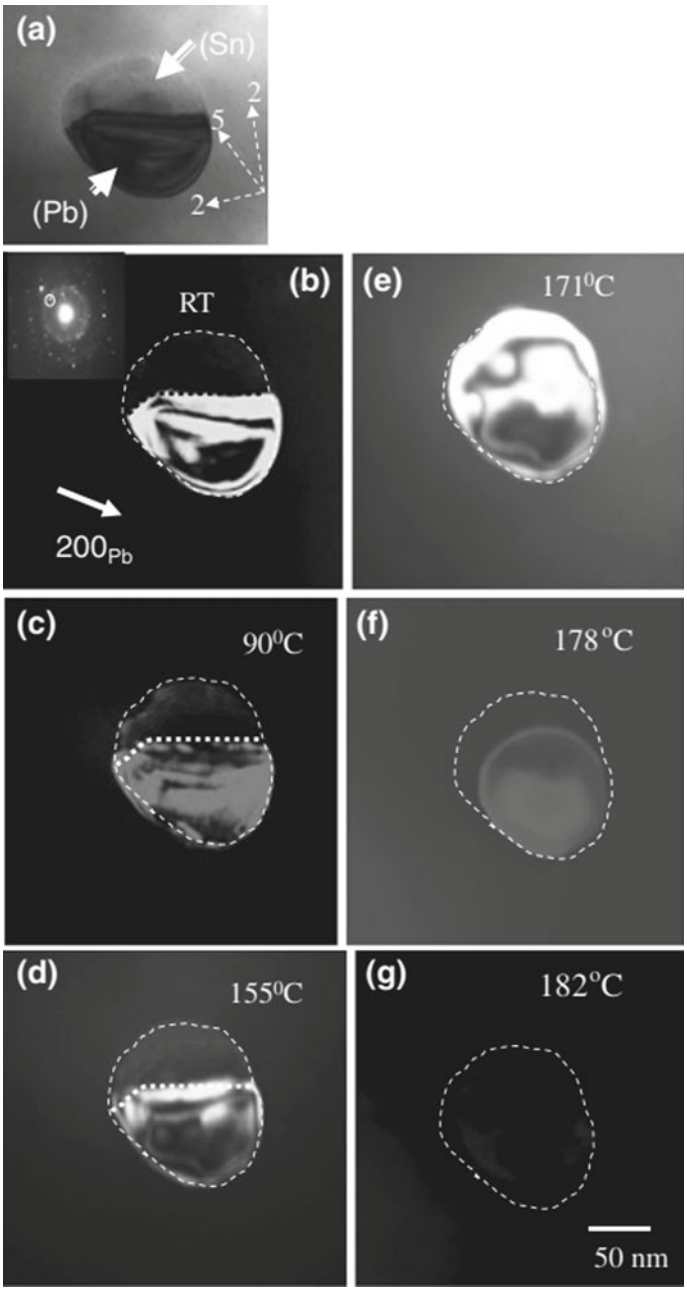

Fig. 8 Dark-field images obtained using in situ melting TEM study of **a** Pb–Sn eutectic biphasic particle within a matrix grain: a bright field micrograph; **b** RT; **c** 90 °C; **d** 157 °C; **e** 171 °C; **f** 178 °C and **g** 182 °C (Tiwari et al. 2020)

4 Other Kind of *In-Situ* Holder and Their Applications

I. **Environmental *In-situ* TEM**

A conventional TEM requires a high vacuum (order of 10^{-6} tor or higher) inside the specimen chamber to yield the operation of electron source as well as to minimize scattering apart from the sample (Boyes and Gai 1997; Gai et al. 2008), whereas various processes with primary importance in material science, for example, catalytic reactions or crystal growth, are participating in high gas pressure or atmospheric pressures. A detailed characterization procedure for understanding the kinetics of these processes by electron microscopy is to sample, *ex-situ* at various reaction times. On the other hand, accurate dynamics information of the complete transformation during, such as gas-phase catalytic process or vapor–liquid–solid growth is merely possible to acquire by carrying out *in-situ* reaction inside the TEM. Thus, the further led to the development of dedicated TEM and a representing technique known as environmental electron microscopy (Boyes and Gai 1997; Gai et al. 2008).

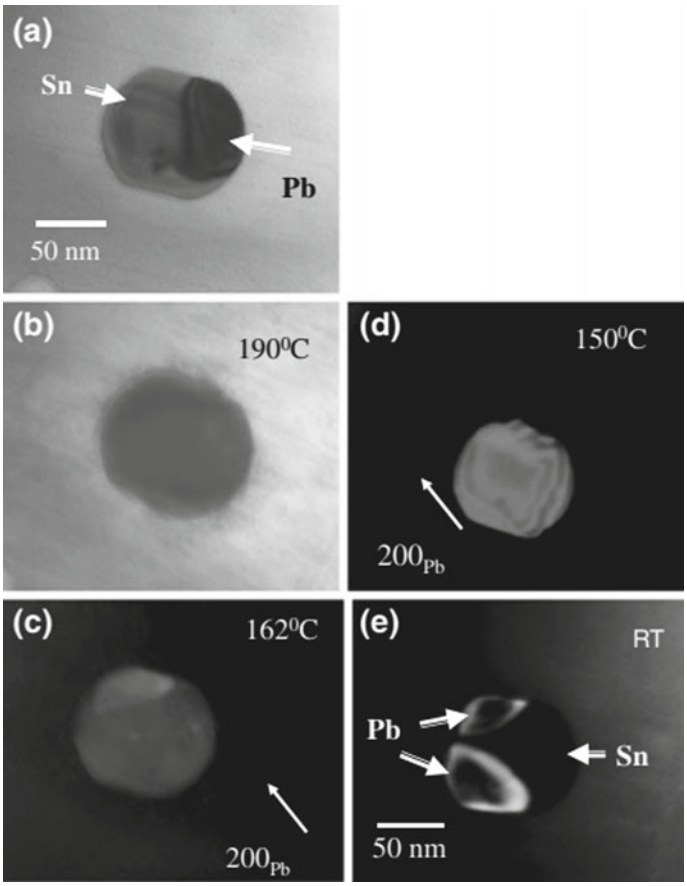

Fig. 9 **a** Bright-field image of the biphasic particle at room temperature; **b** at 190 °C, Dark-field images obtained using in situ TEM study of the biphasic particle within a matrix grain: **c** 162 °C; **d** 150 °C and **e** room temperature (Tiwari et al. 2020)

High-resolution environmental electron microscopy was developed in 1997 by Boyes and Gai (1997), which was built by few modifications of the electron chamber of a company Philips CM30 electron microscopy (Gai et al. 1995). Figure 11 shows the schematic representation of environmental electron microscopy setup. In the environmental TEM setup, differential pumping is attached by turbomolecular pumps (TMOs) or molecular drag pumps (MDPs) among the apertures. Subsequently, Hitachi (https://hitachi-hta.com/products/electron-ion-and-probe-microscopy/transmission-electron-microscopes/h-9500-300kv-te), FEI (https://www.fei.com/products/transmission-electron-micro-scopes/titan/etem.aspx), and JEOL (https://www.jeolusa.com/PRODUCTS/Transmission-Electron-Microscopes-TEM/Analytical-Data-Optimization/Practical-Remote-In-Situ-Microscopy-PRISM) all developed customized environmental TEM equipment based on the same approach. Despite the fact that these TEMs are more costly than the conventional electron microscopy, these instruments are going more accessible to the scientific community as well as acquiring many attentions and popularities. Most importantly, when environmental TEM module is attached to an aberration-corrected optics, instruments develop extremely powerful in probing any transformation behavior at very high resolution, underneath varying gas atmosphere and high temperature. The greater advantage of having aberration-corrected optics is in the potential to acquire high atomic resolution images in a single exposure (Gai et al. 2010). Recently, a method has been developed where gas is introduced around the sample through a gas injection nozzle, which is equipped on a sample heating holder. In this modified assembly, other components like objective lens pole pieces, specimen chamber, and the vacuum system are remained unaltered. These electron microscopies are relatively less complicated and expensive, which permits imaging of gas *in-situ* processes at an atomic resolution at room temperature (RT).

II. **Electrical Holders**

Electrical transport measurements of single or array of 1D nanostructures are generally determine by employing electrical probing stations with subsequently developing interaction *via* electron or optical beam lithography (Gai et al. 2008). Nowadays, TEM has improved and developed in terms of electrical

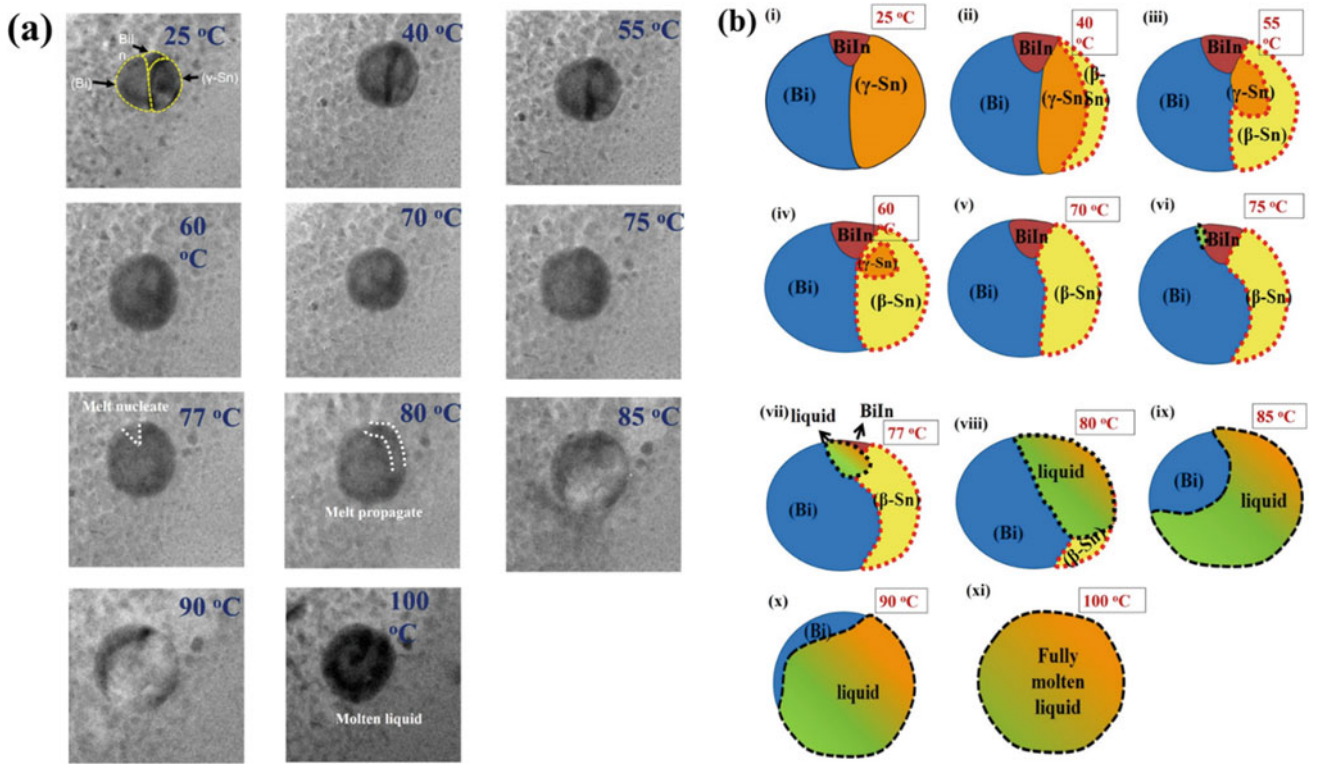

Fig. 10 **a** A series of bright field micrographs showing the melting sequence of tri-phasic Nanoparticles in IQC matrix at different temperature; **b** (i–xi) Schematic illustration of the melting process of tri-phasic Bi-In-Sn alloy Nanoparticles (Gai et al. 2008)

transport measurements. Several suppliers are available in the market, such as Gatan, Hummingbird, Ab, and Nanofactory Instruments. Generally, there are two types of the electrical holder, first, with integrated circuitry for adjoining micro-fabricated chips. This approach utilizes prefabricated circuitry prepared by lithography on Si chips comprising thin silicon nitride membranes. Few more forms of TEM holders are commercially available from Nanofactory Instruments AB using micro-fabricated circuitry. Second is with piezo-driven nanoprobe contact. In this approach, there is a large investment for buying a completely dedicated piezo-driven stage. However, both types of holders are equally important, and they can also be utilized for the selective heating experiment of nanoscale materials (Mølhave et al. 2006).

III. **Mechanical Stages**

These kinds of stages are specifically used for atomic force microscopy (AFM) and nanoindentation techniques. They are commonly utilized to probe the mechanical properties of nanomaterials. In this technique, it uses fine tips (probes) interacting with the specimen surface. However this tip/specimen interaction does not provide any visualized independently except inferred only. These are based on two general approaches: (a) micro-fabricated microelectromechanical system (MEMS) that are equipped inside TEM sample arm (Peng et al. 2008) and (b) assigned nanoindentation holder including piezo-driven probes incorporated with the specimen arm (Tang et al. 2012). In this, the load is employed using a thermal actuator on one end of the free-standing sample and is determined on the other end, utilizing a differential capacitive load sensor. Similarly, in electrical probing, AFM or piezo-driven nanoindenter specimen holders are frequently employed to investigate the mechanical properties of growth of nanowires (Zhu and Espinosa 2005).

IV. **Liquid Cells**

It remained a challenge for decades for the microscopy community to observe a liquid sample under an electron microscope due to lots of problems in sustaining a large volume of the liquid sample inside the electron column (Ruska 1942). From the last decade, 'liquid cells' design has overcome all the limitations for high-resolution electron microscopy (Williamson et al. 2003). This gained immediate attention in the bio and life sciences community at the same time it opened the vast possibility in the material science

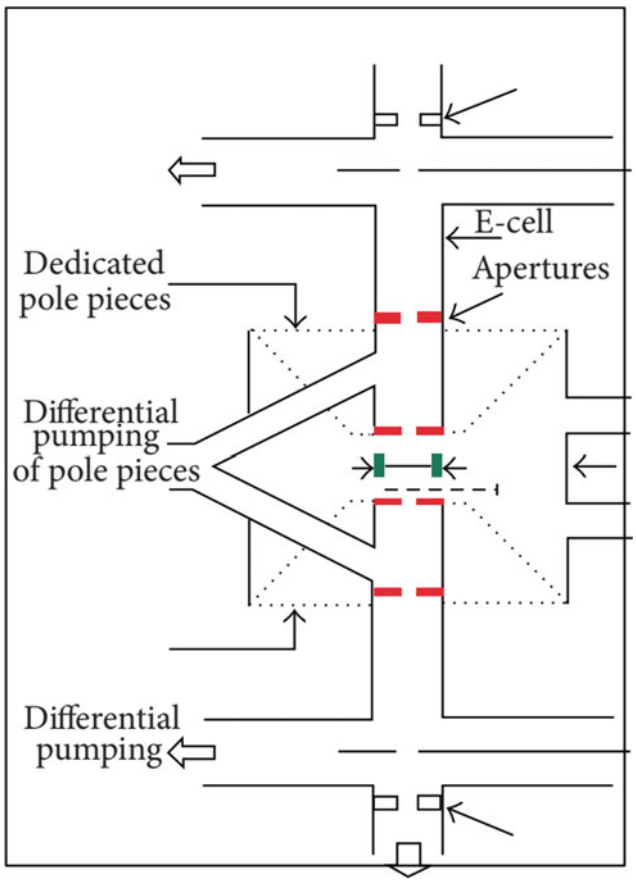

Fig. 11 Schematics of environmental TEM set-up featuring differential pumping, dedicated apertures, and pole piece, 1997 adapted from Boyes and Gai (1997)

community. The liquid cell setup is remarkably distinct from the environmental *in-situ* electron microscopy in that it has the potential to support stable and thin liquid layers. The design of liquid cell shows a hermetically completely sealed that confines the liquid into a layer of micrometer thick inside the thin electron transparent window. The electron transparent window is prepared by silica or silicon nitride (Grogan et al. 2011). Recently, an approach has been developed using single-layered graphene sheets to hold small pockets of liquid. The significant advantage of this method is that due to very less electron scattering volume as compared to silicon nitride or silica-based liquid cell, it contributes to good lattice resolution imaging.

V. Lasers and Ion Beam Irradiation

In general, laser or ion sources are integrated part of the electron column of scanning electron microscopy (SEM) because of large specimen column. At present, all the important producers of microscopes have systems named MultiBeam (JEOL), Crossbeam (Carl Zeiss), and Dual Beam (FEI) that support SEM and focus ion beam (FIB) has the ability to do on a single platform. However, ion beam capabilities for electron microscopy can be prepared on custom-built systems. Few laboratories persuade ion beam setups such as France, UK, USA, and Japan. Minimal studies have been dedicated by *in-situ* TEM ion beam systems on nanomaterial study. Laser sources are incorporated with an electron microscope, and this can be utilized to generate heat and activate reactions inside the specimen. On the other hand, such a design is commercially not available yet. In a general system, the TEM column is modified to equip with the laser beam facilities. Typically, the laser first allows to triggering a reaction or employing definite stimuli within the specimen, while in second it is used to assure the emission of the electron source. Nowadays, an alternative and more cost-effective route has been developed by using inexpensive micro-fabricated light sources or optical fibers and attached with the electron microscopy specimen arm (http://www.nanofactory.com/news.asp?id=59&type=news).

5 Conclusion

In-situ transmission electron microscopy (TEM) has become a prominent tool for materials characterization. It provides an important fact on the structural dynamics of a nanomaterial during phase transformations and further ability to relate a material's properties and structure. *In-situ* microscopy is anticipated to continue to impact the wide range of fields of sciences and technology, allowing for a deeper understanding of nanoalloy materials dynamics and function as well as an in-depth examination of real-time conditions. These nanomaterials can theoretically exhibit novel properties and thus have immense technological implications. The comprehension of the stability and phase transformation of such particles is central to designing alloys for potential future applications.

Acknowledgements KT and KB would like to thank Advanced Imaging Centre (AIC) at IIT Kanpur and office of Dean R&D for providing extended microscopic facilities.

References

Banhart F (2008) In-situ electron microscopy at high resolution. World Scientific

Bhattacharya V, Chattopadhyay K (2007) Mater Sci Eng A 449:1003–1008

Bhattacharya V, Bhattacharya P, Chattopadhyay K (2002) In: Materials science forum. Trans Tech Publ. pp 427–432

Boyes E, Gai P (1997) Ultramicroscopy 67:219–232

Brinker CJ, Scherer GW (2013) In: Sol-gel science: the physics and chemistry of sol-gel processing. Academic Press (2013)
Butler E, Hale K (1981) North-Holland 9:239
Byrappa K, Adschiri T (2007) Prog Cryst Growth Charact Mater 53:117–166
Calvo F (2013) Nanoalloys: from fundamentals to emergent applications. Newnes
Calvo F (2015) Phys Chem Chem Phys 17:27922–27939
Chattopadhyay K (2005) Trans Indian Inst Met 58:1057–1067
Chattopadhyay K, Bhattacharya P (2003) Materials research: current scenario and future projections. vol 130
Chattopadhyay K, Bhattacharya V (2004) Embedded metal and alloy nanoparticles. In: Encyclopedia of nanoscience and nanotechnology. American Scientific Publishers, pp 217–232
Chattopadhyay K, Bhattacharya V (2009) J Indian Instit Sci 89
Chattopadhyay K, Goswami R (1997) Prog Mater Sci 42:287–300
Chen Q, Peng L-M (2011) Ultramicroscopy 111:948–954
Dehm G, Howe JM, Zweck J (2012) In-situ electron microscopy: applications in physics, chemistry and materials science. Wiley
Devi MM, Biswas K (2015) Mater Chem Phys 166:207–214
Devi MM, Tiwari K, Biswas K (2019) Metall and Mater Trans A 50:3959–3972
Fecht H, Perepezko J (1989) Metall Trans A 20:785–794
Fecht H, Zhang M, Chang Y, Perepezko J (1989) Metall Trans A 20:795–803
Ferrando R (2016) Structure and properties of nanoalloys. Elsevier
Ferrando R, Jellinek J, Johnston RL (2008) Chem Rev 108:845–910
Gai P, Boyes E (2010) J Phys: Conf Ser
Gai PL, Kourtakis K (1995) Science 267:661–663
Gai PL, Sharma R, Ross FM (2008) MRS Bull 33:107–114
Garcia Esparza AT (2011)
Grogan JM, Rotkina L, Bau HH (2011) Phys Rev E 83:061405
Han X, Zhang Z, Wang ZL (2007) NANO 2:249–271
He B, Zhang Y, Liu X, Chen L (2020) ChemCatChem
http://www.denssolutions.com/en/our-products/sample-heat-ing-systems
http://www.nanofactory.com/news.asp?id=59&type=news
http://www.protochips.com/products/aduro.html
https://hitachi-hta.com/products/electron-ion-and-probe-microscopy/transmission-electron-microscopes/h-9500-300kv-te
https://www.fei.com/products/transmission-electron-micro-scopes/titan/etem.aspx
https://www.gatan.com/products/tem-specimen-holders/heating-situ-holders
https://www.jeolusa.com/PRODUCTS/Transmission-Electron-Microscopes-TEM/Analytical-Data-Optimization/Practical-Remote-In-Situ-Microscopy-PRISM
Idrees Y (2013) Microstructural evolution in Zr and Zr alloy Excel under ion irradiation. McGill-Queen's University Press, Kingston
Jellinek J (2008) Faraday Discuss 138:11–35
Johnson E, Johansen A, Dahmen U, Gabrisch H, Hagege S (2000) Lawrence Berkeley National Lab., CA (United States)
E. Johnson, A. Johansen, L. Sarholt, U. Dahmen, in: Journal of Metastable and Nanocrystalline Materials, Trans Tech Publ, 2001, pp. 267–274.
Jones RW (1990) The Institute of Metals 1990:128
Khan PY, Biswas K (2015) J Nanosci Nanotechnol 15:309–316
Khan PY, Devi MM, Biswas K (2015) Metall and Mater Trans A 46:3365–3377
Krivanek OL, Chisholm MF, Nicolosi V, Pennycook TJ, Corbin GJ, Dellby N, Murfitt MF, Own CS, Szilagyi ZS, Oxley MP (2010) Nature 464:571–574
LaGrange T, Campbell GH, Reed B, Taheri M, Pesavento JB, Kim JS, Browning ND (2008) Ultramicroscopy 108:1441–1449
Massalski T (1992) Phase Diagrams. pp 206–210
Mei Q, Lu K (2007) Prog Mater Sci 52:1175–1262
Mølhave K, Gudnason SB, Pedersen AT, Clausen CH, Horsewell A, Bøggild P (2006) Nano Lett 6:1663–1668
Peng B, Locascio M, Zapol P, Li S, Mielke SL, Schatz GC, Espinosa HD (2008) Nat Nanotechnol 3:626–631
Ruska VE (1942) Kolloid-Zeitschrift 100:212–219
Siem* E, Johnson E (2005) Philosophical Magazine. 85:1273–1290
Sinclair R (2013) MRS Bull 38:1065
Suryanarayana C (1991) Materials Science and Technology
Suryanarayana C (2001) Prog Mater Sci 46:1–184
Tang D-M, Ren C-L, Wang M-S, Wei X, Kawamoto N, Liu C, Bando Y, Mitome M, Fukata N, Golberg D (2012) Nano Lett 12:1898–1904
Tiwari K, Biwas K, Palliwal M, Majumdar B, Fecht H-J (2020) J Alloy Compd 155160
Urban KW (2009) Nat Mater 8:260–262
Williamson M, Tromp R, Vereecken P, Hull R, Ross F (2003) Nat Mater 2:532–536
Zewail AH (2010) Science 328:187–193
Zewail AH, Thomas JM (2010) 4D electron microscopy: imaging in space and time. World Scientific
Zhu Y, Espinosa HD (2005) Proc Natl Acad Sci 102:14503–14508
Ziegler JF (2012) Ion implantation science and technology. Elsevier (2012)

Fostering Morphological Mutations to Metal Nucleobase Complexes

R. Kamal Saravanan, Ilesha Avasthi, Rajneesh Kumar Prajapati, and Sandeep Verma

1 Introduction

Nucleobases are critical component of DNA and RNA and are also been encountered as versatile molecules for crafting aesthetically pleasing metal coordinated supramolecular motifs, owing to nitrogen atoms predisposed for coordination and non-covalent interactions (Amo-Ochoa and Zamora 2014; Sivakova and Rowan 2005; Verma et al. 2010). In addition, their metal coordination ability could be tuned by functionalization with metal binding groups at suitable positions (Verma et al. 2010; Mohapatra and Pratibha 2017). These diverse coordination modes of modified purine derivatives has been exploited to create complex supramolecular architectures exhibiting remarkable applications in material science as well as in biology (Mohapatra and Pratibha 2017, 20112011). Moreover, nucleobases have also been invoked to form interesting self-assemble patterns on various surfaces such as HOPG, Mica, Si, and Au. (Saravanan et al. 2018). The ordered self-assembly pattern of nucleobases and their metal-coordinated frameworks on various substrates have critically been analyzed by using electron microscopy.

Scanning and transmission electron microscopes (SEM and TEM) are among the most versatile and powerful tools deployed to decipher the microstructure, morphological and elemental composition of panoply of materials ranging from metal nano-structures, carbon nanotubes, inorganic–organic hybrids to biological samples, bacteria, and viruses. In present article, we have demonstrated the extensive use of electron microscopy in characterization of AuNPs decorated modified purine-blended electrospun fibers for sensing applications and morphological study of metal–nucleobase coordination polymers.

2 AuNPs Decorated Nucleobase-Blended Electrospun Nanofibers: SERS Sensor

Electrospun fibers obtained by electrospinning technique serve as a promising avenue toward the development of smart functional materials, owing to its high porosity, mechanical strength, and large surface-to-volume ratio (Xue et al. 2019; Peng et al. 2016). Recently, metal nanoparticles immobilized electrospun fibers have gained significant attention due to their potential applications in catalysis (Qiao et al. 2018), sensing (Su et al. 20142014) and tissue engineering (Yadid et al. 2019), to name a few. Moreover, AuNPs decorated electrospun fibers have also been successfully studied as surface enhanced Raman scattering (SERS) substrates for the sensing of various analytes (Chen et al. 2017). Morphology of electrospun fibers, as well as metal nanoparticles incorporated electrospun fibers, have been analyzed critically by electron microscopy techniques (Xue et al. 2019; Zhang and Yu 2014).

During our critical effort to fabricate metal nanoparticles decorated electrospun fibers, we have prepared electrospun nanofibrous mats with varying concentrations of 8-mercapto-9-propyladenine (L) and polyacrylonitrile (PAN) by blending L with PAN polymer (Saravanan et al. 2020). The morphology of as-obtained electrospun fibers were analyzed by field emission scanning electron microscopy (FESEM) leading to entangled, long and continuous fibers (Fig. 1). These fibrous mats were further incubated with citrate-capped AuNPs, and resulting nanocomposites were characterized by various electron microscopy techniques such as SEM and TEM, as well as Fourier-transform infrared (FTIR) spectroscopy and powder X-ray diffraction. Careful inspection by SEM revealed that concentration of AuNPs on electrospun fibers has been enhanced with

R. Kamal Saravanan · I. Avasthi · S. Verma
Department of Chemistry, Indian Institute of Technology Kanpur, Kanpur, UP 208016, India

R. K. Prajapati (✉)
Center for Nanoscience and Soft Nanotechnology, Indian Institute of Technology Kanpur, Kanpur, UP 208016, India
e-mail: rajkp@iitk.ac.in

K. Biswas et al. (eds.), *Electron Microscopy in Science and Engineering*, IITK Directions 6,
https://doi.org/10.1007/978-981-16-5101-4_9

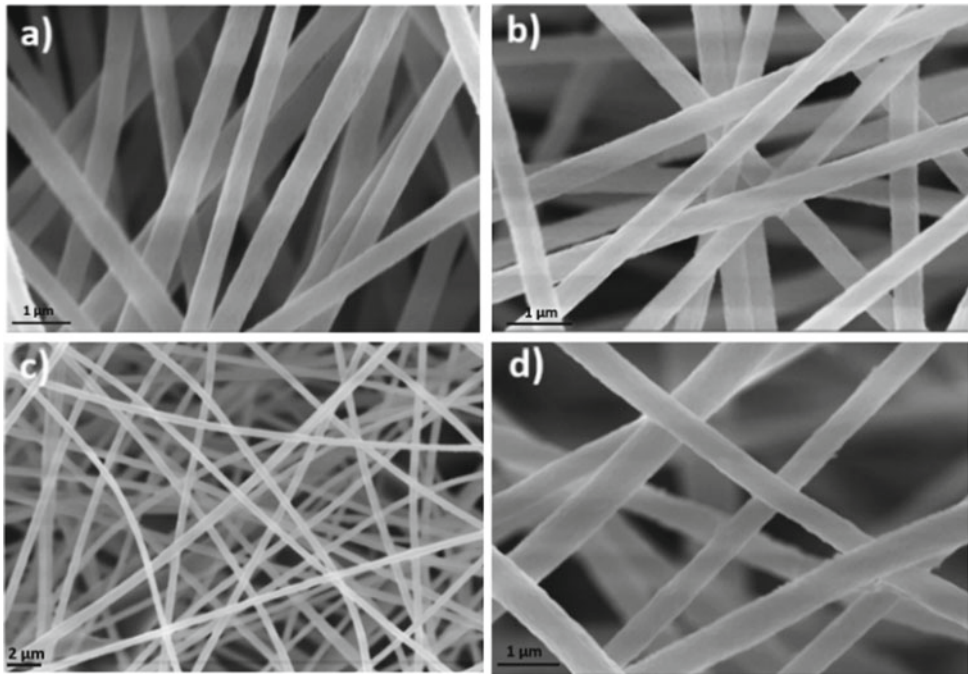

Fig. 1 SEM images of PAN/L electrospun nanofibers with various blend ratios a100/0 (P1); b 90.9/9.1 (P2); c 83.33/16.67 (P3); d 66.66/33.34 (P4) (% w/w). Reproduced with permission from Ref. (Saravanan et al. 2020) The Royal Society of Chemistry

increase in percentage of L (Fig. 2a–h), while Fig. 2i represents the HRTEM image of AuNPs/P4 nanocomposite (with 33% w/w of L) which indicates the presence of AuNPs on electrospun fibers.

Further, AuNPs decorated electrospun fibers nanocomposites were employed for SERS based detection of uric acid in aqueous solution, which is an important biomarker associated with several diseases. AuNPs/P_4 nanofibers composites (with 33% w/w of L) detected uric acid up to 10^{-7} M with the estimated average enhancement factor (AEF) for uric acid in SERS spectra to be 1.14×10^4 (640 cm^{-1} band) and 1.058×10^4 (882 cm^{-1} band). The limit of detection (LOD) was calculated by using regression method for 640 cm^{-1} peak and was found to be 1×10^{-7} M (Saravanan et al. 2020). The LOD achieved by our substrate was found to be lower than that of reported in literatures by various techniques.

3 Exfoliation of Cadmium–Purine Coordination Polymer

Layered frameworks when subjected to exfoliation result in 2D nanosheets through intercalation and isolation processes and can potentially be converted to 1D nanoscale structures.

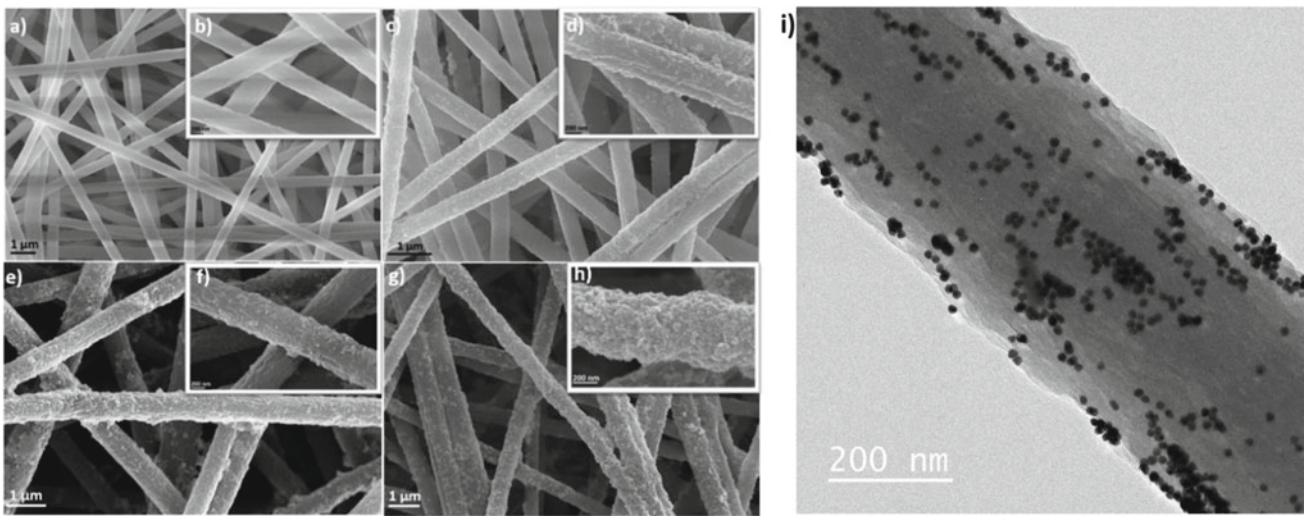

Fig. 2 FESEM images of AuNPs decorated PAN/L electrospun nanofibrous mats of P1 a, b; P2 c, d; P3 e, f and P4 g, h; and i HRTEM image of AuNPs/P4 composite. Reproduced with permission from Ref. (Saravanan et al. 2020) The Royal Society of Chemistry

These nanostructures inherit functional properties from their 3D bulk analogs. Herein, we have synthesized a derivative of adenine and subsequently its layered Cd(II)–purine coordination framework which was subjected to sonication-assisted liquid-phase exfoliation in ethanol or isopropanol to achieve 2D nanosheets (Avasthi et al. 2019). The same process of exfoliation when carried out in chloroform or THF resulted in 1D nanofibers. Further, a distinct conversion of nanosheets to nanofibers was also established at low temperatures. The characterization and analyses of the nanostructures and their conversion processes could successfully be achieved using scanning electron microscopy (SEM) and transmission electron microscopy (TEM) in addition to atomic force microscopy, energy dispersive X-ray (EDX), PXRD, and FTIR analyses.

Figure 3 depicts the SEM and TEM images of distinct nanosheets and long and continuous nanofibers obtained after exfoliation. Figure 4, however, highlights the conversion process of nanosheets to nanofibers in chloroform as recorded through SEM. Furthermore, these nanostructures

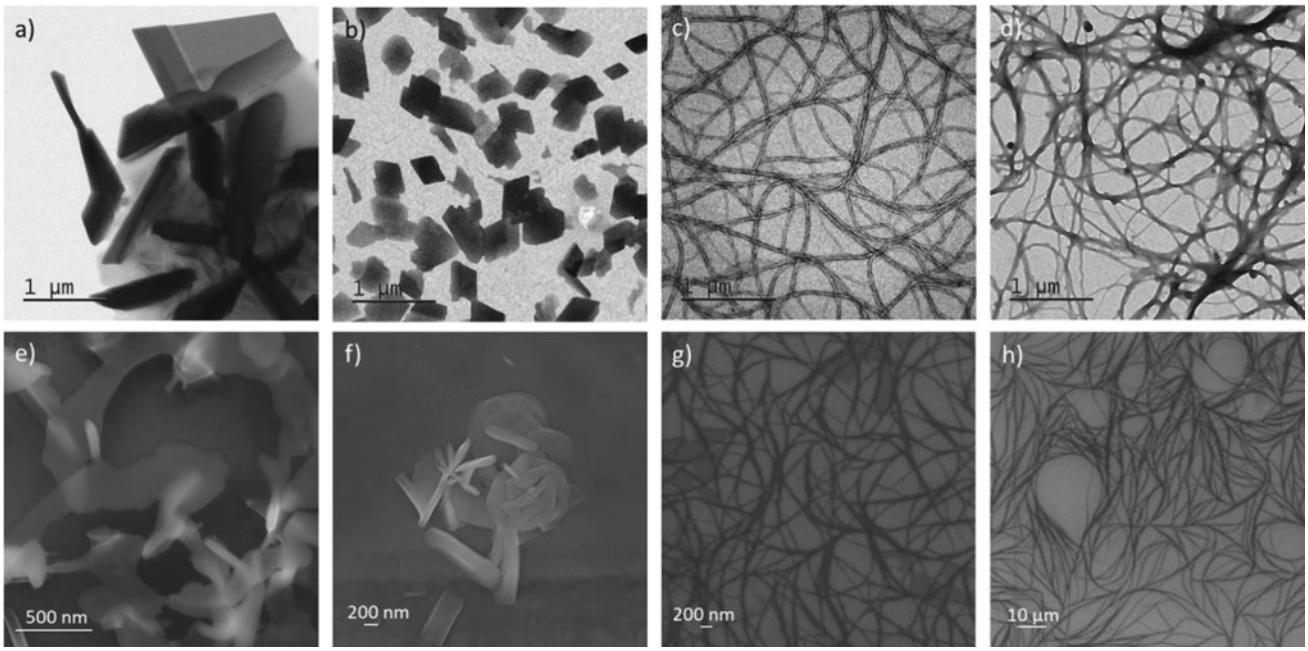

Fig. 3 TEM images of exfoliated Cd(II) complex in **a** isopropanol, **b** ethanol, **c** chloroform and **d** THF; SEM images of exfoliated Cd(II) complex in **e** isopropanol, **f** ethanol, **g** chloroform and **h** THF (where ethanol, isopropanol yield nanosheets and chloroform, THF yield nanofibers). Reproduced with permission from Ref. (Avasthi et al. 2019) © 2019 WILEY-VCH Verlag GmbH & Co. KGaA, Weinheim

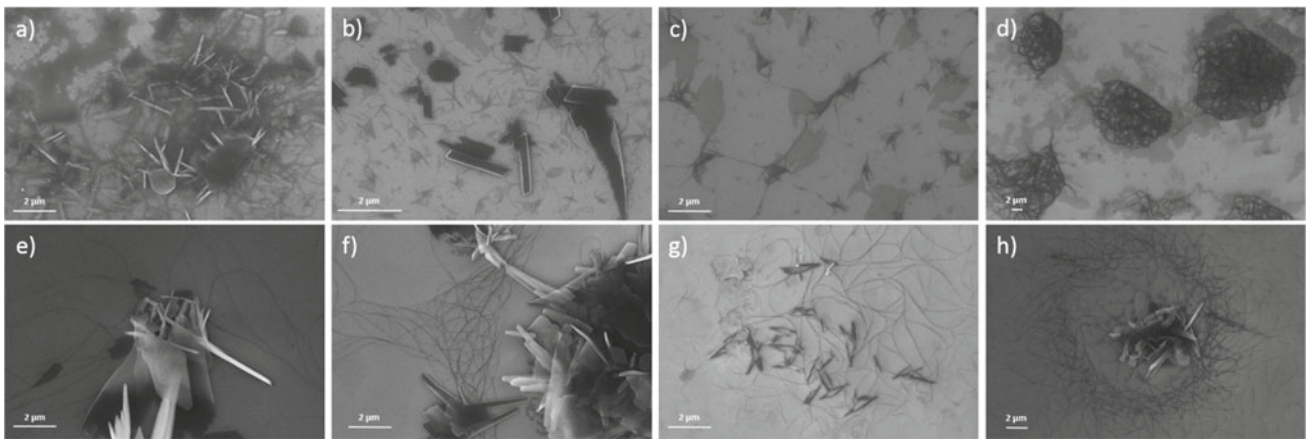

Fig. 4 Time-dependent SEM of Cd(II) complex exfoliated and incubated at 4 °C in chloroform at **a** 0-day, **b** 1-day, **c** 2-day, **d** 4-day and in THF at **e** 0-day, **f** 1-day, **g** 2-day, **h** 4-day demonstrating the transformation of nanosheets to nanofibers Reproduced with permission from Ref. (Avasthi et al. 2019) © 2019 WILEY–VCH Verlag GmbH & Co. KGaA, Weinheim

were probed for their elastic and capacitive properties using amplitude modulation-frequency modulation atomic force microscopy and Kelvin probe force microscopy, respectively, which revealed their potential applications in electronics and energy devices.

4 Copper–Purine Coordination Polymer: Thin Film Precursor

In another report, four N9 derivatives of 6-chloropurine were synthesized to subsequently achieve six Cu(II) complexes (Avasthi et al. 2017). These complexes were further established as thin film precursors to give copper(II) oxide thin films on quartz and Si(111) substrates by spin coating, first at room temperature in air and then CVD treatment at 650˚C. Thin films were prepared at this temperature under two conditions: (a) in air and (b) in inert atmosphere (under N_2) under standard pressure (760 Torr), on quartz and Si (111). The films were characterized using EDX, PXRD, and Raman spectroscopy followed by morphological study under SEM.

The films obtained on Si (111) surface under the two conditions has been shown in Fig. 5. The films were then subjected to electrical characterization using four-point probe method to calculate their sheet resistance indicating that rationally devised Cu(II) purine complexes could possibly find useful applications as a source/drain or gate of thin film transistor or as electrode in LEDs and solar cells (Wanjala et al. 2016) or in high-speed integrated circuits (Cale et al. 2000).

In conclusion, we have outlined the synthesis of modified purine blended electrospun fibers, which subsequently incubated by AuNPs and their morphology was investigated by using electron microscopy techniques. In addition to morphology of fibers, decoration of AuNPs on the surface of electrospun nanofibers was clearly revealed by SEM and TEM analysis as electron microscopes are versatile tool to analyze metal nanoparticles/electrospun fiber composites. Furthermore, As-fabricated AuNPs/electrospun fibers composites were demonstrated as potential substrate for SERS-based detection of uric acid with the detection limit of 10^{-7} M concentration. Detection of uric acid by such substrate might offer newer design paradigms for the sensors of biologically relevant molecules and biochemical pathways. Moreover, we have also exploited electron microscopy, for the characterization of nanostructures obtained as consequences of exfoliation of cadmium-purine coordination polymer, as well as to analyze the thin film made by copper–purine coordination polymer. The electron microscopy has not only allowed us to characterize the structures on the surface but also provided a deeper insight to establish their function at the nanoscale. These fundamental studies have assisted in establishing profound structure–property relationships which pave way for the development of useful functional molecular systems for various purposes. Such self-assembled novel nucleobase metal coordination polymers are envisaged to have potential applications in fabrication of smart functional materials.

References

Amo-Ochoa P, Zamora F (2014) Coordination polymers with nucleobases: from structural aspects to potential applications. Coord Chem Rev 276:34–58

Sivakova S, Rowan SJ (2005) Nucleobase as supramolecular motifs. Chem Soc Rev 34:9–21

Verma S, Mishra AK, Kumar J (2010) The many facets of adenine: coordination, crystal patterns, and catalysis. Acc Chem Res 43:79–91

Mohapatra B, Pratibha, Verma S (2017) Directed adenine functionalization for creating complex architectures for material and biological applications. Chem Comm 53:4748–4758

Imaz I, Rubio-Martínez M, An J, Solé-Font I, Rosi NL, Maspoch D (2011) Metal-biomolecule frameworks (MBioFs) ChemComm 47:7287–7302

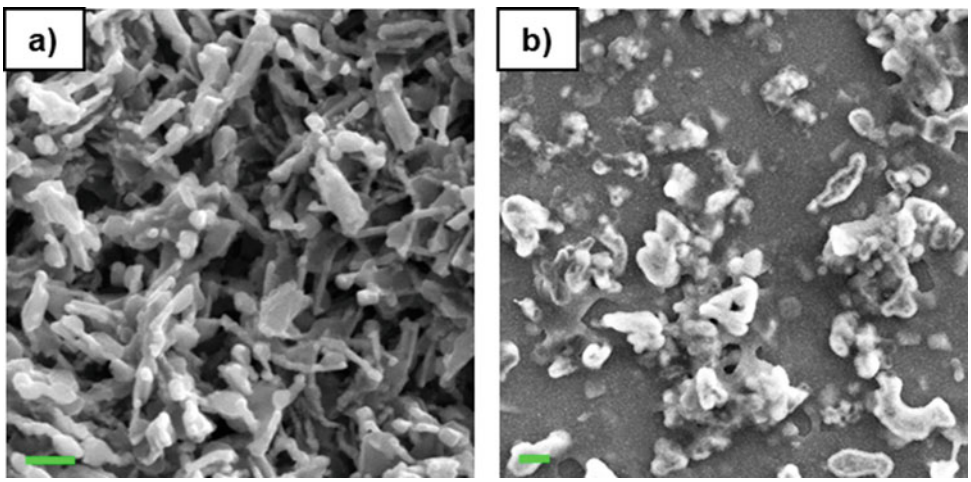

Fig. 5 SEM (Scale: 2 μm) for thin films in **a** air and **b** inert cond. (under std. pressure). Reproduced with permission from Ref. (Avasthi et al. 2017) The Royal Society of Chemistry

Saravanan RK, Avasthi I, Prajapati RK, Verma S (2018) Surface modification and pattern formation by nucleobases and their coordination complexes. RSC Adv 8:24541–24560

Xue J, Wu T, Dai Y, Xia Y (2019) Electrospinning and electrospun nanofibers: methods materials and applications. Chem Rev 119:5298–5415

Peng S, Jin G, Li L, Li K, Srinivasan M, Ramakrishna S, Chen J (2016) Multi-functional electrospun nanofibers for advances in tissue regeneration, energy conversion and storage, and water treatment. Chem Soc Rev 45:1225–1241

Qiao Z, Shen M, Xiao Y, Zhu M, Mignani S, Majoral J-P, Shi X (2018) Organic/inorganic nanohybrids formed using electrospun polymer nanofibers as nanoreactors. Coord Chem Rev 372:31–51

Su Z, Ding J, Wei G (2014) Electrospinning: a facile technique for fabricating polymeric nanofibers doped with carbon nanotubes and metallic nanoparticles for sensor applications. RSC Adv 4:52598–52610

Yadid M, Feiner R, Dvir T (2019) Gold nanoparticle-integrated scaffolds for tissue engineering and regenerative medicine. Nano Lett 19:2198–2206

Chen C, Tang Y, Vlahovic B, Yan F (2017) Electrospun polymer nanofibers decorated with noble metal nanoparticles for chemical sensing. Nanoscale Res Lett 12:451

Zhang C-L, Yu S-H (2014) Nanoparticles meet electrospinning: recent advances and future prospects. Chem Soc Rev 43:4423–4448

Saravanan RK, Naqvi TK, Patil S, Dwivedi PK, Verma S (2020) Purine-blended nanofiber woven flexible nanomats for SERS-based analyte detection. Chem Commun 56:5795–5798

Avasthi I, Kulkarni MM, Verma S (2019) Exfoliating a Cd II—purine framework: conversion of nanosheets-to-nanofibers and studies of elastic and capacitive properties. Chem A Eur J 25:6988–6995

Avasthi I, Khanna S, Tripathi SK, Verma S (2017) N9 substituent mediated structural tuning of copper-purine complexes: chelate effect and thin film studies. CrystEngComm 19:5202–5213

Wanjala KS, Njoroge WK, Ngaruiya JM (2016) Optical and electrical characterization of ZnS: Sn thin films for solar cell application. Am J Condens Matter Phys 6:1–6

Cale TS, Merchant TP, Borucki LJ, Labun AH (2000) Topography simulation for the virtual wafer fab. Thin Solid Films 365:152–175

Interplay of Stresses, Interfaces, and Nanoscale Effects: *TEM Investigations*

Anandh Subramaniam, R. M. Raghavendra, Ganesh Iyer, and Arun Kumar

1 Defects in Crystals

Defects are typically classified based on their dimensionality (http://home.iitk.ac.in/∼anandh/E-book.htm) (Fig. 1). One inevitable defect in all real single crystals is the surface. In mechanics, the surface is sometimes referred to as the traction-free surface; albeit the fact that, in reality the under-coordination of the atoms at the surface lends to surface stress. Surface stress in metals is tensile in nature and leads to the compression of the crystal. Vacancies and dislocations are other common defects present in crystals. Dislocations, which are endowed with long range stress fields, can interact with the stress fields associated with other defects. The stresses under discussion are 'residual' in nature (Fig. 2). In typical polycrystalline materials, the effect of surface is limited, while the role played by grain boundaries (an internal interface) is prominent. The type and distribution of defects constitutes the defect structure in a material. Phases, defects and residual stresses and their distributions constitute a microstructure, which governs 'structure sensitive properties' (Fig. 3).

In nanoscale systems, two effects gain prominence: interactions due to the proximity of interfaces and the altered energetics of defects. Selected examples of the consequences of the same are (Schodek et al. 2009; Nalwa 2004): the destabilization of vacancies, a crystal becoming spontaneously dislocation free, and the alteration in the deformation mechanism. More such effects are highlighted in the current article.

In this article, the work of our group at IITK is kept primarily in view (Kumar et al. 2013a,2014; Rani et al. 2015,2017; Iyer et al. 2017), and the readers may refer to standard literature to gain a broader view of the subject matter. The focus of our group is on theoretical, computational, and experimental investigations of metastable microstructures, which include nanomaterials, coherent systems, internal interfaces, and crystalline defects. Three examples are considered to elucidate the interplay between stresses, interfaces, and geometry. These are: (i) the stabilization of a coherent state, (ii) an anomalous lattice expansion in spherical metals shells, and (iii) the alteration of the critical size for nucleation during a solid-to-solid diffusional phase transformation. The 'geometry' being referred to relates to features of the sample. We will come across interesting concepts, which include 'depth sensitive lattice fringe imaging,' 'liquid-like nucleation in nanoscale films,' and 'Poisson effect-driven anomalous lattice expansion in metal nanoshells.' These examples will serve to highlight the power of the use of transmission electron microscopy in conjunction with computational models. A range techniques associated with TEM/STEM (scanning transmission electron microscopy) have been used in the investigations, which include bright field imaging (BFI), high-resolution lattice fringe imaging (HRLFI), high-angle annular dark field imaging (HAADF), electron energy loss spectroscopy (EELS), and Moiré fringe contrast imaging. It will become amply clear to the reader that these studies provide insights into nanoscale phenomena which are practically inaccessible by other means.

Notes to the reader: The symbol r^* has been used for the critical radius in multiple contexts, each distinct from the other. The reader must be careful to distinguish these physically diverse scenarios. The meaning of the terms like domain, body, sample, crystal, and film has to be 'deciphered' keeping the context in view.

A. Subramaniam (✉) · R. M. Raghavendra
Materials Science and Engineering, Indian Institute of Technology, Kanpur, India
e-mail: anandh@iitk.ac.in

G. Iyer
Department of Mechanical Engineering, Institute of Infrastructure Technology Research and Management, Ahmedabad, Gujarat, India

A. Kumar
Department of Physics, J.C. Bose University of Science and Technology YMCA, Faridabad, Haryana, India

K. Biswas et al. (eds.), *Electron Microscopy in Science and Engineering*, IITK Directions 6,
https://doi.org/10.1007/978-981-16-5101-4_10

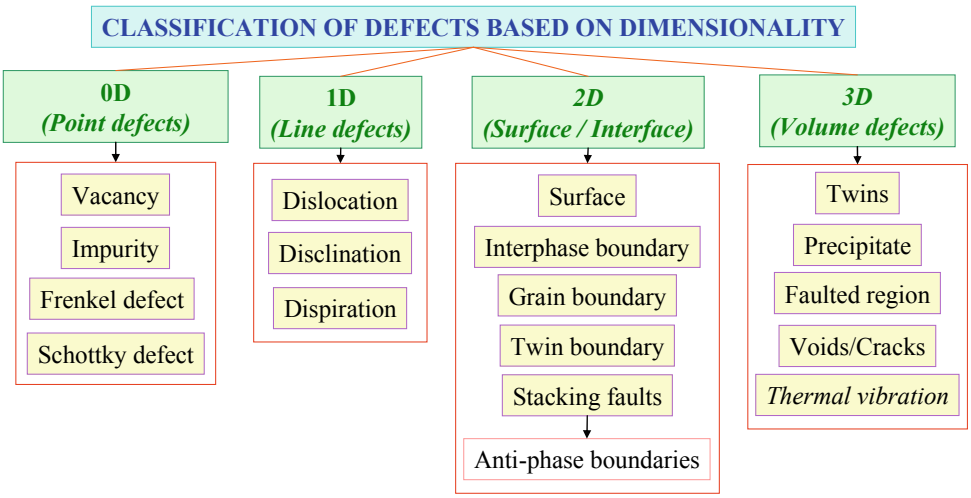

Fig. 1 Classification of defects in crystals based on dimensionality

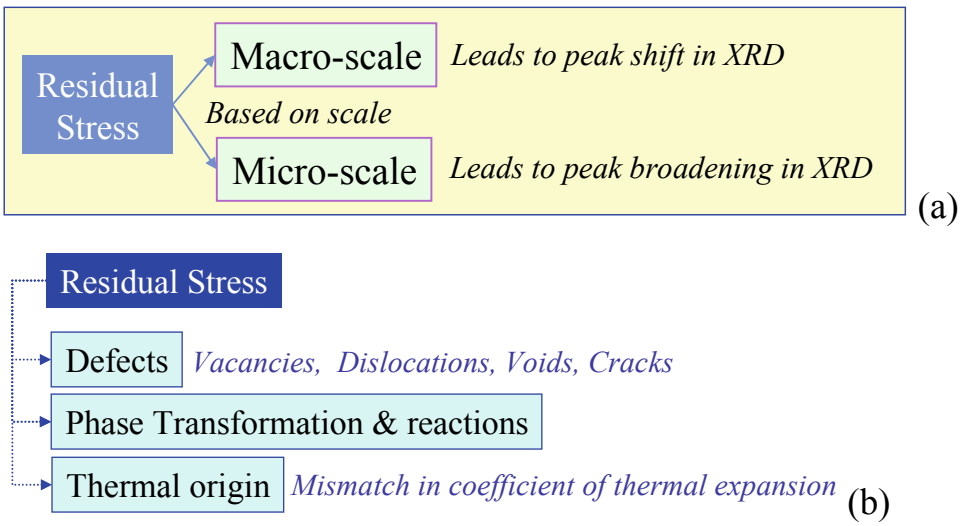

Fig. 2 **a** Classification based on scale and **b** origins of residual stresses in materials

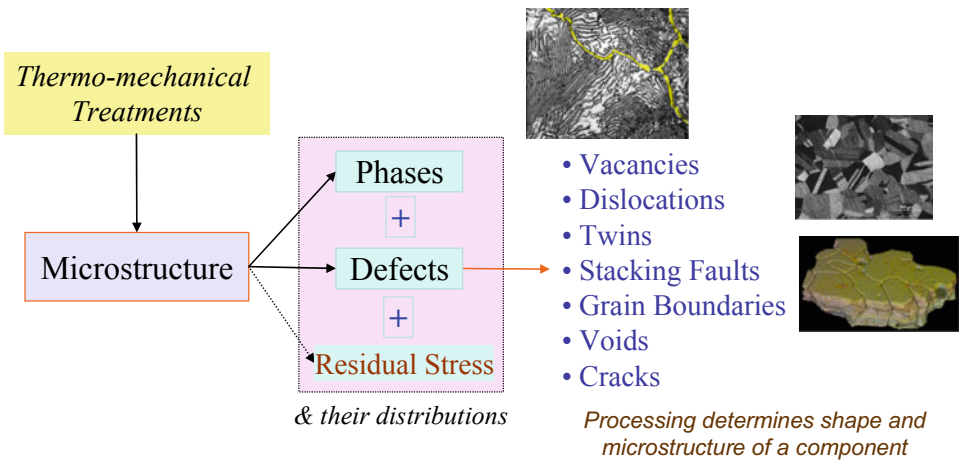

Fig. 3 'Functional' definition of microstructure. Thermo-mechanical treatments can be used to engineer the microstructure. The microstructure determines the 'structure sensitive properties'

2 The Interplay of Stresses, Interfaces, and Geometry

2.1 Dislocations in Finite Bodies

An illustrative system to comprehend the interplay of stresses, interfaces, and geometry is the study of dislocations in semi-infinite and nanoscale bodies. As alluded to before, the stresses being referred to in the current context are residual stresses. The stress fields of defects and the associated energetics are altered in finite bodies. In nanoscale systems, these effects are accentuated manyfold. An edge dislocation in a finite body can serve as a model example to illustrate the concepts involved. The stress fields of an edge dislocation in an infinite body (plot of σ_{xx} contours) is shown in Fig. 4a. If the body is semi-infinite, with the presence of a proximal free surface, the stress state is modified (Fig. 4b). As less volume of material is stressed, the energy of the dislocation is reduced, with respect to that in an infinite body. The energy of the system decreases with distance, and this results in an 'image force' (the gradient of the energy field is the force field). The image force is so termed, as the force of attraction toward the surface, can be computed using the construction of an 'image dislocation.' This force is a 'configurational force' and hence has to be seen in a different light as compared to that we typically exposed to.

As the dislocation is positioned within a few Burgers vectors from the surface, domain deformations and the interaction of the core of the dislocation with the surface

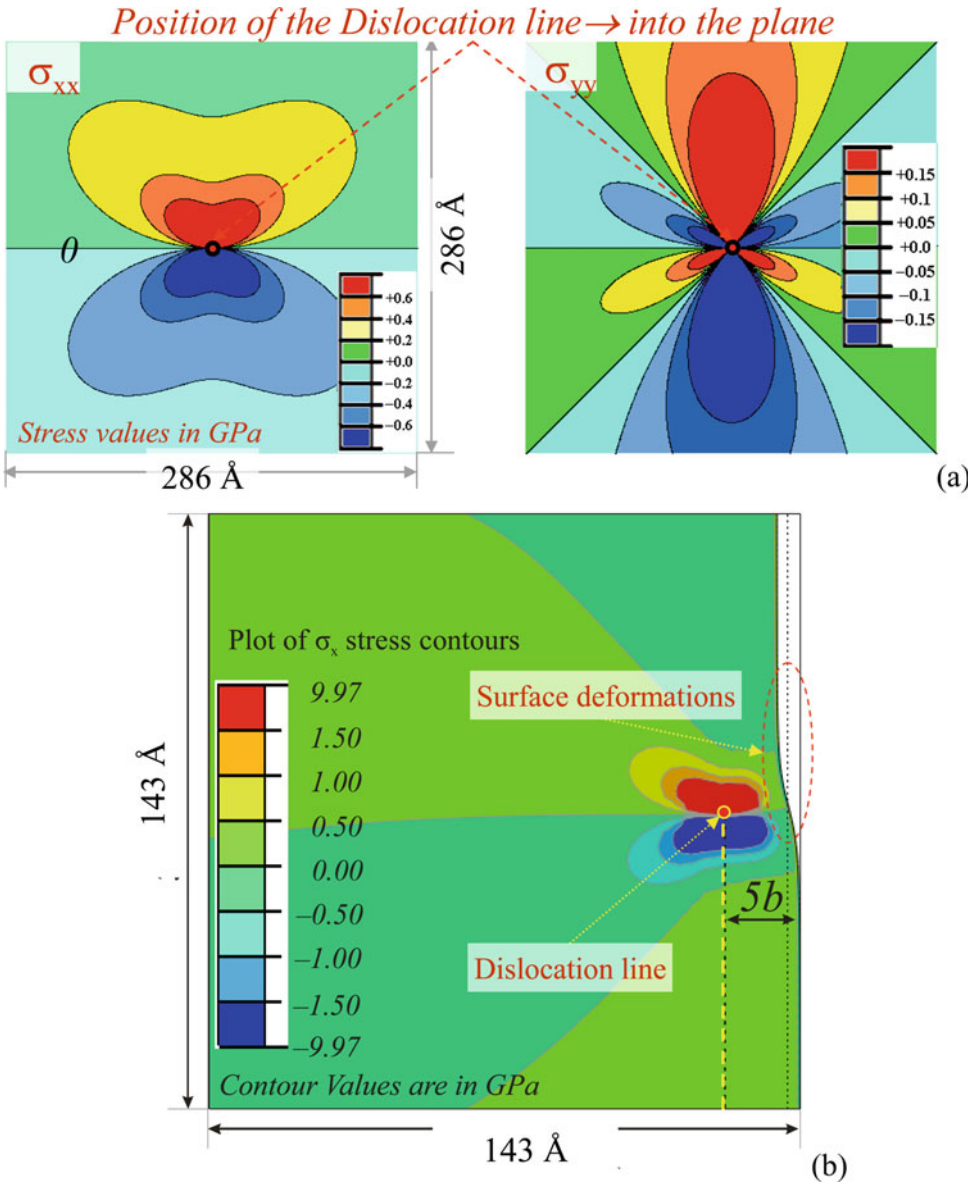

Fig. 4 **a** Edge dislocation in an infinite body. Note the left–right mirror symmetry and the top–bottom 'mirror-inversion' symmetry (which 'reflects' tensile stresses to compressive stresses). (b) In a semi-infinite body, with a proximal free-surface. The symmetries present in (a) are broken here

assume prominence. These effects further alter the energetics and forces involved. Eshelby showed in 1953 that a screw dislocation can be stabilized in a thin cylinder (Eshelby 1953). The corresponding scenario with regard to an edge dislocation was elucidated in 2012 by Kumar and Subramaniam (2012a) (the reader may refer to an article in directions for further details (Subramaniam and Kumar 2014)). In both these cases, the geometry of the body (thin cylinder or thin plate), its deformation under the stress fields of the dislocation, and concomitant reduction in the energy of the system results in the stabilization. Interestingly, in the case of the edge dislocation in a thin plate, the dislocation may exist in a state of neutral equilibrium (Kumar and Subramaniam 2011). For the case of two dislocations in a thin plate, we may observe the existence of 'metastable states of negative stiffness' along with 'unstable states of positive stiffness' (Kumar and Subramaniam 2013a).

This traction-free boundary condition existing at the free-surface is altered due to surface stresses. The stress state of the system is altered as shown in Fig. 5. Under these circumstances, an edge dislocation may experience a torque in addition to the force (Raghavendra 2018). In general, the 'geometry of the system' (the type of surface, the type of dislocation, the orientation of the dislocation, etc.) will determine the force and torque on the dislocation. For specific configurations, this can result an equilibrium position for the dislocation (Raghavendra 2018). It is interesting to note that after more than six decades a second origin of an equilibrium position for an edge dislocation has emerged! Perhaps, equally amazing is the fact that a monopole can experience a torque!

Image forces can result in regions near surfaces to become spontaneously dislocation free. This happens when the image force exceeds the Peierls force (PN force). Nanocrystals can become completely dislocation free due to this effect (Khanikar and Subramaniam 2010). As we show later, interfacial misfit loops are also subject to these considerations and can lead to the stabilization of a coherent precipitate.

2.2 Nucleation of Crystals in an Amorphous Matrix

In this and the next sub-section, we discuss two relate phenomena: nucleation and growth. There exists a propensity for an undercooled system to transform. First-order transformations proceed via nucleation and growth (David 2009). Nucleation occurs uphill in Gibbs free energy (G), while growth occurs downhill in 'G.' Nucleation involves the formation of the product phase of a certain minimum dimension, referred to as the critical radius (r^*). 'Embriyos' smaller than r^* revert to the parent phase, while 'super-critical' nuclei grow to facilitate the phase transformation.

Nucleation of crystals from an amorphous matrix serves as model system from both microscopic and mechanics point of view due to the following reasons (Pooja Rani and Raghavendra 2007).

1. It is easy to control the degree of transformation, as compared to that from a liquid.
2. Only the crystallite will give rise to lattice fringes in the HRLFI technique.
3. The matrix is isotropic and hence its elastic properties are captured by only two elastic moduli.
4. Homogeneous nucleation predominates.

It is to be noted that point (iv) is in stark contrast to nucleation in a typical crystalline solid, wherein, heterogeneous nucleation preferentially occurs at various defect sites.

The volume occupied by the nucleus (crystallite) is different from that of the glass, and hence, the transformation involves strains. The associated strain energy tends to oppose the nucleation process and with thus lead to an increase in the value of r^*, as compared to that for the nucleation of a crystal from a liquid. In the ambit of the classical nucleation theory (CNT), the process of nucleation occurs by a 'statistical random fluctuation' and the value of r^* is given by:

$$r^* = \frac{2\gamma}{(\Delta G_V - \Delta G_S)} \tag{1}$$

where, $\Delta G_S = \frac{E_{Strain}}{V}$ is the misfit strain energy per unit volume.

If the process of nucleation occurs close to a surface or in nanocrystals, the strain energy penalty is reduced, which results in a reduction in the value of r^*. Given that the thickness of a typical TEM sample is of the order of 10–50 nm, this naturally serves as nanoscale system. The details with respect to other geometries differ; however, the essential physics remains the same. The Cu-Zr-Al bulk metallic glass (BMG) serves as a model system for the study of nucleation due to the following reasons. (i) Glass can be formed by reasonably slow cooling. (ii) The diffusion is sluggish at room temperature, and hence, the occurrence of transformation during characterization (like TEM) is negligible. (iii) By working at a temperature in the 'nucleation dominant regime,' we can practically suppress growth.

The size of crystallites formed on devitrification can be determined by HRLFI. Other competing TEM techniques can also give us a rapid and accurate measure of the sizes, e.g., 'zero defocus' Fresnel contrast imaging (Bhattacharyya

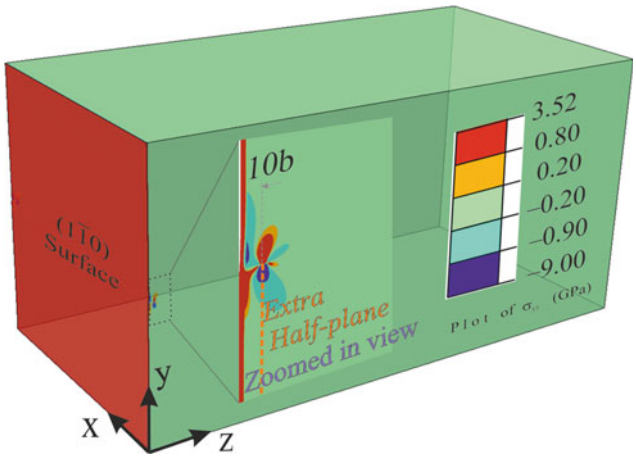

Fig. 5 Stress fields associated with an edge dislocation (plot of σ_{yy} contours) in a semi-infinite body, in the presence of surface stresses. The stress state is simulated using finite element method (FEM). The dimensions of the body are 500b × 500b × 1000b (b = 2.863 Å)

et al. 2006). The strain energy involved in the formation of the nucleus can be computed finite element method. A model for the same is shown in Fig. 6a. Figure 6b shows the state of stress (plot of σ_{yy} stress contours) in the presence of a nucleus (crystallite of $Cu_{10}Zr_7$).

The variation in the strain energy associated with a nucleus for two cases is shown in Fig. 7: (i) varying thickness of the amorphous film and (b) position of the crystal within the film (varying height). As expected, it is seen that the strain energy cost for nucleation decreases with a decreasing thickness of the amorphous film or as the nucleus is positioned closer to the surface. The computation of the r^* for homogeneous nucleation, via a plot of the change in the Gibbs free energy $(\Delta G_{homo}(r))$ with size of the nucleus (r), is shown as an inset to the figure. Three cases of nucleation of a crystals considered are: (i) from the liquid, (ii) at the center (t = 4 nm), and (iii) in a bulk matrix. As expected, the value of r^* increases with an increased cost of strain energy $r^*_{liquid} < r^*_{thin\ film} < r^*_{bulk}$.

Experimentally, the BMG sample can be made using suction casting. In the Cu-Zr-Al system, the composition of $(Cu_{64}Zr_{36})_{96}Al_4$ has good glass forming ability with a critical cooling rate of 40 K/s and critical diameter of 7 mm (Tanya Aycan Baser and Marcello Baricco 2008). Figure 8a shows the selected area diffraction (SAD) pattern showing the formation of amorphous structure. The corresponding real space image is shown in Fig. 8b (which displays the typical 'salt and pepper' contrast). Heat treatment of the BMG to induce nucleation was carried out in two kinds of samples: (i) bulk sample and (ii) nanoscale thin film (thinned down TEM samples). The crystallite/nuclei which first forms on annealing is $Cu_{10}Zr_7$ (Cmca, oC68, a = 12.68 Å, b = 9.31 Å, c = 9.35 Å (Alessandro Figini Albisetti 2012)).

As indicated before, the TEM specimen can be used as a nanoscale thin film. The thickness of the sample is an important parameter and can be determined using EELS. The EELS spectrum can be used to determine the local thickness of the sample (t) (Malis et al. 1988):

$$t = \lambda \ln\left(\frac{I_T}{I_0}\right) \tag{2}$$

where, I_0 and I_T are the areas under the zero loss peak and the entire spectrum and 'λ' is the inelastic mean free path. Using the standard values from literature, the local thickness of the sample can be determined (within about 20% accuracy). Figure 8c shows an EELS spectrum obtained using an in-column energy filter system in a Zeiss Libra 200FE instrument (a FEG gun instrument with a resolution of 0.9 Å, operating at 200 kV).

In the case of the bulk sample, the annealing was carried out first (200 °C for 4 h) followed by thinning to form a TEM sample. In the second case, the samples where thinned first followed by annealing (200 °C, 10 min). The choice of

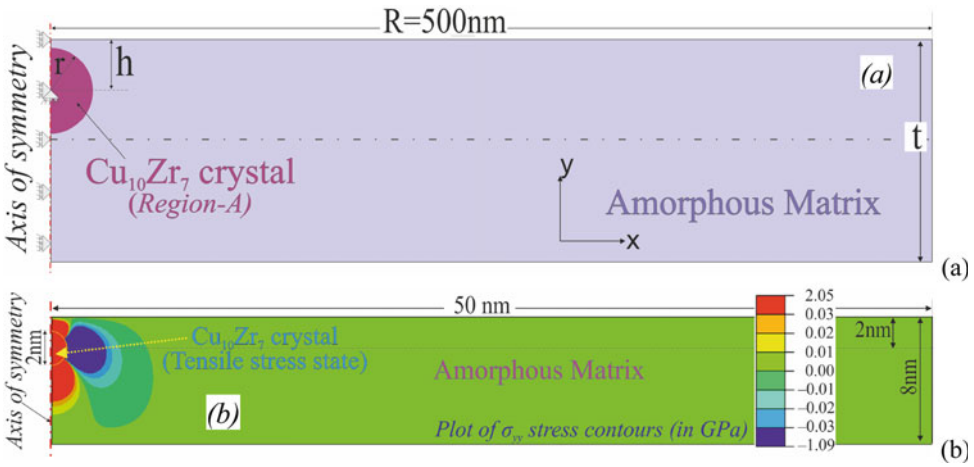

Fig. 6 **a** Finite element model used to compute the strain energy due to nucleation (of a crystal of radius 'r') in a thin film (of thickness 't'). Eigenstrains are imposed in region-A to simulate the stress state in the presence of a crystal. **b** Plot of σ_{yy} stress contours due to nucleation (r = 1 nm, h = 2 nm t = 8 nm)

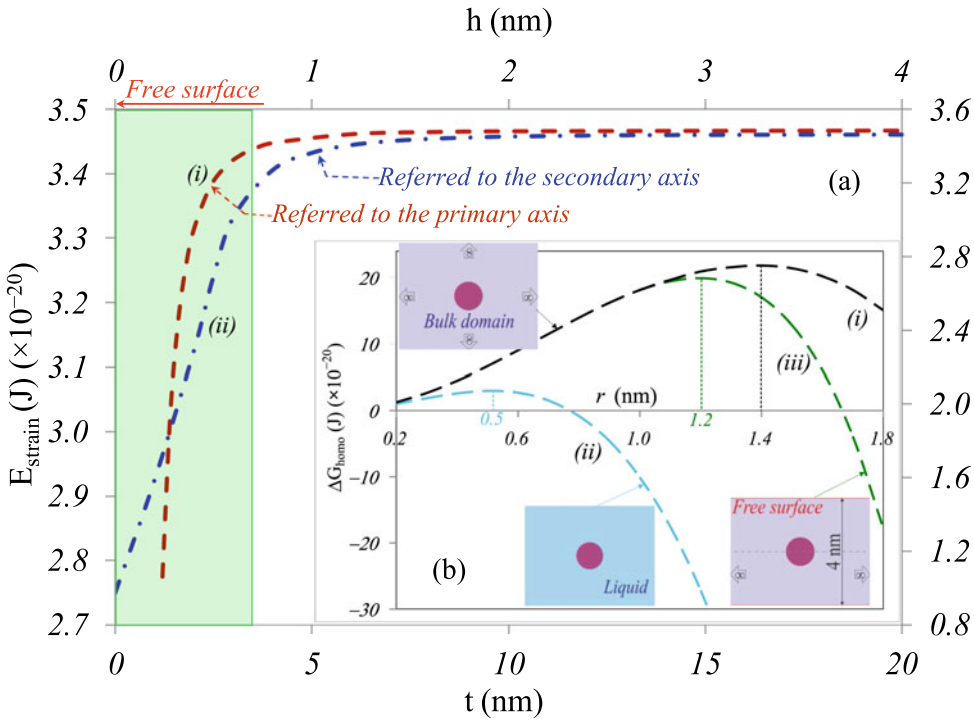

Fig. 7 Variation of strain energy (E_{strain}) with: **a** (i) 't' and (ii) 'h.' **b** Variation in ΔG_{homo} versus 'r' for nucleation in: (i) the bulk, (ii) the liquid, and (iii) the center of a film (t = 4 nm). Nanoscale effects predominate in the shaded region

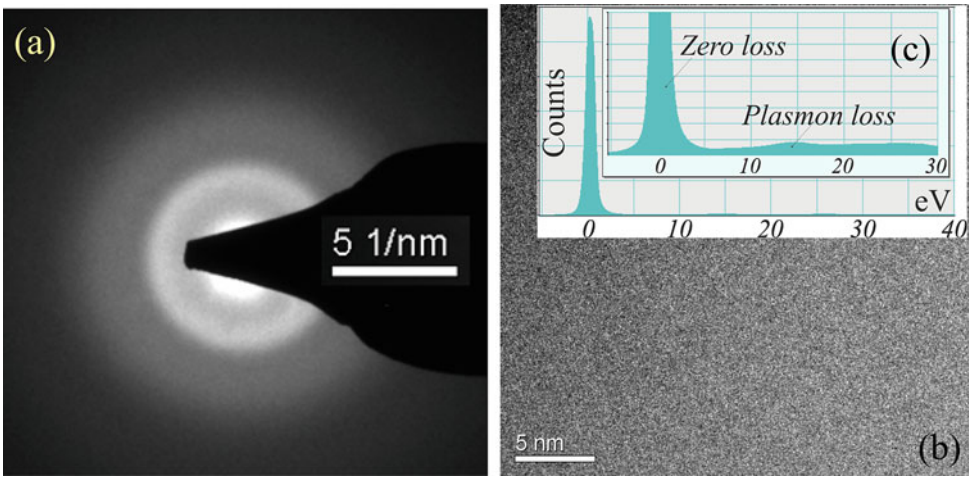

Fig. 8 **a** Diffuse rings in the SAD pattern showing the formation of an amorphous structure (suction cast $(Cu_{64}Zr_{36})_{96}Al_4$ alloy). **b** The corresponding real space image (showing 'salt and pepper' contrast). **c** An EELS spectrum acquired from region of diameter 10 nm (inset shows a region close to the zero loss peak). This spectrum can be used in the computation of the thickness of the specimen (as described in the text)

the temperature is to be in the nucleation-dominant regime and to minimize any growth of the crystallites (Fig. 9a). These rates can be computed using the classical nucleation theory (Kumar et al. 2013a; Karthika Suresh and Radhakrishnan and P. Kalaichelvi, 2016). The size of the nucleus can be determined by HRLFI (Fig. 9b). This technique is associated with an 'error bar' of at least one digital pixel (~0.032 nm).

Figure 10 is a 'busy plot' which shows the variation of r^* with thickness of the sample, along with other features. The following data is shown in the figure. (i) Experimentally measured and computed values of r^*_{bulk}, (ii) r^*_{liquid}, (iii) $r^*_{thin\ film}$ (computed and experimental), and (iv) $r^*(h)$ (with t = 8 nm). The experimentally determined value of r^*_{bulk} ~ 1.41 nm. Based on the data, we can make the following observations. (i) A very good match exists between

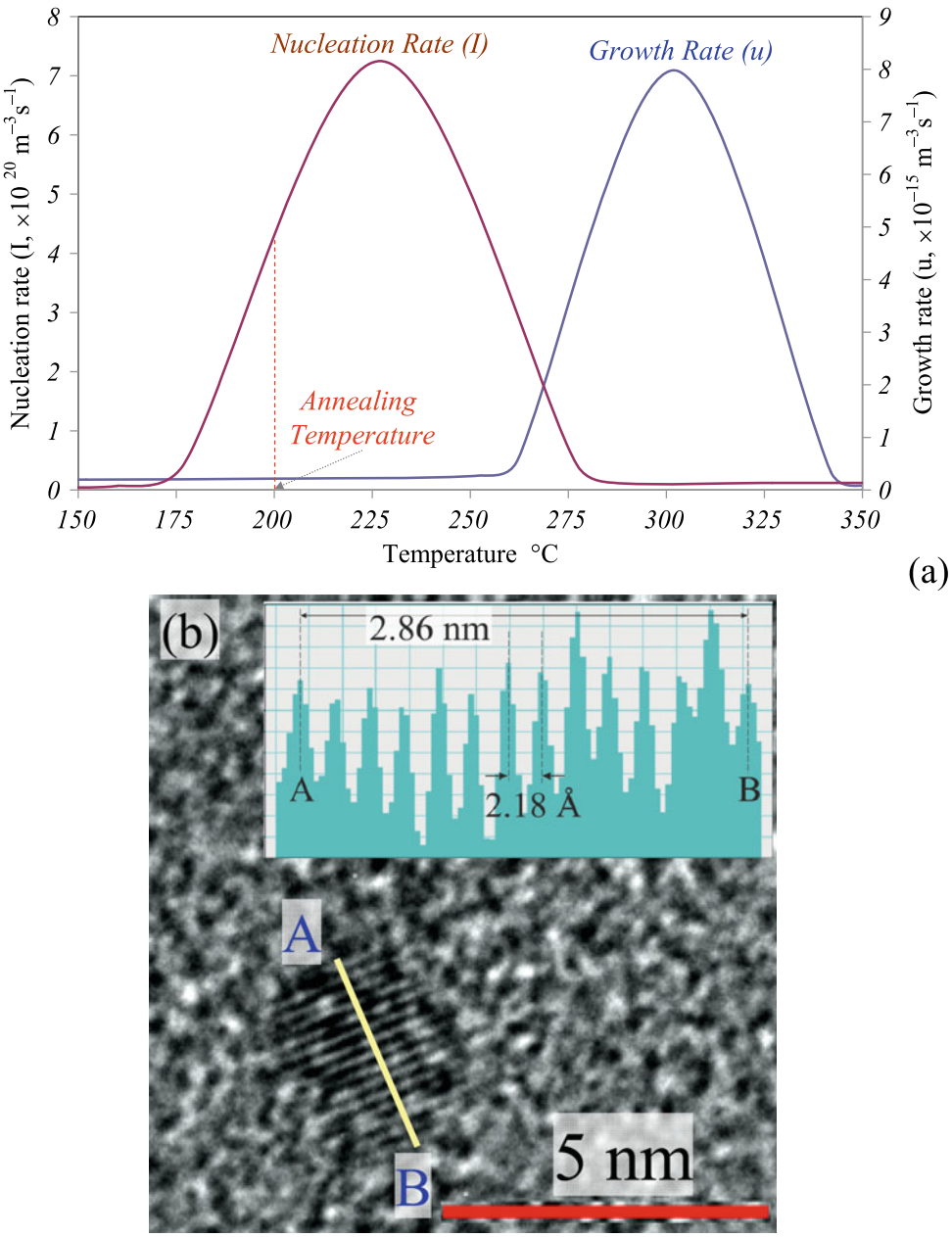

Fig. 9 **a** Plot of nucleation and growth rates for the crystallization of $Cu_{10}Zr_7$ crystal from the $(Cu_{64}Zr_{36})_{96}Al_4$ BMG. **b** HRLFI from a crystallite (d = 2.86 nm) embedded in an amorphous matrix. Inset shows a plot of the intensity across the line AB

the computed and experimental values of r^*_{bulk}. (ii) The decrease in the value of r^* for films with thickness less than $\sim$ 9 nm is prominent. (iii) r^* decreases from the center toward the surface. This implies that a nucleation behavior approaches that from a liquid (i.e., $r^* \rightarrow r^*_{\text{liquid}}$) in case of nucleation in: (i) thin films and (ii) for positions of the crystal close to the surface.

A noteworthy feature is that 'bulk like' behavior is retrieved for films as thin as 12 nm. The variation of r^* with 'h' implies that we can perform '*depth (z) sensitive lattice fringe imaging*,' that is, determine the position (h) of the nuclei from lattice fringe images, This is interesting as lattice fringe images usually do not contain depth information related to the features observed.

2.3 Growth of Precipitates in Nanocrystals

In many systems, the precipitate is coherent with the matrix in the initial stages and progressively becomes semi-coherent and incoherent on growth. The terms 'coherent and 'semi-coherent' apply to interfaces, but are often used as adjectives to precipitates (as a whole). It is to be noted that precipitates can have some interfaces which are

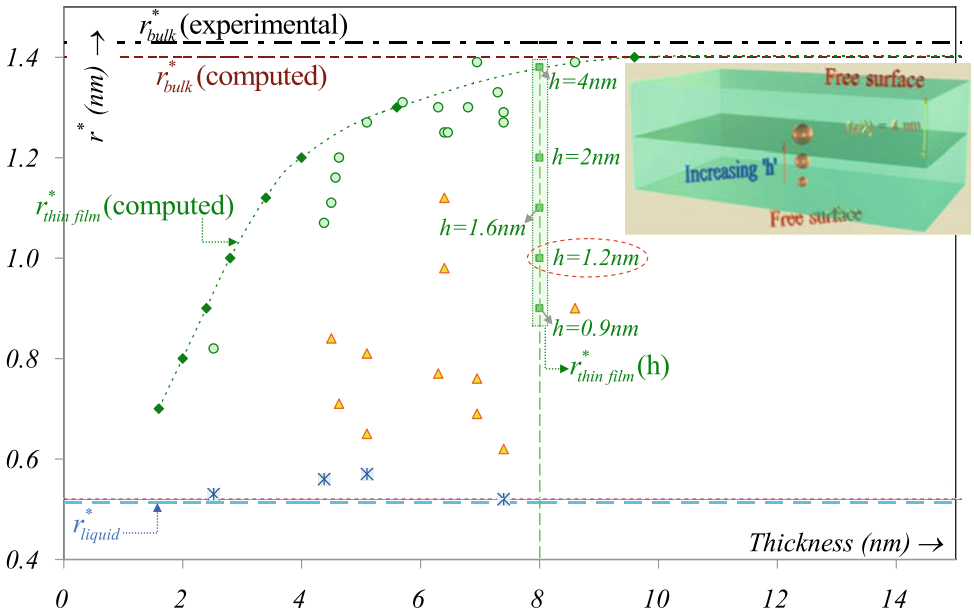

Fig. 10 Overlay of computed and experimental results. (i) The variation of r^*_{thinfilm} (computed) with 't.' (ii) r^*_{bulk} (computed and experimental) and r^*_{liquid}. (iii) Measurements using HRLFI. (iv) Variation of r^*_{computed} with 'h' (t = 8 nm, enclosed in a vertical box). Discrete point corresponds to measurements made using HRLFI. Inset to the figure shows a schematic of case (iv)

coherent with the matrix and others which are semi-coherent. The precipitation of γ-Fe (Fe-2 wt.% Cu) precipitate from a Cu-2wt.% Fe alloy has served as a model system for study for decades (Brown et al. 1968; Woolhouse and Ipohorski 1971; Watanabe et al. 2008). In this system, concomitant with the transitions of the interface character (Fig. 11), there occurs a shape transition and further a phase transformation of the metastable γ-Fe to the stable α form. Many systems, wherein precipitation occurs from a super-saturated solid solution, have been well studied in the context of precipitation hardening. The mechanism of the interaction of a dislocation with the precipitate switches from 'glide through the precipitate' (particle cutting) to Orowan bowing, as the interface character changes from coherent to incoherent (http://home.iitk.ac.in/∼anandh/E-book.htm).

On solutionizing a Fe-2 wt.% Cu alloy and subsequently heat treating at lower temperatures (e.g., 550 °C), the metastable γ-Fe precipitate nucleates. The precipitate is endowed with a coherent interface to reduce the chemical interfacial energy (local), at the expense of strain energy ('long range'). The strain energy of a spherical precipitate of radius 'r_p' in an infinite isotropic matrix is given by Matthews (1979):

$$E^{\text{strain}}_{\text{ppt}} = \frac{8\,\pi\, r_p^3 f_m^2\, G_{\text{ppt}}}{3} \frac{(1+\nu_{\text{ppt}})}{(1-\nu_{\text{ppt}})} \tag{3}$$

where 'G' is the shear modulus, 'ν' is the Poisson's ratio, 'f_m' is the lattice misfit between precipitate and matrix. The subscript 'ppt' refers to the precipitate.

On growth beyond a critical size (r^*), the precipitate becomes semi-coherent via the formation of interfacial misfit

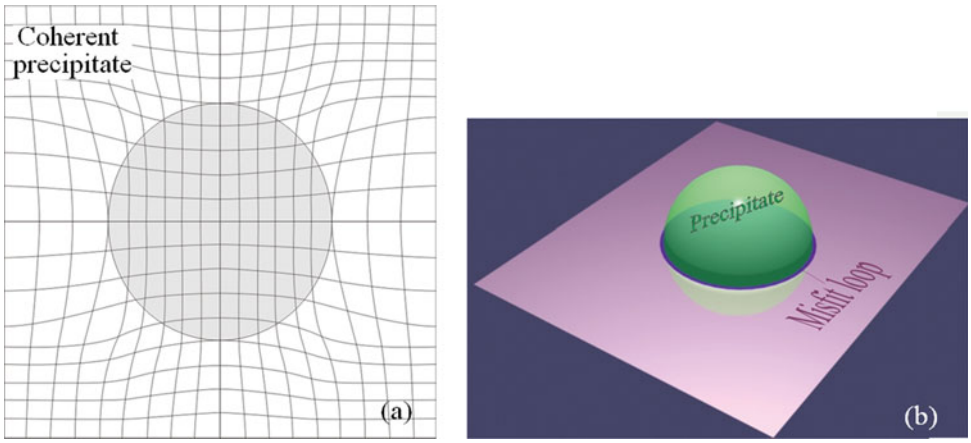

Fig. 11 Schematics showing the change in the character of the interface of a coherent precipitate on growth (e.g., in the γ-Fe precipitate in the Cu-2wt.% Fe alloy). **a** Coherent state with distortion of the atomic planes. **b** Semi-coherent with an interfacial misfit dislocation loop

dislocation loops (Matthews 1979). The energy (E_d) associated with circular a dislocation loop (of radius 'R') in an infinite body is given by Nabarro (1967):

$$E_d \approx \frac{Gb^2}{2(1-\nu)} R\left[\ln\left(\frac{8R}{\varepsilon}\right)+1\right] \tag{4}$$

where 'b' is the modulus of the Burgers vector and 'ε' is the 'core' cut-off radius (usually assumed to be in the range of 'b' to 5b). The 'core energy' has to be determined using atomistic models and is usually about 10% of the total energy of the system (Hirth and Lothe 1968; Bollmann 1970).

The critical size for the formation of the first loop along the 'equator' of the precipitate is (Woolhouse and Ipohorski 1971):

$$r* = r^*_{\text{bulk}} = \frac{b}{8\pi\,\omega(1-\nu)}\left[\ln\frac{8r*}{b}+\frac{3-2\nu}{4(1-\nu)}-1\right] \tag{5}$$

where $\omega = [(1+\nu)f_m]/[3(1-\nu)]$ (Jesser 1969) is referred to as the strain parameter.

For the case of an interfacial misfit loop, the tensile and compressive fields lie in different materials. In finite bodies the stress state of the precipitate and the dislocation loop are altered with respect to that in an infinite body. If the precipitate is close to a free-surface, then domain deformations can lead to partial relaxation of the stress fields. In scenarios such as these, FEM has proved to be a powerful tool not only in determining the stress state of the body, but also in the computation of critical parameters related to the system (Kumar et al. 2014).

The discussions above, regarding the critical size for the formation of a misfit loop, were based on global energy considerations. An alternate view point is based on a local force balance (Kumar et al. 2013a). The local forces on the loop involve radial and circumferential/tangential forces, and off interface stability is a distinct possibility. It is interesting to note that a precipitate of a lower radius than the critical radius (i.e., $r_c < r^*$) can 'stabilize' an interfacial loop due to force balance on the loop. In this case, the line tension force tending to shrink the loop balances the coherency stresses trying to expand the loop. It is to be noted that at r_c it is not energetically favorable to form a loop. The value of r_c can be computed using:

$$r_c = \frac{b}{16\pi\,\omega\,(1-\nu)}\left[\ln\left(\frac{8r_c}{b}\right)+\frac{3-2\nu}{4(1-\nu)}\right] \tag{6}$$

Subsequent to the formation of a single interfacial misfit dislocation loop, two (Kumar et al. 2013b) and multiple loops can form, which progressively alleviate the coherency stresses and in the limiting case results in an incoherent interface. This scenario of coherent to semi-coherent transition in precipitates represents a 3D analog of that occurring in epitaxial films (Subramaniam 2004; 2003), wherein the edge component of the misfit dislocation is responsible for stress relief. Configurational forces on the dislocation have also been evaluated in these systems (Subramaniam and Ramakrishnan 2003), along with interesting effect arising from finite size domains (Arun Kumar and Kavitha and Anandh Subramaniam, 2012; Kumar and Subramaniam 2012b).

Figure 12 shows the FEM simulated stress state in the presence of precipitates of two different sizes. In (a), the precipitate is coherent, while in (b), it is semi-coherent. The

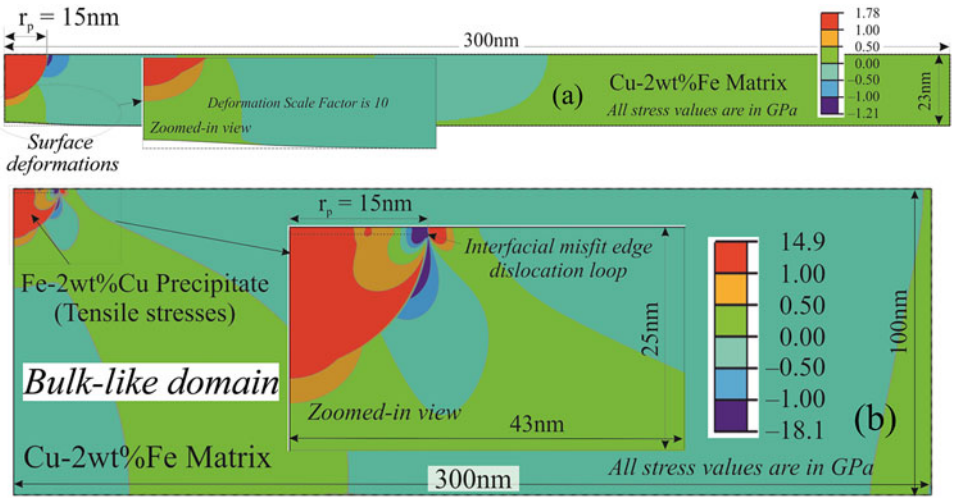

Fig. 12 Stress state (plot of σ_{yy} contours) due to coherent and semi-coherent precipitates. Symmetrical half of the film is shown in the figures. **a** Coherent precipitate in a nanoscale thin film (T = 46 nm). The inset shows a zoomed-in view, highlighting domain deformations arising due to the coherency stresses. **b** The state of stress in the presence of interfacial misfit edge dislocation loop in a 'thick' domain with T = 200 nm. The radius of the precipitate (r_p) is 10 nm

deformation of the domain due to the stress fields is to be noted in (a). The reversal in the state of stress (from tension to compression) due to the change in the character of the interface (in the vicinity of the dislocation) is to be noted.

Figure 13a, b shows methodology to determine the critical size (r^*). Figure 13a shows the plots of strain energy of the system as a function of the radius of the precipitate (r_p), with and without a misfit dislocation loop, in a 'bulk domain' (the thickness of the film (T) is 200 nm). Figure 13b shows the corresponding plot for a thin film (T = 46 nm). It is seen that at smaller sizes of the precipitate, the energy of the system increases on the introduction of a misfit loop. The

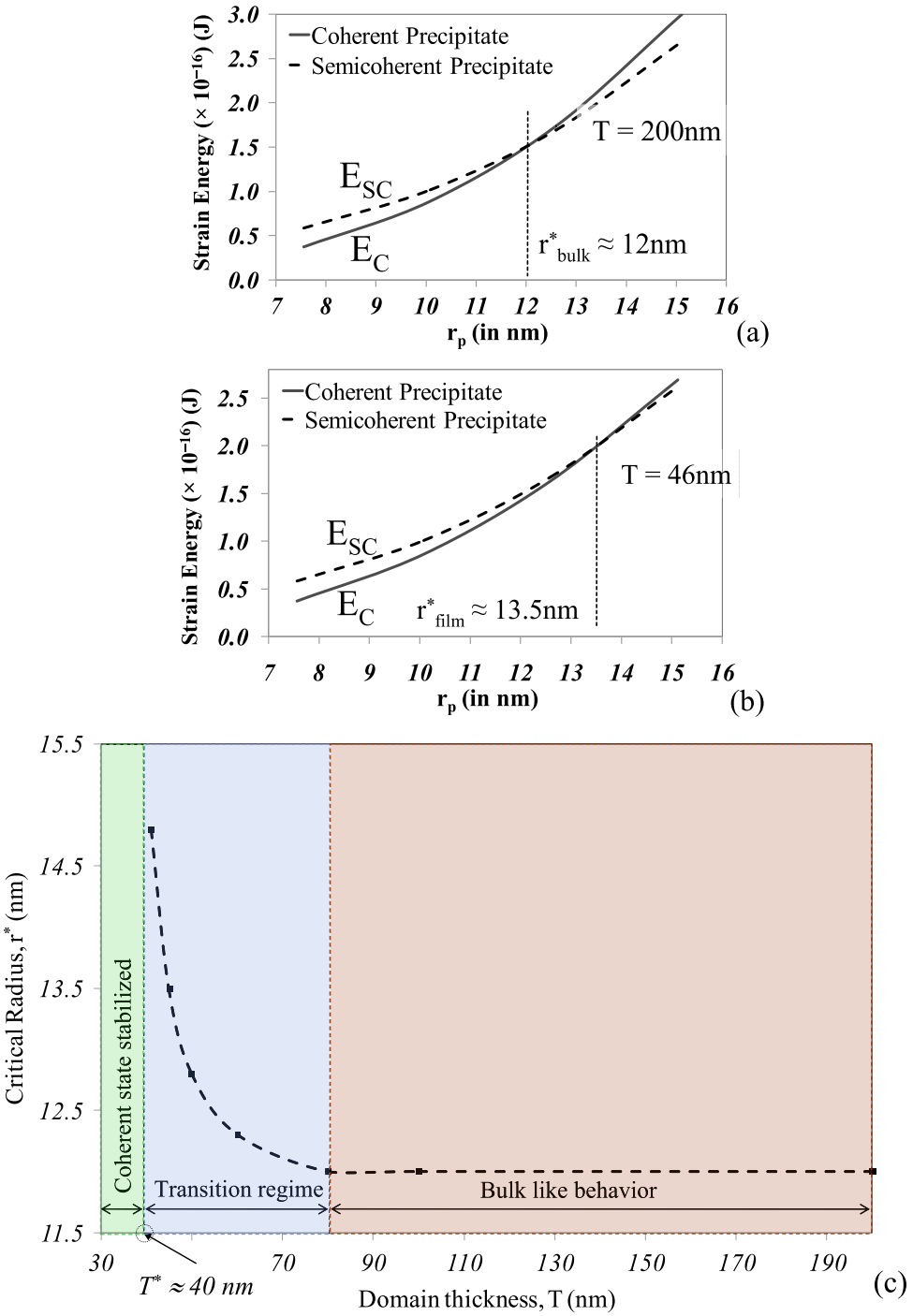

Fig. 13 Plot of strain energy of the system as a function of the radius of the precipitate (r_p), with and without a misfit dislocation loop: **a** bulk domain (T = 200 nm) and **b** nanoscale thin film (T = 46 nm). The intersection of the two curves gives the value of critical radius (r^*). (c) Variation in the critical radius (r^*) with the thickness of the film (T). Below a thickness of about 40 nm (= T^*), the coherent state is stabilized

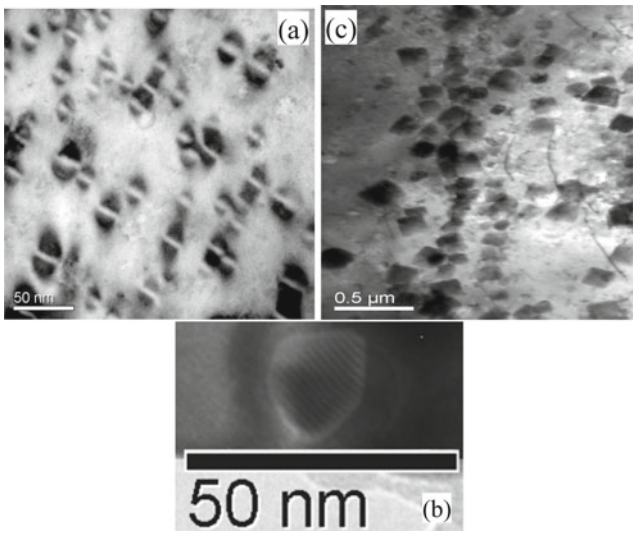

Fig. 14 TEM micrographs depicting the three stages during the growth of precipitates in a bulk sample. **a** A bright field image showing the coffee bean contrast associated with coherent precipitates (aged at 550 °C for 12 h). **b** Moiré fringe contrast arising due to an array of misfit dislocations at the interface of a semi-coherent precipitate (aged at 550 °C for 24 h). **c** Cuboidal incoherent precipitates, which lack strain field contrast (aged at 750 °C for 48 h). The value of the critical size r^* determined experimentally is about 11 nm

cross-over of the curves represents the critical size beyond which the semi-coherent state is energetically stabilized. As the thickness of the film is decreased, the strain energy due to a coherent precipitate reduces. Below a certain value of the thickness of the domain, the magnitude of r^* shows a sharp increase (Fig. 13c). It is seen from the figure that below a thickness of about 40 nm (labeled as T^*) the coherent state is stabilized.

In Fig. 14, we can see the different stages occurring during precipitate growth: (a) coherent precipitates (with strain field contrast), (b) semi-coherent precipitate (with moiré fringe contrast), and (c) incoherent precipitates. The typical 'coffee bean' contrast in the bright field image arises due to strain fields associated with the coherent precipitate (the crystal planes are locally bent to be at the Braggs' condition). An array of misfit loops decorates the interface in the semi-coherent precipitate and gives rise to the Moiré fringe contrast. This represents the partially relaxed state. On further growth, the precipitates lose their coherency and become cuboidal in shape.

In Fig. 15, precipitation has been carried out in a TEM sample (which is a thin film). The sizes of the coherent precipitates are to be noted. The deviation from the typical coffee bean contrast in the BFI is also to be noted. The heat treatment process has led to a variation in the thickness of the sample. This is best appreciated by creating a thickness map using scanning transmission electron microscopy (STEM) (Fig. 16). This local variations in thickness can play a role in the stabilization of coherent state (Rani et al. 2015).

In the picture presented above, certain interesting features have been omitted. Regarding precipitates in finite domains (like thin cylinders), the coherent state is stabilized in two different size regimes of the precipitate: one at small sizes and other at large sizes. In the intermediate size regime, the semi-coherent state is stable (Rani et al. 2017). This is reminiscent of the reentrant phase transition in condensed matter systems. This picture is true for cylinder diameters above a certain critical value. A phase diagram can be drawn, demarcating regions of stability of the coherent and semi-coherent states (Rani et al. 2017).

2.4 Surface Stress Actuated Lattice Expansion in Metal Nanoshells

We have already noted that surface stress can have profound effects in finite domains. Surface stress is tensile in metallic materials and can be compressive in polar surfaces. In nanocrystals, the compression induced by tensile surface stress can cause a reduction in the lattice parameter (Kumar and Subramaniam 2013b), and this fact has remained an unchallenged observation. In hollow metallic structures, the stress on the outer surface tends to compress the material, while that on the inner surface has the opposite effect. Hence, the resultant between the stress existing in the inner and outer surfaces determines the altered lattice parameter. Thus, hollow metal shells are an interesting class of structures, wherein there is interplay between geometry, stress, and scale. It is noteworthy that hollow spheres have been investigated in diverse contexts, which include anodes for batteries (Iyer et al. 2016), gas entrapment (Zheng et al. 2014; Shervani et al. 2017), and drug delivery (Subramaniam 2020).

Surface stress can be simulated by a two-scale methodology (Kumar and Subramaniam 2013b). The method was developed based on a concept proposed by Shuttleworth (Amstad and Reimhult 2012), wherein the atoms constituting a surface is brought into registry with the bulk by the introduction of biaxial eigenstrains. The parts to this computation are: (i) the determination of the lattice parameter of a layer (or bilayer) of atoms using density functional theory (DFT) and (ii) use of this value in a finite element model to compute the surface stress. The methodology allows us to study the effect of inner and outer surface stresses independently. This approach, albeit being approximate, can be

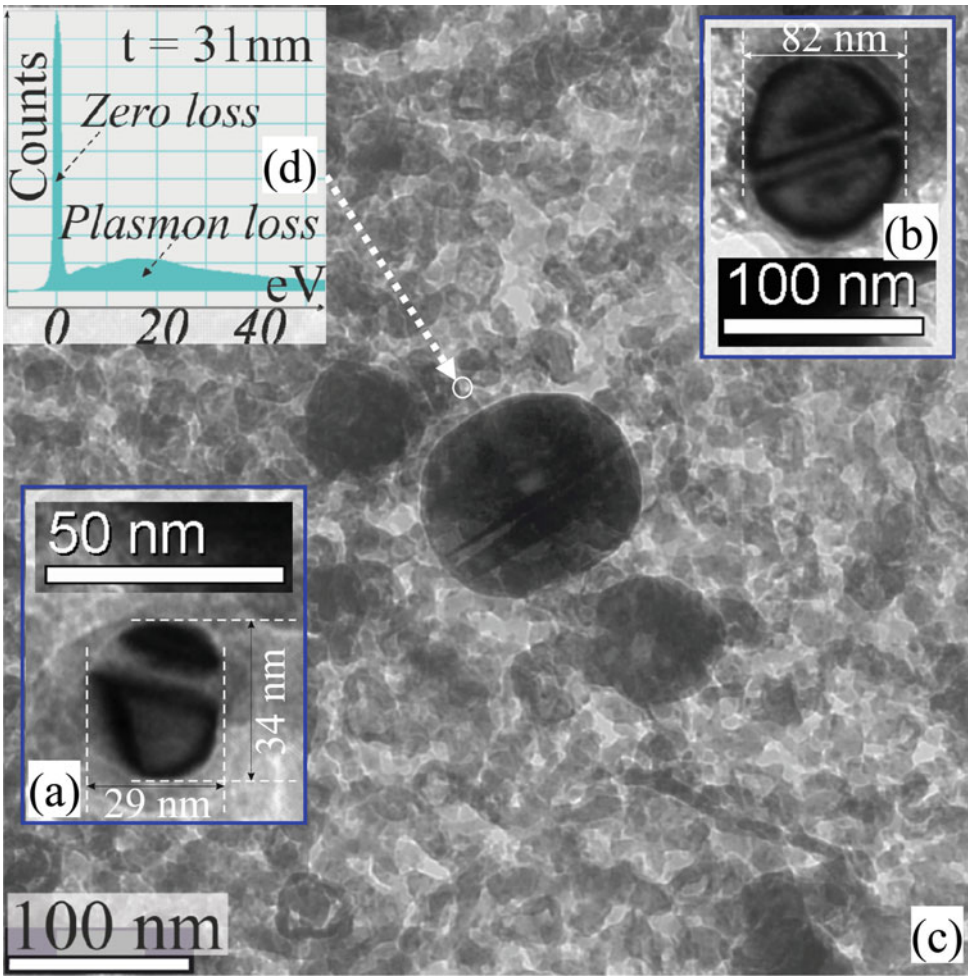

Fig. 15 TEM bright field images indicating the presence of coherent precipitates in thin film samples (**a**–**c**). The variation from the typical coffee bean contrast is to be noted. The sizes of the precipitate are considerably larger than r^*_{bulk}. **d** EELS spectrum is used to determine the local thickness

applied to lengthscales, wherein techniques like molecular dynamics prove to be time-consuming.

Let us consider a Ni nanoshell with an outer diameter (OD) of 80 nm and study the effect of varying shell thickness on the lattice parameter. By 'switching on' the outer and inner surface stress independently, we can study their effects on the lattice parameter, followed by a simulation, wherein the combined effect can be evaluated. The lattice parameter under consideration is along the radial direction (a_{radial}). Figure 17 shows the variation in lattice parameter with shell thickness. Three regimes can be identified in the plot: (i) thick shell (R1), (ii) thin shell (R2), and (iii) very thin shell (R3). In the thick shell regime (R1), the behavior is similar to that for a nanoparticle, wherein there is a reduction in a_{radial}. This occurs due to the domination of the outer surface stress (over the inner surface stress). In the case of thin shells (region R2), the reverse of the thick shell case is observed (i.e., the inner surface stress dominates over the outer one), and this leads to an increase in a_{radial}. This is an interesting result, as this is the first time that surface stress-mediated lattice expansion has been reported, in a metallic system. In both the regimes R1 and R2, the outer surface stress tends to compress the particle; which is but expected. The strange feature in the plot is R3, wherein the outer surface stress causes an expansion of the lattice. This implies that in R3 the lattice expansion is even more pronounced.

At the heart of this effect is the role of the Poisson's ratio (ν), and this can be evaluated by artificially varying the magnitude of 'ν' in the simulations (discrete points in Fig. 17). For values of 'ν' above the natural value for that for Ni ($\nu_{\text{Ni}} = 0.34$), the effect is accentuated, while for lower values, the opposite is observed. For a value of $\nu < 0.2$, the anomalous behavior vanishes.

Experimentally, Ni hollow spheres are easy to synthesize, and hence, results obtained can be compared with the

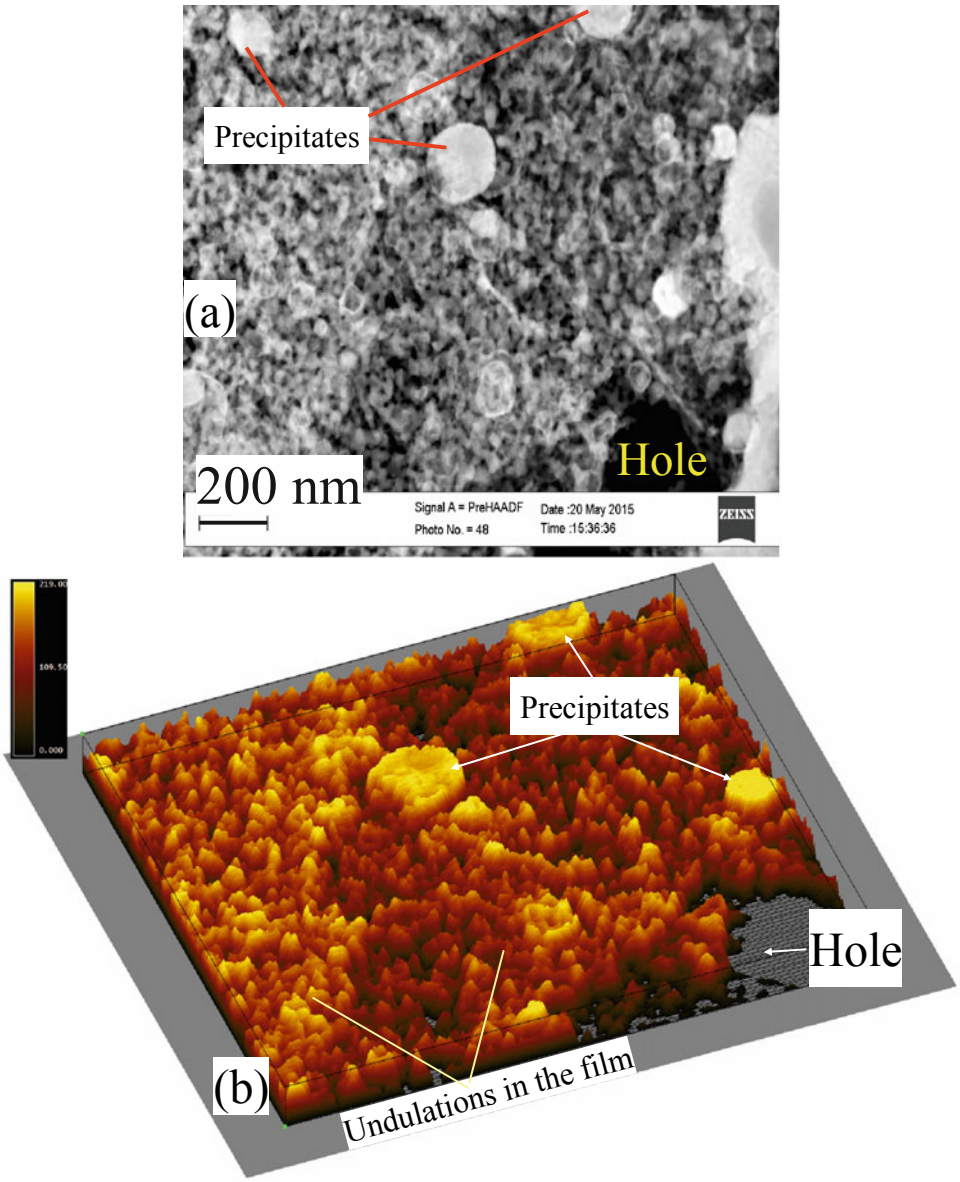

Fig. 16 **a** STEM map from a region with a coherent precipitate. **b** A thickness profile computed from STEM map. The local variations in the thickness are to be noted

computations. The effect of internal pressure on the lattice parameter of Ni hollow spheres has also been investigated (Shuttleworth 1950). The experimental confirmation of the aforementioned computational observations comes via TEM investigations (Fig. 18). Three sample HRLFI are shown in the figure, corresponding to the three regimes. It is difficult to obtain lattice fringes from thick shells, and hence, this has been replaced by a sample nanocrystal. The dimensions of the nanostructures and the corresponding a_{radial} values obtained are as follows. (1) Nanoparticle (D = 6 nm): $a_{\text{radial}}^{\text{exp}}$ = 3.46 Å, (2) thin walled MNS (OD = 150 nm, t = 25 nm): $a_{\text{radial}}^{\text{exp}}$ = 3.63 Å, And (iii) very thin walled MNS (OD = 100 nm, t = 10 nm): $a_{\text{radial}}^{\text{exp}}$ = 3.81 Å. It is seen that the experimental observations corroborate well with the computational results (Iyer et al. 2017).

A point to be noted is that obtaining HRLFI of 'ideal quality' is very difficult. This arises from multiple factors like: the stability of the particle under the electron beam and the difficulty in obtaining lattice fringes perpendicular to the radial direction. Needless to point out, multiple samples need to be studied to obtain repeatable results.

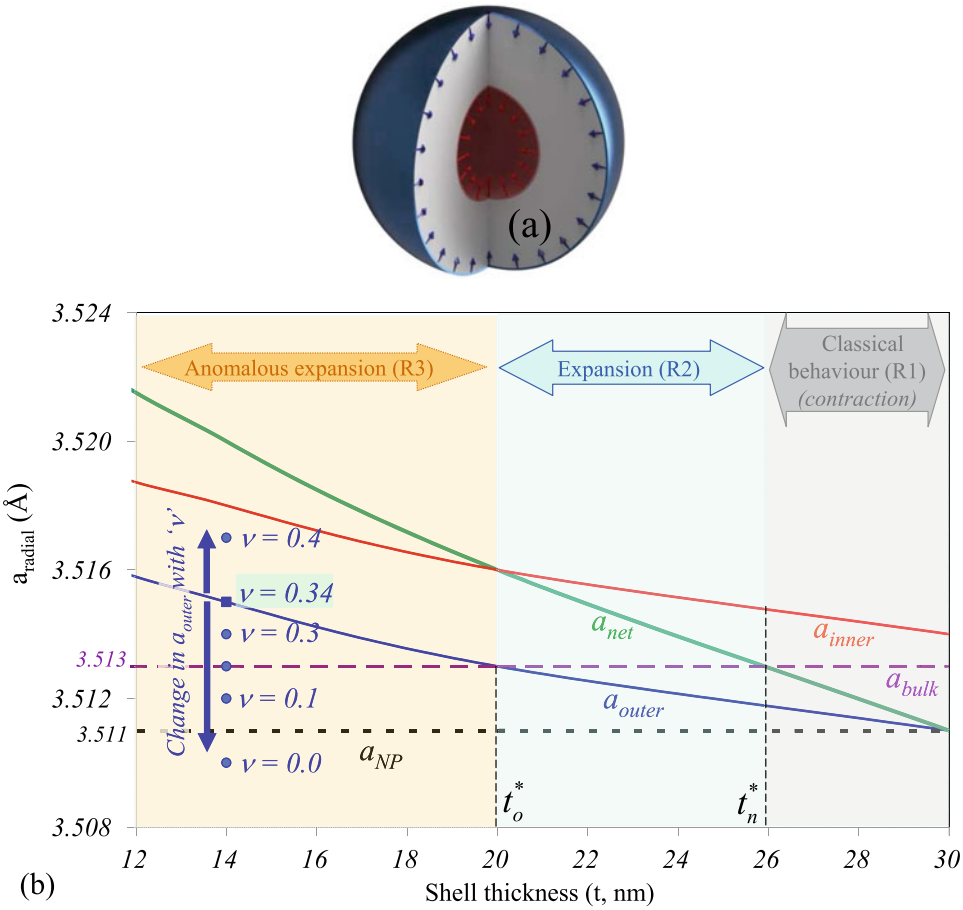

Fig. 17 **a** Schematic showing the effect of surface stresses existing on the outer and inner surfaces. **b** Variation in lattice parameter (a_{radial}) with shell thickness (Ni with OD = 80 nm). The effect of outer, inner, and combined surface stress on the lattice parameters is plotted as separate curves (labeled as a_{outer}, a_{inner}, and a_{net}). The effect of the value of Poisson's ratio on the lattice parameter (t = 14 nm, $\nu \in (0 \text{ to } 0.5)$) is overlaid on the figure. The horizontal lines correspond to the bulk lattice parameter (a_{bulk}^{Ni}) and that of a nanoparticle (a_{NP}). The nanoparticle has only outer surface stress acting on it

3 Musings

It is clear from the case studies considered that multiple tools are required to fully characterize the structures and to comprehend the physics involved. Multiple TEM techniques serve to reveal many facets of the sample and highlight the power of the tool.

If experimental techniques provide the 'body' of an investigation, then theories and computations endow it with a 'mind'. Hence, no investigation can be considered as complete without the synergistic role of experiments and computations. It is expected that better experimentation (along with the use of additional tools) and computations with higher accuracy can further unveil hitherto unanticipated secrets.

In one of the examples considered, it was noted that nanoscale effects are observed at relevant lengthscale of the order of few nanometers and 'bulk' behaviors was retrieved at a scale of greater than 12 nm. Specific systems have been considered to elucidate a specific effect (e.g., the Cu-Fe system was considered in the context of the stabilization of the coherent precipitate); however, it is expected that the observations have a much broader applicability.

4 Concluding Remarks

Transmission electron microscopy has proved to be a ubiquitous tool for the study of nanoscale structures and phenomena. Powerful computational tools have provided a firm conceptual footing to these investigations. Diverse techniques like high-resolution lattice fringe imaging, Fresnel contrast imaging and Moiré fringe imaging help unravel various facets related to the sample.

One can discover new effects and phenomena in nanocrystals, which have no 'bulk' counterparts. These include (i) the stabilization of the coherent precipitates, (ii) anomalous lattice expansion in hollow metallic shells, and (iii) 'liquid-like nucleation' in a solid-state diffusional transformation. Interestingly, surprises in this area are coming thick and fast and not surprisingly transmission electron microscopy is playing a major role in these discoveries.

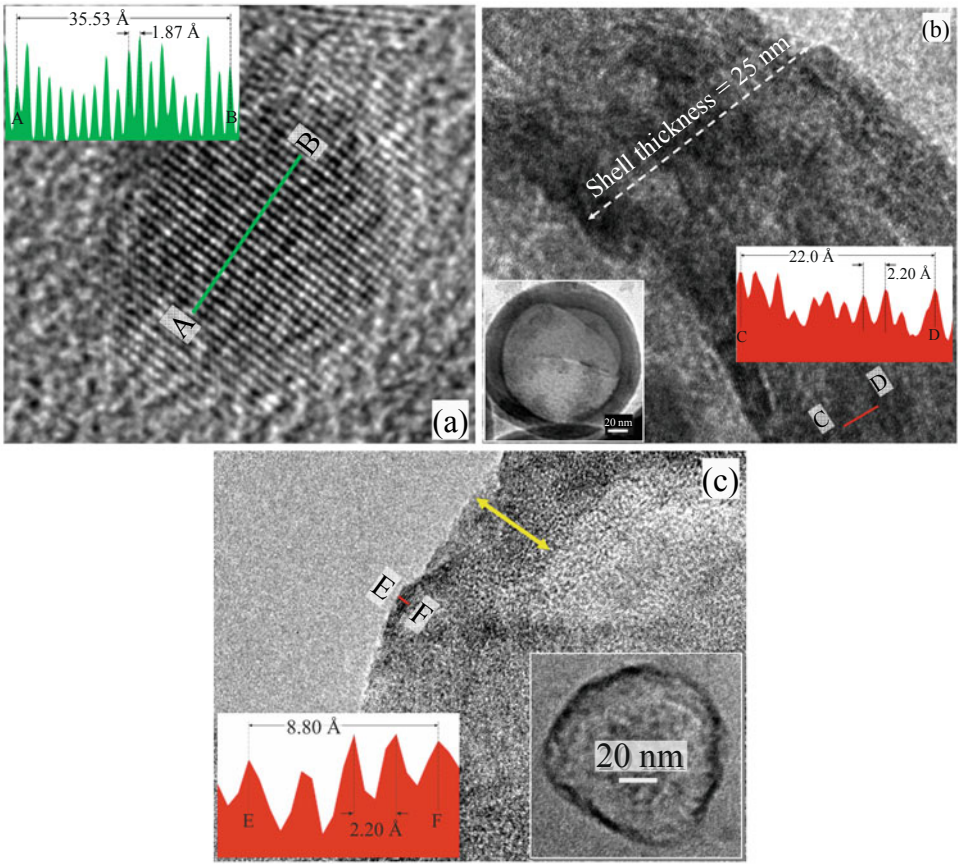

Fig. 18 HRLFI to determine the lattice parameter along the radial direction. **a** Nanoparticle (diameter = 6 nm). **b** A thin shell structure (OD = 150 nm, t = 25 nm). **c** A very thin shell structure (OD = 100 nm, t = 10 nm). The lattice spacing is measured using intensity patterns obtained across the lines in the HRLFI (AB, CD, and EF). Micrographs in the inset to (b) and (c) are bright field images from the hollow shells

The interconnectedness between stress, interfaces, and geometry may be considered ubiquitous, and it is expected that research with these facets in view will unveil amazing new phenomena and discoveries.

Acknowledgements The authors acknowledge the contributions of group members: Dr. Suboohi Sherwani and Dr. Pooja Rani for their contributions to the work, on which this article is based. Further we would like to acknowledge our collaborators and co-authors: Prof. Raj Pala, Dr. Raghvendra Tiwari, Dr. B. Vishwanadh, Prof. Somnath Bhattacharyya, Prof. Sri Sivakumar, Dr Gargi Mishra, Mr. Deb De, Prof. Kantesh Balani, Dr. Kawsar Ali, and Dr. Ashok Arya.

References

Albisetti AF, Biffi C, Tuissi A (2012) Synthesis and structural analysis of $Cu_{10}Zr_7$. J Alloys Compd 544:42

Amstad E, Reimhult E (2012) Nanoparticle actuated hollow drug delivery vehicles. Nanomed J 7:145

Kumar A, Kavitha KG, Subramaniam A (2012) Interfacial edge dislocation Interactions with free-surfaces in nanocrystals. J Nanosci Nanotechnol 11:1

Baser TA, Baricco M (2008) Glass forming ability of $(Cu_{50}Zr_{50})_{96}M_4$ (M=None, Al, Nb) bulk metallic glasses. Rev Adv Mater Sci 18:71

Bhattacharyya S, Subramaniam A, Koch CT, Ruhle M (2006) Aspects regarding measurement of thickness of Intergranular glassy films. J Microsc 221:46

Bollmann W (1970) Crystal Defects and Crystalline Interfaces. Springer-Verlag, Berlin

Brown LM, Woolhouse GR, Valdrè U (1968) Radiation-induced Coherency Loss in a Cu-Co Alloy. Philos Mag 17:781

David A (2009) Porter. Phase Transformations in Metals and Alloys, CRC Press, Boca Raton, Kenneth E. Esterling and Mohamed Y. Sharif

Eshelby JD (1953) Screw dislocations in thin rods. J Appl Phys 24:176

Gupta A, Shervani S, Amaladasse F, Sivakumar S, Balani K, Subramaniam A (2019) Enhanced reversible hydrogen storage in Nickel Nano hollow spheres. Int J Hydrog Energy 44:22032

Hirth JP, Lothe J (1968) Theory of Dislocations. McGraw-Hill, New York

Iyer G, De D, Kumar A, Pala R, Subramaniam A (2016) two scale simulation of surface stress in solids and its effects. Appl Surf Sci 371:343

Iyer G, Shervani S, Mishra G, De D, Kumar A, Sivakumar S, Balani K, Pala R, Subramaniam A (2017) Poisson effect driven anomalous lattice expansion in metal nanoshells. Appl Phys Lett 110:131603

Jesser WA (1969) On the theory of loss of coherency by spherical precipitates. Philos Mag 19:993

Suresh K, Radhakrishnan TK, Kalaichelvi P (2016) A review of classical and nonclassical nucleation theories. Cryst Growth Des 16:6663

Khanikar P, Subramaniam A (2010) Critical size for edge dislocation free free-standing nanocrystals by finite element method. J Nano Res 10:93

Kumar A, Subramaniam A (2011) Materials analogue of zero stiffness structures. Philos Mag Lett 91:272

Kumar A, Subramaniam A (2012a) Stable edge dislocations in finite crystals. Philos Mag 92:2947

Kumar A, Subramaniam A (2012b) Finite substrate effects on critical thickness in epitaxial systems. J Adv Mater Res 585:39
Kumar A, Subramaniam A (2013a) Negative, zero and positive stiffness in extended Eshelby plates. Philos Mag Lett 93:703
Kumar A, Subramaniam A (2013b) Position dependant critical thickness in finite epitaxial systems. Appl Surf Sci 275:60
Kumar A, Kaur G, Subramaniam A (2013a) Critical sizes for coherent to semicoherent transformation in precipitates. Int J Mater Res 104:1171
Kumar A, Gautam M, Subramaniam A (2013b) On the Formation and Stability of Two Misfit Dislocations in the Cu-γFe System. J Mech Mater Struct 7:135
Kumar A, Gautam M, Subramaniam A (2014) Critical sizes for the stabilization of coherent precipitates. J Appl Phys 115:193509
Malis T, Cheng SC, Egerton RF (1988) EELS log-ratio technique for specimen thickness measurement in the TEM. J Electron Microsc Tech 8:193
Matthews JW (1979) In: FRN Nabarro (eds.), Dislocations in Solids. North-Holland Publishing Company, New York
Nabarro FRN (1967) Theory of crystal dislocations. Clarendon Press, Oxford, p 75
Nalwa, Singh H, Ed (2004) Encyclopedia of nanoscience and nanotechnology. American Scientific Publishers, Los Angeles, p 10
Rani P, Raghavendra RM, Subramaniam A (2020) On the variability of critical size for homogeneous nucleation in a solid-state diffusional transformation. arXiv:2007.02112
Raghavendra RM, Ganesh Iyer D, Kumar A, Subramaniam A (2018) Surface stress mediated image force and torque on an edge dislocation. Philos Mag 98:1731
Rani P, Kumar A, Vishwanadh B, Bhattacharyya S, Tewari R, Subramaniam A (2015) Stabilization of coherent precipitates in nanoscale thin films. Philos Mag 95:4130
Rani P, Kumar A, Vishwanadh B, Ali K, Arya A, Tewari R, Subramaniam A (2017) Liquid like nucleation in free-standing nanoscale films. Nanoscale (Communication) 9:12283
Schodek D, Ferreira P, Ashby M (2009) Nanomaterials, nanotechnologies and design: an introduction to engineers and architects. Butterworth-Heinemann
Shervani S, Mukherjee P, Gupta A, Mishra G, Illath K, Ajithkumar TG, Sivakumar S, Sen P, Balani K, Subramaniam A (2017) Multi-mode Hydrogen Storage in Nanocontainers. Int J Hydrog Energy 42:24256
Shuttleworth R (1950) The surface tension of solids. Proc Phys Soc A 63:444
Subramaniam A (2004) Critical thickness of equilibrium epitaxial thin films using finite element method. J Appl Phys 95:8472
Subramaniam A, Shervani S, Gupta A, Balani K (2020) Gases in nanocontainers, smart nanocontainers: micro and nano technologies. Elsevier p 499
Subramaniam A, Balani K, http://home.iitk.ac.in/∼anandh/E-book.htm.
Subramaniam A, Ramakrishnan N (2003) Analysis of thin film growth using finite element method. Surf Coat Tech 167:249
Subramaniam A, Kumar A (2014) Edge dislocations in finite crystals: special effects and strange phenomena. Mech Solids Directions 14:88
Watanabe D, Watanabe C, Monzen R (2008) Effect of coherency on coarsening of second-phase precipitates in Cu-base alloys. J Mater Sci 43:3946
Woolhouse GR, Ipohorski M (1971) On the interaction between radiation damage and coherent precipitates. Proc R Soc A 324:415
Zheng G, Lee SW, Liang Z, Lee HW, Yan K, Yao H et al (2014) Interconnected hollow carbon nanospheres for stable lithium metal anodes, Nat Nanotechnol 9:618

JEOL 7100F FESEM: Advanced Center for Materials Science

JEOL 7100 field-emission scanning electron microscope (FESEM) was commissioned in service, in latter half of 2014. Ever since, this machine has been giving service to the entire IITK campus community, and beyond, day in and day out. It has run for over 4000 h for imaging and over 5000 h for EBSD. This state-of-the-art equipment is capable of resolving upto 3 nm at 15 kV. It is equipped with an ET detector (SE) and a retractable BSE detector. It has a Zr-O/W emitter. Some of the features of the equipment are.

Accelerating Voltage: 0.5 to 30 kV

Probe Current: 10^{-12} to 2 x 10^{-7} A

Tilt: -5°–70°

Rotation: 360°

Apart from these, it is equipped with some state of the art accessories which further enhance its characterization abilities.

EDS: Oxford Nano Analysis

EBSD: Oxford Nordlys detector

Stage: Gatan MT 2000E High temperature tensile stage (Tensile load: 5 KN; Temperature: RT to 500 °C)

Who can get time on this machine: Anyone from the country can make a request for time on this machine; however, researchers of IITK are given a preference.

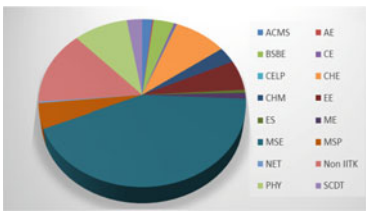

How to book: Researchers from IITK can book through the online booking system, the link to which is at ACMS website. Others can contact the concerned person. This facility would soon be available on I-STEM.

Contact		
Mr. M. Siva Kumar	**ACMS-112;**	**Email**: **rmuthu@iitk.ac.in**
P.I. Prof. Kantesh Balani	**Biomaterials lab**	**Email**: **kbalani@iitk.ac.in**

K. Biswas et al. (eds.), *Electron Microscopy in Science and Engineering*, IITK Directions 6,
https://doi.org/10.1007/978-981-16-5101-4

JEOL JSM 6010 LAW-SEM: Advanced Center for Materials Science

This is a compact SEM for the quick image analysis with high resolution and compositional information. The integral EDS detector can be used for micro-compositional analysis.

BSE Resolution: 5 mn at 20 kV

Magnification: 5–300000x

Accelerating voltage: 0.5 to 20 kV

Automatic SEM condition set-up based on sample type

Who can get time on this machine: Anyone from the country can make a request for time on this machine; however, researchers of IITK are given a preference.

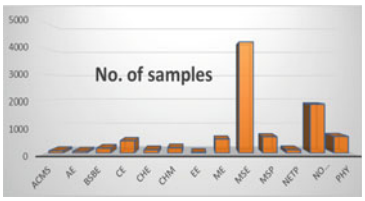

How to book: Researchers from IITK can book through the online booking system, the link to which is at ACMS website. Others can contact the concerned person. This facility would soon be available on I-STEM.

Contact		
Mr. M. Siva Kumar	**ACMS-112;**	**Email**: **rmuthu@iitk.ac.in**
P.I. Prof. Kantesh Balani	**Biomaterials lab**	**Email**: **kbalani@iitk.ac.in**

FEI QUANTA 200 W-SEM: Advanced Center for Materials Science

FEI Quanta 200 is a tungsten filament based scanning electron microscope (W-SEM). This equipment is more than 15 years old and still functioning as new. This equipment provides very high resolution SE and BSE images.

All types of materials ranging from metals to ceramic to powders to polymers, and even biological samples can be analysed in this machine. Some of the features of the equipment are:

SE Resolution: 2 nm at 20 kV

Accelerating Voltage: 0.5–30 k V

Magnification: 5–500,000X

Who can get time on this machine: Anyone from the country can make a request for time on this machine; however, researchers of IITK are given a preference.

Contact		
Mr. M. Siva Kumar	**ACMS-112;**	**Email**: **rmuthu@iitk.ac.in**
P.I. Prof. Kantesh Balani	**Biomaterials lab**	**Email**: **kbalani@iitk.ac.in**

How to book: Researchers from IITK can book through the online booking system, the link to which is at ACMS website. Others can contact the concerned person. This facility would soon be available on I-STEM.

EVO 18 SEM: Biomedical Science and Bioengineering

EVO 18 SEM is an environmental scanning electron microscope (E-SEM) from Carl Zeiss, Germany. This equipment was installed in BSBE at 2011 and since then it has been operational continuously for 10 years now. The equipment is capable of imaging/analysing various types of samples, for example, metals, ceramics, and polymers, and hydrated samples, for example biological.

Filament: Tungsten

Secondary e-image resolution: 50 nm (Depends on sample)

E-SEM mode: The Variable pressure detector can analyze non-conducting and hydrated samples

BSE Detector: Available

EDX detector: Available

Tilt: 0°-60°

Rotation: 360° Degree

EHT: 200 V–30 kV **Magnification**: **50** ~ 100 K (Depends on sample)

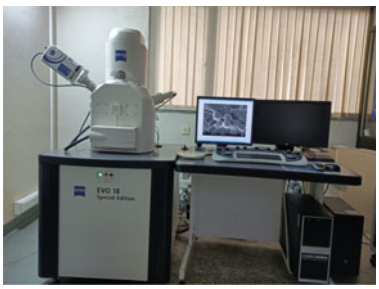

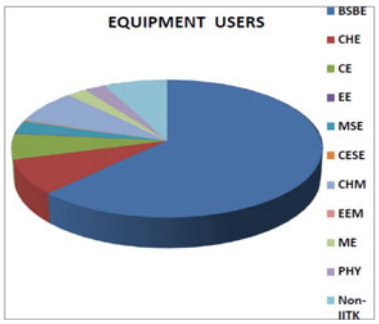

Who can get time on this machine: Anyone from the country can make a request for time on this machine; however, researchers of IITK are given a preference.

How to book: Researchers from IITK can book through an e-mail to the operator, for which the contact details are available at BSBE website.

Contact		
Mrs. Shraddha Singh	**BSBE T-111;**	**Email**: **ssinghs@iitk.ac.in**
P.I. Prof. D.S. Katti	**BSBE LN 16**	**Email**: **dsk@iitk.ac.in**

Field Emission Gun-Scanning Electron Microscope: Chemical Engineering

Post Graduate Research Laboratory (PGRL) is a user facility in the Department of Chemical Engineering at IIT Kanpur that provides sophisticated instruments and services for academic and industrial researchers to explore various research problems and address a variety of scientific and engineering challenges. In-house equipments at PGRL include a TESCAN high resolution Field Emission Gun-Scanning Electron Microscope (FESEM) MIRA^3 with STEM detector also by TESCAN and an EDS detector by OXFORD.

Salient Features of the Electron Microscope and the Detectors:

PGRL has a high brightness Schottky emitter field emission scanning electron microscope which offers multiple imaging modes for high-resolution imaging, wide field-of-view, or large depth-of-focus. The microscope can be operated at accelerating voltages from 1 to 30 kV. Imaging at very high resolution (1 nm at 30 keV and 2 nm at 1 keV) is possible with certain types of specimens. Its superb performance, particularly at low accelerating voltages (*i.e.*, 0.2–1 kV using Beam Deceleration Mode), makes it especially suitable for imaging the surface detail of polymeric, biological, and other low-density materials. In-lens (In-Beam Mode) secondary and back-scattered electron detectors enable very short working distances. Standard chamber secondary and back-scattered electron detectors are also available for larger working distances, and thus, larger fields of view.

Energy Dispersive Spectroscopy (EDS) Analysis provides elemental and chemical analysis of a sample inside the SEM with options of Point & ID and detailed elemental maps. The EDS detector at PGRL is LN_2 free type based on latest Silicon Drift Detector technology**.** It has a large SDD crystal size of 50 mm^2. The detectable element range is from Beryllium (Be) to Californium (Cf). The EDS system has following resolution Carbon (better than 56 eV), Fluorine (better than 65 eV) and Mangenese (better than 124 eV).

The TESCAN-STEM detector with simultaneous Bright Field (BF) and Dark Field (DF) imaging have a resolution of 0.8 nm at 30 kV. The detector consists of three semiconductor sensors for bright field and dark field imaging. Simultaneous acquisition has been provided for bright and dark field imaging and mixing of these two signals is also possible.

Contact		
MR. Rajesh Singh	**PGRL-302**	**Email**: **rajeshsg@iitk.ac.in**
P.I. Dr. Debjani Banerjee	**PGRL-302**	**Email**: **debjani@iitk.ac.in**

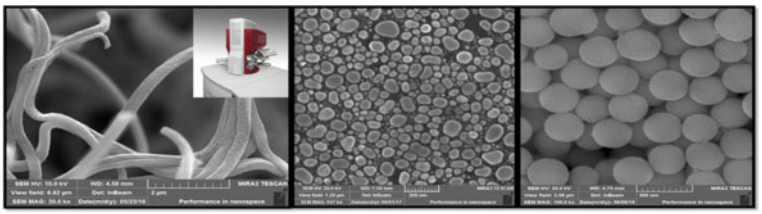

FEI Nova NanoSEM 450: Materials Science and Engineering

Nova NanoSEM 450 field-emission scanning electron microscope (FESEM) was commissioned in service, in the latter half of 2015. Ever since, this machine has been giving service not only to the entire IITK community but also to other academic institutes and industry all across the country. The primary features of the FESEM are as follows:

Resolution: 1.0 nm @ 15 kV Accelerating Voltage: 200 V–30 kV

Max Probe Current: 100 nA XY = 110 mm, Z = 25 mm, Tilt = +75 to −15°, 5 axis, motorized, eucentric stage Various Detectors:

In-lens SE detector (TLD-SE) Everhardt-Thornley SE Detector Low vacuum SE Detector (LVD) BSD in all modes

Continuous mixing of SE and BSE electrons

Integrated plasma cleaner. High and low vacuum operation. Apart from these, it is equipped with some state of the art accessories which further enhance its Characterization abilities.

TEAM-EDS Basic analysis system for SEM include OCTANE Plus. TEAM-EBSD Analysis system with Hikari XP

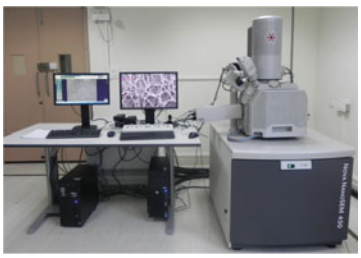

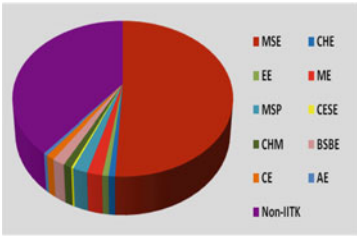

Who can get time on this machine: Anyone from the country can make a request for time on this machine; however, researchers of IITK are given a preference.

How to book: Researchers from IITK can book through the online booking system (Link: https://www.iitk.ac.in/mse/MSE-Facilities/SEM/) located in MSE website. Others can contact the concerned person mentioned below. This facility would soon be available on I-STEM.

Contact		
Ms. Samata Samal	**AIF-T101**	**Email**: **samata@iitk.ac.in**
P.I. Prof. Kantesh Balani	**Biomaterials Lab**	**Email**: **kbalani@iitk.ac.in**

CARL ZEISS EVO 50: Materials Science and Engineering

The CARL ZEISS EVO 50 has been in service since 2007. Ever since, this machine has been giving service not only to the entire IITK community but also to other academic institutes and industry all across the country. This SEM runs with Tungsten electron gun, which gives the highest current stability among all types of emitters.

Accelerating Voltage: 0.2–30 kV

Probe Current: 10^{-12} to 4.91 x 10^{-6}A

5-Axes Motorised Compucentric

Specimen Stage X = 80 mm

Y = 80 mm

Z = 35 mm

T = 0°–90°

R = 360° (continuous)

Resolution: 3.0 nm @ 30 kV

Detectors: SE in HV-Everhart–Thornley BSD in all modes quadrant semiconductor diode

Apart from these, it is equipped with some state of the art accessories which further enhance its characterization abilities.

EDS: Oxford Nano Analysis

EBSD: Oxford Nordlys detector

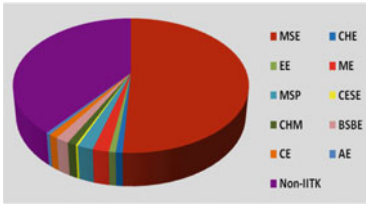

Who can get time on this machine: Anyone from the country can make a request for time on this machine; however, researchers of IITK are given a preference.

How to book: Researchers from IITK can book through the online booking system (Link: https://www.iitk.ac.in/mse/MSE-Facilities/SEM/) located in MSE website. Others can contact the concerned person mentioned below. This facility would soon be available on I-STEM.

Contact		
Ms. Samata Samal	**WL-103A**	**Email**: **samata@iitk.ac.in**
P.I. Prof. Kantesh Balani	**Biomaterials Lab**	**Email**: **kbalani@iitk.ac.in**

CARL ZEISS SIGMA FESEM: Mechanical Engineering

This machine has been in service since 2011. It has a high-resolution imaging capability with a resolution of 5 nm. It is equipped with Energy Dispersive Spectroscopy (EDS) from Oxford Instruments for identifying and quantifying elemental compositions and a retractable Backscatter Electron (BSE) Detector to effectively display the compositional differences in the specimen. This machine is fitted with Evacuator Plasma de-contaminator for clearer images with soft non-conducting materials. A sputter coater is available for gold coating. Apart from these, Gatan 300 N micro-tensile stage is also available.

Features: Acceleration Voltage: 0.1–30 kV

Stage: 5-axis motorised Cartesian, controlled through joysticks/software.

Tilt: −100 to 900

Rotation: 3600 continuous

Booking: A slot can be booked by researchers from within or outside the institute. A slot request can be made through IITK Facility Management Portal. Slot request has to be made only 48 h before the commencement of the slot. Signed copy of the form has to be submitted to Mr. Anurag Goel (NL216).

Current Usage: The set-up is currently used by researchers from various academic departments of IIT Kanpur and the start-ups incubated at the SIIC IIT Kanpur.

Contact		
Ms. Mr. Anurag Goel	**NL-216**	**Email**: **agoel@iitk.ac.in**
P.I. Dr. Manjesh K. Singh	**Old IME Lab**	**Email**: **manjesh@iitk.ac.in**

Transmission Electron Microscope: Materials Science and Engineering

The Electron Microscope Facility (EM Facility) comprises a FEI Tecnai T20 Ultra Twin Transmission Electron Microscope. This microscope equipped with STEM detector, EDS detector, HAADF detector and Gatan digital imaging system. This microscope fitted with thermionic Gun compatible with W and LaB6, which operates at 200 kV. This analytical TEM provides nearly complete microstructural analysis such as imaging, micro-diffraction, nano-diffraction, CBED, lattice imaging, elemental analysis, STEM imaging, HAADF imaging for range of materials including metals, ceramics, semiconductors, thin films, polymers and biological materials. This machine attains a maximum resolution of 1.4 A° and the magnification extends up to 1 MX.

Contact		
Mr. Manohar Oraon	WL-207	Email: moraon@iitk.ac.in
P.I. Prof. Vivek Verma	FB-418	Email: vvivek@iitk.ac.in